Bioabsorbable composite laminates of PLA reinforced with surface-modified Mg wires for orthopedic implant applications

by

SYED WAHAAJ ALI RIZVI

A dissertation submitted in partial fulfillment of the requirements for the degree of Doctor of Philosophy in

Material Science and Engineering

Universidad Carlos III de Madrid

Advisors:
Javier Llorca
Carlos Daniel González Martínez

Tutor:
Mónica Campos Gómez

July 2023

This thesis is distributed under license “Creative Commons **Attribution – Non Commercial – Non Derivatives**”.

To,

My beloved wife Fatima & Amma, Baba

ACKNOWLEDGMENTS

First of all, I want to thank my principal supervisors, Javier Llorca and Carlos Gonzales at IMDEA materials institute with the help of a saying of Ali ibn Abi Talib to acknowledge their efforts and character:

"A person's intellect becomes apparent through his dealings, and a man's character is known by the way he exercises authority"(Ali ibn Abi Talib)

I found my supervisors cooperative in dealings and always supportive in my training with a humble attitude. I learned many things from them, which I will carry on in my life to continue their legacy to benefit myself and others. I also want to thank Dr. Alexander Kopp, who provided me with guidance and Leon Tillman for assistance during my industrial secondment at Meotec GmbH, where I made significant achievements by developing a Continuous PEO system.

Being a mechanical engineer and able to deal with biological cells was not possible without Dr. Monica Echeverry. I want to thank her for teaching me biological tests. She was always available for healthy discussions. I also acknowledge the help of Guillermo and Jesus in Biological tests.

Technicians are *magicians*; without their support, I could not have accomplished my many tasks. I want to acknowledge the help of Vanessa, Jose Luis, and Javier Garcia the technicians from IMDEA, who brought my ideas like, wire placement system, push-out test, and thermoforming into the real world. Smooth completion of this Ph.D. thesis was impossible without cooperative administrative staff of IMDEA materials and many colleagues, especially Cillian, Carolina and Yuyao.

If I have seen further, it is by standing on the shoulders of giants (Isaac Newton)

I also want to thank thousands of humans in history who discovered the knowledge on which my thesis depends and they made it available to us for further advancements.

From an underprivileged background without proper schools to the completion of Ph.D. from a reputable institute like IMDEA material and under a prestigious Marie Curie program was impossible without prayers, hard work, and sacrifice of my father (Zakir) and mother (Shamim). I am certainly thankful to them. This ~4 years journey of Ph.D. would have been difficult without my wife (Fatima), who moved with me to Spain away

from her parents, sacrificed her many interests and gave me moral support in difficult times.

Lastly, I want to acknowledge financial support by the European Union's Horizon 2020 research and innovation programme under the European Training Network BioImpant (Development of improved bioresorbable materials for orthopedic and vascular implant applications), Marie Skłodowska-Curie grant agreement No 813869.

PUBLISHED AND SUBMITTED CONTENT

Journal articles

- S. Kovacevic, W. Ali, E. Martínez-Pañeda, J. LLorca, Phase-field modeling of pitting and mechanically-assisted corrosion of Mg alloys for biomedical applications, Acta Biomater. 164 (2023) 641–658. https://doi.org/10.1016/j.actbio.2023.04.011
  The experimental part of this publication is included in chapter 3 of the thesis.

- W. Ali, M. Echeverry-Rendón, G. Dominguez, K. van Gaalen, A. Kopp, C. González, J. LLorca, Bioabsorbable WE43 Mg alloy wires modified by continuous plasma-electrolytic oxidation for implant applications. Part II: degradation and biological performance, Biomater. Adv. 147 (2023).
  https://doi.org/10.1016/j.bioadv.2023.213325
  The content of this publication is wholly included in chapter 3 of thesis.

- W. Ali, M. Li, L. Tillmann, T. Mayer, C. González, J. LLorca, A. Kopp, Bioabsorbable WE43 Mg alloy wires modified by continuous plasma-electrolytic oxidation for implant applications. Part I: Processing, microstructure and mechanical properties, Biomater. Adv. 146 (2023) 213314. https://doi.org/10.1016/j.bioadv.2023.213314
  The content of this publication is wholly included in chapter 3 of thesis.

- Mohammad Marvi-Mashhadi, Wahaaj Ali, Muzi Li b, Carlos Gonz´alez, Simulation of corrosion and mechanical degradation of additively manufactured Mg scaffolds in simulated body fluid, J. Mech. Behav. Biomed. Mater. 126. 126 (2022). https://doi.org/10.1016/j.jmbbm.2021.104881
  The content of this publication is not included in this thesis. The main contribution of the author of the thesis in this publication was the development pitting corrosion model.

- W. Ali, M. Echeverry-Rendón, A. Kopp, C. González, J. LLorca, Strength, corrosion resistance and cellular response of interfaces in bioresorbable poly-lactic acid/Mg fiber composites for orthopedic applications, J. Mech. Behav. Biomed. Mater. 123 (2021) 104781. https://doi.org/10.1016/j.jmbbm.2021.104781.
  The content of this publication is not included in this thesis.

- W. Ali, M. Echeverry-Rendón, A. Kopp, C. González, J. LLorca, Effect of surface modification by plasma-electrolytic oxidation on interfacial strength, corrosion mechanisms and cytocompatibility of bioabsorbable PLA/Mg wire composites. **(under revision in NPJ materials degradation)**
  The content of this publicaiton is wholly included in chapter 4 and 5 of thesis.

Journal articles to be submitted

- W. Ali, A. Kopp, C. González, J. LLorca, Bioabsorbable composite laminates of PLA reinforced with PEO-modified Mg wires for orthopedic implant applications. Part I: Manufacturing, mechanical and degradation perfomance **(Expected submission in July 2023)**
  The content of this publication will be mainly from chapter 4 and 5 of thesis.

- W. Ali, J. Ordoño, A. Kopp, C. González, M. Echeverry-Rendón, J. LLorca, Bioabsorbable composite laminates of PLA reinforced with PEO-modified Mg wires for orthopedic implant applications. Part II Cytotoxicity, proliferation and differentiation **(Expected submission in July 2023)**
  The content of this publication will be mainly from chapter 6 of thesis.

Conference presentations:

- 32th Annual Conference of the European Society for Biomaterials, September 2022, *Biocompatibility, mechanical and degradation behavior of bioresorbable composite of PLA matrix reinforced by Mg fibers for orthopedic applications***,** Bordeaux, France (**Poster presentation**)

- 14th Symposium on Biodegradable Metals, August 2022, Effect of processing conditions on mechanical and in vitro degradation behavior of magnesium WE43 alloy wires, Alicante, Spain **(Oral Presentation)**

- 11th European Solid Mechanics Conference, July 2022, *Mechanical behavior and cytotoxicity of the bioresorbable composite of PLA reinforced with PEO coated Magnesium fibers for orthopedic applications*, NUIG, Galway, Ireland **(Oral Presentation)**

- 20th European Conference on Composite Materials, June 2022, *Manufacturing, mechanical and degradation behavior of Mg/PLA bioresorbable composite laminates for orthopedic applications*, EPFL, Lausanne, Switzerland **(Oral Presentation and conference paper)**

ABSTRACT

Bioabsorbable metal-polymer composites of magnesium (Mg)/poly-lactic acid (PLA) can overcome some of the challenges associated with non-degradable metals (Ti, stainless steel, etc.) as well as degradable metals (Mg, Zn, Fe, etc.) and degradable polymers (PLA, PLGA, etc.) in orthopedic implant applications. This thesis deals with the development of manufacturing process for surface modification of bioabsorbable Mg wires and Mg wires/PLA composites and the detailed characterization of mechanical, degradation and biological performance. Microstructure of cold-drawn Mg wire could be tuned by processing conditions which allowed to tailor its mechanical and corrosion properties. However, wire strength dropped to negligible values in just 24 h of *in vitro* degradation due to fast and pitting corrosion. To overcome this limitation, a novel and scalable strategy of Continuous Plasma Electrolytic Oxidation (C-PEO) process was developed for seamless surface modification of Mg wires that introduced a protective oxide layer on the surface of Mg wires which improved corrosion resistance and strength retention of wires (100 MPa after 96 h) and favored cells adhesion. Mg and PEO-modified Mg wires were used to manufacture unidirectional and multi-directional Mg/PLA composite laminates by hot compression. Mechanical, degradation and biological properties of the composites were studied at both constituent and bulk levels. The mechanical response of composites in tension, compression, and in-plane shear was characterized and was found to be dependent on the orientation of wires. Push-out tests revealed that the PEO oxide layer increased the strength and toughness of the interface between the Mg wire and PLA, which was reflected in the high ductility of unidirectional (in longitudinal tension) and quasi-isotropic composites. Interface strength and bulk mechanical properties of composites decreased during *in vitro* degradation of 42 days. It was found by180 days long *in vitro* degradation study that the presence of Mg wires accelerated the degradation in comparison to pure PLA, while Mg wires were completely corroded, whereas PEO modification suppressed the corrosion of Mg wires. Finally, composites were found to be cytocompatible, and favored proliferation and differentiation of cells. In summary, Mg/PLA composite is a suitable candidate for the next generation of bioabsorbable orthopedic implants, such as fixation plates, as its mechanical properties can be tailored by stacking sequence of Mg wires while at the same time, the degradation rate can be controlled by PEO surface modification of Mg wires.

The wise aim at perfection

(Ali ibn Abi Talib)

TABLE OF CONTENTS

CHAPTER 1: INTRODUCTION

1.1. Bone

Skeleton is the most important organ of the human body made up of 206 bones of different shapes and sizes. Bones facilitate the movement of the human body by the transmission of loads between different parts by tendons, ligaments and bone-to-bone contact. Their functions also include the protection of certain organs (e.g., the heart and brain) from mechanical damage, and as reservoirs of minerals and medium–marrow– for the development of blood cells and essential cells for the immune system. The wholistic properties of bones, such as density, mechanical performance, etc., are controlled by structural properties and chemical composition (mainly mineral-collagen content), which depends on evolutionary and environmental factors and vary in human beings with respect to their age, gender, anatomical site, etc. [1][2]. Bones can be short (e.g., tarsal), long (e.g., tibia and femur), flat (e.g., skull and ribs), irregular (e.g., vertebrae), and sesamoid (e.g., patella) [3].

1.1.1. Structure

Bone has a natural hierarchical structure with different features at each scale which control the overall mechanical behavior of bones. At the macroscopic level, bones can be divided into cortical and cancellous (trabecular) regions, which are commonly observed in long bones such as the femur and tibia (Fig. 1). The outer region of bone is composed of hard and dense (5-10% porosity) protective shell called cortical bone while the inner region of cancellous bone is porous (typically 75-95%) and filled with marrow [2]. Usually, the thickness of cortical bone in load-bearing bones (pelvic, tibia, femur) is larger to provide high strength. Cancellous bone is present in vertebrae, proximal ends of long bone, etc. and its porosity is architected in the direction of principal stresses to maximize the bone strength following Wolff's law as shown in Fig 1b. This composite structure provides high specific stiffness and strength as well as good energy dissipation capabilities [4].

At the micro-level scale, bone structure can be further divided into lamellar and woven bone. Lamellar bone is organized along the long axis of bone and can be arranged circumferentially below the periosteum or concentrically (osteon) away from the

periosteum. Osteon consists of several concentric layers (3-7 μm thick) –each with different orientation– of the anisotropic matrix of collagen fibers interdigitated with mineral plates. The central part osteon is called the Haversian canal, oriented in the direction of the osteon, while the short transverse channels connecting the Haversian canals are called Volkmann's canals. The system of canals provides space for blood vessels, nerves, and connective tissue, which supply the osteocytes (old osteoblasts embedded in bone matrix) and other bone cells with nutrients and oxygen, as shown in Fig. 1.1. On the contrary, woven bone is a weak and disorganized tissue which is quickly formed during early stages of fracture healing and eventually replaced with lamellar bone by remodeling.

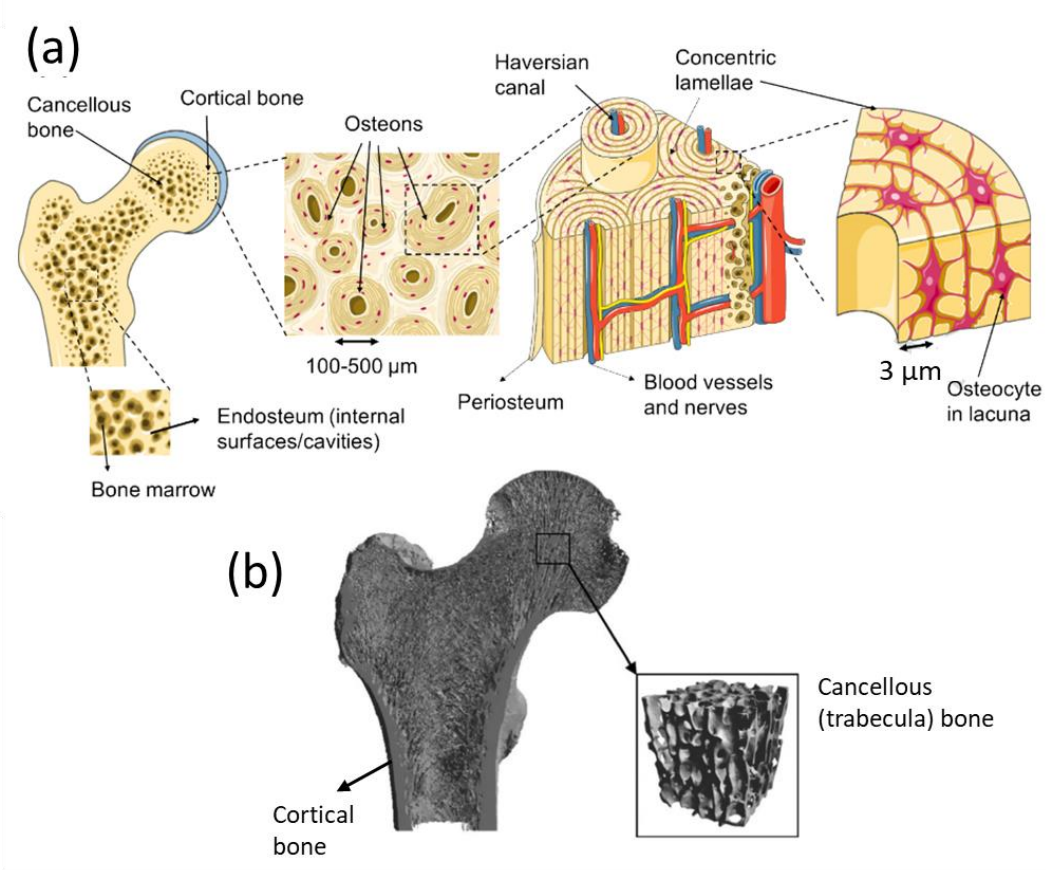

Fig. 1.1. (a) Multiscale structure of bone [3] (b) Cortical and cancellous bone [4]

1.1.2. Composition

At the nano-scale, bone is mainly composed of an organized organic matrix of type 1 collagen mineralized with nano-crystalline apatite $(Ca_{10}PO_4)_6(OH)_2$ with a small quantity of water and non-collagenous proteins, as shown in Fig. 1.2. The amount and maturity of the Type I collagen in bone, and cross-links between its fibers affect strength, stiffness and toughness of bone tissue. The apatite mineral (rod or plate-shaped) nucleates in the spaces between collagen fibrils and also in the ends as well as in the gap between longitudinal fibrils with their c-axis aligned in the direction of structure of bone. There are also multiple bone cells that work together in maintaining the structure and composition of bone and can be categorized into bone resorbing and bone forming cells, as summarized in Table 1.1. [2][3][5]

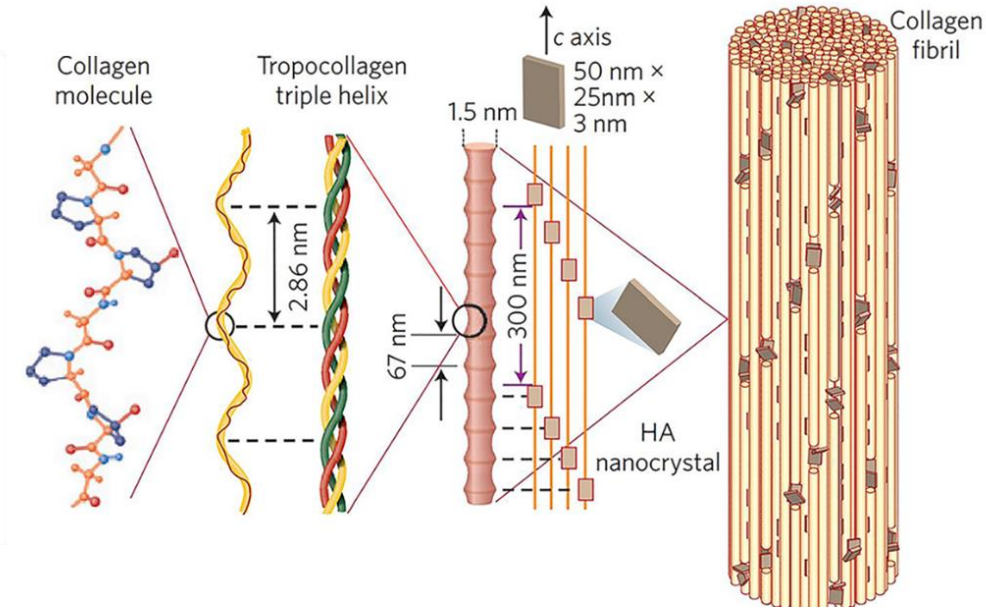

Fig. 1.2. Hierarchical structure of bone at the nano-scale [5]

Table 1.1. Source and main functions of bone cells [2]

Cell type	Source	Main functions
Osteoclasts	Fusion of monocytes from bone marrow	Break down and resorb old bone tissue; participate in mineral homeostasis
Osteoblasts	Differentiated from mesenchymal stem cells in bone marrow and other tissues	Synthesize and deposit new bone tissue; regulate activity of osteoclasts; participate in mineral homeostasis
Osteocytes	Former osteoblasts that have become embedded within bone matrix	Regulate bone metabolism; maintain structural integrity of bone tissue; sense mechanical stress and strain on bone
Bone lining cells	Osteoblasts that have become quiescent	Maintain communication between osteocytes and each other; regulation of minerals; bone remodeling in response to chemical and mechanical stimuli

1.1.3. Mechanical behavior of bone

The geometrical structure and composition of bone determine the mechanical behavior of the whole bone at the macroscopic level and varies in human beings with respect to their age, gender, anatomical site, etc [1]. Ideally, bone should have sufficient strength to avoid failure and high stiffness for minimum metabolic energy consumption in bone deformation during daily activities. Nature has crafted the mechanical properties of each bone according to their functional requirement. For instance, bones in ear are very stiff because it has to transfer sound waves efficiently. Similarly, long bones of children are more compliant (less stiff) as compared with adults to handle shocks [2] .

The mechanical behavior of bones is variable among different bones and humans but cortical bone is stiff and can withstand high stresses as compared to cancellous bone. For instance, the compressive strength of cortical bone can reach up to 150 MPa with a failure strain of ~ 3%, while cancellous bone can withstand lower stresses (~50 MPa) but with much higher failure strains (~50%) [6] (Fig. 1.3a). At the microscopic level,

the mechanical behavior of bone depends of several factors like density, the orientation of osteons, collagen-mineral composition etc. Generally, cortical bone is stiff along the long axis because osteons are oriented in this direction as compared to the transverse direction (Fig, 1.3b). Bone is a dynamic tissue, and its structure and composition change with modeling and remodeling phenomena over a period of time. As shown in Fig. 1.4, the tensile and compression strengths in both males and females decreases with the age due to osteoporosis. Male bones usually have higher strengths owing to the evolutionary differences. Similarly, the elastic modulus (stiffness indicator) also depends strongly on the density (mass per unit volume) of bone and increases with bone density. Cancellous bone has elastic modulus < 5 GPa, while it varies between 10 to 28 GPa for cortical bone.

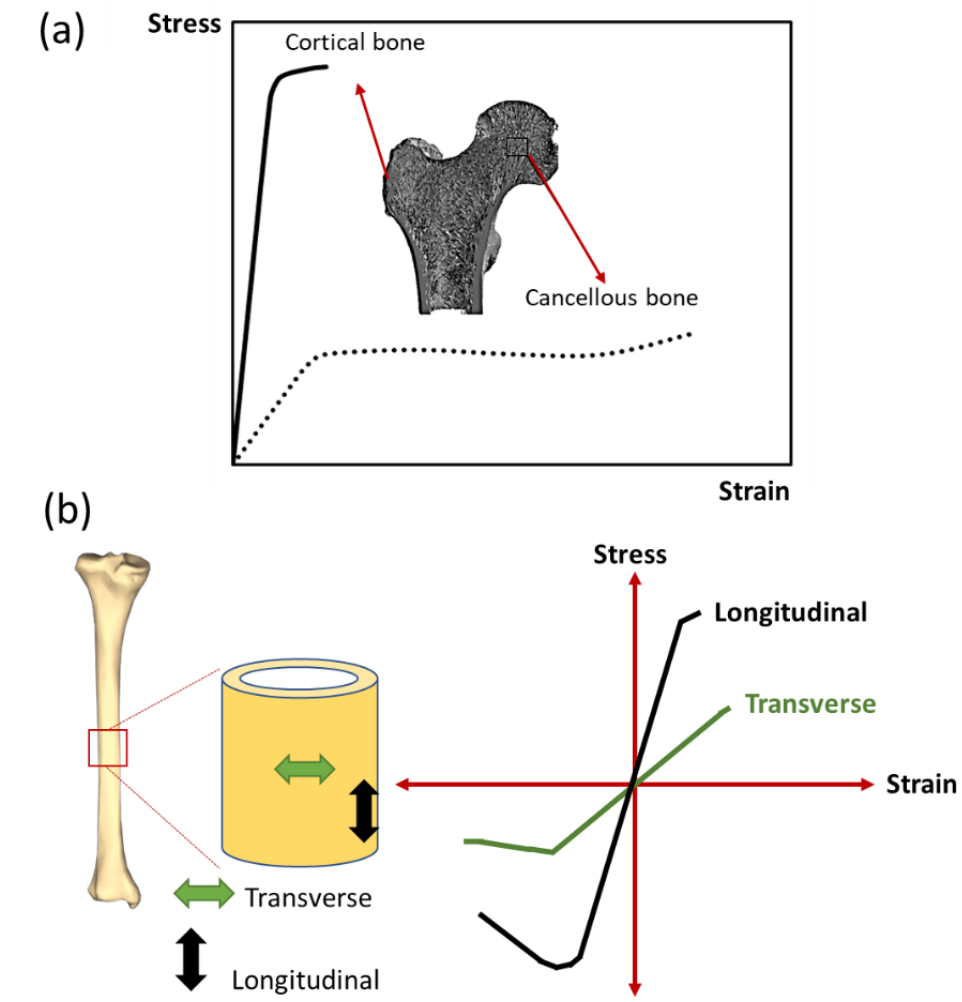

Fig. 1.3. (a) Schematic of stress-strain behavior of cortical and cancellous bone in compression. (b) Schematic of stress-strain behavior of cortical bone in transverse and longitudinal directions in tension and compression. Schematics have been drawn based on data from [6][7].

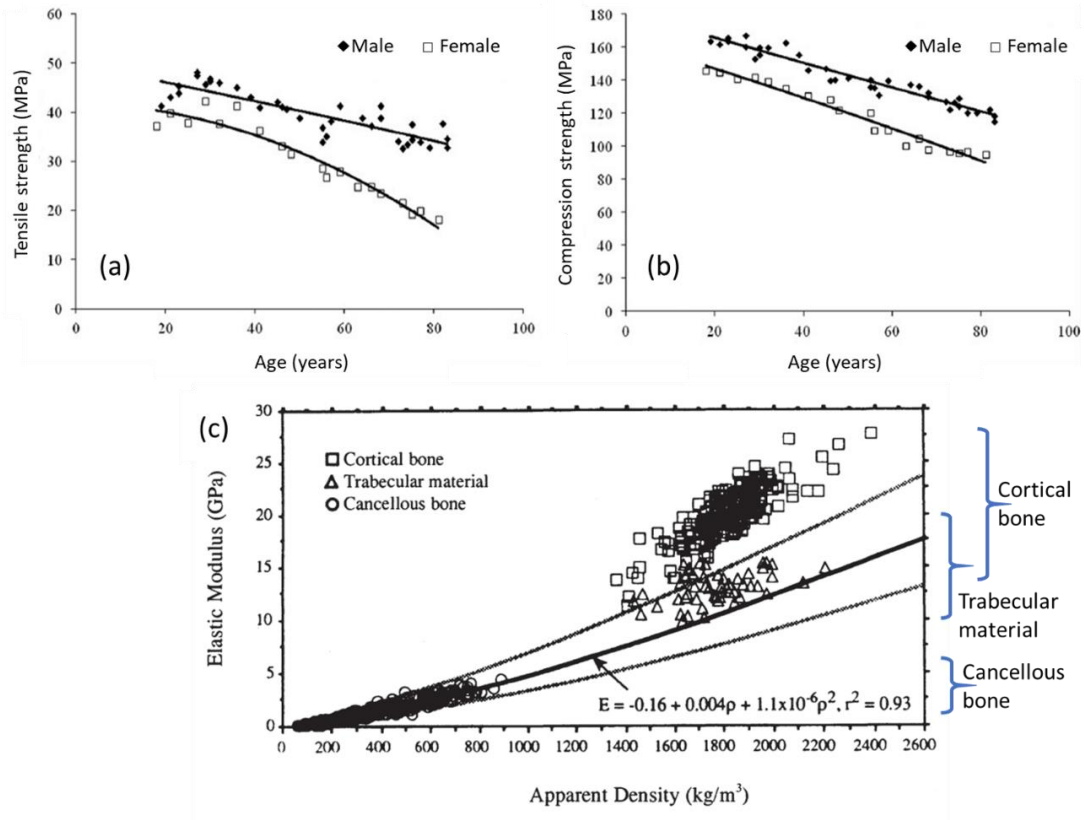

Fig. 1.4. Tensile strength (a) and compressive strength (b) *vs.* age for the femur cortical bone [8]. (c) Elastic modulus *vs.* apparent density for cancellous (circles) and cortical (squares) bone [2]. Blue brackets show an approximate range of modulus values for each type of bone.

1.1.4. Bone fractures

Bone fractures is one the most common human diseases. Fractures can occur by extrinsic causes such as trauma from vehicle accidents, sports injuries, and falls, etc. where high impact loads fracture bone. Intrinsic causes of bone fracture include certain pathologies that weaken the bone structure, such as osteoporosis or bone cancer. In these cases, the bone may fracture as a result of normal or minimal levels of stress that would not typically cause a fracture in a healthy bone [9]. A recent study, conducted by Swedish Fracture Register (SRF), found that mean age of fracture was 57.9 years and ~65 % fractures occurred in women confirming that elderly women are more prone to bone fractures. The five bones accounted that account for more than 50% of all fractures are the distal radius, proximal femur, ankle, proximal humerus, and metacarpal fractures [10]. There were 3.5 million reported fractures caused by bone fragility in the European Union in 2010, with an economic healthcare cost of 37 billion euros. These figures are expected to rise by 25% by 2025 [11]. There is a standard classification of

bone fractures developed by AO/OTA for every bone depending on type of bone, location within bone, pattern of fracture and degree of displacement and fragmentation [12]. A typical classification for long-bone fracture is shown in Fig. 1.5. Implant designers use the classification to design suitable implants as well as surgeons for suitable guidelines of treatment and implant selection.

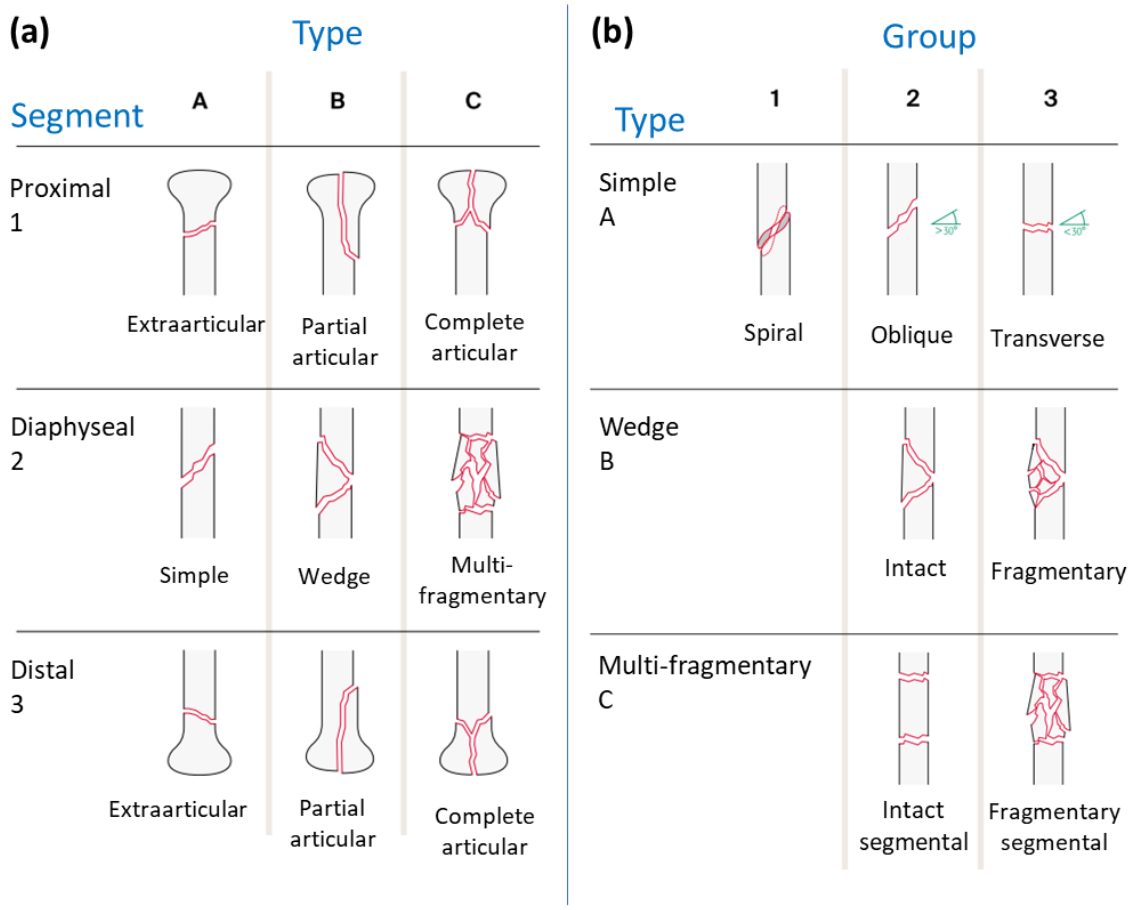

Fig. 1.5. Classification of long-bone fractures by AO foundation [12], (a) Classification according to segment of bone and (b) further classification for diaphyseal fractures based on type of fracture.

1.1.5. Healing process

Bone is a dynamic tissue that undergoes constant remodeling to adapt to changes in mechanical stresses and to repair defects. It has the ability to regenerate and heal without leaving any scar, returning to its original form and function over a period of time depending on the severity of defect [13]. Bone is formed by the combination of intra-membranous and endochondral ossification in embryo and children, while the latter is absent in adults, and bone is formed directly by osteoblasts during healing. The mechanical stability and displacement between fractured ends of the bone are the most

crucial factors influencing the healing process. An initial (or later during healing period) misalignment can lead to a non-union or mal-union of bone. The natural healing process of a typical bone fracture is a cascade of events and can be categorized into four distinguishable but overlapping events, as shown in Fig. 1.6 [2][14]. It starts with an inflammatory response of 3-7 days, resulting in hematoma formation at the fracture site by supplying mesenchymal stem cells and osteoprogenitor cells from periosteum and marrow, which quickly differentiate into bone forming cells. Then periosteal (external) and medullary (internal) calluses are formed by osteoblasts, also called soft callus (or woven bone or cartilaginous material). It takes a week or two for this soft callus to produce enough minerals which after further calcification, are eventually replaced by a hard or bony callus. The callus formation stage is also influenced by mechanical stresses which can affect the differentiation pathways of cells [15] and optimal interfragmentary movement at fracture site has shown efficient healing [4]. The last phase is remodeling of bone which can begin as early as the third week after the fracture and can take years to complete. At this stage, bone restores its internal structure, and also its original shape and contour and hard callus is slowly replaced with secondary lamellar bone. Overall, the healing process is complex and influenced by many factors, such as mechanical loads, type of bone, patient condition, etc. [14]. The process of bone healing in the presence of an implant (peri-implant healing) is similar as explained above but, in this scenario, *de novo* bone can form (if the material is osteoconductive) between implant and bone by a phenomenon known as distance and contact osteogenesis which depends on surface chemistry and topography of implant. Moreover, the high contact pressure between the implant and bone can negatively affect healing processing [16].

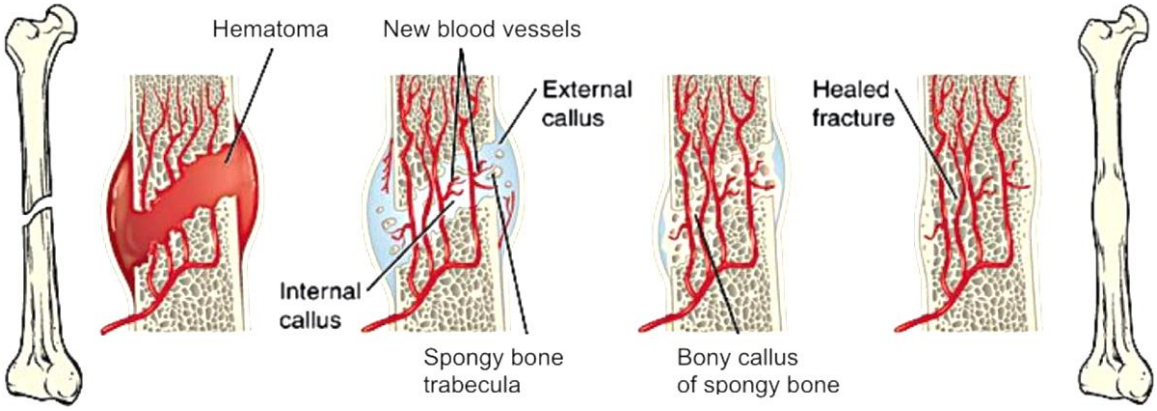

Fig. 1.6. Natural healing process of bone: (1) hematoma formation, (2) soft callus, (3) hard callus, and (4) remodeling [14].

1.2. Orthopedic devices for fracture fixation

Bone can naturally recover, but some defects require clinical interventions for proper healing using fixation devices and tissue grafts. Trauma or orthopedic fixation is a sub-category of orthopedics devices that aims to repair bone fracture which cannot heal without the use of implants [17]. The main goal of an orthopedic fixation is to reduce and immobilize the bone fracture site during the healing process. The reduction of fracture site can be achieved non-surgically (external manipulation of bone) or surgically by use of internal and/or external fixation devices (Fig. 1.7). Commonly used internal fixation devices include pins, wires, intramedullary nail, plates and screws [18][19] while external fixators include bar or ring fixator clamped with screws or pins passing percutaneously. External fixators offer minimal damage to soft tissue but limit the patient's mobility; second surgery is necessary to restore mobility. On the other hand, internal fixators such as, plates and screws, are surgically implanted at the fracture site with the goal of preventing its movement and ensuring proper distribution of loads at the fracture line [20]. In many cases, the internal fixators are implanted for permanent stay and removed when bone has to grow (in children) or when it causes infection, swelling or fails mechanically, etc. [19]. The field of fracture fixation devices has matured in the last century with the multitude of innovative devices commercially available in the market from which a surgeon chooses a suitable option depending on the scenario [17].

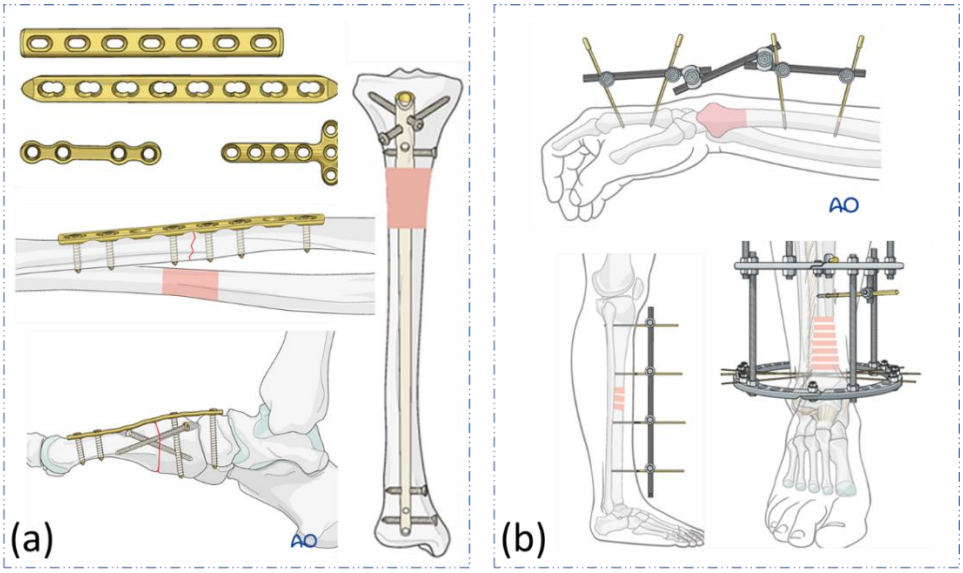

Fig. 1.7. Schematics of commonly used orthopedic fixation devices: (a) internal fixators and (b) external fixators [21].

1.3. Design requirements of internal fixation device

The biological environment of the internal fixation device consists of highly corrosive medium and mechanical loads. Therefore, the device must be designed to have certain functionalities. High concentration of chlorine ions, various amino acids and proteins present in body fluids makes corrosion a severe concern to implant (especially for metals). In addition, dissolved oxygen and interaction with cells and bacteria also influence corrosion of devices. Therefore, the device should be bioinert and corrosion resistant, particularly in non-degradable materials. It should be non-toxic and should have suitable mechanical properties (strength, stiffness, fatigue resistance, etc.). Ideally, it should promote bone healing (osteoconductive) or at least doesn't impede the natural healing process. The device structure, especially thickness and width, should be designed to have optimal stiffness (to minimize stress shielding). It should also contain carefully designed features like contours, holes and chamfers (for plates), and threads (for screws) for proper mechanical stability with bone. Moreover, the material properties of the device like toughness, elasticity, radiopacity, resorption, bioactivity, surface treatment, and sterility are required as per application [17][22][23].

1.4. Non-degradable metals for orthopedic fixation

Conventional materials for orthopedic devices can be categorized into metals, polymers and ceramics. Metals stand out as the most utilized biomaterials for orthopedic fixation devices due to its high corrosion resistance, workability, and high strength and stiffness, providing them large fracture toughness compared to polymers and ceramics [23]. Established non-degradable polymers include Polymethyl methacrylate (PMMA), which is used as bone cement, while in ceramics, Al_2O_3 and ZrO_2 are used on the surface of implants [24] but their applications are limited due to their poor mechanical properties. Best choice metals for orthopedic fixation include stainless steels, Co-Cr alloys, and Ti and its alloys, which are used in applications such as spinal fixation, bone fixation (screws, plates, nails, wire), and artificial joints, etc. [23]. These can be processed to have different mechanical properties (Fig. 1.8). Stainless steel offers high strength and ductility but its high stiffness produces stress shielding in bone, leading to osteoporosis. Its stiffness can be reduced by making thinner plates, but it compromises the fatigue behavior. As an alternative Ti and its alloys (Ti-6Al-4V) are preferred for internal fixation devices such as bone plate due its lower stiffness, high strength, greater fatigue resistance and osteoconductive nature [20]. Also, the oxide film formed on the Ti surface is more stable, making it safer from the adverse effects of released ions in the human body [24]. Co-Cr alloys offer excellent wear resistance and are currently used as established material in heads of the artificial knee and hip joint heads [23]. However, Cr^{3+} ions raises serious health concerns if released into the human body [24].

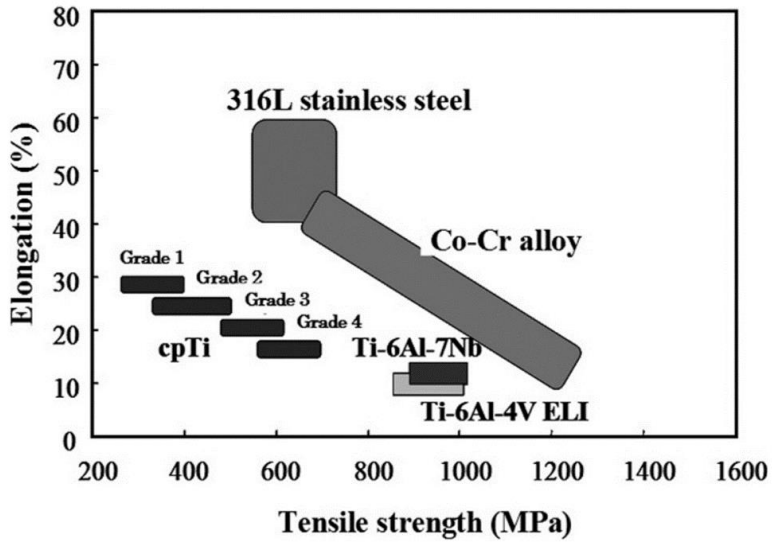

Fig. 1.8. Relationship between elongation to fracture and tensile strength of conventional metals [23].

1.4.1. Challenges

Conventional metals are and probably will maintain their position as the most used biomaterial in orthopedic fixation devices, but following challenges associated with them drive the quest for new materials [9][24][25][26]:

1. High stiffness than human bone can cause stress shielding effect on the bone which leads to inefficient healing and osteoporosis.
2. A second surgery to remove the implant is necessary in many scenarios, such as pediatric fractures, and to avoid long-term side effects, which increases the overall recovery cost. Patients often bear limited mobility for several days/months after implant removal.
3. Metal alloying offers limited independence in tailoring the mechanical and biological properties of materials. For instance, the addition of an alloying element might improve mechanical performance but can compromise biocompatibility.
4. The release of metal and alloying element ions poses serious dangers to health.
5. Other complications include soft tissue irritation, palpability, malunions, etc.

1.5. Bioabsorbable materials

Thanks to advances in medical technology, a wide range of bioabsorbable (or bioresorbable or biodegradable) materials have been developed for different tissue engineering applications, which partially solved a main challenge related to non-degradable implants i.e. permanent stay inside the human body and, in many cases, an

inevitable second surgery for implant removal to avoid long-term complications. Bioabsorbable devices are designed to be safely absorbed in the human body after completing their intended functions through different degradation mechanisms, which depend on the material properties of the device and the host's immune response [27]. As depicted in Fig. 1.9, mechanical properties (stiffness and strength) of bioabsorbable materials degrade over time as a result of mass loss by biocorrosion, while stiffness and strength of tissue increases as a result of healing. The interplay between the drop and gain in mechanical properties of implant and tissue plays a critical role in the successful outcome [28]. Many bioabsorbable materials, including polymer, ceramic, metals, and composites, have received market approval for applications in orthopedic fixation (interference screws for ACL reconstruction, screws and plates for maxillofacial surgery), wound closure (sutures and dressings), cardiovascular (stents), etc [27]. With the development of new bioabsorbable materials, their acceptability is also increasing. In a randomized survey about the perception of implants, 95% of patients considered the removal of implant as the most negative aspect and appreciated the “resorbable” feature [29]. However, non-degradable implants cannot be replaced in every application, like spinal fusion, hip and knee joint replacement, etc.

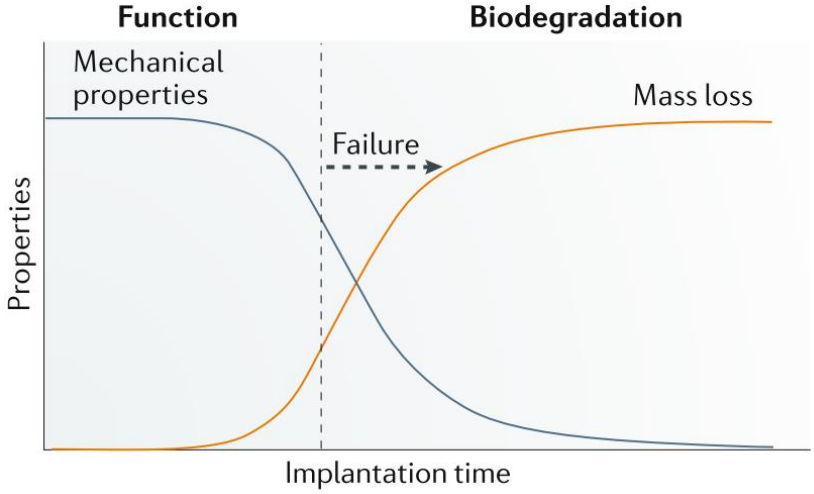

Fig. 1.9. Desired relationship between mechanical properties and mass loss of bioabsorbable implant after implantation [27].

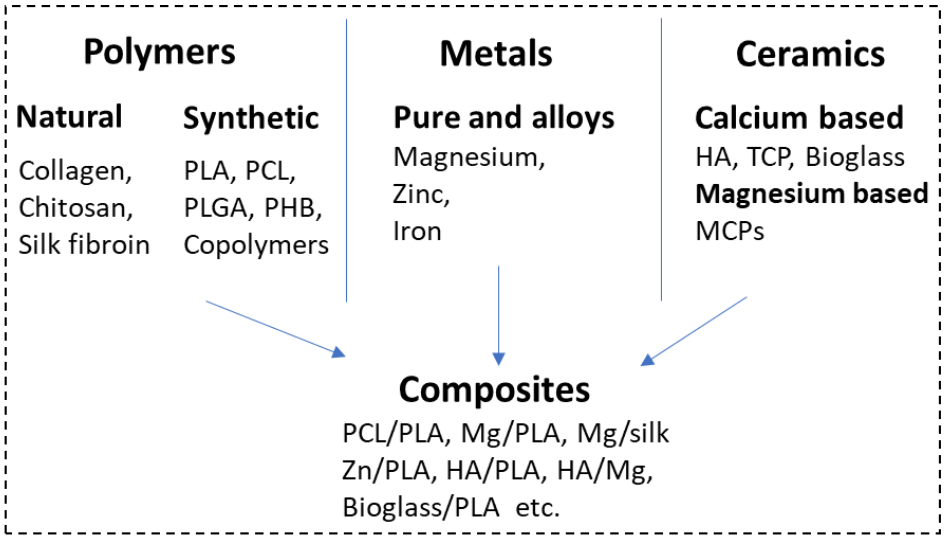

Fig. 1.10. Different bioabsorbable materials

Bioabsorbable materials include polymers, ceramics, metals, and their composites (Fig. 1.10). They support the fractured/weak tissue construct while degrading completely overtime through different mechanisms. Bioabsorbable polymers can be categorized into natural and synthetic polymers [27]. Natural polymers derived from animals or plants, such as collagens, gelatins, and polysaccharides, have been successfully used as sutures and dressings for wound closure [30]. Collagen particles have been used to improve mechanical properties and proliferation of osteoblasts of composite scaffolds [5]. Most recently, silk proteins (*Bombyx Mori*) have also drawn attention due to their excellent biocompatibility and unique mechanical properties. There is a large source to harvest natural polymers, but they show a considerable batch-to-batch variation (as in silk fibroin), primarily due to different degumming conditions. Synthetic bioabsorbable polymers, such as PLA, PGA and copolymers, can be manufactured with reproducible properties which can be tailored by molecular weight, cross-linking, crystallinity, etc. [31]. Polyglycolide acid (PGA) sutures were the first synthetic bioabsorbable polymer device that entered the market in the 1960s. PGA had a fast degradation rate, and later Poly-Lactic acid (PLA) was also developed with a slower degradation rate [30]. Polymer degradation results in acidic by-products that can locally decrease the pH near the implant and enhance the inflammatory response. A study published in 1999 compared adverse tissue responses of orthopedic fixation devices made up of PGA (fast degrading) and PLA (slow degrading) polymers and reported 5.3% and 0.2% incidences, respectively. The adverse response was also delayed in the case of PLA

revealing some relation between the degradation rate and adverse response [32]. In the last two decades, understanding of the degradation kinetics of synthetic polymers has improved significantly [33] and, as a result, a considerable number of approved orthopedic fixation devices (such as Fig. 1.11a) and vascular stents exist in the market. They are, however, limited to low-load bearing applications because polymers have poor mechanical properties [27].

Biodegradable metals (Mg-based, Zn-based, and Fe-based) have also emerged as potential candidates for bioabsorbable devices. Metals have superior mechanical properties (elastic modulus, strength and toughness) as compared to polymers. They also have good formability, osteogenic capacity, and antibacterial properties. Mg alloys are the most studied for implant applications such as fixation plates, screws, pins, wires, and stents, because of their low elastic modulus (~45 GPa), good strength as well as biosafety, biodegradability, and radiopacity. Advancements in alloying and surface treatments also played a crucial role in the clinical translation of Mg alloys into fixation screws and stents (Fig. 1.11c). Fe alloys have slow degradation rate and produce insoluble degradation products, which restricts their usage. Zn alloys offer a moderate degradation rate, higher stiffness (~90 GPa) but much lower strength than Mg, and stand for the next potential candidate after Mg.

Bioabsorbable ceramics such as hydroxyapatite (HA), di and tri-calcium phosphate (DCP and TCP), etc., could beideal candidates for bone tissue engineering because the mineral phase extracellular matrix (ECM) is made up of similar elements, but the brittle nature of these ceramics limits their wide usage in internal fixation devices. Their applications include calcium phosphate- and magnesium phosphate-based bone cements [34], HA enhanced non-degradable PEEK (surface treated) polymer for spinal implant [35], and HA/PLLA bioabsorbable composites (Fig. 1.11d) for maxillofacial fractures [36].

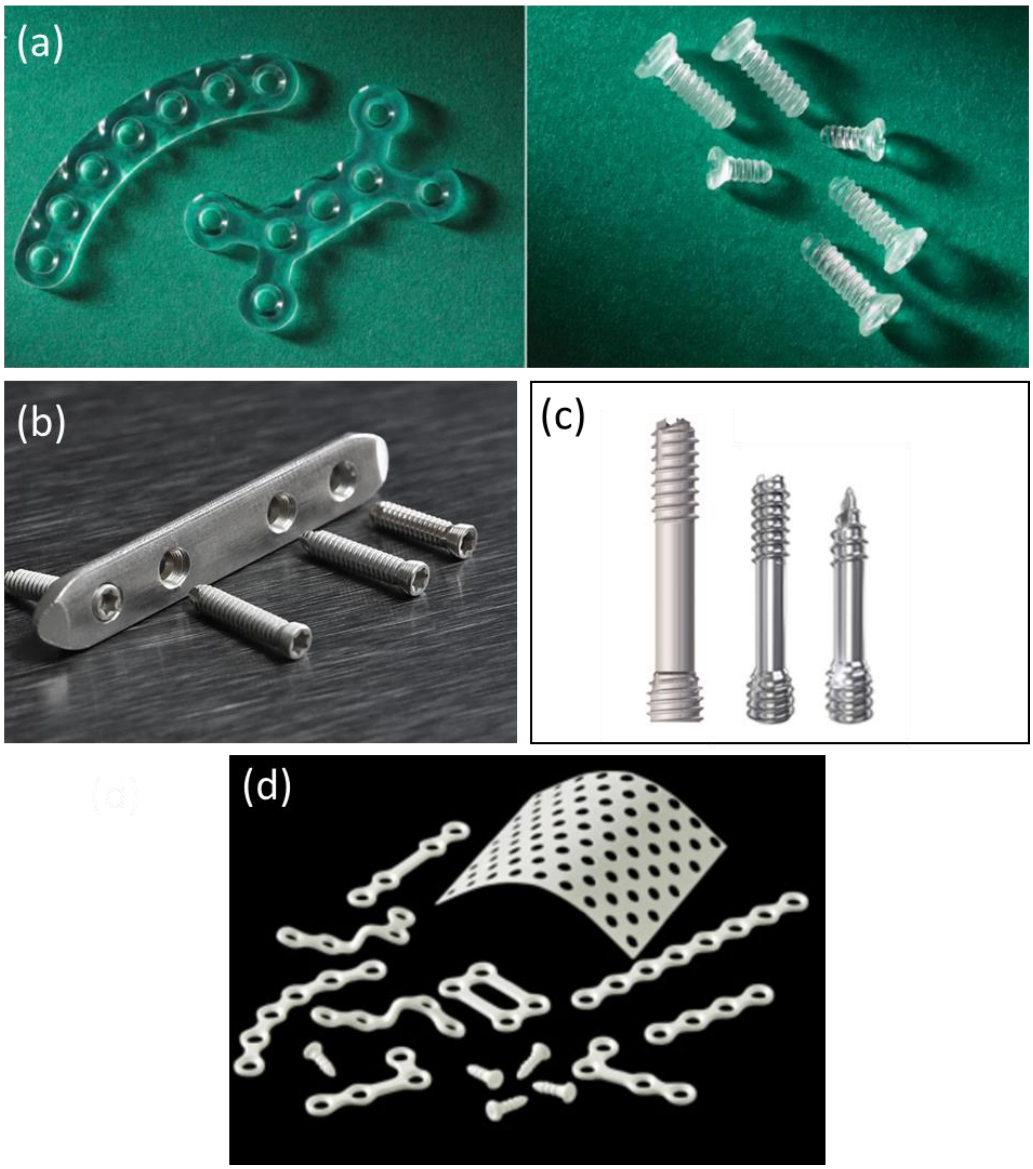

Fig. 1.11. Bioabsorbable plates and screws of (a) polymer, Inion CPS® system [20], (b) magnesium, BioMg® [37], (c) magnesium, MAGNEZIX® CS [38] and (c) HA/PLLA composite, OSTEOTRANS^{TM} MX [39].

1.5.1. Immune response for implants and *in vivo* degradation mechanism

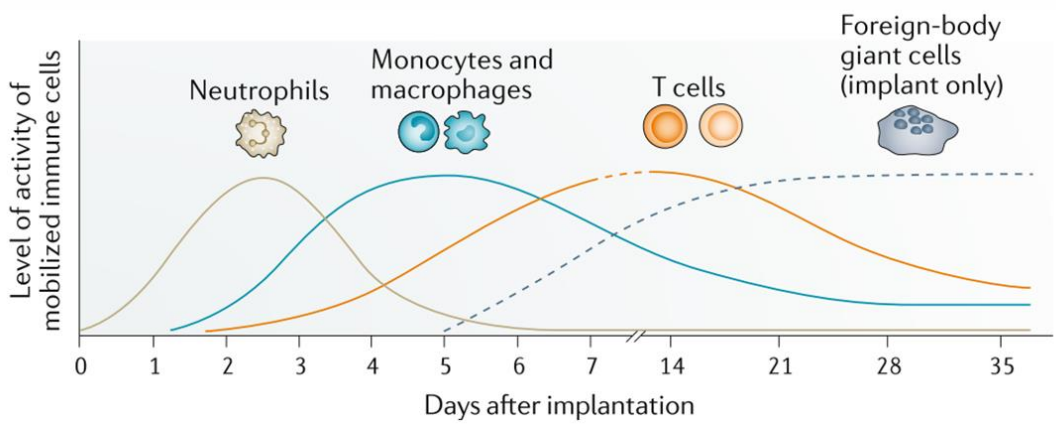

Fig. 1.12. The level of activity of different immune cells after injury with respect to time elapsed [27].

The introduction of an implant (a foreign material) inside the human body activates the host's innate and adaptive immune response through the activity of different cells over time (Fig 1.12). The innate response is an acute and non-specific response that is immediately activated upon implantation. First, proteins are adsorbed on the implant surface as the implant comes in contact with blood. These proteins draw cells like neutrophils, followed by monocytes and macrophages. Binding between the protein layer and the integrin receptors present on these cells releases pro-inflammatory cytokines. These secreted proteins work as messengers and draw more cells. Macrophages are the most relevant cells to determine the long-term host response to implants. The wide spectrum of phenotypes of macrophages perform different functions, e.g. M1 macrophages are pro-inflammatory, while M2 macrophages are anti-inflammatory and favor tissue healing. The timely switch from M1 to M2 promotes optimal tissue modeling and implant integration. The later stage of immune response is an adaptive immune response which is a specific immune response and is initiated by dendritic cells and macrophages by the presentation of antigens to T cells. The T cells secrete pro-inflammatory and anti-inflammatory cytokines, which also regulate M1 and M2 phenotypes of macrophages [27][30].

The immune response becomes more complex in the case of bioabsorbable materials because the innate immune response to non-degradable materials is primarily driven by protein adsorption onto the implant surface, which does not change. In contrast, the innate immune response to bioabsorbable implants is stage-dependent and is influenced by continous changing surface properties and/or the release of degradation products.

The host response mainly depends on surface-related events and constantly changing surface properties during degradation can lead to variations in protein composition and conformation within the absorbed protein layer, resulting in different response levels. For both non-degradable and degradable implants, an imbalance of M1 over M2 macrophages can lead to the fibrous encapsulation of the implant, a foreign body reaction (FBR), which is detrimental to tissue healing. For bioabsorbable materials, macrophages perform two main functions: 1) release enzymes and reactive oxygen species that help to break down the implant, and 2) to phagocytose the implanted material after it starts to disintegrate and release debris or macromolecules [27].

The above-explained immune response is dependent on the surface properties of the implant material. Bioabsorbable polymers maintain their surface properties over a long period of time and at the same time, release degraded molecular chains from the surface. On the other hand, the surface of bioabsorbable metals is transformed into a corrosion layer, a completely different scenario than the base metal. Another factor that must be considered is the surface of the implant near tissue (e.g. fixation plate attached to fractured bone), where the host response could be altered by the presence of other cells participating in tissue formation [40]. For instance, osteoblasts can form a monolayer on the surface of biocompatible materials with less surface reactivity like PLA and Mg surfaces modified by plasma electrolytic oxidation (PEO), which can alter the degradation rate of implant and, in turn, affect the host response. The generalized degradation mechanisms of different types of bioabsorbable materials by immune response have been summarized in Table 1.2. and explained in detail in section 1.6.2 and section 1.7.2 for PLA and Mg, respectively.

Table 1.2. *In vivo* degradation mechanisms of bioabsorbable materials [27][30][41][42]

Bioabsorbable materials	*In vivo* degradation mechanism
Natural polymers	• Enzymatic degradation by extracellular liquids as the main mechanism. • Hydrolysis initiates surface and/or bulk degradation. • Phagocytosis.
Synthetic polymers	• Hydrolysis initiates surface and/or bulk degradation. • Enzymatic degradation and oxidation by extracellular liquids. • Phagocytosis.
Metals	• Corrosion (anodic and cathodic) reactions on the surface of metal to form oxides, hydroxides and hydrogen gas. • Deposition of calcium and phosphate compounds in corrosion layer forming apatite-like calcified layer. • Resorption of calcified layer by osteoclasts in Mg-based bone fixation scenario. • Phagocytosis of corrosion product/debris.
Ceramics	• Solution-driven dissolution in extracellular liquids. • Cell-mediated material resorption, mainly by osteoclasts • Surface degradation and/or bulk in case of porosity and polymer-based composite.

1.6. Bioabsorbable Poly-lactides (PLA)

1.6.1. Introduction

Bioabsorbable Poly-Lactic acid (PLA) or 2-hydroxy propionic acid is a thermoplastic polymer that belongs to poly α-esters group and is the most established synthetic polymer for bioabsorbable medical devices. Its structure is shown in Fig. 1.13. Lactic acid is obtained by fermentation of starch from corn, sugarcane, etc., and the polymer is synthetized by direct polycondensation of lactic acid or ring-opening polymerization of lactide dimer. PLA has two stereoisomers and can be produced in the form of PLLA,

PDLA, or PDLLA. Two enantiomerically pure homopolymers (PLLA and PDLA) and a collection of racemic PDLLA polymers with different d and l monomer contents allow tailoring the physical properties over a wide range, as shown in Table 1.3. Furthermore, PLA can be blended with other polymers like PGA and PCL to manufacture copolymers with unique physical properties, which are particularly helpful in tailoring the mechanical and degradation rate while degradation products of each polymer in a copolymer remain the same as of the parent polymer. PLA and its copolymers can be processed via solvent-assisted (casting, electrospinning, etc.) or melt-assisted (compression, injection, melt spinning, 3D printing etc.) methods into a variety of forms such as fibers, films, particles, tubes, scaffolds and porous structure, and molded to shapes commonly used in medical devices [43][44].

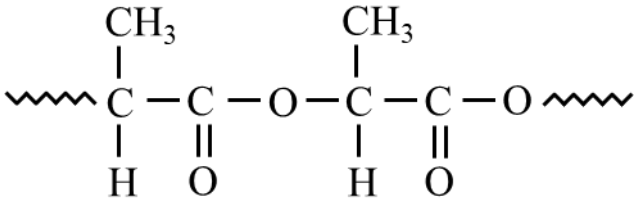

Fig. 1.13. Schematic of the chemical structure of PLA polymer

Table 1.3. Properties of bioabsorbable polymers used in orthopedic implants [30][43]

Polymer	**Elastic modulus (GPa)**	**Tensile Strength (MPa)**	**Tensile Strain (%)**	**Absorption time**
Poly-L-lactide (PLLA)	2.7 – 4.14	40 – 67	3 – 10	1 – 5.7 years
Poly-DL-lactide (PDLLA)	1 – 3.45	20 – 60	2 – 10	12 – 16 months
Polyglycolide (PGA)	6 – 7	60 – 80	1.5– 20	6 – 12 months
Polycarpolactone (PCL)	0.2 – 0.4	20 – 30	18 – 37	24 – 48 months
Poly-L-lactide-co-glycolactide (PLGA)	1 – 3	40 – 55	2.5 – 10	1 – 12 months

1.6.2. Degradation mechanisms

The physical properties of PLA achieved as a result of processing conditions and the environment determine its degradation rate. For instance, temperature, pH (alkaline and acidic nature), surface area, and enzymatic activity increases the degradation rate while high molecular weight and crystallinity decrease it. *In vitro* degradation of PLA is achieved via hydrolysis while in vivo, in addition to hydrolysis, enzymatic degradation and oxidation by extracellular liquid, and phagocytosis by cells also take place. It is believed that hydrolysis is the main mechanism also during *in vivo* degradation of PLA because enzyme molecules are large and cannot diffuse into bulk PLA. However, after excessive degradation of PLA, enzymes enter into the bulk and take an effective part in degradation. Phagocytosis mechanism also gets more relevant when PLA starts to disintegrate and release debris [30].

In the hydrolysis mechanism, degradation of PLA is initiated when water molecules diffuse into PLA and completely saturate it within in short time (1-2 days for *in vitro*), depending on the thickness [45]. In neutral or acidic environments, long chains of PLA are hydrolyzed by cleavage of ester bonds resulting into two chains having carboxylic and alcohol end groups (Fig. 1.14). Smaller chains can diffuse out of bulk PLA while large chains remain inside. This accumulation of PLA chains with a carboxylic terminal group initiates an autocatalytic effect and accelerates further the bulk degradation [44]. This continuous degradation makes chains smaller and smaller by random scissions until these are small enough to exit the bulk [46]. The molecular chains enter into the tricarboxylic-acid cycle and are eventually eliminated from the body as carbon dioxide and water [27]. After several months or years, PLA starts to get porous, providing more surface area for transport of water and small PLA chains and complete degradation is achieved [30]. In terms of mass loss, hydrolysis can either proceed by bulk degradation or surface erosion modes (Fig. 1.15). Bulk degradation is relatively fast and heterogenous due to the autocatalytic effect as compared to surface erosion. The above-explained mechanism is valid for bulk degradation, which usually takes in thick samples. However, surface erosion is more relevant for thinner specimens (like fiber and films) because chains with carboxylic terminal groups can escape more easily from thin samples and degradation takes place from the surface by the ease of transport of water molecules and smaller chains [30][47].

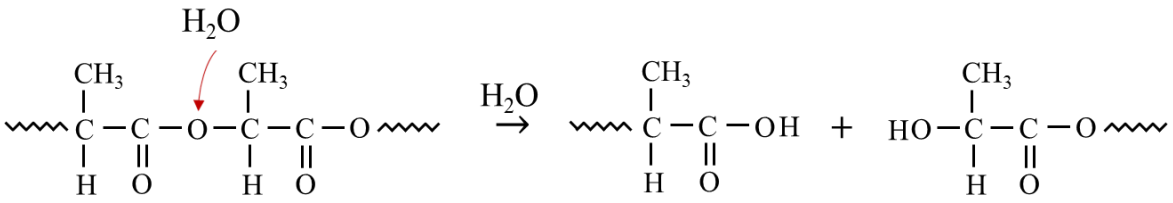

Fig. 1.14. Hydrolysis of PLA in neutral and acidic environments resulting in two chains with carboxylic and hydroxyl end groups.

Fig. 1.15. Schematic of surface erosion (top) and bulk degradation (bottom) [30].

1.6.3. Clinical translation

Bioabsorbable polymer devices of PLLA, PDLLA, PGA and their copolymers were approved by FDA authority in the US and authorities of different countries in the 90's. They are primarily used for low-load bearing applications, which include cardiovascular stents, fixation screws, pins and plates, interference screws, suture anchors, and craniomaxillofacial fixation devices (Table 1.4). The typical degradation rate of PLLA is very slow and not suitable for orthopedic applications and most devices are made from copolymers. Since PLA also lacks bioactivity, ceramic powders of HA and TCP were also added to improve the bioactivity.

Table 1.4. Commercial implants of bioabsorbable PLA-based systems [48] [49]

Product	Device	Material	Application	Absorption time
GrandFix Gunze, Japan	Plate and screw	PLLA	maxillofacial	> 3 years
SonicWeld KLS Martin, Germany	Plate and screw	PDLLA	maxillofacial	12 – 30 months
LactoSorb Zimmer Biomet, USA	Plate and screw	PLLA/PGA (85/15)	maxillofacial	12 – 18 months
ComposiTCP Zimmer Biomet, USA	Screw	β-TCP/PLDL (30:70)	ACL reconstruction	-
SuperFIXORB-MX Teijin Medical Corp, Japan	Plate	μ-HA/PLLA (40:60)	maxillofacial	5.5 years
Inion OTPS Inion INC, Finland	Plates, screw and meshes	PDLLA	maxillofacial	2-4 years
Rapirsorb DePuy Synthes	Plates, screw and meshes	PLLA/PGA (85/15)	maxillofacial	~12 months
Aptitude Amaranth Medical, US	Coronary stent	PLLA	Cardiovascular	> 36 months
DESolve Elixir Medical, USA	Coronary stent	PLLA	Cardiovascular	12 – 24 months

1.6.4. Challenges

PLA has not been able to solve all problems associated with non-degradable metals, and quest for a better material is still going on. Moreover, it has introduced some challenges associated [32][49]:

1. Low mechanical properties, especially elastic modulus, which is much lower than bone, limiting its application in orthopedics.
2. Extended degradation time (typically years), longer than bone healing period. Blending of PLA with PGA can reduce the degradation time but increases the risk of complications.
3. Lack of bioactivity and therefore, it does not participate in bone healing.
4. Release of acidic by-products which can lead to adverse tissue response.
5. PLA shows fewer complications than PGA, but there are still considerable reports on adverse tissue responses which include osteolysis, swelling, disintegration, etc.

1.7. Bioabsorbable Magnesium (Mg)

1.7.1. Introduction

In 1878, Edward C. Huse was the first to treat bleeding vessels by using Mg wire ligatures [50], but no Mg-based device could be clinically approved until 2013 because of the concerns with its high corrosion rate and lack of understanding of *in vivo* degradation mechanisms. Many bioabsorbable magnesium-based devices secured regulatory approval in the last decade for orthopedic, cardiovascular and dental applications [27]. Mg density is between 1.74 to ~1.9 g/cm^3 (depending on the alloy), in the range of natural bone (1.8 – 2.1 g/cm^3). It is essential to human metabolism and is the fourth most abundant cation in the human body, with about half of the total magnesium stored in bone tissue. The normal concentration of magnesium in extracellular fluids ranges between 0.7 and 1.05 mmol/l, and its balance is maintained through the regulation of the kidneys and intestines [51]. Mg has suitable mechanical, corrosion and biological properties as compared to Fe and Zn, which could be tailored by processing conditions, alloying, and surface treatments. The elastic modulus (~45 GPa) and yield strength (97 – 600 MPa) are close to the natural bone (5–23 GPa, 35–283 MPa) [52] and degrades safely *in vivo* if properly designed [53][42]. Mg degrades by corrosion reactions and releases $Mg(OH)_2$ and H_2 gas. $Mg(OH)_2$ is commonly used in medicine for antacids and is effectively metabolized by the liver and eliminated through the kidneys, while H_2 gas at a tolerable level is also safely absorbed [17].

Based on reports in the literature, magnesium alloys systems can be grouped into four major categories: (a) pure Mg, (b) Rare earth elements based (AE, WE, MgY, etc.), (c) Al-containing alloys (AZ, LAE, etc.) (c) and (d) Al free alloys (WE, MgCa, MgZn, etc.) [54]. Alloying and processing conditions tune the microstructure (grain size, precipitates, intermetallic phases) of Mg, which in turn can improve the mechanical, corrosion and biological response [50][55]. Mg implants are easily manufactured by conventional deformation techniques, but processing-induced microstructural changes must be considered to achieve desired mechanical and corrosion properties in the final product. Fixation plates are manufactured by milling as-cast ingots. Pins and nails can be made by extrusion for ingots to rods with desired diameter, while additional turning steps can be performed to get screw threads [26]. Cardiovascular stents of Mg are made by extrusion of thin tubes followed by laser cutting, while thin wires which have

potential applications in wound closure and bioabsorbable sensors can be achieved by direct extrusion or hot/cold drawing [55]. Chaya et al., [56] and, most recent Rendenbach et al., [26] reported safe degradation of pure Mg and WE43MEO alloy (with and without surface treatment) orthopedic fixation devices (plates and screws) in animal model. Screws degraded inside bone while plates integrated with host bone and excessive bone was also formed on plates. Jahn et al., [57] implanted intramedullary nails of Mg2Ag alloy in mice. Incorporation of Ag reduced the activity of osteoclasts which resulted in enhanced bone formation and complete healing was achieved by complete absorption of nails in 210 and 133 days with and without fracture, respectively. Numerous *in vivo* studies with successful outcomes and rising of number clinically approved devices show that Mg is a promising candidate as bioabsorbable implant material.

1.7.2. Degradation mechanisms

In vitro degradation mechanisms of magnesium differ with respect to *in vivo* degradation because of the effect of the presence of organic compounds (proteins and amino acids) and cells in the latter. However, understanding of *in vitro* mechanisms is important to screen materials and lays the foundations for understanding *in vivo* mechanisms.

In vitro degradation tests are usually performed in buffer solutions like SBF, HBSS and PBS. Most studies use Simulated Body Fluid (SBF) to simulate the corrosion of Mg because it contains all major inorganic compounds present in the biological environment [50][58]. As soon as Mg comes in contact with SBF, water molecules rapidly react with the Mg surface, forming a layer of $Mg(OH)_2$ and releasing H_2 gas. This layer is not stable in the presence of Cl^- ions, leading to the formation of soluble $MgCl_2$ and OH^- ions. As a result of the deterioration of the $Mg(OH)_2$ layer, the uncorroded Mg surface is exposed and the corrosion reactions progress by the subsequent formation and dissolution $Mg(OH)_2$. Calcium and Phosphate ions present in the solution start to deposit within the corrosion layer leading to the formation of Ca-P phosphates and carbonates. Even though the corrosion layer becomes thicker during the corrosion process, it is not compact enough to inhibit the corrosion and complete degradation of the Mg implant is achieved *in vitro* [50].

The *in vivo* degradation mechanism of Mg becomes more complex because of the combined effect of inorganic ions (Ca^{2+}, Cl^{-}, OH−, HPO_4^{2-}, $H_2PO_4^{-}$, HCO_3^{-}, and CO_3^{2-}), organic molecules (glucose, amino acids, and protein) and different cells (osteoblasts, osteoclasts, macrophages) (Fig. 1.16) and is not fully understood yet [40]. Rapid changes on the surface of Mg take place within seconds after implantation and determine the host immune response, as explained in Section 1.5.2. Corrosion initiates in formation and dissolution of $Mg(OH)_2$, and release of Mg ions by corrosion and the availability of Ca ions in the biological environment favors the deposition of carbonate and phosphate-based compounds of Ca and Mg in the corrosion layer. Corrosion continues inwards and the corrosion layer thickens up to several microns in few hours. The effect of different organic compounds and proteins on the corrosion rate and composition of corrosion layer is also complicated [40][59]. For instance, glucose (a common organic nutrient) increased the formation of Ca–P precipitates on the corrosion layer of Mg in a buffer solution, and improved the corrosion resistance [60]. Albumin protein reduced the corrosion of Mg at low dose but accelerated in high concentration [61]. Overall, the combined effect of proteins on corrosion rate and composition of corrosion layer is difficult to understand as the physiological environment contains large number of proteins. Proteins draw a variety of cells as part of the immune response. During *in vitro* studies, it has been reported that monolayer of cells can reduce the degradation of materials and can also alter the composition of the corrosion layer. In turn, corrosion products affect the functionality of cells and, particularly in case of Mg, their proliferation and differentiation are strongly dependent on the concentration of Mg ions.

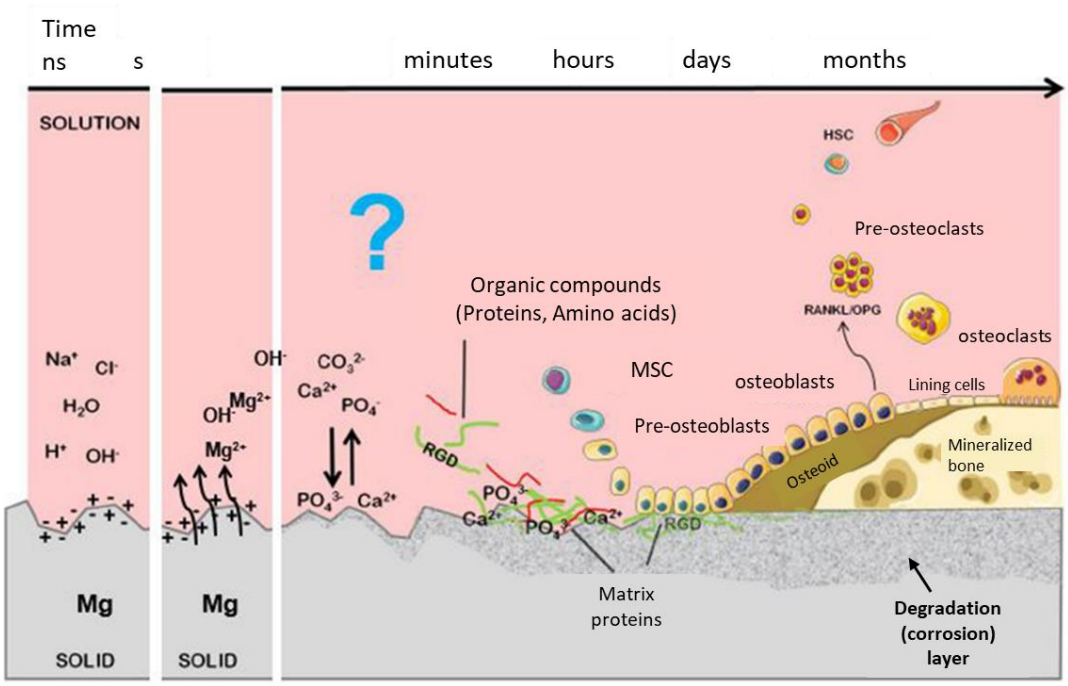

Fig. 1.16. Schematic of multiple processes occurring after implantation of Mg-based materials [40].

Overall, the interface between the corrosion layer and the biological environment is highly dynamic and absorption of Mg is dependent on the tissue in which it is present. For instance, screws and pins are encapsulated in bone and have variable exposure to marrow within depth. Fixation plates have more blood contact on one face and to bone on the other, while nails have more exposure to marrow.

Recent *in vivo* reports on the degradation of Mg in bone (e.g. screws) show that the implant is replaced with the formation of new bone overtime. For instance, WE43 screws implanted in the long bones of pigs were completely replaced with bone tissues in 12 months. While after 6 months, lamellar bone (far) and woven bone (nearest) were found around the corrosion layer [26]. The underlying mechanisms of *in vivo* bone formation are reported by Lee et al. [42]. Mg implants continuously corroded (biodegradation) in the bone environment by fluids. Ca–P layer deposits in the corrosion layer near to the interface and transformed into a biomimicking calcified matrix which is resorbed by osteoclasts, followed by new bone formation by osteoblasts (Fig. 1.17).

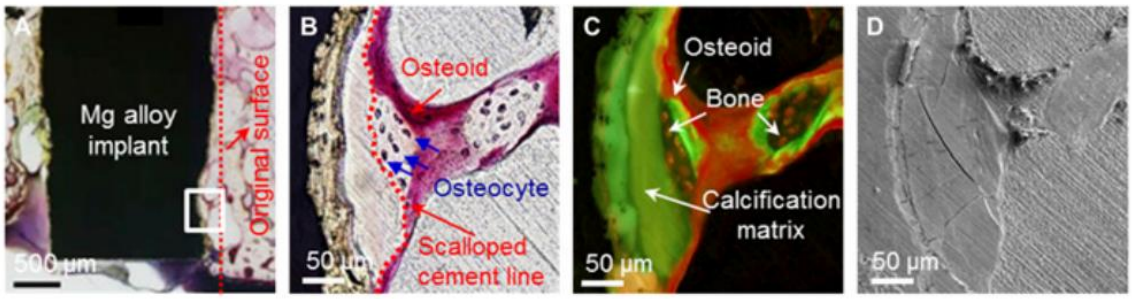

Fig. 1.17. Histological and scanning electron microscopy images of rabbit femoral condyle after 8 weeks of implantation of cylindrical Mg alloy implant [42]. (A) Implant–bone interface, Red line shows original surface line of implant. Magnified image of bone formation region observed by (B) light microscopy, (C) fluorescence microscopy, and (D) scanning electron microscopy.

1.7.3. Clinical translation

Mg achieved clinical translation in the last decade with number of devices and companies. In 2013, Syntellix GmbH (Germany) received CE mark for Mg Mg-Y-Re-(Zr)-based MAGNEZIX compression screws and then BIOTRONIK SE & Co. KG (Germany) for cardiovascular stents. Most recently in 2023, Bioretec Ltd. (Finland) received FDA approval for the first-ever bioabsorbable metal (Mg-based) screw to be marketed in the US. A number of approved devices have been summarized in Table 1.5. Two trends are common in translated devices of Mg i.e., the use of alloys and surface treatments, essential to achieve suitable properties.

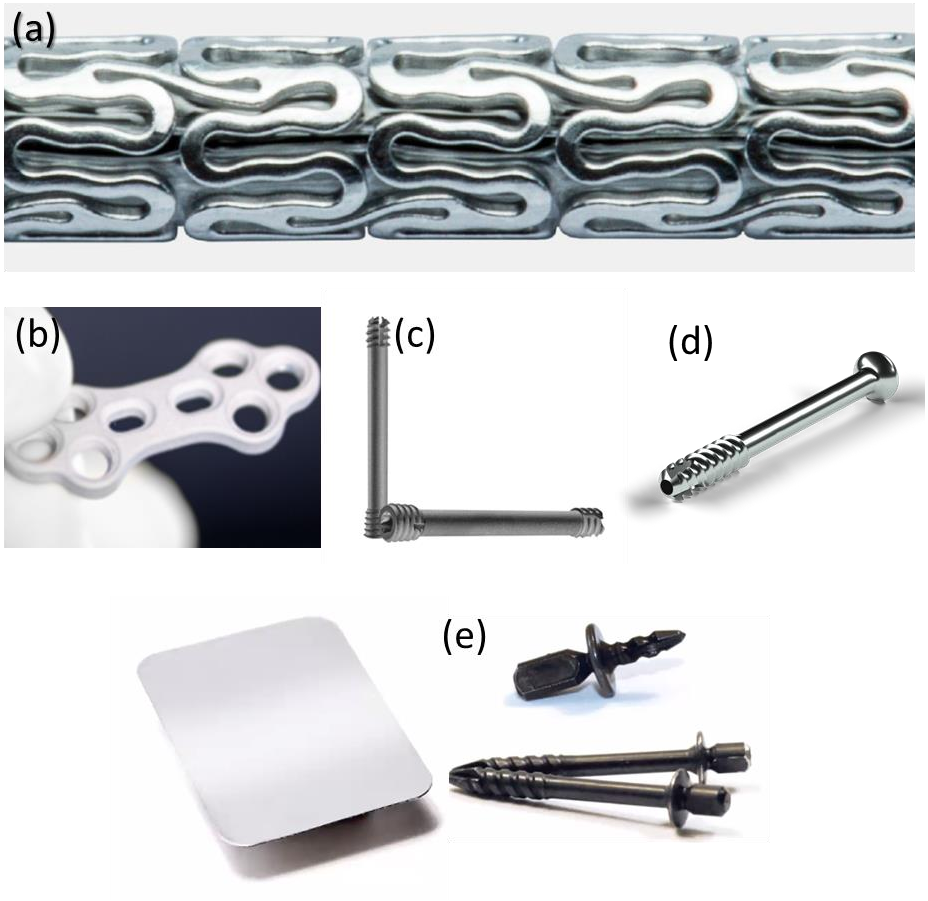

Fig. 1.18. Commercial magnesium-based implants: (a) cardiovascular stent: Magmaris (Biotronik), (b) (c) bone fixation: mm.X plate system and screws (Medical Magnesium), and (d) bone fixation: RemeOs screw (Bioretec), (e) Dental: NovaMag membrane and screws (Biotiss).

Table 1.5. Commercial implant of bioabsorbable magnesium systems

Product	Device	Coating	Application	Status
RemeOs Bioretec, Finland	Screw	-	Fixing misalignments, fragments stabilization	FDA and CE mark
MAGNEZIX Syntellix, Germany	Screw and pins	-	Fixing misalignments, fragments stabilization	CE mark
mm.CS MedicalMagnesium, Germany	compression screw	PEO treatment	Fixing misalignments, fragments stabilization	CE mark
Magmaris Biotronik, Germany	Coronary stent	Sirolimus/PLLA	Cardiovascular	CE mark
UNITY-B	Biliary stent	Sirolimus/PLLA	Help draining obstructed bile ducts	CE mark
mm.X plate MedicalMagnesium, Germany	fixation plate	PEO treatment	Fracture fixation	FDA breakthrough designation
NOVAMag Botiss, Germany	Membrane and screws	Fluoride coating on Screws	Guided Bone Regeneration in Dental	Pre-clinical trials

1.7.4. Challenges

Despite the high potential of Mg alloys for bioabsorbable applications, few devices exist in the market and only for limited applications due to the following challenges:

1. Controlling corrosion rate to keep released by-products under tolerable levels.
2. Controlling pitting corrosion, which leads to unexpected mechanical failure of device.
3. Lack of understanding of the long-term effect of alloying elements in the human body.
4. Lack of understanding of *in vivo* degradation mechanisms.
5. Development of new devices based on thin wires and sheets, which require excessive deformation and change properties dramatically.
6. Lack of understanding of absorption mechanisms of surface coatings.

1.8. Bioabsorbable Mg/PLA composite

1.8.1. History, processing and synergetic advantages

In the early 2000s, the concept of Mg-based polymer bioabsorbable composite for biomedical applications was realized by incorporating $Mg(OH)_2$ into PLGA for

cartilage tissue engineering [62] and drug delivery [63] applications by fabricating PLGA microspheres. Researchers aimed to harness advantages of release of Mg^{2+} ions and tailoring the degradation rate of the polymer. However, direct use of $Mg(OH)_2$ with polymer does not provide any mechanical advantage due to powdered state of $Mg(OH)_2$ and causes rapid degradation of PLA during processing and *in vitro* degradation. Up to the knowledge of author, the first report of incorporating Mg metal into polymerss for biomedical applications was reported by a Spanish patent WO2 2011/161292A1 [64] in 2011. The idea was attractive as compared to direct use of $Mg(OH)_2$ because during *in vitro* or *in vivo* degradation Mg particles (embedded in polymer) would corrode from surface ($Mg \rightarrow Mg(OH)_2 \rightarrow Mg^{2+}$) and provide controlled release of Mg ions. The synergetic advantages of using Mg metal and PLA to make composites has been summarized in Table 1.6. Their combination in the form of composite material is attractive to overcome the limitations of each other. The main advantage of Mg/PLA composite is the opportunity to tailor mechanical, degradation, and biological properties by changing the amount, size, distribution, and orientation of Mg reinforcement within the PLA matrix. Particularly for orthopedic fixation devices, Mg/PLA is attractive as many reports showed the osteogenic effect of Mg ions [65], and can be processed into various configurations (Fig. 1.19 and Table 1.7) such as film, rod, plate and porous scaffolds. Another important advantage is the neutralization effect between degradation by-products of Mg and PLA. Last but not least, Mg incorporation also alters drug release profiles which could be interesting for drug delivery applications [66].

Table 1.6. Summary of synergetic advantages

Property	Magnesium	PLA	Advantage as composite
Mechanical properties	Higher than bone	Lower than bone	• Customization of mechanical by tailoring amount, size, and orientation of Mg reinforcement.
Resorption time	Short	Long	• Overall degradation time can be optimized by the amount, size and surface area of Mg reinforcement. • Mg degrades slower as polymer matrix protects it from fast corrosion. • Degradation of PLA is accelerated in the presence of Mg.
Degradation products	Basic	Acidic	• Neutralization can take place to control pH.
Osteogenic effect	High	Low	• Osteogenic effect by controlled release of Mg ions
Drug loading potential	Yes/surface coatings	Yes/bulk loading	• Mg incorporation can control drug release profiles from composite

In last decade, several configurations of Mg/PLA composites have been reported (Fig. 1.19) with advantages and disadvantages. Mg particles composites are most studied as compared to other configurations as they provide an easy route to manufacture PLA-based composites by extrusion as well as personalized scaffolds devices by 3D printing. They present low mechanical properties and accelerated degradation during *in vitro* experiments due to the large surface area of Mg particles [65][67]. There is only one report [68] on fabrication of short/random Mg wires reinforced PLGA matrix by solvent casting and hot compression, which increase in tensile strength and cell adhesion but mechanical properties are expected to degrade rapidly in this configuration similar to Mg particles. Li et al. [69] pioneered the fabrication of PLA matrix unidirectionally reinforced with Mg wires by hot compression and, since then several studies reported the mechanical and degradation behavior of this composite [45][70][71]. This configuration provides the highest mechanical properties in the wire direction but is very weak perpendicular to the wires. There is only one study on the use of braided wires inside PLA matrix. This configuration could be interesting to achieve balanced mechanical properties but the volume fraction of Mg wires is limited and introduces plastic strains at knotting points which can result in uneven degradation of Mg wires

[72]. In summary, following trends could be deduced about the development of Mg/PLA composites from the literature. (1) Mg particles are studied most to reinforce PLA matrix followed by long wire reinforcement, (2) solvent casting, extrusion, 3D printing and hot compression are most utilized processing techniques for manufacturing, and (3) interfacial treatment of Mg is an additional tool to improve performance of composite.

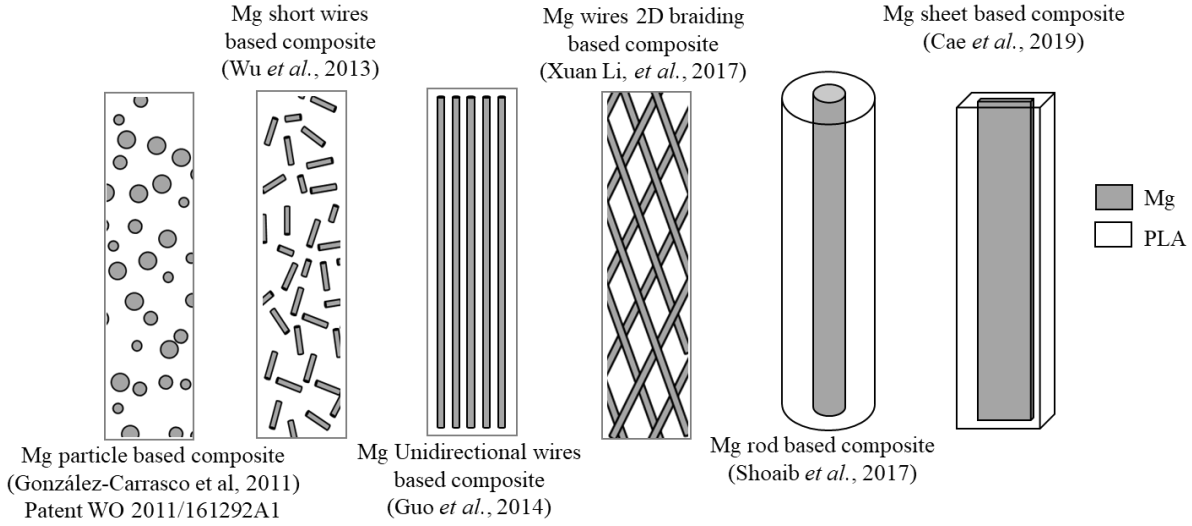

Fig. 1.19. Different configuration of Mg/PLA composites in literature with references of their first report: particle [64], short wires [68], unidirectional reinforcement [73], braided wire [72], Mg rod [74], Mg sheet [75].

Table 1.7. Mg/PLA composites in literature

Ref	Mg Reinforcement	Matrix	Interface treatment	Manufacturing Processing	Device
[76]	Mg (AZ31) wire in 50% V_f, Ø0.3 mm, unidirectional	PDLLA	HF acid treatment of Mg wires	Lamina Stacking/Hot compression	Plate
[77]	Mg (AZ31) wire in 10% V_f, Ø0.3 mm, unidirectional	PLA	PEO treatment of Mg wires	Lamina Stacking/Hot compression	Plate
[72]	Mg (AZ31) wires in 7% V_f, Ø0.3 mm, braided at 30°	PLA	PEO treatment of Mg wires	Hot compression	Plate
[68]	Mg (AZ31) short wires in 4% W_f , Ø0.250 mm,	PLGA	-	Solvent casting/Hot compression	Film
[78]	Mg particles in 35 % V_f Ø < 0.1 mm	PLGA	-	3D printing	Porous scaffold
[79]	Mg particles in 35 % V_f Ø < 0.1 mm	PDLLA	-	Extrusion/3D printing	Porous scaffold
[65]	Mg particles in 35 % V_f Ø < 0.5 mm	PDLLA	TMSPM saline coupling agent on Mg particles	Injection molding	Rod
[80]	Mg particles in 35 % V_f Ø < 0.5 mm	PDLLA	PEI and CTAB surfactant adsorption on Mg particles	Solvent casting	Film
[81]	Mg particles Ø < 0.5 mm	PDLLA	-	Extrusion	Tube/Stents
[82]	Mg particles in 2-4 % W_f Ø < 0.4 mm	PDLLA	-	Solvent casting	Film
[67]	Mg particles in 7 % W_f, Ø0.06 mm	PLLA	HF acid treatment of Mg wires	Solvent casting/Extrusion	cylinder
[83]	Mg particle Ø0.106-0.212 mm	PLGA	-	Solvent casting/Salt leaching	Porous scaffold
[84]	Mg particle in 2~5 % W_f, Ø0.1 mm	PLA	-	Solvent casting/Melt casting	-
[85]	Mg particle Ø0.125 mm, 2-5% w_f	PLA	-	Filament production by Extrusion	Filament
[86]	Mg (AZ31) rod l=60mm, Ø2.44mm	PDLLA	HF acid treatment of Mg rod	Injection molding/Cladding	Rod
[87]	Mg (AZ31) rod l=60mm, Ø2.44mm	PDLLA	PEO treatment of Mg wires	Injection molding/Cladding	Rod
[75]	Mg (Mg2Zn) sheet t=2mm	PDLLA	HF acid & PEO treatment of Mg sheet &	Hot compression	Plate
[88]	Mg (AZ91) sheet	PLA	HF acid treatment of Mg rod	Solvent casting	Film

Here, PLA is written in matrix column where specific type of PLA is not mentioned

1.8.2. Interfacial treatments between Mg and PLA

Several strategies to improve the interface between Mg and PLA are summarized in Table 1.7. They provide additional possibilities to improve mechanical, degradation rate and biological performance of Mg/PLA composites. Ali et al, [89] reported rapid loss interfacial strength during in vitro degradation of Mg wires/PLA composite and recommended interfacial treatments to maintain strength retention of wire-based composites. In the literature of Mg/PLA composites, Mg surfaces have been treated with hydrofluoric acid [45][67], saline coupling agents [65] and surfactants [90] as well as electrochemical treatments by anodizing [74] and plasma-electrolytic oxidation (PEO) [69][91]. In fact, orthopedic fixation devices (plates and screws) of Mg modified by PEO have already shown excellent *in vivo* performance with enhanced bone formation around the implant [26][92]. Therefore, using PEO surface-modified Mg wires seems promising for manufacturing Mg/PLA composites for orthopedic fixation devices.

1.8.3. Current development status

Studies in the literature have proposed Mg/PLA composites for a wide range of biomedical applications such as cardiovascular stents [93], orthopedic fixation platew [94], dental bone regeneration [83], and wound dressing [81]. Mg/PLA composites are a novel material, and most of the studies are focused on material and process development and characterization of mechanical, in vitro degradation behavior and basic biocompatibility. One major shortcoming is the use of non-medical grade PLA polymer and the lack of understanding of the complete degradation mechanisms. No comprehensive report on interfacial degradation mechanisms between Mg and PLA is available. Up to the knowledge of the author, there are only three in vivo studies [65][78][83] on Mg(particle)/PLA composite and only for the orthopedic scenario. Brown et al, [83] performed *in vivo* testing of porous Mg/PLGA composite scaffold in dogs for bone regeneration in a dental socket. Scaffolds decreased inflammation in pure PLGA scaffolds and enhanced osteogenesis. Yu et al, [65] placed Mg(particles)/PLLA composite cylinders in epicondyle bones of rat and reported no changes in the Mg ions concentration in serum and also found bone formation around the implant due to the osteogenesis effect of Mg ions. Probably, the first *in vivo* study performed with 3D

printed Mg particle/PLGA scaffolds (lattice) was by Long et al, [78] to treat osteosarcoma. Scaffolds eradicated tumor and promoted cortical and trabecular bone formation.

In terms of clinical translation, there is only one CE-approved device that could be considered close to bioabsorbable Mg/PLA composite. UNITY-B (QualiMed, Germany), is a bioabsorbable biliary stent for draining obstructed bile ducts (Fig. 1.20). Skeleton is Mg-based which supports the structure while muscle a PLA polymer that provides protection to the skeleton during stent expansion and degradation.

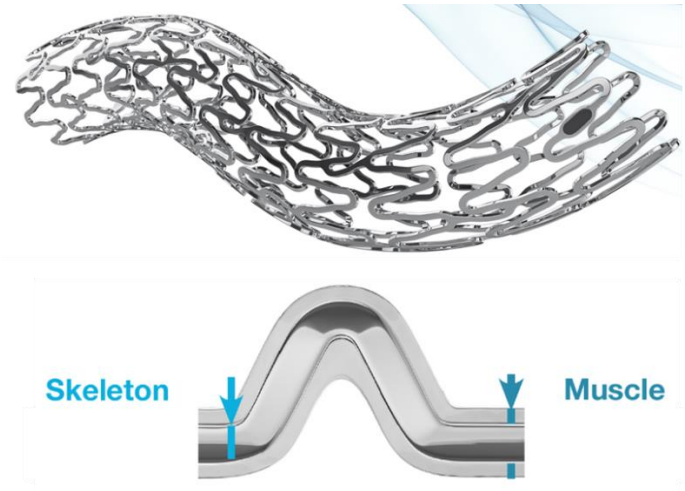

Fig. 1.20. UNITY-B Endoscopic Balloon Expandable Biodegradable Stent System having CE mark where Skeleton is magnesium metal while Muscle is thick polymer coating [95]

From the above discussion, it can be concluded that Mg/PLA is a novel and emerging bioabsorbable composite with good *in vivo* results. The concerns about Mg/PLA degradation products are mitigated with the approval of UNITY-B stent, a motivation for regulatory procedures of Mg/PLA composites. We can expect to see more development in Mg/PLA composite in coming decade as Mg-based devices are gaining market approvals which will give confidence in development of medical devices of Mg/PLA composites.

1.8.4. Challenges

There is no doubt that Mg/PLA composites have opened more possibilities for the application of bioabsorbable materials and overcome some limitations of Mg and PLA when they are used alone. However, the following challenges need to be addressed:

1. Lack of understanding of the degradation mechanisms of the composite as a whole and its constituents i.e. Mg/Interface/PLA, and how they affect each other.
2. Composites with Mg particles have mechanical properties similar PLA while Mg wire-based composites provide good mechanical properties in the direction wires.
3. Controlled positioning of wires/particles within PLA matrix.
4. Determining the right composition depending on the application.
5. Improvement of interface strength between Mg and PLA.
6. Lack of understanding about the interaction of Mg alloying elements with PLA matrix.

1.9. Motivation and objectives

Bioabsorbable materials have the potential to replace conventional non-degradable metallic materials such as Ti, stainless steel, etc., in a wide range of orthopedic applications. Conventional metals provide excellent mechanical properties and biocompatibility, but they remain in the body permanently and may hinder the growth of natural tissue, an important issue in the case of children. Moreover, complications associated with the presence of a foreign element within the body (irritation of tissues, implant corrosion, loosening of the device, etc.) may require a second surgery for removal [26][49]. Alternatively, bioresorbable metals (such as Mg and its alloys) and polymers (such as Poly-Lactides, Poly-Glycolides and their copolymers) have been explored in recent years [65]. Poly-Lactides (PLA) are easy to process and have been used successfully for drug delivery, orthopedic implants, wound closure etc. [49]. Nevertheless, they present long degradation times (typically years) and low mechanical properties and generate acidic by-products during degradation that can lead to an inflammatory response of surrounding tissue [30]. In the last decade, Mg alloy-based devices have been tested to fix bone fractures or treat vessel stenosis mainly in Germany, but also in China and Korea. Initiated by companies such as Syntellix GmbH (Hannover, Germany), BIOTRONIK SE & Co. KG (Berlin, Germany), and recently Medical Magnesium GmbH (Aachen, Germany), Mg-Y-Re-(Zr)-based stents and screws achieved approval for use in the European medical device market [96]. Mg alloys have good mechanical properties and biocompatibility. However, the rapid corrosion of Mg in the physiological environment can lead to unpredictable mechanical failures, high local alkalinity, and hydrogen gas accumulation in nearby tissues [55][92].

Their combination in the form of composite material is attractive to overcome the limitations of each other. The main advantage of Mg/PLA composite is the opportunity to tailor mechanical, degradation, and biological properties of composite by changing type (particle, wire, sheet, etc.), surface treatment, amount (volume fraction), size (diameter, thickness, etc.), distribution and orientation of Mg reinforcement within PLA matrix. Mg/PLA composites are attractive, particularly for orthopedic fixation devices as many reports showed the osteogenic effect of Mg ions [65][78].

Mg particles provide an easy route to manufacture composites by extrusion and 3D printing but they decrease mechanical properties and accelerate the degradation of composite during *in vitro* experiments while the supply of Mg^{2+} ions from composite degradation improves *in vitro* cytocompatibility and *in vivo* bone formation [65][67] [78][97]. Reinforcement of PLA matrix with Mg wires leads to large improvement in stiffness and strength with respect to PLA [45][69], and accelerates (to a lower extent than Mg particle due to lower surface area) the degradation composite, neutralizes acidic by-products [98] and improve the biocompatibility [99]. However, the mechanical properties of wire-based composite perpendicular to the direction of wires are limited and hinder their application in orthopedic devices like fixation plates which bear different kinds of loadings. Therefore, developing a new configuration of Mg/PLA composites with different ply orientations of Mg wires could be interesting.

Controlling the mechanical and chemical degradation of Mg/PLA composite is another challenge and is mainly dictated by the corrosion of Mg reinforcement. Interfacial strength between Mg wire and PLA matrix drops rapidly due to corrosion of Mg wires inside PLA matrix wires which weakens the macroscopic mechanical properties of composite like stiffness, fatigue and toughness [89]. Corrosion of Mg wires can be only controlled up to some extent by means of annealing and alloying. Surface treatments, such as Plasma Electrolytic Oxidation (PEO) provide significant protection against corrosion [50]. In fact, orthopedic fixation devices (plates and screws) of Mg modified by PEO have recently shown excellent *in vivo* performance with enhanced bone formation around the implant [26][92] and PEO-treated compression screws have received clinical approval in EU market [100]. Therefore, the use of PEO surface-modified Mg wires seems to be a promising candidate to manufacture Mg/PLA composites for orthopedic fixation devices, but it requires modification of the

conventional PEO process to a continuous process as a large amount of wires are needed for the composites.

Against this backgroud, the main goal of the thesis is to develop novel bioabsorbable composite laminates of PLA matrix reinforced by surface-modified Mg wires with optimized mechanical, degradation and biological performance for orthopedic applications. The following key objectives are set for this purpose:

1. Develop a continuous Plasma Electrolytic Oxidation (PEO) process for seamless surface modification of Mg wires to produce PEO-treated Mg wires in large quantities, which will be used as reinforcement in Mg/PLA composite.
2. Develop fabrication process of manufacturing uni-directional and multi-directional laminates of Mg/PLA composites with controlled positioning and orientation of wires (Fig. 1.21).
3. Mechanical, *in vitro* degradation, and biocompatibility characterization of constituents of composite, i.e., Mg wire (with and without PEO), interface and PLA matrix.
4. Mechanical and *in vitro* degradation characterization of uni-directional and multi-directional Mg/PLA composite with and without PEO surface treatment.
5. Asses the biocompatibility of Mg/PLA composite laminates.

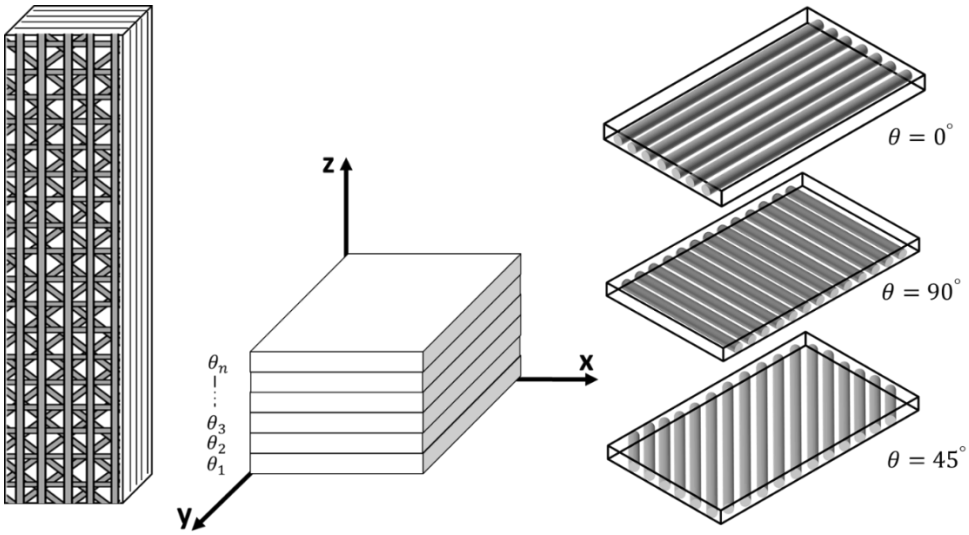

Fig. 1.21. Schematic of a new configuration for Mg/PLA composite proposed in this thesis. Several plies stacked together (left), and single ply (on right) show distribution and orientation of Mg wires within the ply.

1.10. Structure of thesis

This thesis is organized into different chapters to facilitate the reader in understanding the development process and characterization of the Mg/PLA composite. **Chapter 2** deals with process development for (1) continuous Plasma Electrolytic Oxidation for seamless surface modification of Mg wires and (2) manufacturing of Mg/PLA composite laminates. In **Chapter 3**, effect of continous PEO surface treatment on mechanical, corrosion and biocompatibility of wires is presented which sets the stage for understanding the degradation behavior of Mg/PLA composites. Detailed mechanical characterization of composite laminates of Mg/PLA composite with and without PEO surface-modified wires is presented in **Chapter 4** along with the characterization of the interface by push-out tests. **Chapter 5** deals with the effect of interaction between Mg wire, interface and PLA matrix during *in vitro* degradation and links it with the macroscopic degradation mechanism of Mg/PLA composite. Cell attachment, viability, proliferation and differentiation behavior of pre-osteoblasts was studied in **Chapter 6** to assess the biocompatibility of Mg/PLA composite by direct/indirect cell culture experiments. Finally, the conclusion and future work are summarized in **Chapter 7**.

CHAPTER 2: MANUFACTURING PROCESSES

The chapter presents the manufacturing of Mg wires by cold drawing and the surface treatment of the wires by means of a novel continuous Plasma Electrolytic Oxidation (C-PEO) process, which was optimized to achieve a porous and homogenous oxide layer. This oxide layer is shown to protect Mg wires against corrosion and to improve cytocompatibility. Finally, the fabrication of Mg/PLA composites by compression molding is presented to produce multi-directional composite laminates without and with PEO surface modification of the Mg wires.

2.1.Fabrication of Mg wires modified by continuous plasma-electrolytic oxidation

2.1.1. Motivation

Bioabsorbable metallic wires of magnesium have received attention due to their suitable mechanical properties (elastic modulus of 40-45 GPa and tensile strength in the range 100-600 MPa) [52], faster degradation rate than their counterparts (iron, zinc, and molybdenum) and biocompatibility [26] in a wide range of biomedical applications. Their applications include staples, sutures, and meshes for wound closure [101], cardiovascular stents [102], bioresorbable electronic sensors [103], tumor treatment [104], etc. Mg wires of 0.10 mm [71] and 0.30 mm [45] diameter have also been used as unidirectional reinforcement of poly-lactic acid polymers [105]), and are excellent for manufacturing bioabsorbable composites with high mechanical properties and degradation performance for orthopedic applications.

Manufacturing of wires from pure Mg [106] and its alloys [101] have been reported by direct extrusion at high temperatures (230ºC-450ºC). However, this process limits the minimum diameter of the wire (often > 500 µm) and is not very robust in terms of geometrical accuracy, among others. Cold drawing still depicts the standard manufacturing method to process metallic wires to achieve very thin diameters [107]. However, cold drawing is limited by the strong plastic anisotropy of Mg alloys, which is associated with their hexagonal close-packed lattice structure [108]. This plastic anisotropy can be reduced by the addition of different alloying elements [109]. Cold drawing of Mg alloys containing rare earths (Mg-RE) is favored by the reduction in texture [110] and shows potential to realize thin wires, which have recently been reported by several groups [52][101] and microstructure of the Mg wires can be tailored

through thermal treatments to optimize mechanical properties and corrosion rate during drawing stages or on the final product.

Despite the increasing number of potential applications, the current limitations of Mg wires as bioabsorbable materials need to be critically evaluated. The first – and the most relevant one – is the high corrosive reactivity of Mg within the body, which leads to an increase in the local pH due to a higher concentration of OH^- ions and to the formation of H_2 gas accumulations that – above certain thresholds – can cause an inflammatory response of the surrounding tissue [111]. This problem is particularly relevant in the case of Mg wires or porous scaffolds with a high specific surface [112]. In addition, magnesium dissolution is generally associated with pitting corrosion, as reported in numerous *in vitro* studies [71], which in particular affects the mechanical integrity of thin wires and makes it difficult to ensure that the reduction in strength over time is matched with device requirements and ingrowth of surrounding tissue. Improvements in corrosion resistance and in the severity of pitting corrosion of Mg wires have been reported through alloying with RE and application of suitable thermal treatments [52][111][113][114] but much larger reductions in reactivity seem, however, necessary for the development of the next generation Mg wire-based implants that meet all requirements for potential biomedical applications.

In this context, surface modification is the most effective strategy to control Mg corrosion, i.e. degradation [51]. Among different possibilities, Plasma Electrolytic Oxidation (PEO) showed the most suitable to significantly reduce the degradation rate while concurrently improving the cytocompatibility of magnesium implants [26] [115]. A micro-porous oxide layer is formed on the surface during the PEO process, which serves as an effective barrier between the Mg substrate and the surrounding physiological environment. The morphology of this oxide layer can be controlled by various variables, e.g., electrical parameters (voltage, current, frequency, etc.) or electrolyte composition, which both affect the barrier properties as well as the overall cytocompatibility of such surface-modified Mg alloys [116]. While PEO is generally well-established Mg alloys [117], but the conventional PEO process only allows for the modification of distinct segments of wire [118] that fit into the electrolyte bath but cannot be scaled up to larger amounts by its discontinuous nature of the processing.

To overcome these limitations, a new strategy has been developed for upscaling the production of optimized Mg wires by cold drawing, thermal treatments and continuous PEO process. Manufacturing of Mg WE43 alloy wires of 0.3 mm in diameter by cold drawing and the surface treatment of the wires by means of a novel continuous Plasma Electrolytic Oxidation (C-PEO) process is detailed below.

2.1.2. Raw materials

Billets of Mg alloy WE43MEO with nominal composition 1.4 – 4.2 % Y, 2.5 - 3.5 % Nd, <1 % (Al, Fe, Cu, Ni, Mn, Zn, Zr) and balance Mg (in wt.%) were produced by directional gravity chill casting, homogenized by T4 heat treatment and machined to remove surface oxidation and allow for indirect extrusion to rods with a diameter of D = 6 mm (Meotec GmbH, Aachen, Germany). In the second step, these rods were cold drawn to wires of D = 1.5 mm (Fort Wayne Metals Research Products Corp., Indiana, USA), which then were used as a precursor material for succeeding cold drawing steps to get 0.3 mm in diameter wires in this study.

2.1.3. Cold drawing of Mg wires

The Mg wires of diameter D = 1.50 mm were used as the starting material for cold drawing process. An oil-based lubricant (Drawlub AL 4686, PETRFER, Chemie H. R Fischer GmbH + Co. KG, Germany) was used in 28 steps to achieve the final diameter D= 0.30 mm following the drawing schedule reported in our publication [55]. The die was made of carbide material with 6^{o} half angle (Fig. 2.1) [119]. The drawing speed for the first pass was 0.8 m/min and 4 m/min for the last pass. The speed was increased proportionally according to the ratio between the surface area to volume (1/D) for intermediate passes. Brief annealing of the wire at 450^{o}C was performed after every pass in an in-line positioned throughput tubular oven of 350 mm in length at the same speed as of the preceding drawing pass, leading to a continuous heat treatment process and thus decreasing necessary off times for annealing the coiled wires by heat treatment after every pass. Finally, lubricant traces were removed by passing the wires continuously through an ultrasonic bath filled with ethanol.

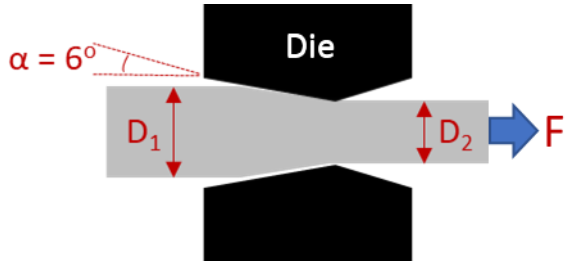

Fig. 2.1. Schematic depiction of the cold drawing process. The wire having diameter D_1 passes through the die by applying force F to reach the final diameter D_2. The half angle used for the die was $\alpha = 6^{o}$.

Mg wires of 0.30 mm in diameter were successfully manufactured to the extent of 34% and 13% cold work (CW34 and CW13). In the case of CW34, the last three passes were achieved without intermediate annealing and, thus, more cold work was introduced to wires. With regards to length, Mg WE43MEO alloy wires of 0.30 mm in diameter were successfully manufactured up to lengths of 20 m. However, it should be noted that reduction of wire breaks could be significantly reduced, and longer lengths of Mg wire achieved by using diamond dies, optimization of annealing conditions, and a more suitable lubricant in future endeavors. The CW13 wires were later subjected to annealing heat treatment at 400ºC for 5 s or 10 s (HT400-5 and HT400-10) or at 450ºC for the same durations (HT450-5 and HT450-10). The brief annealing times of 5 s and 10 s were chosen to match the facilitated drawing speeds. The wires produced with different processing conditions were tested by tension and corrosion tests to understand the relationship between processing-microstructure-property.

2.1.4. Surface modification by continuous plasma electrolytic oxidation process

The demand for surface-modified magnesium wire is expected to significantly increase in the future. Therefore, a scalable process for continuous production of PEO surface-modified Mg wires is an important milestone to pave the way for the industrial application of PEO-modified bioabsorbable wires like Mg/PLA composites for orthopedic fixation. Conventionally, Mg wires cannot be surface-modified by PEO in continuous mode as the wire can burn, i.e., deteriorate, in three locations [117]: (1) at the anode/wire interface, (2) at the electrolyte/air interface, and (3) within the electrolyte. The first scenario terminates the fabrication because the wire might break in two, while the other two cases severely damage the surface modification by black

burn marks, but do not intersect the continuously fed wire. To overcome these limitations, the process was modified by (1) shifting anode/wire contact outside the electrolyte bath and (2) optimizing the surface modification speed as well as electrical parameters.

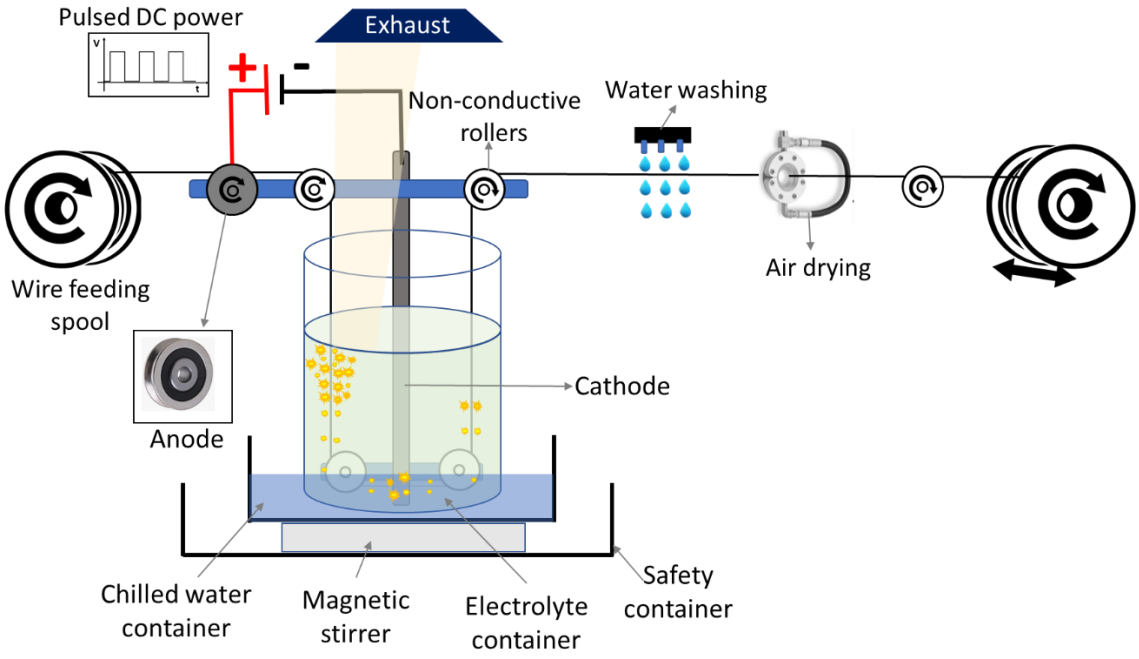

Fig. 2.2. Schematic depiction of the continuous PEO process for surface-modification of Mg wires. Yellow flashes inside the bath show the position and intensity of sparks when the wire passes through the bath in the presence of an electric field.

The processing scheme is depicted in Fig. 2.2. The spooled HT450-5 Mg wire with 0.30 mm in diameter was mounted on an insulated structure and fed by a stainless-steel roller, which acted as the anode. A vertical stainless-steel fixture, that acted as the cathode, was placed inside the phosphate-based electrolyte bath (Kermasorb®, Meotec GmbH, Aachen, Germany). Electrical current was supplied using a power source (LAB/HP15600, ET System Electronic GmbH, Germany) in pulsed mode with a current density of 15A/dm^2 at either 250 Hz (PEO250) or 500 Hz (PEO500) to study the effect of frequency on surface quality. The bath temperature was regulated between 20^{o}C to 34^{o}C by suspending chilled water around the bath and constant stirring of the electrolyte with a magnetic stirrer inside the reaction vessel. The surface modification speed was kept at 1.35 m/min, leading to the wire spending approximately 20 s within the bath. After leaving the electrolyte, the wire was rinsed by a water jet generated by a pump (MS-4/6 Analog Pump, Ismatec™, Germany) to remove residuals of the

electrolyte, dried in air (Air Wipe 009, Airmasters, Germany), and continuously coiled on a spool at the end of the bench. The setup was carefully designed and encapsulated, ensuring electrical safety and the proper collection of process gases by a flexible exhaust system. The SEM images (Fig. 2.3) show the porous oxide layer generated by continous PEO process on Mg wires.

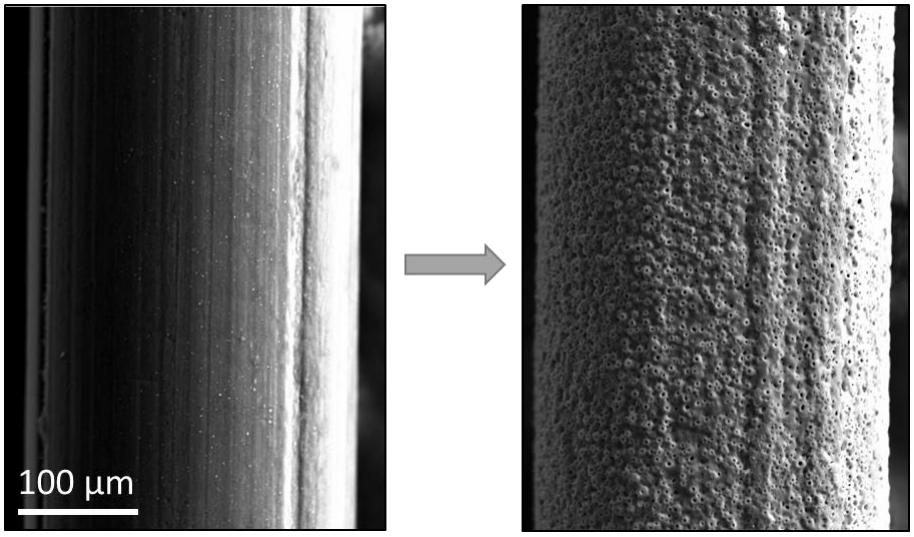

Fig 2.3. Secondary electron SEM image of Mg wire (a) before and (b) after continuous PEO surface modification

The continuous PEO process allowed the production of sufficient amounts of surface-modified wires for biomedical devices overcoming the limitation of the conventional PEO process which can handle only discrete work pieces (or small segments in the case of wires [120]). In conventional PEO, the section of the workpiece is always in contact with anode where the quality of surface modification is compromised. In continuous PEO, the wire passes freely through the electrolyte, thus providing an overall uniform surface modification of the wire. The parameters of continuous PEO were optimized in this study to introduce PEO in a short time. The myriad of studies on conventional PEO process for Mg alloys suggest that the PEO processing time is generally in the order of a few minutes (typically 2~15 min) [118] [121], but we successfully produced a homogenous PEO oxide layer in a few seconds which is crucial for large-scale production of surface modified Mg wires.

2.2. Fabrication of customized Mg wires/PLA composite laminates

2.2.1. Motivation

As discussed in section 1.8, bioabsorbable Mg/PLA composites are potential candidates for orthopedic fixation device applications. Among different configurations of Mg/PLA composite (Fig. 1.19), the wire-based configuration provides the highest mechanical properties in the direction of the wire and the lowest (even below those of pure PLA) in the transversal direction. But an orthopedic implant may need balanced mechanical properties in all directions or, at least, above a given threshold in the transversal direction. This can be achieved by using multidirectional laminates, as already illustrated in Fig. 1.21, following the classic strategies used in fiber-reinforced composites. Thus, the orientation of the wires in each ply of the laminate selected to achieve the optimum mechanical properties (stiffness, strength) in different orientations depending on the application (patient-specific or customized) with the help of classical laminate theory or finite element simulations.

Hot pressing of alternatively stacked PLA and Mg wires laminas is the established process to manufacture unidirectional Mg wire reinforced PLA composites [45][69]. However, composites manufactured by this technique show irregular distribution of the Mg wires as well as important misorientations within PLA matrix. In order to optimize the composite properties, three parameters should be controlled (Fig 2.4) during the processing of the composite: (1) orientation of the wires within lamina, (2) distance between wires within lamina and (3) distance between two laminas of Mg wires. Therefore, the conventional hot press strategy has to be modified to control these parameters. In addition, feasibility of additional processes -like adaptation to curved surface and machining - is also necessary for patient-specific implants.

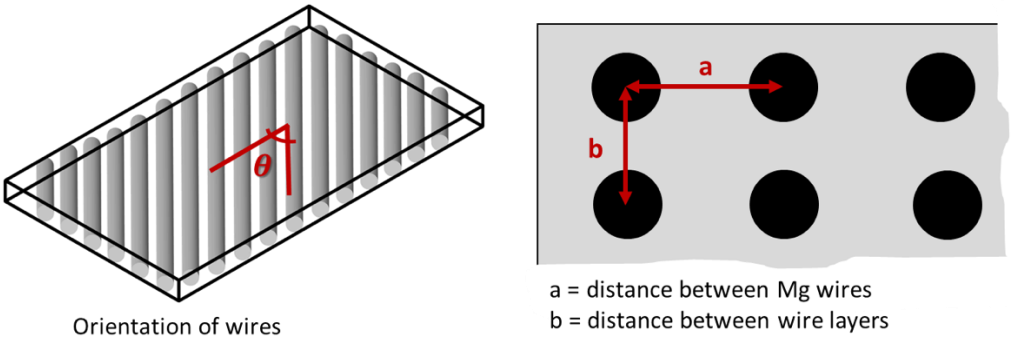

Fig. 3.4. Schematic depiction of the desired orientation of Mg wires in a single lamina (left) and of distances between Mg wires (right).

2.2.2. Materials

Magnesium WE43MEO alloy (Meotec GmbH, Aachen, Germany) was chill-casted and wires were manufactured by indirect extrusion to produce rods with 6 mm in diameter (Meotec GmbH, Aachen, Germany) followed by successive cold drawing and annealing steps to achieve a diameter of 0.3 mm (Fort Wayne Metals Research Products Corp., Indiana, USA). The surface of the Mg wires was modified by the continuous PEO process detailed in section 2.1.4 by passing the wire through a phosphate-based electrolyte bath (Kermasorb®, Meotec GmbH, Aachen, Germany) at the frequency of 500 Hz. This process led to a homogeneous and porous oxide layer of approximately 8 µm in thickness on the wire surface and the appearance of the wire turned from bright silver to white (Fig. 2.5). Pellets of medical-grade copolymer of PLA (Purasorb PLDL 7038, Corbion, Netherlands) were used as raw material to prepare pure PLA laminas.

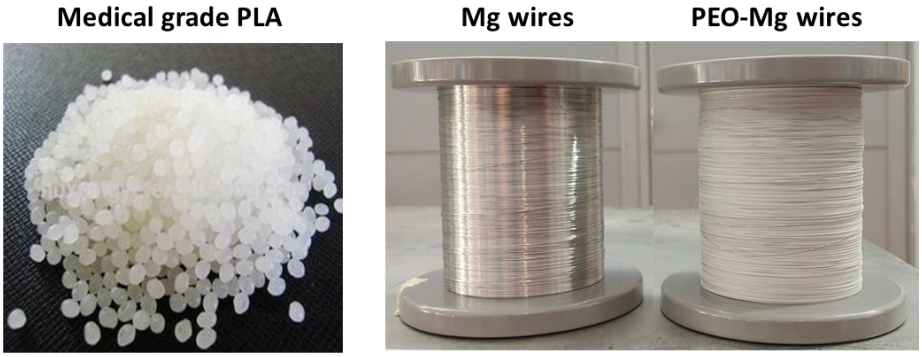

Fig. 4.5. Optical images of the raw materials used in the manufacturing of composite. Medical- grade PLA (Purasorb PLDL 7038) pellets were purchased (Corbion, Netherland) and Mg wires of WE43MEO alloy were drawn and annealed (Fortwayne metals, US) and then surface-modified by continuous PEO (Meotec GmbH, Germany).

2.2.3. Compression molding

Composite laminae were manufactured in three steps, which are summarized in Fig 2.6. Firstly, unidirectional Mg wire laminas of either Mg or PEO-Mg wires (modified by C-PEO process) were transferred from a spool to a plate attached with a rotating motor while another motor was attached to a linear drive. The transfer process was carried out by keeping the wires under slight tension, and the speeds of both motors were adjusted to achieve desired distance between Mg wires within the lamina. This distance was estimated from the number of Mg wire laminas and the desired volume fraction of Mg wires in the composite. After the wires were wounded on the plate, additional tension was provided by the screw mechanism attached to the end of the plate. In case of PEO-Mg wires, care was taken during this process to avoid the cracking of the surface oxide layer. Moreover, PEO-Mg wires were heat-treated at 450ºC to remove the residual stresses in the wire and ensure that the wire remains straight during the consolidation stage. Then, a PLA/chloroform (1g/20ml) slurry was poured onto the wire laminae, the chloroform evaporated and PLA precipitated among the wires. The unidirectional Mg wire lamina was then cut with scissors and placed with a particular orientation in the mold.

In the second step, PLA laminas with a thickness of ≈0.35 mm were prepared by hot pressing of pellets in a mold cavity at 230 ºC and cut to the desired dimensions. In the final third step, PLA and wire laminas (with different wire orientation) were alternatively stacked into a mold of 120 mm x 12 mm or 50 mm x 50 mm and consolidated by hot pressing at 180ºC, leading to fully dense Mg wires reinforced PLA composites with an average Mg wire volume fraction of ~20%.

Optical images of unidirectional Mg/PLA and PEO-Mg/PLA composites are shown in Fig. 2.7. They confirm the excellent alignment of the Mg wires without and with PEO modification. Similarly, quasi-isotropic laminates (Fig. 2.8) also show that the wires in each lamina are oriented in the desired direction and inter-lamina and intra-lamina distances between Mg wires were roughly equal showing the robustness of processing strategy. Moreover, the oxide layer was not damaged during fabrication of PEO-Mg/PLA composites and PLA penetrated into its pores as shown in Fig. 2.9.

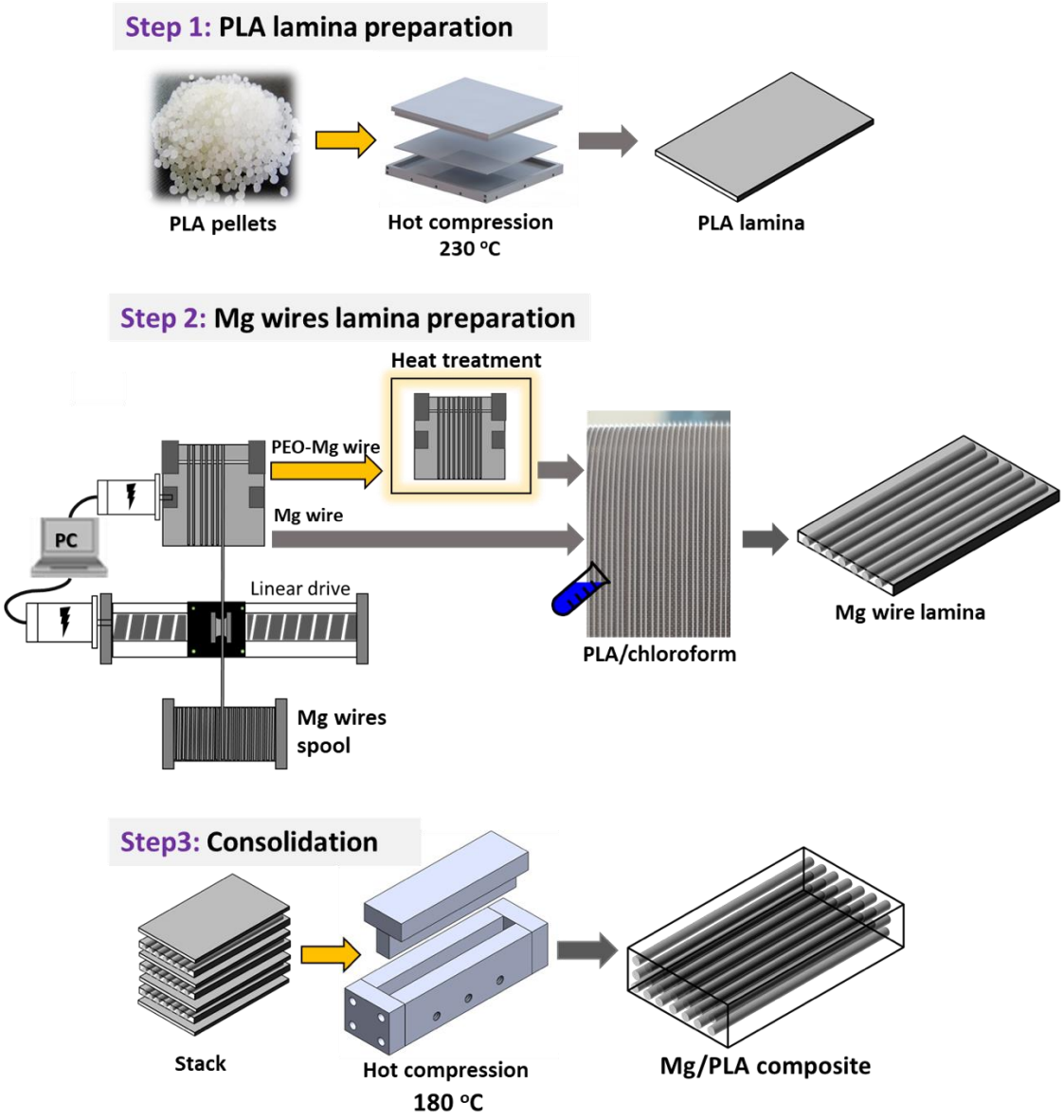

Fig. 5.6. Schematic depiction of three steps to manufacture Mg/PLA composites.

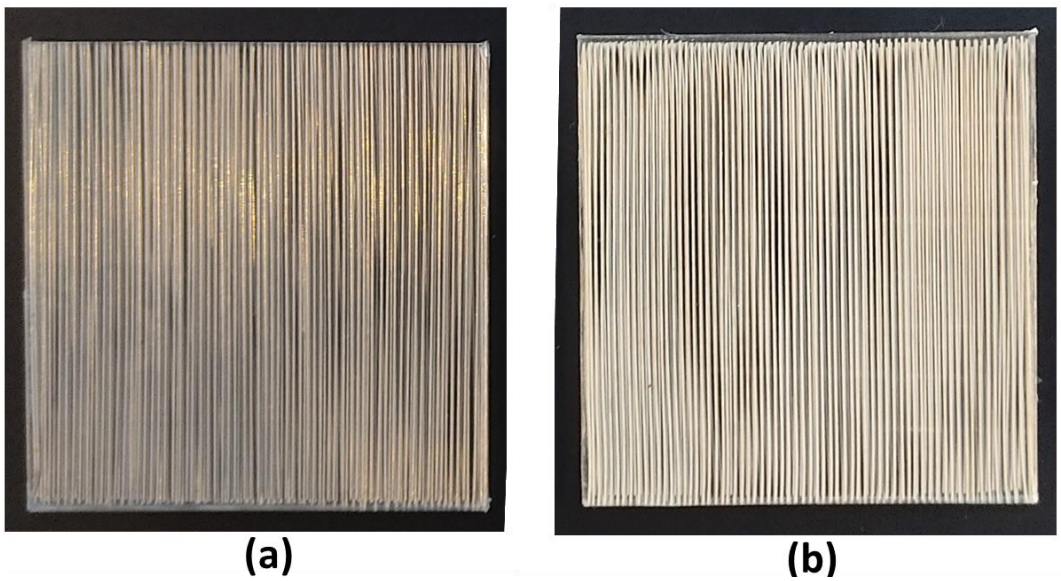

Fig. 6.7. Optical images of unidirectional (a) Mg/PLA and (b) PEO-Mg/PLA composite laminates.

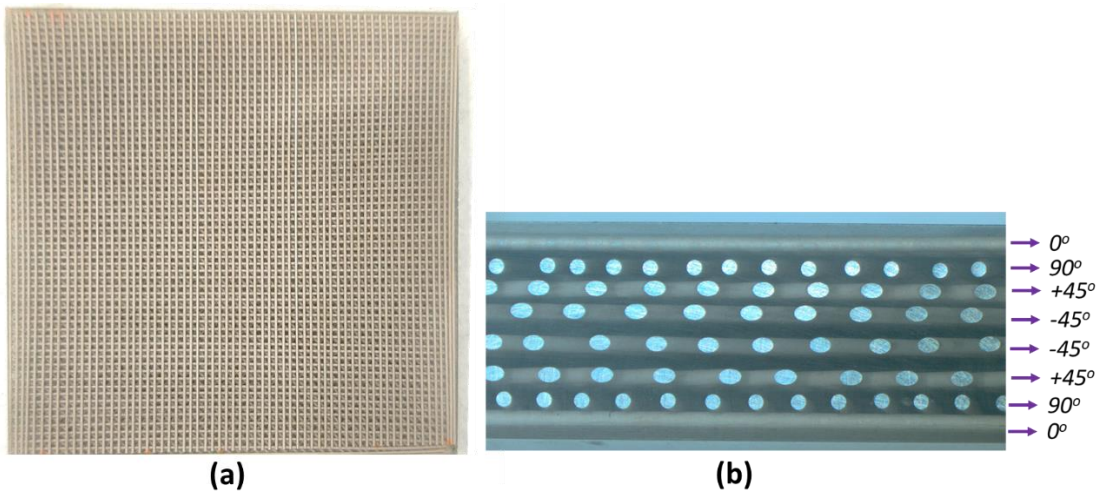

Fig. 7.8. (a) Optical images of quasi-isotropic PEO-Mg/PLA composite laminate $[0/90_4/-45]_s$ and (b) optical micrograph of the laminate showing the approximately equal spacing between wires within a lamina and between two laminas of wires.

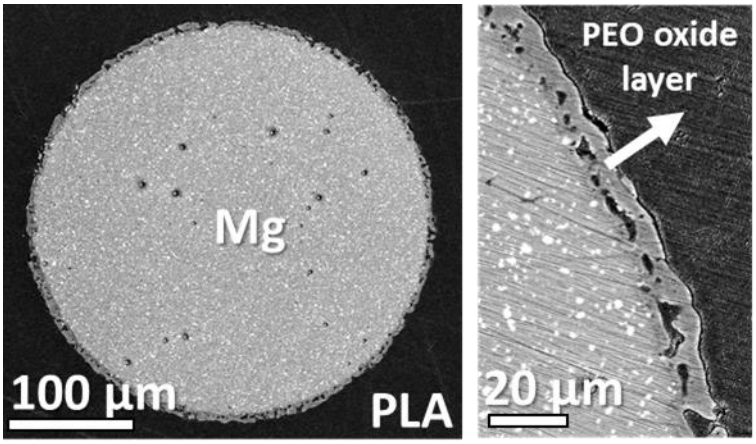

Fig. 8.9. Back-scattered electron micrograph of the PEO surface-modified Mg wire cross-section within the PLA matrix. The PEO oxide layer was not damaged during fabrication.

2.2.4. Additional processing by thermoforming and machining

Flat plates manufactured by hot compression molding led to composites with optimum stacking sequence of Mg wires, but the feasibility of additional processes was also studied towards the fabrication of patient-specific implants. The intended application of the Mg/PLA composite in this study is a fracture fixation plate, which in many cases require curved surfaces or surfaces adapted to the bone geometry. Therefore, vacuum-based thermoforming was used for surface adaptation of the Mg/PLA composite flat plate to a curved surface. As a proof of concept, a flat plate of Mg/PLA composite with $[\pm 45]_s$ stacking sequence and 50 mm x 50 mm x 2 mm was prepared by compression molding. The plate was cut to 10 mm x 50 mm x 2 mm with a CNC milling machine to be used in vacuum thermoforming. A femur model (3B Scientific) made up of PVC was purchased and the Mg/PLA plate was placed at a curved section at the proximal femur. The plate was sealed with nylon film (Wrightlon 7400, Airtech) and vacuum was created which resulted in application of pressure equal to the atmospheric pressure. The vacuum bag containing the femur and the platewas placed in an oven at 85 ^{o}C for 1 hour. The resulting Mg/PLA composite plate was completely adapted to the surface of femur (Fig. 2.10a) without altering the orientation of the wires within laminas. Machinability of the bone plate to create holes, chamfers, fillets, etc. is another important requirement for orthopedic fixation plates. Therefore, several machining processes such as CNC milling, drilling, punch cutting, grinding and polishing were successfully applied on composite plate. A unidirectional plate of PEO-Mg/PLA was

cut to 50 mm in length with a punch, and then fillets were created on both ends by grinding. Finally chamfered holes were created by standard bits in drilling machining (Fig. 2.10b).

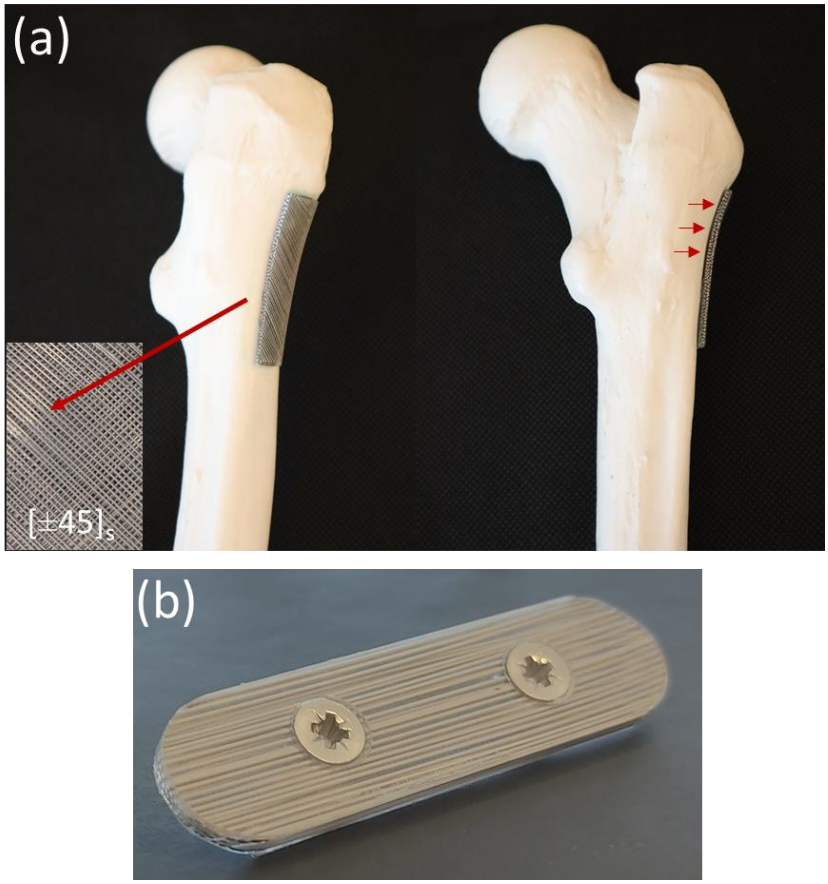

Fig. 9.10. Optical image of (a) cross-ply laminate of Mg/PLA composite after surface adaptation to a femur surface by vacuum thermoforming and (b) unidirectional PEO-Mg/PLA composite laminate after machining.

2.3. Conclusions

A novel strategy to manufacture Mg wires of 0.30 mm in diameter by cold drawing followed by continuous surface treatment by plasma electrolytic oxidation is presented. The novel strategy is easily scalable to produce large quantities of surface-modified Mg wires for biomedical applications with significantly improved corrosion resistance and, thus, improved mechanical properties and cytocompatibility due to the presence of a continuous PEO oxide layer. Moreover, the conventional hot compression process to

manufacture Mg wires reinforced PLA composite was modified, and multi-directional Mg/PLA composite laminates were produced with controlled positioning and orientation of wires within the laminate. Additional processing by thermoforming and machining was also showed as a proof of concept to manufacture Mg/PLA implants with customized mechanical properties (specially stiffness), adaptable surface and customized shape. For the first time, PEO surface-modified Mg wires were used in Mg/PLA composites, providing additional possibilities to reduce the degradation rate of the composite.

CHAPTER 3: MECHANICAL PROPERTIES, CORROSION RESISTANCE AND BIOCOMPATIBILITY OF Mg WIRES

In previous chapter, cold drawing and a novel manufacturing strategy for continuous surface-modification of Mg wires by PEO was presented. This new strategy seems suitable for upscaling Mg wires production and opens new opportunities for the use of Mg wires, such as their use as reinforcement of bioresorbable polymeric matrices. This chapter aims to explore the relationship among processing conditions (degree of cold work, annealing temperature and time, PEO parameters), the microstructure of the wires (grain size, dislocation and precipitate structures, oxide layer thickness, porosity and composition) and properties (mechanical and corrosion behavior). Moreover, biological performance of the wires with and without PEO is discussed [50].

3.1.Experimental techniques

3.1.1. Materials

Mg wires of 0.3 mm in diameter were manufactured by cold drawing following the strategy reported in section 2.1.3. Two wires (CW34 and CW13) were manufactured to the extent of 34% and 13% cold work. In addition, wires manufactured with 13% of cold work were subjected to four different annealing heat treatments lasting 5 s and 10 s at either 400ºC (HT400-5 and HT400-10) or 450ºC (HT450-5 and HT450-10). Moreover, wires with 13% cold work, followed by annealing at 450ºC for 5 s (CW13) were additionally surface modified by continuous PEO treatments at two frequencies 250 Hz (PEO250) and 500 Hz (PEO500) in frequency, leading to a continuous process (C-PEO) to convert the surface of the Mg wires and introduce a functional oxide layer [50].

3.1.2. Tensile testing of wires

The mechanical properties of wires ($n = 3$) in tension were measured on an electro-mechanical testing machine (ProLine Z010, ZwickRoell GmbH & Co. KG, Germany) at room temperature. The gauge length of the wires was 200 mm, and the tests were carried out under displacement control at an average crosshead speed of 5 mm/min with a 10 kN load cell [55]. To study the effect of *in vitro* in c-SBF on the tensile properties,

wires were 40 mm longer at both ends (total length of 280 mm) and sealed with a rubber coating (Liquid rubber coating, Mibenco, Germany) to protect the ends from degradation and, hence, to avoid failure in the gripping zones during the tensile tests. At least 4 samples were used for tensile on degraded wires. Average tension properties of wires with different processing conditions were compared using one way ANOVA.

3.1.3. Microstructure characterization

The grain size and texture of the wires were determined by means of electron backscatter diffraction (EBSD). To this end, wire cross sections were mounted in a conductive resin, mechanically grounded with SiC paper to 4000 grit, and then polished with 3 µm and 1 µm diamond paste. The polished samples were etched for 10s with an etchant consisting of 1% HNO_3, 24% distilled water and 75% ethylene glycol. The EBSD scan was carried out with FE-SEM Apreo 2S LoVac (ThermoScientific, Netherlands) equipped with an Oxford-HKL EBSD detector at 20 kV and 2.7 nA with a step size of 0.2 µm. The grain size and inverse pole figures were obtained by post-processing the EBSD map with the software Oxford® HKL Channel-5 (Oxford Instruments Limited, Oxford, United Kingdom).

The dislocation structures and precipitates were analyzed by means of transmission electron microscopy (TEM). Thin foils (< 100 nm) were prepared from the transverse cross-section of the wires by focused ion beam (FIB) in an FEI Helios NanoLab 600i dual-beam FEI-SEM (FEI, Netherlands). TEM analysis was carried out in a FEI Talos (FEI, Netherlands) equipped with a field emission gun operating at 200 kV. Both bright field (BF) images in TEM mode and high-angle annular dark field (HADDF) images in scanning-transmission electron microscopy (STEM) mode were acquired. Chemical composition mapping was performed under STEM mode with a SuperX Energy dispersive X-ray (EDX) detector. The acquisition time was set between 20 and 30 min, and the data were analyzed with the Bruker QUANTAX software.

To analyze oxide layer created by PEO and corrosion of wires, the wires were mounted in the epoxy resin and grounded to 4000 SiC paper, followed by polishing with 3 µm diamond suspension and 0.2 µm SiO suspension. The thickness of the oxide layer created by PEO was estimated from at least 15 measurements randomly taken from the cross-sectional view. For pitting quantification, random cross-sectional images of degraded HT450-5 (n = 20) and PEO500 (n=8) were also taken with an optical

microscope (VK-X3000, Keyence Deutschland GmbH, Germany). The microstructural features of the oxide layer and corrosion mechanisms from longitudinal and transverse surfaces using SEM/EDX (Zeiss EVO MA15, Germany) at an accelerated voltage of 15~20 kV[55][50].

3.1.4. In vitro degradation tests

In vitro degradation tests of the Mg wires were carried out at 37°C in 100 mL of simulated body fluid (c-SBF) with a composition (per liter) of 8.035 g NaCl, 0.355 g $NaHCO_3$, 0.225 g KCl, 0.176 g $K_2(HPO_4)$, 0.145 g $MgCl_2$, 0.072 g Na_2SO_4 and 50 mL of Tris buffer at pH 7.5 [122]. The ratio of c-SBF volume to the wire surface area was approximately 0.5 mL/mm^2 (> 0.2 mL/mm^2 as recommended by ASTM G31-72 [123]). Wires of 280 mm in length with 4 mm sealed at both ends were placed inside the glass burette with the lower end fixed at bottom level of the burette and the burettes were immersed into sealed plastic bottles filled with media. The degradation rate was monitored by the generation of hydrogen gas as a function of time, which was normalized with respect to the initial surface area of the wire [55][50].

3.1.5. Cell culture testing

The biocompatibility of the wires was tested following ISO 10993-1 and 10993-5. Indirect and direct tests were carried out using MC3T3-E1 pre-osteoblasts. Extracts for the indirect tests were obtained by immersion of the Mg wires (6 cm^2/mL) in the α-MEM medium (Invitrogen, USA), supplemented with 10% FBS, followed by incubation for 24 h at 37°C. 10.000 cells/cm^2 were seeded in a 96-well cell culture plate and incubated for 24 h at 37°C with 5% CO_2 concentration. Then, the culture medium was replaced with the concentrated and diluted extracts and incubated for another 24 h and the mitochondrial activity of the cells was measured by MTT assay. For this purpose (3-(4, 5-dimethyl thiazolyl-2)-2, 5-diphenyltetrazolium bromide) MTT (Sigma-Aldrich, Germany) was prepared in a concentration of 5 mg/mL and added to the cells in a proportion of 10 µl of MTT stock solution by 100 µl of culture medium. Cells were incubated for 3 h protected from light. After that, formazan crystals were dissolved by adding DMSO (Sigma-Aldrich, Germany), and the absorbance of the solutions was measured at 570 nm in a spectrophotometer (Tecan Infinite Mplex). Mitochondrial activity (%) was calculated using the value obtained from the control

sample of pure culture medium as a reference. The experiments were performed in triplicates for each sample [50].

For the direct tests, Mg wires with and without surface modification by PEO were first immersed in complete culture medium for 24 h to undergo some degradation and then used to study the cell-material interaction. Mg wires were mounted on a thin frame of medical grade poly-lactic acid (PLA) (Purasorb 7038, Corbion, Netherlands) obtained from a hot-pressed sheet of PLA of 0.8 mm in thickness. The ends of the wires were glued to the frame by using a PLA/chloroform solution where chloroform was evaporated after attachment. This experimental setup enabled analysis of the Mg wires under the microscope because wires remained in a stable position during handling. The Mg wires glued to the PLA frame and sheets of Titanium (99% Ti, Alfa Aesar) control were placed in 12-well plate and culture medium with 10,000 cells/cm^2 was added to wells. Then plates were incubated for 24 h. Afterwards, the cell-material interaction was analyzed using immunofluorescent microscopy. Cell morphology was then studied by labeling the cytoskeleton of the cells with phalloidin (Invitrogen, USA) and the nucleus with Dapi (Sigma-Aldrich, Germany). Fixed cells were treated with 0.1% Triton X-100 for 10 min, then cells were washed with PBS and labeled with Alexa 488 and Dapi for 1 h. Finally, cells were observed under a confocal microscope (Olympus FV3000, Japan). Cell morphology was also analyzed under SEM (Zeiss EVO MA15, Germany). For this purpose, fixed cells were washed with PBS and then dehydrated with an increasing concentration of ethanol in PBS (30, 50,70, 80, 90, and 100%) followed by overnight drying in air. The processed cells were then analyzed using back-scattered electrons at an accelerated voltage of 5-7 kV [50].

3.2.Results and discussion

3.2.1. Effect of processing conditions on microstructure of Mg wires

Processing of the Mg wires by cold drawing, as described above, led to a microstructure with small grain size and a strong basal texture, as it has already been reported in other investigations [52][101][111][113]. An example of the microstructure of the wires in the transverse cross-section can be found in the EBSD map in Fig. 3.1, which corresponds to the wire HT450-5 (13 % cold drawing followed by annealing at 450 ºC during 5 s). The average grain size was 1.4 ± 0.7 μm, and the wires showed a strong

texture with the prismatic {10-10} planes parallel to the cross-section and the basal planes parallel to the drawing direction. The EBSD maps of the wires subjected to 34% cold-drawing without additional heat treatment, as well as of wires subjected to 13% cold drawing and additional annealing for different times and temperatures were similar. The EBSD maps did not show any evidence of recrystallization during annealing, but large differences in orientation were found inside each grain (denoted by the changes in the color). Those are indicative of strains gradients within the grains, which are associated with large densities of geometrically necessary dislocations near the grain boundaries (Fig. 3.1).

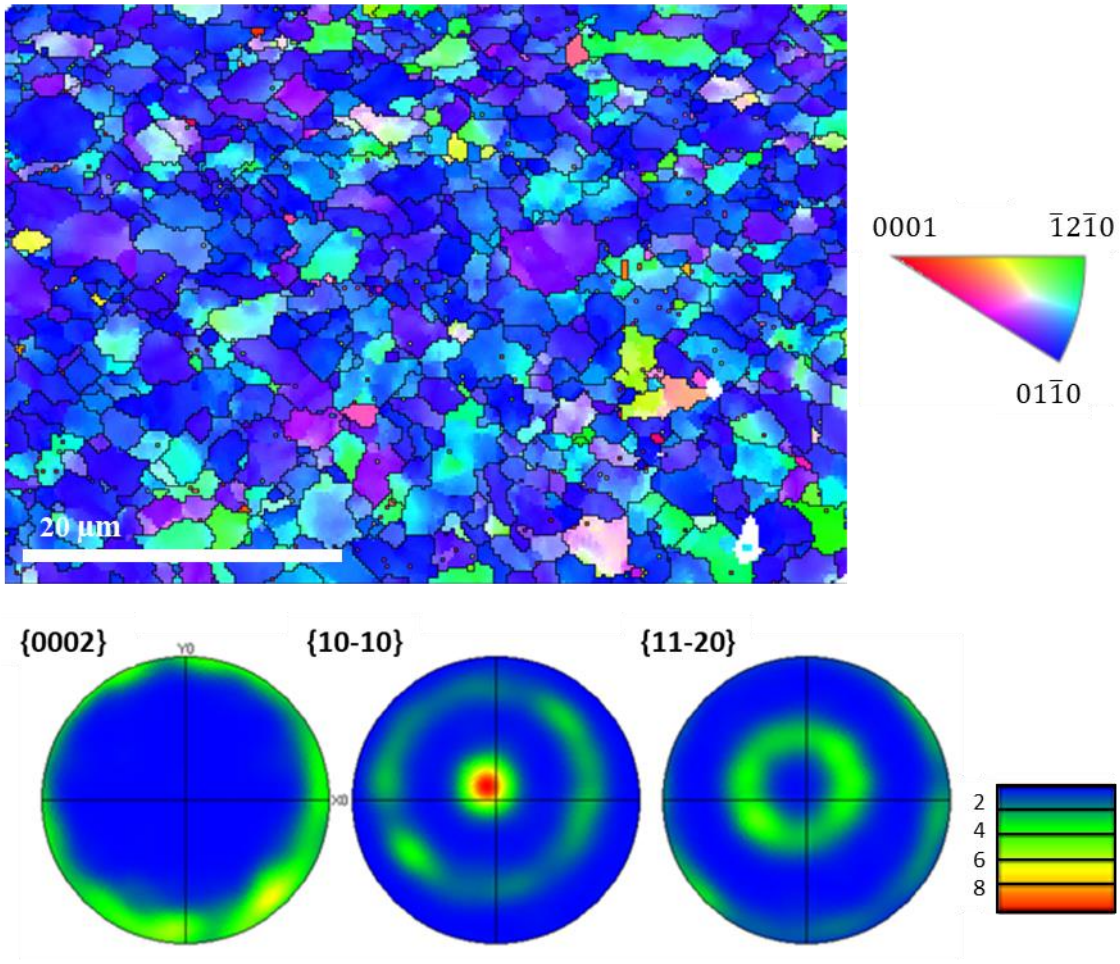

Fig. 3.1. (a) EBSD map of the transverse section of the HT450-5 wire showing the grain structure and orientation with respect to the wire axis. (b) Inverse pole figures showing the orientation of the different planes with respect to the wire axis. The numbers in the legend stand for multiples of random distribution.

The microstructure of the transverse cross-section of the wires was analyzed at higher magnification by means of TEM. Bright-field TEM micrographs of the CW34 and HT450-5 wires are shown in Fig. 3.2. Large globular shape precipitates (marked with

yellow arrows) with an average diameter of 0.5 to 1.5 µm can be found in both microstructures. The EDX analysis of the precipitate composition in Fig. 3.2b shows that the large precipitates were rich in Nd and Y. Obviously, the presence of these precipitates was not triggered by the annealing treatments after cold drawing, as they were found in the CW34 wire that was not annealed after cold drawing.

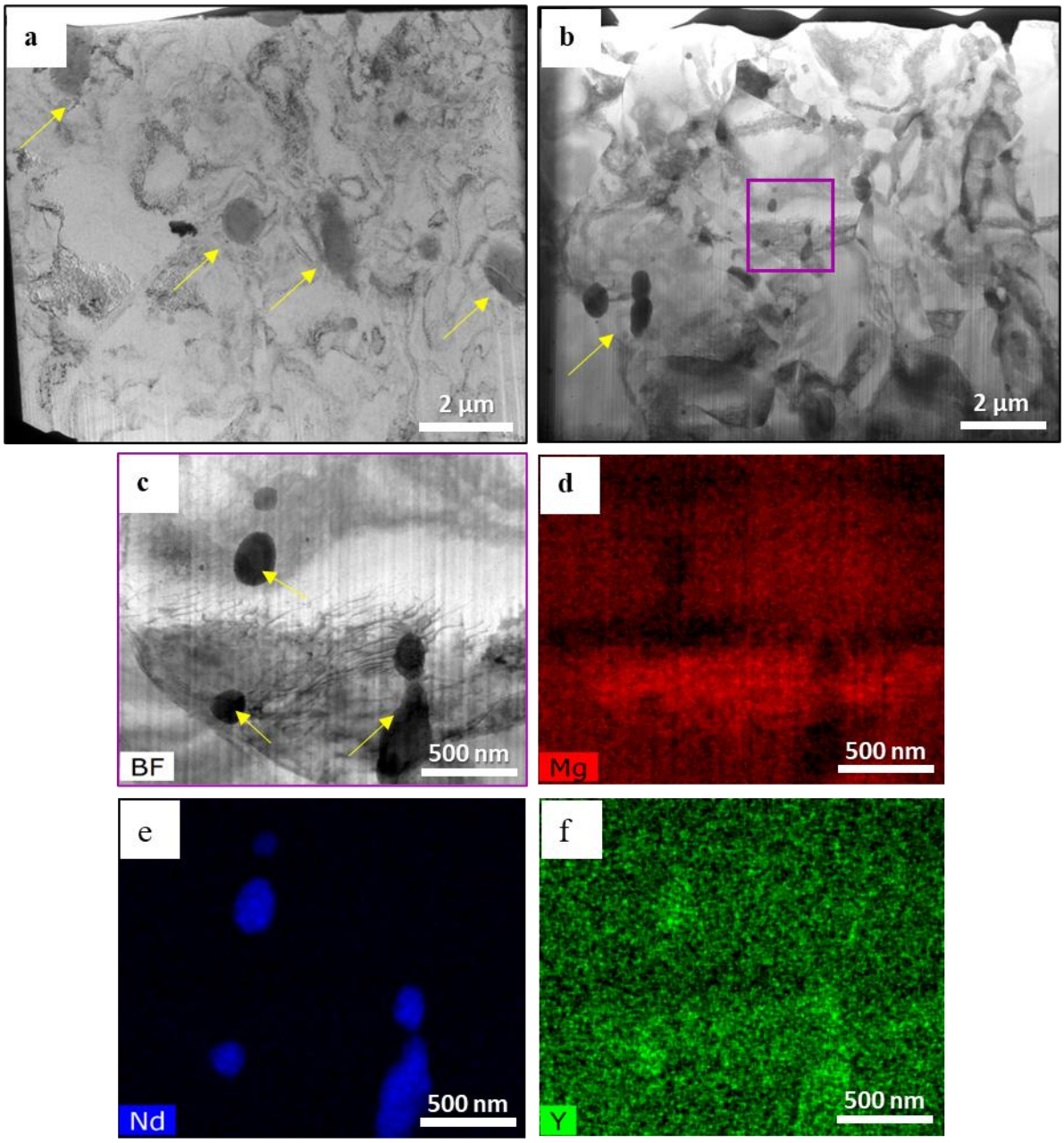

Fig. 3.2. (a) Bright-field TEM image of the transverse section of the CW34 wire. (b) Idem of the HT450-5 wire. Large globular precipitates are indicated by yellow arrows in both images. (c) High resolution bright-field TEM of the region marked by a purple square in (b) and (d-f) EDX results show the chemical composition of the large globular precipitates, which are rich in Nd and Y .

Large dislocation densities are found near the grain boundaries in the wire cold drawn up to 34 % without annealing (Fig. 3.3a). Short annealing of the wires after cold drawing has two main effects. The first one is large reduction in the dislocation densities near the grain boundaries, as shown in Fig. 3.3b for the HT450-5 wire being annealed for 5s at 450ºC. However, annealing did not remove all the dislocations as temperature and annealing time were not large enough to promote recrystallization of the microstructure, as indicated by the grain structure in Fig. 3.1.

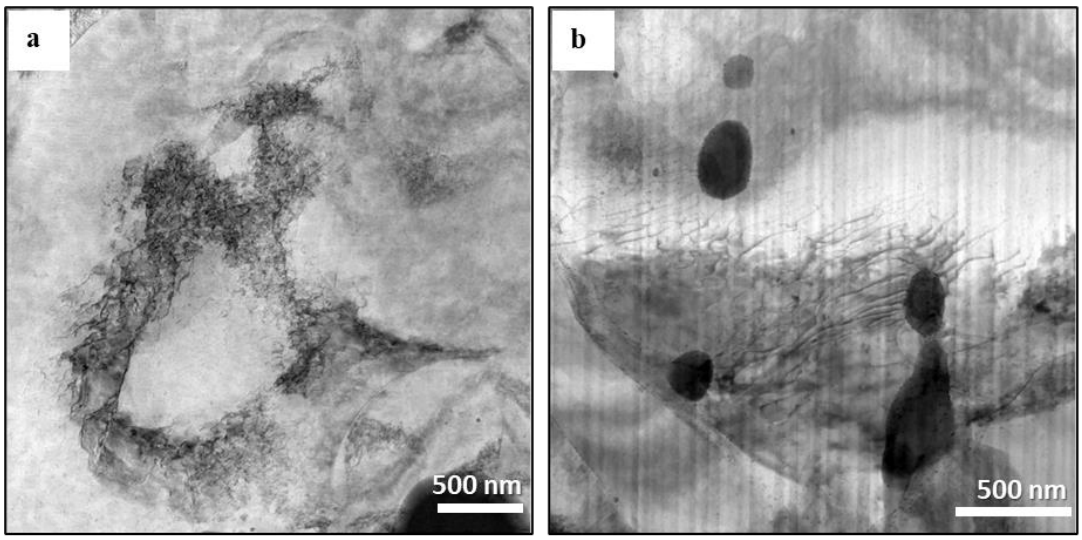

Fig. 3.3. Bright-field TEM images of the transverse cross-section of the Mg wires, showing dislocation structures near the grain boundaries and precipitates. (a) CW34. (b) HT450-5.

The second effect of annealing is shown in the STEM images of the CW34, HT450-5 and HT450-10 wires depicted in Fig. 3.4. The main RE elements in the WE43 alloy (Nd and Y) are homogeneously distributed within the CW34 wire, and there is no evidence of segregation at either grain boundaries or dislocations (Fig. 3.4a). Short annealing during 5s at 450ºC after cold drawing led to an important reduction in the dislocation density and to the segregation of Nd and, to a minor extent, Y at the grain boundaries (Fig. 3.4b). Further annealing up to 10s at 450 ºC, led to the nucleation of small precipitates rich in Nd and Y near the grain boundaries (Fig. 3.4c).

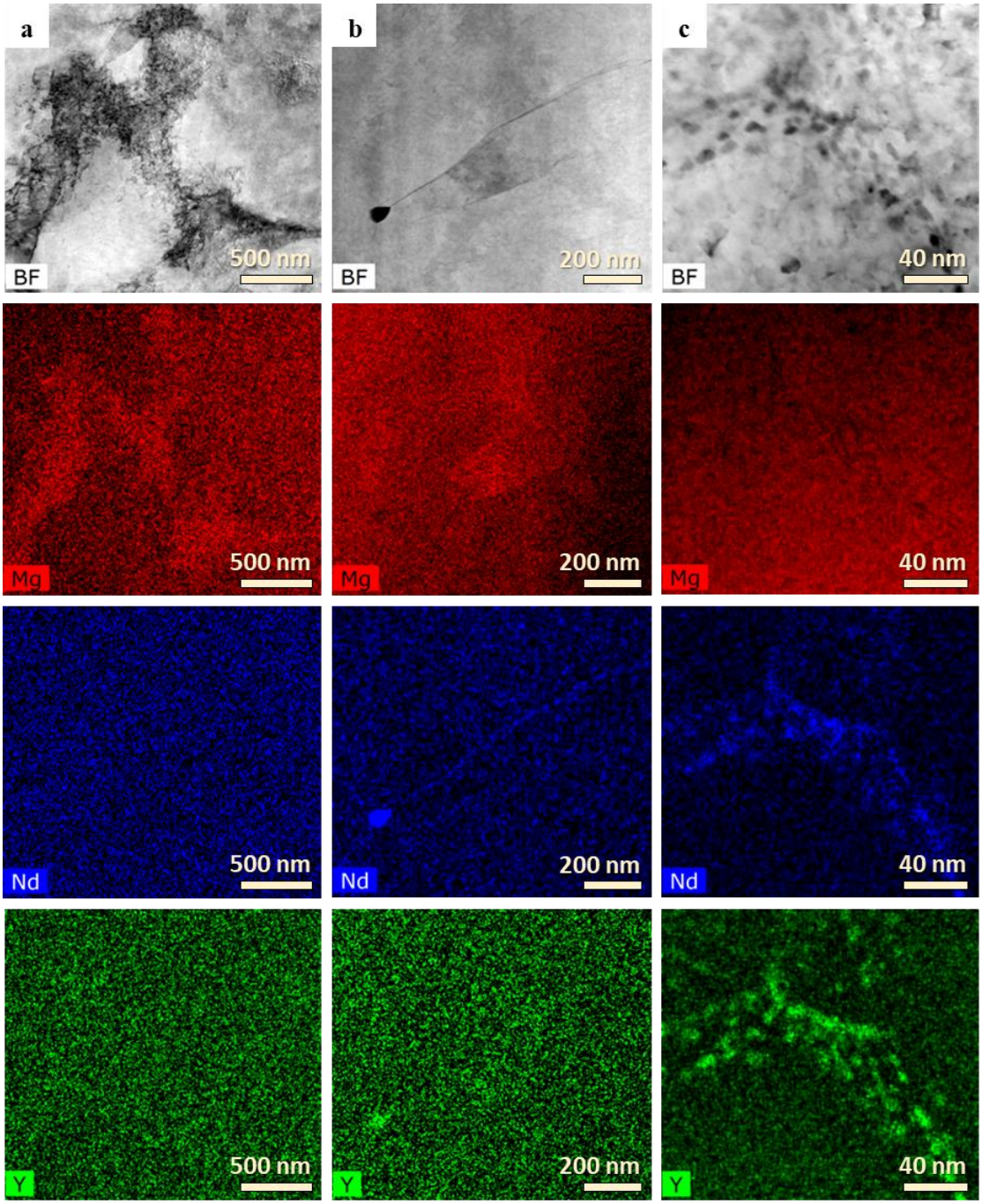

Fig. 3.4. STEM images and EDS maps showing the distribution of Mg, Nd, and Y. (a) CW34. (b) HT450-5 and (c) HT-450-10.

3.2.2. Effect of processing conditions on mechanical and corrosion rate of Mg wires

Representative engineering tensile stress-strain curves of the WE43 Mg wires subjected to different processing conditions are depicted in Fig. 3.5. The average values and standard deviation of the 0.2% offset yield strength, tensile strength and strain to failure are summarized in Fig. 3.5b. The stress was obtained from the load divided by the initial cross-section of the wire, while strains was calculated from the crosshead displacement of the mechanical testing machine divided by the initial gage length. The wires that were not annealed after cold drawing (CW34 and CW13) showed high strength and very poor ductility (< 1%). This brittle behavior agrees with the microstructure of the wires, which showed small grain size (≈ 1 μm) and large dislocation densities within the grains associated with the cold drawing process. Very large external stress has to be applied to promote dislocation motion against the back stresses created by the dislocation pileups at the grain boundaries, leading to brittle failure of the wires. It should be noted that very similar results were obtained for both 13% and 34% of cold work, indicating that 13% cold work is sufficient to promote strain hardening of the wires.

Annealing of the CW13 Mg wires at either 400ºC or 450ºC during 5 s or 10 s however led to significant changes in the stress-strain behavior. The yield strength dropped slightly, and this reduction increased with both temperature and annealing time, while the ductility increased up to 7 % after annealing at 400ºC and up to ≈ 10% after annealing at 450ºC. Annealing did not lead to significant changes in texture or grain size but dramatically reduced the dislocation density within the grains (Figs. 3.1 and 3.3) and thus allowed the activation of plastic slip at lower stresses. Further plastic deformation led to strain hardening and improved the strength and ductility of the wires. Among the different annealing treatments, 450ºC for 5 s led to the optimum combination of strength and ductility.

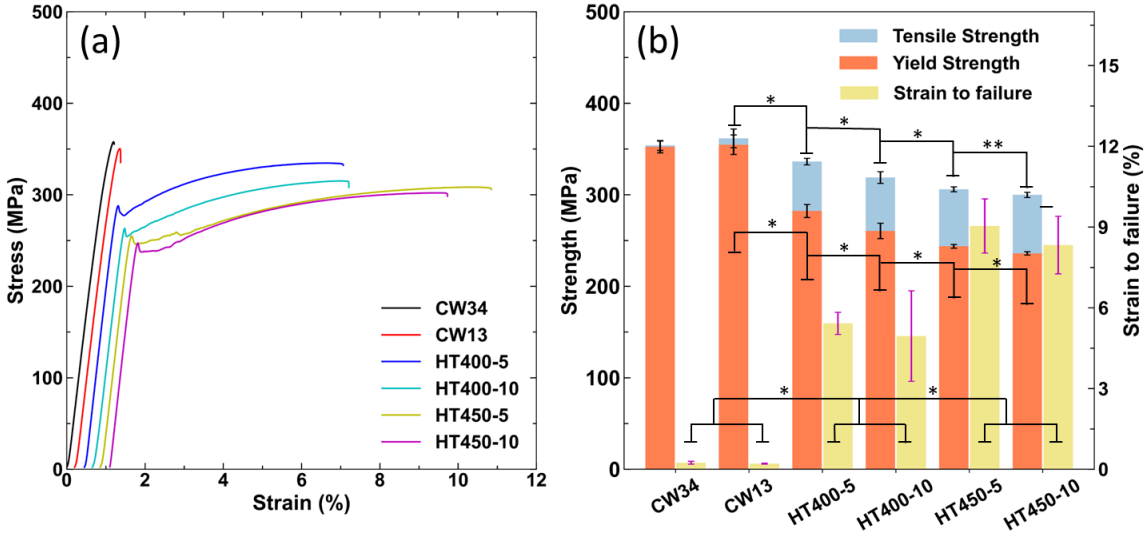

Fig. 3.5. (a) Representative engineering tensile stress-strain curves of WE43 Mg wires undergoing different processing conditions. The different curves are displayed with an offset ≈ 0.2% for the sake of clarity. (b) Summary of tensile properties of the Mg wires with different processing conditions. Here (*) and (**) represents $p < 0.05$ and $0.05 < p < 0.10$, respectively obtained by one-way ANOVA.

The early degradation of the Mg wires in c-SBF at 37ºC was assessed from the release of hydrogen gas and the corresponding results for wires subjected to different processing conditions are plotted in Fig. 3.6. The highest corrosion rate after 1 h of immersion was found for the CW34 wire while the lowest corrosion rate was observed for CW13 wire. Annealing of the CW13 wires led to a slight increase in the corrosion rate after 1 h but the differences between annealing treatments were negligible. After 6 hours of immersion, the lowest corrosion rate was still found for the CW13 wire. Increasing the amount of cold drawing (CW34) or the annealing temperature or time seemed to enhance the corrosion rate. The effect of annealing on the corrosion rate can be related to the nucleation of precipitates at the grain boundaries, as shown in the transmission electron microscopy observations in [124] while the effect of cold work can be linked to the increase in dislocations. It should be noted that the mass loss of the Mg wires after 6 hours of immersion was in the range 20-30%, and the differences in the corrosion rates of the Mg wires subjected to various processing conditions were still found to be very limited. Hence, our results clearly indicate that microstructural changes are not enough to tailor the reactivity of Mg alloys and that strategies based on surface modification are necessary.

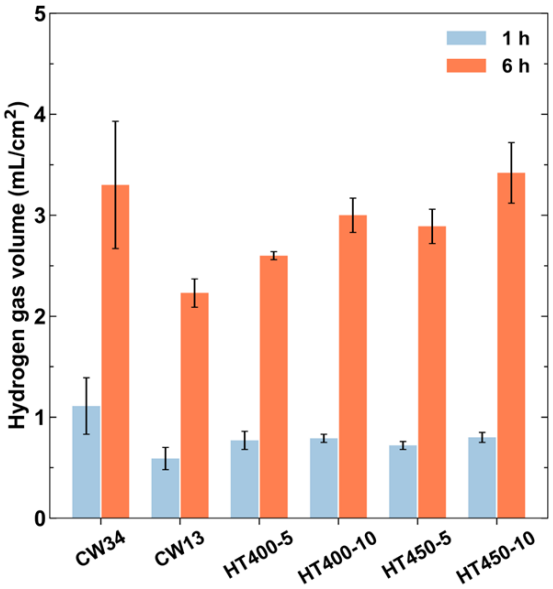

Fig. 3.6. Degradation rate of Mg wires with different processing conditions measured by the hydrogen evolution after 1 and 6 h immersion in c-SBF.

3.2.3. Morphology of wires after continuous PEO surface-modification

PEO surface modification is an electrochemical conversion process based on principles of plasma electrolysis, also known as micro-arc oxidation (MAO) [125][126]. During PEO, the application of a high electrical potential results in strong but short-lived plasma discharges associated high a significant local increase in temperature, leading to a uniform effusion of molten Mg through discharge channels at the surface of the substrate. The molten Mg rapidly reacts during discharge with the chemical compounds of the electrolyte and is immediately quenched by the cold electrolyte bath. An oxide layer builds up within fleeting periods of time because of those plasma ignitions scanning the surface regions exposed to the electrolyte. However, as the oxide layer on the surface grows, the electrical resistance between the anode and cathode increases up to a critical value in voltage, which finally needs to be surpassed by the electrical source or automatically limits film growth and terminates the process. From a chemical standpoint, the oxide layer induced by PEO surface modification comprises contributions from the Mg substrate, electrolyte species which react or are incorporated as well as in some cases from alloying elements. Conclusively, PEO of Mg alloys in the presence of a phosphate-based electrolyte at least leads to oxide rich layers which contain both MgO and $Mg_3(PO_4)_2$ [115][117].

The continuous surface-modification by PEO was performed only on the HT450-5 wires to study the basic mechanism of continuous processing as well as to analyze the most influential parameters. From a qualitative viewpoint, many plasma sparks appeared around the wire as it entered the electrolyte bath during PEO, but the density of sparks decreased and became negligible when the wire exited the bath, as schematically shown in Fig. 2.2. To understand the formation of the surface modification layer, the continuous process was stopped and the cross-sections and lateral surfaces of wire segments from different locations inside the bath were analyzed by optical microscopy and SEM. Images of the wire surface are depicted in Fig. 3.7 after 3, 9 and 20 s in electrolyte bath. The apparent color of the wire turned from silver to off-white with a smooth appearance which is associated with the formation of the porous surface modification and its ceramic nature. These figures indicate that the interface in the facilitated process grows rapidly and is linked to the high density of sparks that are appear when the wire enters the bath. The morphology of the oxide layer, as displayed in Figs. 3.7h and 3.7i, is very similar and the only difference is the thickness whose evolution with time in the electrolyte has been plotted in Fig. 3.8 for PEO processes carried out at a frequency of 250 Hz (PEO 250) and 500 Hz (PEO 500). The layer initially grows rapidly in the first 5 s but apparently, the thickness increases only slowly after 10s. The frequency has very limited influence on the oxide layer thickness after 20 s, leading to average thicknesses of the oxide layers of 8.3 ± 1.3 µm and 7.8 ± 1.3 µm for PEO250 and PEO500, respectively. It was assumed that this layer thickness was appropriate to passivate the Mg wire and further analyses of the morphological features were carried out on wires that spent 20 s in the electrolyte bath during the continuous PEO.

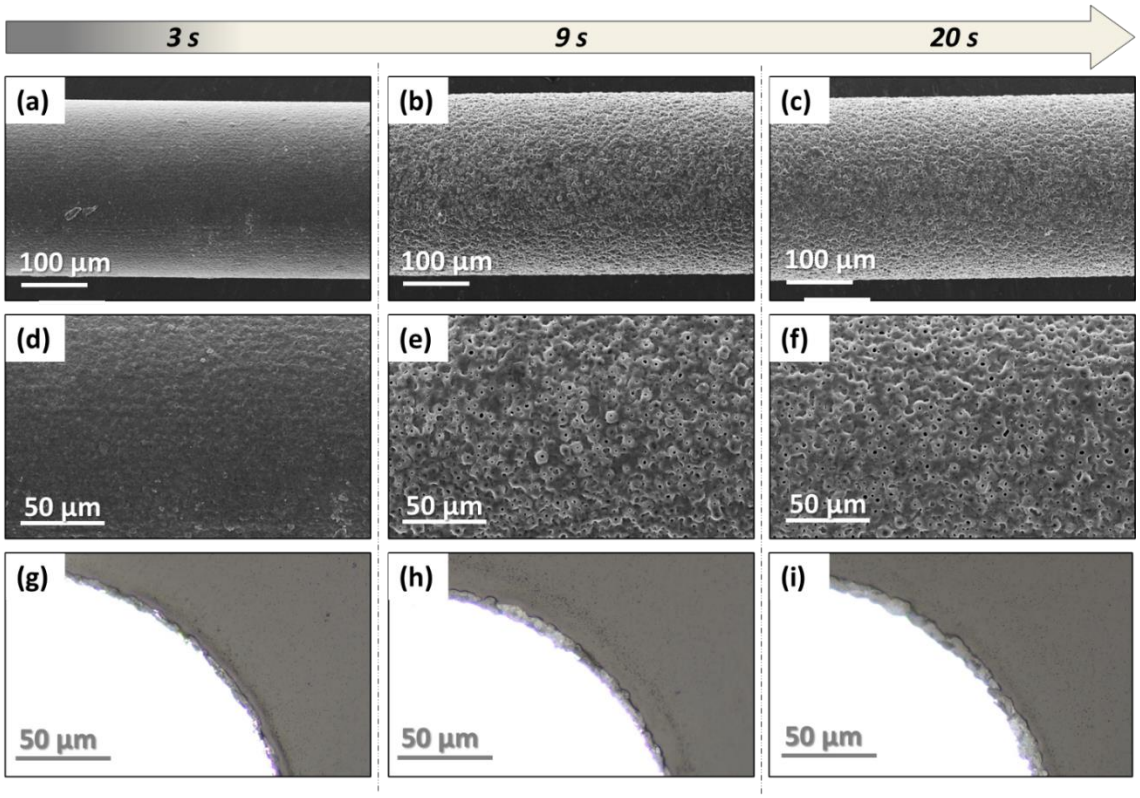

Fig. 3.7. (a-c) Secondary electron SEM image of the oxide layer formed by PEO on the wire surface as a function of time inside the electrolyte bath. (d-e) *Idem* at higher magnification. (g-h) Backscattered electron SEM images of transverse cross-section of the wire as a function of time inside the electrolyte bath. The frequency of the current during PEO was 500 Hz. The arrow on top of the figures shows the evolution of the actual color of the Mg wire with time.

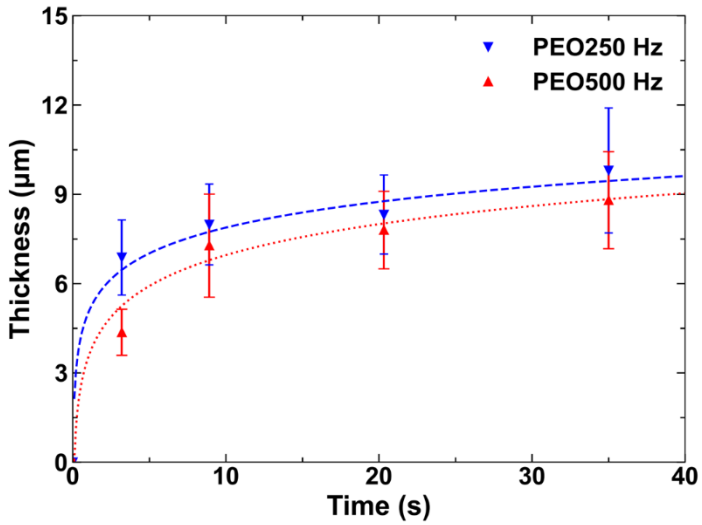

Fig. 3.8. Evolution of oxide layer thickness as a function of the time inside the electrolyte bath carried out at 250 Hz (PEO250) and 500 Hz (PEO500).

The surface morphology of the continuous oxide layer obtained by 20 s immersion in the electrolyte at a frequency of 250 Hz and 500 Hz is shown at high magnification in the secondary electron SEM images in Figs. 3.9a and 3.9b, respectively. The structure of the modification layer perpendicular to the wire axis can be observed in the backscattered electron images of the transverse cross-section depicted in Figs. 3.7c and 3.7d. The oxide layer grown at 250 Hz shows large pores in the middle of the oxide layer, while PEO processing at 500 Hz led to a more compact interface with reduced internal porosity. The analysis of the longitudinal sections of the wires observed by light microscopy (Figs. 3.7e and 3.7f) demonstrates that the thickness of the oxide layer, as well as the microstructure, are constant along the wire length, indicating that the facilitated continuous PEO process is robust and can be applied on continuous wires for serial production.

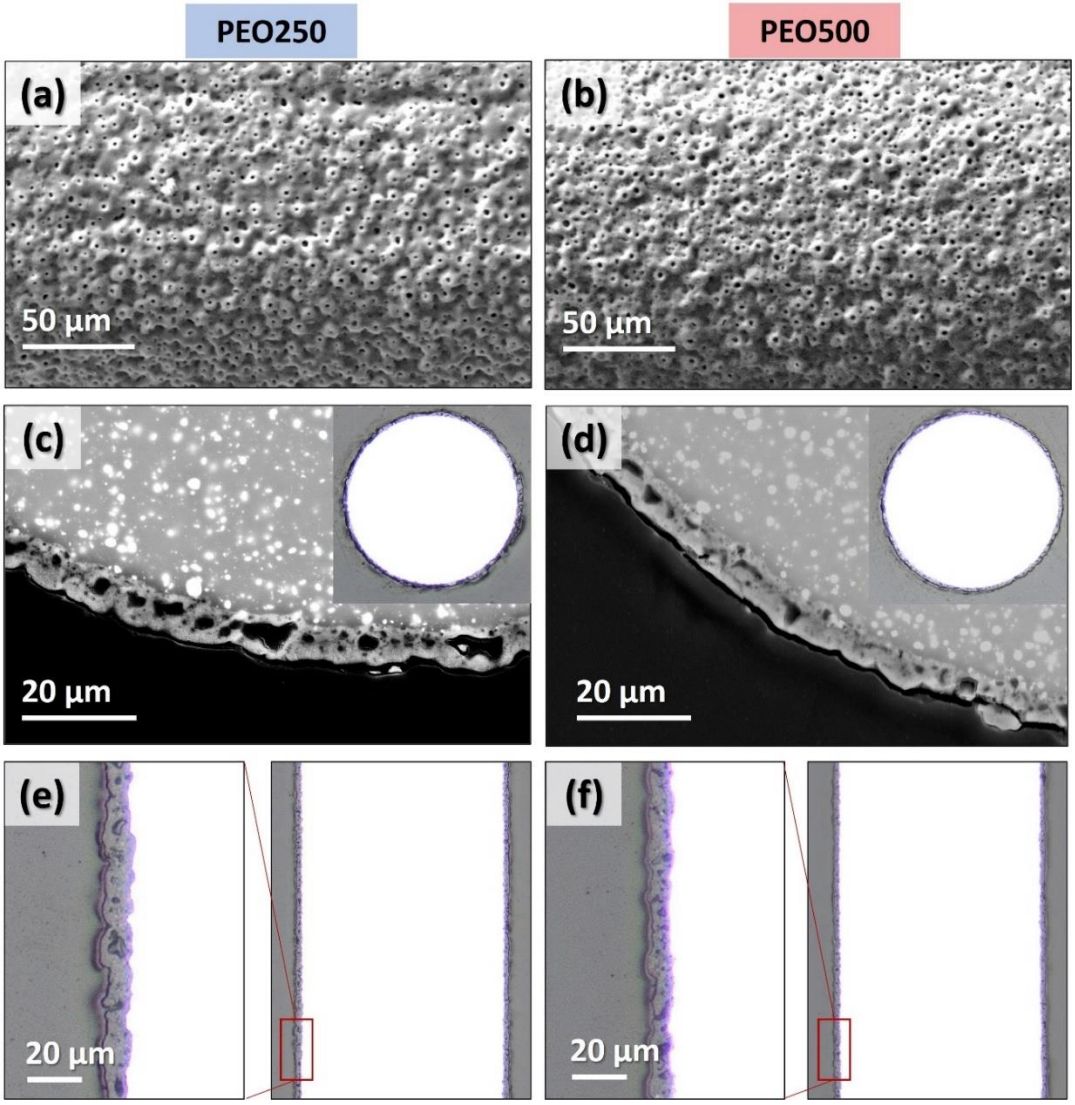

Fig. 3.9. (a) Secondary electron SEM image of the oxide layers formed at 250 Hz. (b) *Idem* at 500 Hz. (c) Backscattered electron SEM images of transverse cross-section of the wire after PEO at 250 Hz. (d) *Idem* at 500 Hz. (e) Light microscopical image of the longitudinal section of wire after PEO at 250 Hz. (f) *Idem* at 500 Hz. The average thicknesses of the oxide layers were 8.3 ± 1.3 µm and 7.8 ± 1.3 for PEO250 and PEO500, respectively.

The chemical composition of the oxide layer can be found in the element composition maps obtained by EDX in the cross-section of the PEO500 wire in Fig. 3.10. They confirm the presence of Mg, P and O, in agreement with previous reports [115][117]. The most likely chemical compounds in the oxide-rich interface layer are MgO and $Mg_3(PO_4)_2$, which appear because of the following reactions:

$$Mg \rightarrow Mg^{2+} + 2e^- \quad (3.1)$$

$$4OH^- \rightarrow 2H_2O + O_2 + 4e^- \quad (3.2)$$

$$Mg^{2+} + 2OH^- \rightarrow Mg(OH)_2 \quad (3.3)$$

$$Mg(OH)_2 \rightarrow MgO + H_2O \quad (3.4)$$

$$3Mg^{2+} + 2PO_4^{3-} \rightarrow Mg_3(PO_4)_2 \quad (3.5)$$

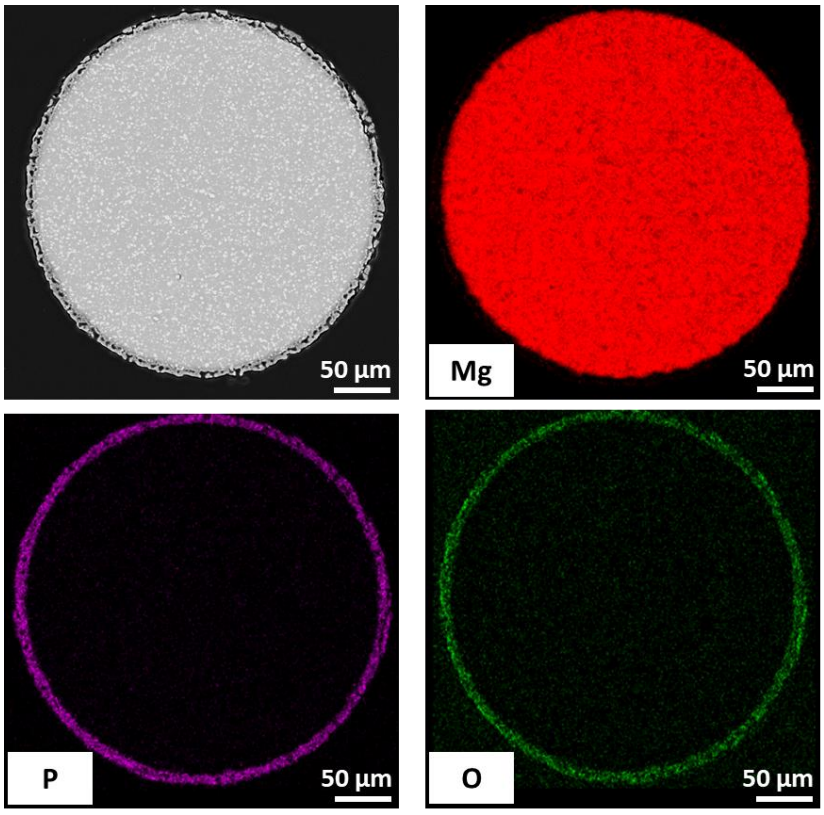

Fig. 3.10. Back-scattered electron SEM image of the cross-section of the PEO500 (top left) and elemental composition mapping obtained by EDX showing the presence of Mg, P and O in the oxide layer.

From a production perspective, cold drawing of metallic wires can lead to the formation of unidirectional grooves and sub-micron cracks at the surface due to deterioration of the die by wear, poor lubrication, etc. These defects do not significantly alter the tensile properties of wire if they are below a certain threshold because plastic deformation alleviates the stress concentrations. However, they are prone to undergo and promote pitting corrosion [127] and, in addition, contaminations can get into such small cavities making it difficult to eliminate by cleaning, thus potentially compromising biocompatibility. Examples of these longitudinal defects can be found in Fig. 3.11a. After the PEO process, the depth of the largest defects has been greatly reduced, while the minor unidirectional drawing lines are entirely removed from the surface. This is because the oxide layer grows outwards and inwards simultaneously, at least at the beginning of the PEO process [128]. Our observations indicate that the total inwards growth was about 1-2 µm and was independent of the frequencies employed for PEO process, at least within the selected time span.

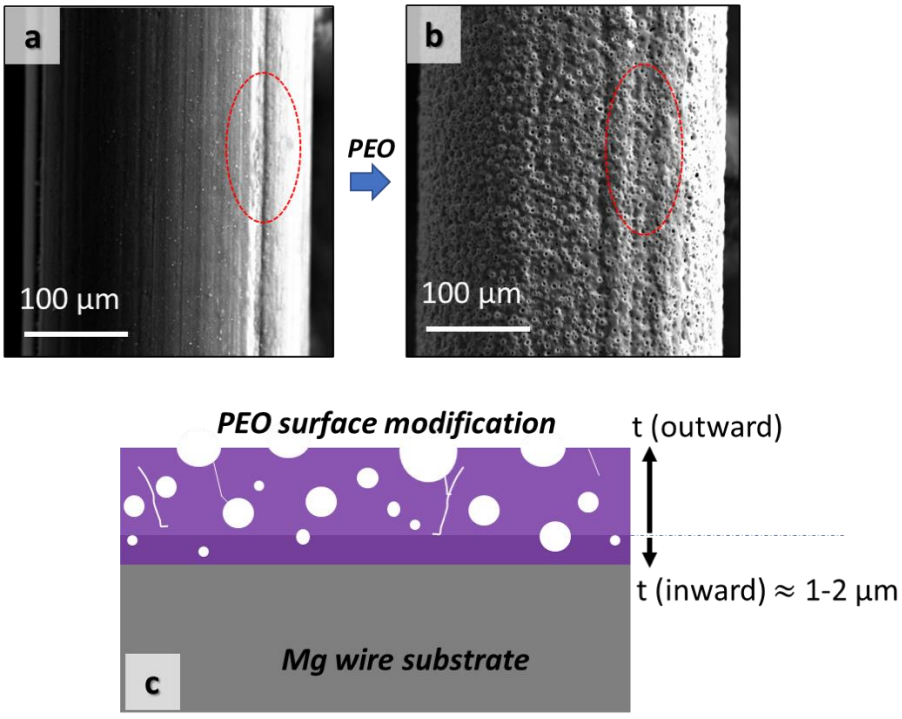

Fig. 3.11. (a) Secondary electron SEM image of Mg wire with longitudinal grooves created during cold drawing (b) Partial healing of the longitudinal grooves because of PEO. (c) Schematic depiction of the defect healing mechanism because of the inward penetration of the oxide layer.

3.2.4. Effect of PEO surface-modification on intact mechanical properties of Mg wires

Representative tensile stress-strain curves of the Mg wires before (HT450-5) and after (PEO250 and PEO500) surface modification are plotted in Fig. 3.12. Surface-modification leads to a slight reduction in the strength of the wires for two reasons. Firstly, the PEO process consumes a distinct portion of Mg at the surface of the wire of 1-2 µm in thickness (Fig. 3.11), which is replaced by a porous oxide layer with higher strength, but limited ductility with regards to mechanical properties. Secondly, PEO is accompanied by an increase in the temperature of the wire, which leads to further annealing, potentially reducing the dislocation density and yield strength. Nevertheless, the average results and standard deviation of yield strength, tensile strength, and ductility before and after PEO in Fig. 3.12b show that the effect of PEO is limited and does not significantly impair the mechanical performance of the tested Mg wires.

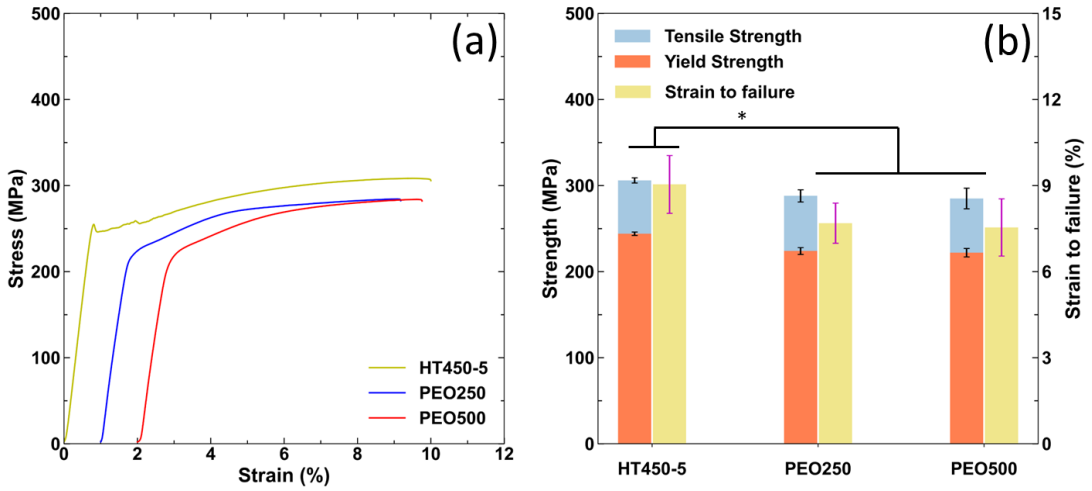

Fig. 3.12. Tensile stress-strain curves of Mg wires before (HT450-5) and after (PEO250 and PE0500) surface modification. The different curves are depicted with an off set of ≈ 1 % for the sake of clarity. (b) Summary of tensile properties of the Mg wires before (HT450-5) and after (PEO250 and PEO500) surface modification. Here, (*) represents $p < 0.05$ obtained by one-way ANOVA.

3.2.5. Effect of PEO surface-modification on mechanical degradation and corrosion behavior of Mg wires

As expected, the continuous oxide layer created by PEO did have a strong effect on the *in vitro* degradation of the Mg wires. The hydrogen volume generated by HT450-5, PEO250 and PEO500 wires as a function of the immersion time in c-SBF at 37ºC is plotted in Fig. 3.13a. The initial corrosion rate (as measured by the hydrogen evolution) was similar for wires without and with oxide layer during the first ≈ 5 h. However, the hydrogen evolution evolved linearly with time in the unprotected wires up to ≈ 20 h while it was significantly reduced for PEO surface-modified wires after 6 - 7 h.

Likewise, the mechanical properties, i.e. tensile strength, of the degraded wires was measured as a function of the immersion time in c-SBF, see Fig. 3.13b. While the strength of the HT450-5 wires decreased to almost 0 after 24 h of immersion in c-SBF at 37ºC, the strength of the wires protected by PEO was > 200 MPa after 24 h and > 100 MPa after 96 h. It should be noted that the decrease in mechanical strength of PEO250 and PEO500 wires was very similar up to 96 h, which agrees with the results of the corrosion tests. The tensile stress-strain curves in Figs. 13.13(c-e) show that the failure strain of all wires decreased with degradation time. Nevertheless, surface modification of the Mg wires by PEO provided higher strain-to-failure in all cases. Tensile tests could not be carried out on wires immersed for longer times than depicted in the figure since they lost mechanical integrity and were too fragile to test reliably.

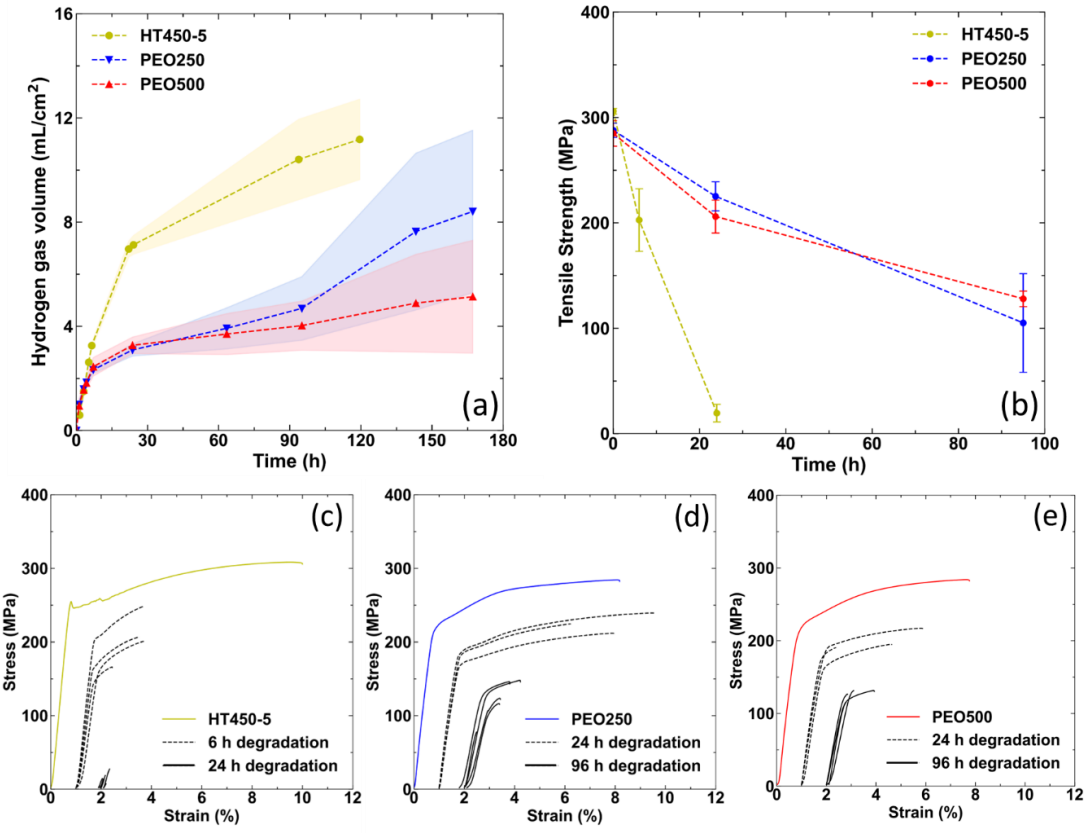

Fig. 3.13. (a) Hydrogen gas evolution as a function of immersion time in c-SBF at 37ºC for Mg wires before (HT450-5) and after (PEO250 and PEO500) surface treatment by PEO. (b) *Idem* for the tensile strength. The lower row shows changes in the tensile stress-strain curves of (c) HT450-5, (d) PEO250 and (e) PE0500 wires as a function of degradation time. Shaded regions in (a) indicate the standard deviation.

The fracture region of the PEO500 wire tested in tension before immersion in c-SBF is depicted in Fig. 3.14a. The fracture surface is oriented at 45º from the tensile loading axis, indicating that the final fracture process took place by shear, a typical mechanism in Mg alloys. The image at higher magnification shows many cracks perpendicular to the loading axis in the oxide layer. They indicate that the oxide layer was well adhered to the Mg wire and failed in tension because of the load transfer during the plastic deformation of the wire. The fracture region of the PEO500 wire deformed after 96 h of immersion in c-SBF is depicted in Fig. 3.14b. It shows a core region of Mg, which also failed by shear, surrounded by a thick circumferential oxide layer, which is homogenously distributed and did not detach from the Mg core. On the contrary, the fractures of Mg wires that were not modified by PEO showed to be fully brittle after 24 h degradation (Fig. 3.14c) and the strain to failure was negligible.

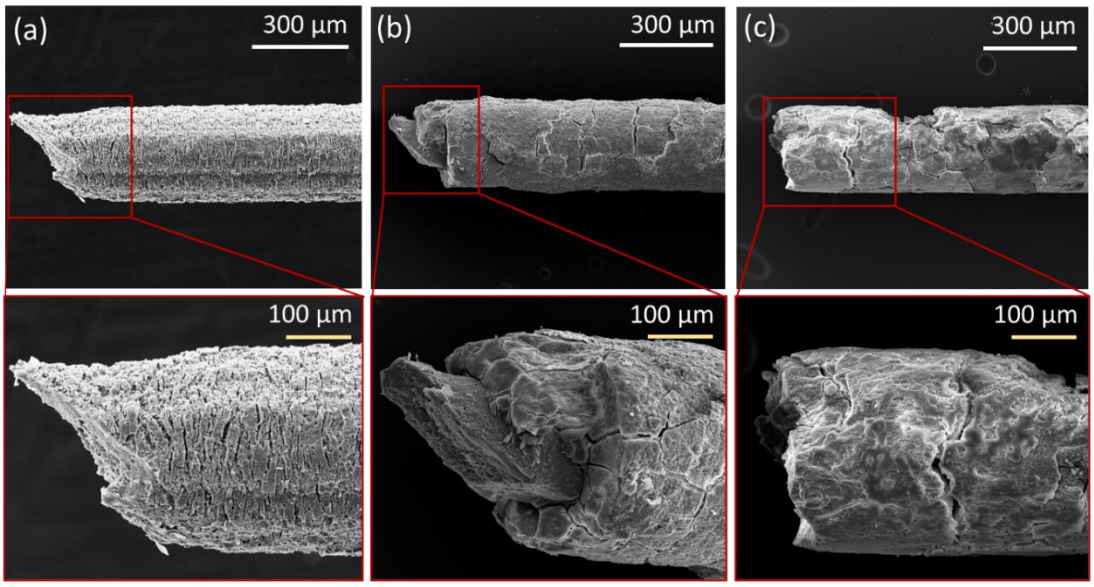

Fig. 3.14. SEM images of Mg wires before and after degradation. (a) Fracture region of the PEO500 wire deformed under tension before immersion in c-SBF. (b) *Idem* after 96 h in c-SBF. (c) Fraction region of a HT450-5 wire after 24 h immersion in c-SBF.

3.2.6. Corrosion mode of Mg wires and PEO surface-modified Mg wires

The presence of the oxide layer created by PEO did not only reduce the average corrosion rate of the wires but also reduced the intensity of pitting corrosion. This is shown in Figs. 3.15a and 3.15b, in which random cross-sections of the Mg wires (including only the Mg section of the wire) are depicted for the HT450-5 wire after 24 h of immersion in c-SBF and for the PEO500 wire after 96 h of immersion in c-SBF, respectively. For the wire without any surface protection by PEO, corrosion was easy to localize in random cross-sections of the wire and the mechanical strength of the wires was quickly reduced to a negligible value within 24 h of immersion. On the contrary, the PEO oxide layer showed to hinder the development of severe pitting corrosion and the Mg cross-section of these wires remained almost circular and intact even after 96 h of immersion in c-SBF.

The differences in corrosion profile were quantified by evaluating the severity of pitting corrosion by image processing using PitScan [122]. To this end, cross-sectional images of degraded wires were analyzed following the procedure detailed in the supplementary information. The metrics that characterize the intensity of pitting corrosion are summarized in Fig. 3.16. They are the uniform corrosion radius in Fig. 3.16a (the radius of the circular section that has the same area as the corroded cross-section), the average

pit depth in Fig. 3.16b (average distance from the degraded cross-section to the uniform corrosion circle), and the maximum pit depth in Fig. 3.16c (maximum distance from the corroded cross-section to the uniform corrosion circle). Fig. 3.16a confirms the hydrogen evolution results reported in Fig. 3.13a and the uniform corrosion radius of PEO500 (113 ± 8.5 µm) was still larger after 96 h than that of the non-surface treated HT450-5 (108 ± 21 µm) after only 24 h. Moreover, the high standard deviation of the uniform corrosion radius of HT450-5 shows the greater variation of mass loss at different cross sections with respect to PEO500. The differences in the intensity of pitting corrosion between both wires also become evident in the average pit depth and in the maximum pit depth as plotted in Figs. 3.16b and 3.16c. The reported localization of damage was responsible for the obvious drop in strength and ductility of the HT450-5 wires when immersed in c-SBF.

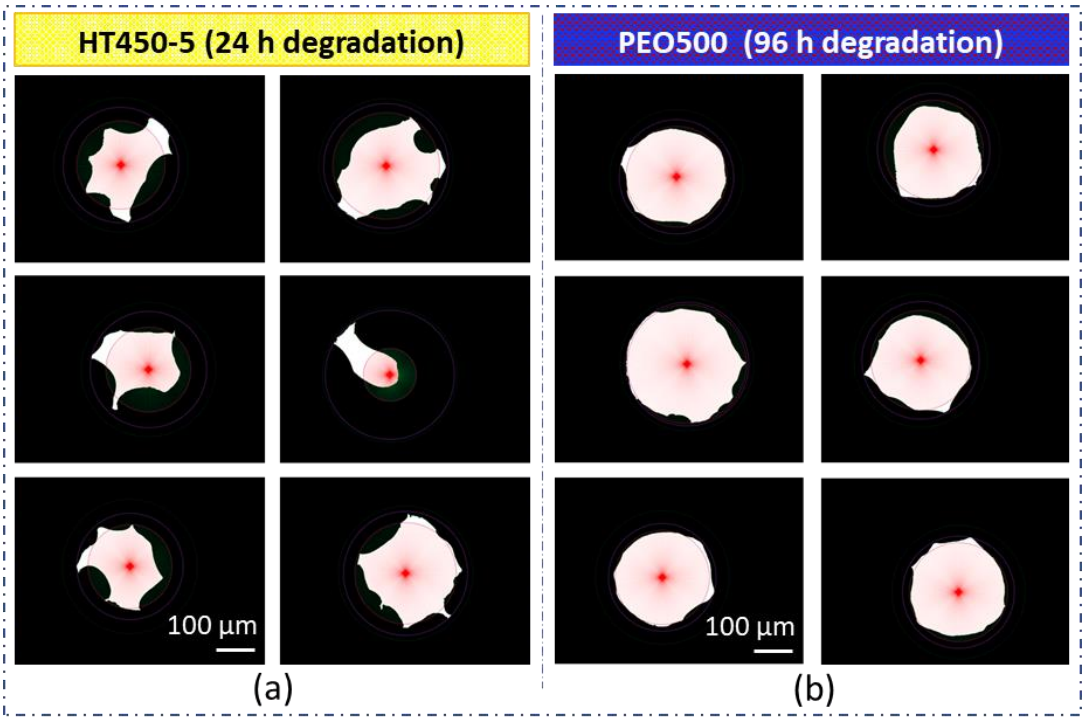

Fig. 3.15. (a) Representative cross-sections of HT450-5 wire after 96 h immersion in c-SBF. (b) Idem of PEO500 wire after 96 h immersion in c-SBF. Red points mark the original center of cross section before degradation. The scale bar of 100 µm is for all cross-sections in this figure.

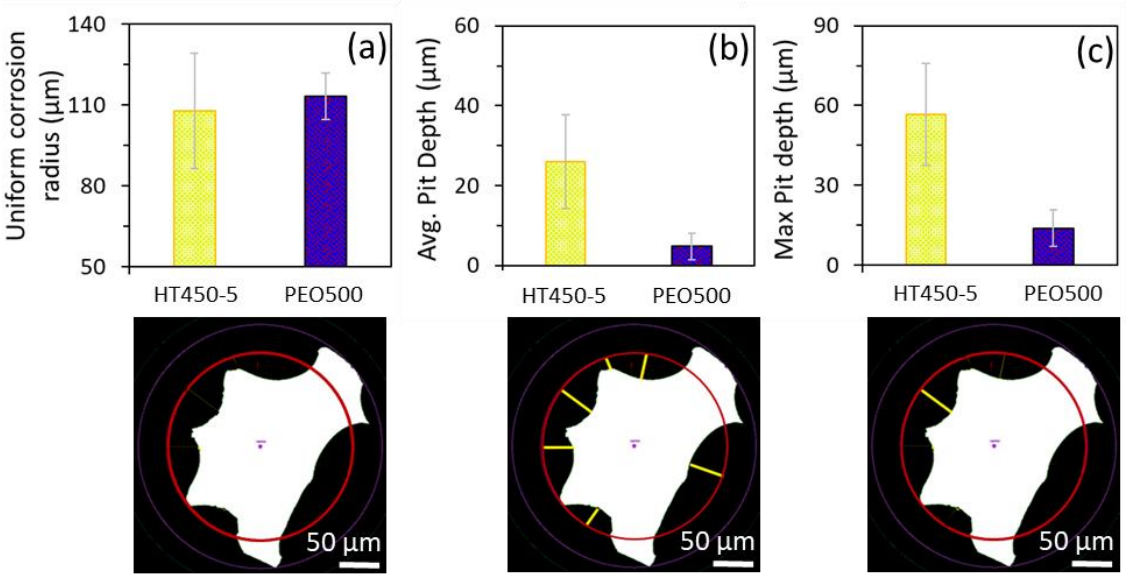

Fig. 3.16. Metrics representing the intensity of pitting corrosion in HT450-5 and PEO500 wires and representative cross sectionns of degraded HT450-5 Mg wire: (a) Uniform corrosion radius (marked by red circle). (b) Average pit depth (each yellow line marks the deepest point of each pit). (c) Maximum pitting depth (marked by yellow line).

3.2.7. Corrosion mechanisms of Mg wires and PEO surface-modified Mg wires

The corrosion mechanisms of the Mg wires without and with surface modification by PEO were elucidated by means of the analysis of the cross-sections of the wires in the SEM and EDX. The one corresponding to HT4505 wire after 24 h of immersion in c-SBF at 37ºC is plotted in Fig. 3.17 confirming the presence of Mg, O, P and Ca in corrosion layer. The cracks in the corrosion layer were induced by dehydration of samples. The interaction of SBF with Mg surfaces is well-established in the literature and has been explained in Section XX [58]. Briefly, water molecules in the c-SBF rapidly react with the Mg on the wire surface, forming a layer of $Mg(OH)_2$ and release H_2 gas (Eq. 3.6). This layer deteriorates in the presence of Cl^- ions leading to the formation of soluble $MgCl_2$ and OH^- ions (Eq. 3.7). With these subsequent corrosion reactions of corrosion progresses towards the interior of the wire.

$$Mg + 2H_2O \rightarrow Mg(OH)_2 + H_2 \quad (3.6)$$

$$Mg(OH)_2 + Cl^- \rightarrow MgCl_2 + 2OH^- \quad (3.7)$$

$$HCO_3^- + OH^- \rightarrow H_2O + CO_3^{2-} \quad (3.8)$$

$$CaCl_2 \rightarrow Ca^{2+} + 2Cl^- \quad (3.9)$$

$$Mg^{2+} + CO_3^{2-} \rightarrow Magnesium\ Carbonates \quad (3.10)$$

$$Ca^{2+} + (HPO_4^{2-}, CO_3^{2-}) + H_2O \rightarrow Calcium\ Phophates\ and\ Carbonates \quad (3.11)$$

The corrosion layer becomes thicker, but it is not compact enough to stop the corrosion by diffusion of SBF solution. The amount of P and Ca decreases from the outer edge of the corrosion layer to the inner core of Mg (Fig. 3.17), suggesting the formation of Ca-P phosphates and carbonates following the reactions indicated above (Eqs. 3.8 – 3.11), in agreement with the recent report of Berit et al. [129]. The reduction in Ca and P concentration with depth is likely due to slow transport of Ca^{2+} ions through the degradation layer, thus promoting its precipitation near the outer edge. The exact composition of Calcium Phosphates depends on the Ca/P ratio [130].

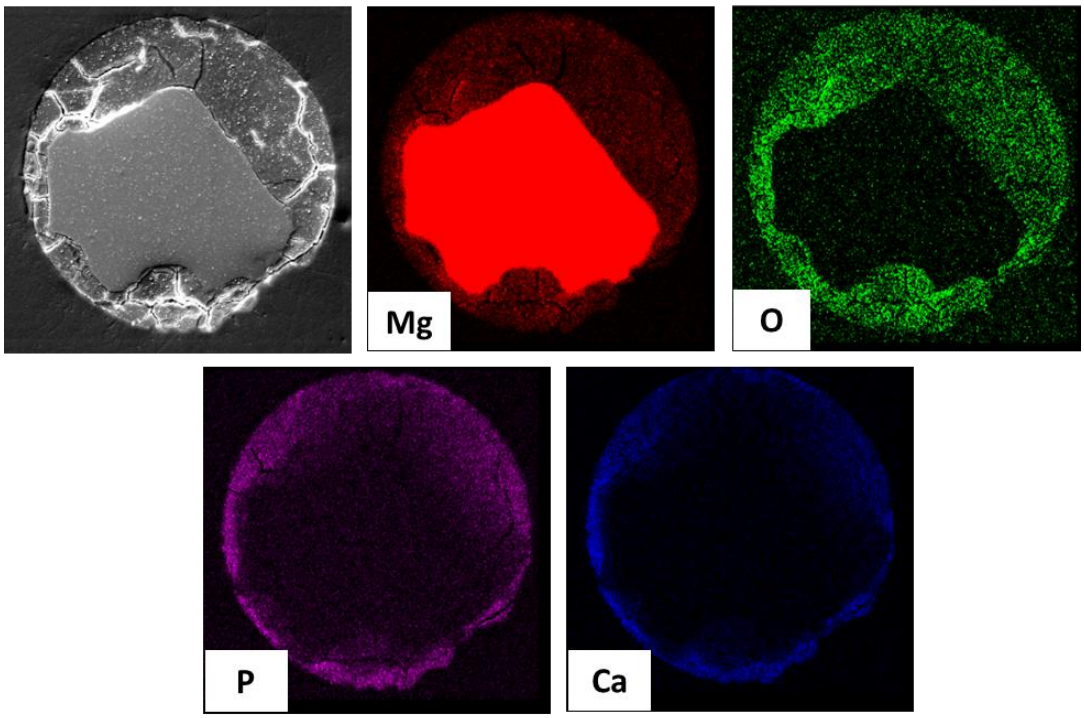

Fig. 3.17. Analysis of the cross-section of the HT450-5 wire in the SEM after 24 h of immersion in c-SBF at 37ºC. The first image is obtained with secondary electrons and the other images stand for the composition maps of Mg, O, P and Ca obtained by EDX.

The corrosion mechanisms in the presence of the oxide layer created by PEO were very different, as shown in the cross-sections of PE500 wire before (Fig. 3.18a) after 96 h (Fig. 3.18b) and 168 h (Fig. 3.19c) of degradation in c-SBF at 37ºC (Fig. 10). The chemical composition of the continuous oxide layer before degradation includes Mg, O and P and, thus, contains MgO and $Mg_3(PO_4)$ [124]. The oxide layer is porous and water molecules from the c-SBF solution are able to reach the surface of the Mg wire, leading to the same corrosion mechanisms described above for HT450-5 wires and to similar values of the initial corrosion rates of both HT450-5 and PEO500 wires. Afterwards, the corrosion rate of the surface-modified wire is reduced and this change is associated with the appearance of a dense layer containing O, Ca and P (Fig. 3.18b). This dense layer is beneath the typical porous oxide layer resulting from the progressive oxidation of Mg to form $Mg(OH)_2$, which is found between the external Ca-P dense layer and the Mg core of the wire. However, the presence of dense Ca-P layers seems to hinder the diffusion of the Cl^- ions and, thus, of the degradation of $Mg(OH)_2$ (Eq. 3.7). As a result, the corrosion rate of the Mg wire is reduced, and pitting corrosion is suppressed. This process continues after 168 h of immersion in c-SBF (Fig. 3.18c) and the dense, continuous Ca-P layer is seen on top the Mg oxide layer while the Mg core with oval shape is still present at the center of the wire.

Thus, the reduced corrosion rate and the uniform degradation in surface-modified WE43 Mg wires can be attributed to the presence of the Ca-P rich layer deposited at the initial stages of corrosion. The Ca-P layer was dense and grew with time, but this dense and continuous Ca-P layer was not found in the HT450-5 wire. There is no evidence in the literature about the formation of dense and continuous Ca-P layer during corrosion of Mg on top of the oxide layer created by PEO and the following hypothesis is advanced to explain its appearance. During the initial stages of corrosion, the oxide layer created by PEO on top of the Mg wire is cracked because of the expansion associated with corrosion. This oxide layer contains $Mg_3(PO_4)_2$ and supply phosphate ions which can react with the Ca^{2+} ions coming from the c-SBF, leading to the precipitation of the Ca-P rich layer on top of the $Mg(OH)_2$ formed during corrosion (Fig. 3.19). The equal intensity of P signal (Fig. 3.19c) in the oxide layer created by PEO and in the Ca-P layer also supports the above argument while the presence of Ca at the location where the inner oxide layer created by PEO used to be is also in agreement with this assumption.

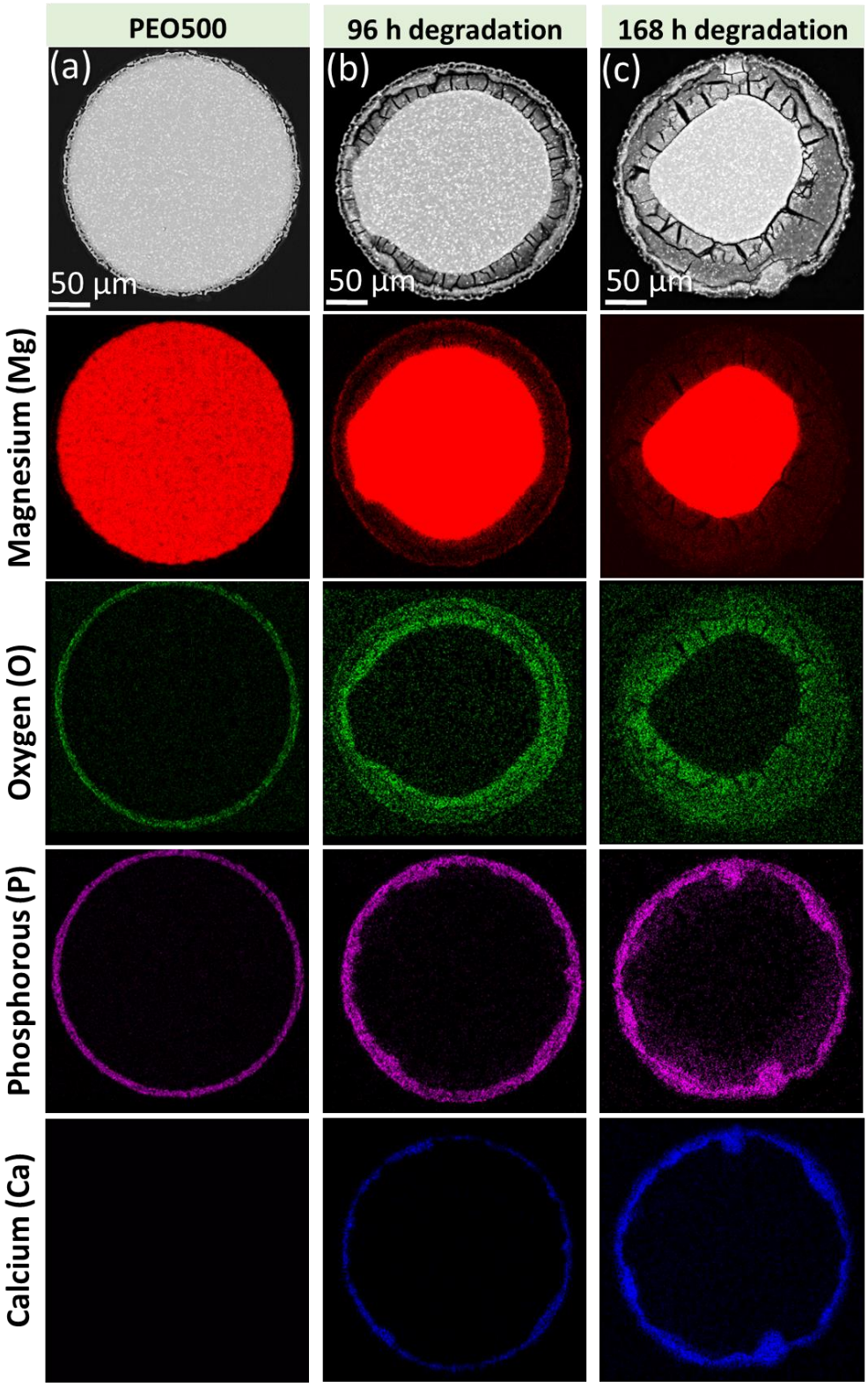

Fig. 3.18. Analysis of the cross-section of the PEO wire (a) before and after (b) 96 h and (c) 168 h of degradation in c-SBF at 37ºC. The first column shows the back-scattered electron image and the other columns present the composition maps of Mg, O, P and Ca obtained by EDX with the distribution.

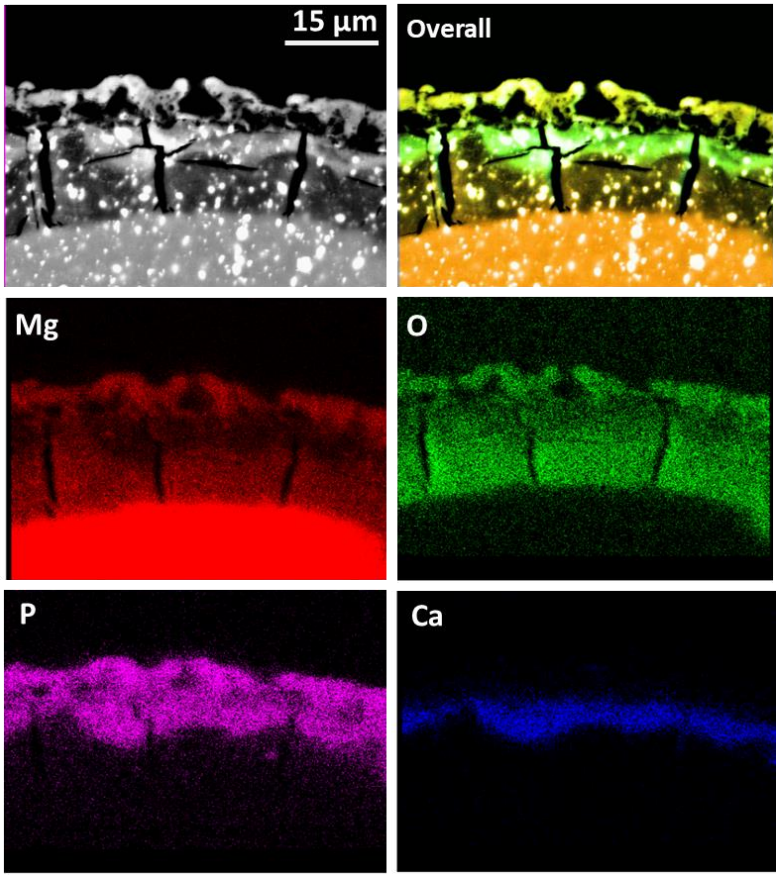

Fig. 3.19. Higher magnification analysis of the surface of the PEO500 wire after 96 h in c-SBF. The first image on the top left shows the back-scattered electron image and the other present the composition maps of Mg, O, P and Ca obtained by EDX.

Cracks were found on the lateral surfaces of the PEO250 (Figs. 3.20a and b) and PEO500 wires (Figs. 3.20c and d) after 96 h and 168h of immersion in c-SBF, respectively. The cracks were formed because of the stress induced by the expansion associated with the corrosion products [131] and facilitate the influx of SBF to the Mg core and the detachment of external corrosion layer. However, the degree of surface degradation depends on the nature of the initial oxide layer produced by PEO. It was much more marked in the PEO250 wire, in which the external corrosion layer is completely detached after 168 h in SBF (Fig. 3.20b). On the contrary, the external oxide layer was mostly intact (Fig. 3.20d) in the case of PEO500, although cracks were also found on the surface. These results confirm the importance of optimizing the electrical parameter of PEO process to slow the degradation of the wires and promote the formation of the Ca-P dense layer upon degradation of Mg core. Moreover, they also explain why the corrosion rate of both PEO-modified wires was similar up to 96 h after

while the corrosion rate of the PEO250 wire increased afterwards. due the detachment and degradation of the PEO oxide layer.

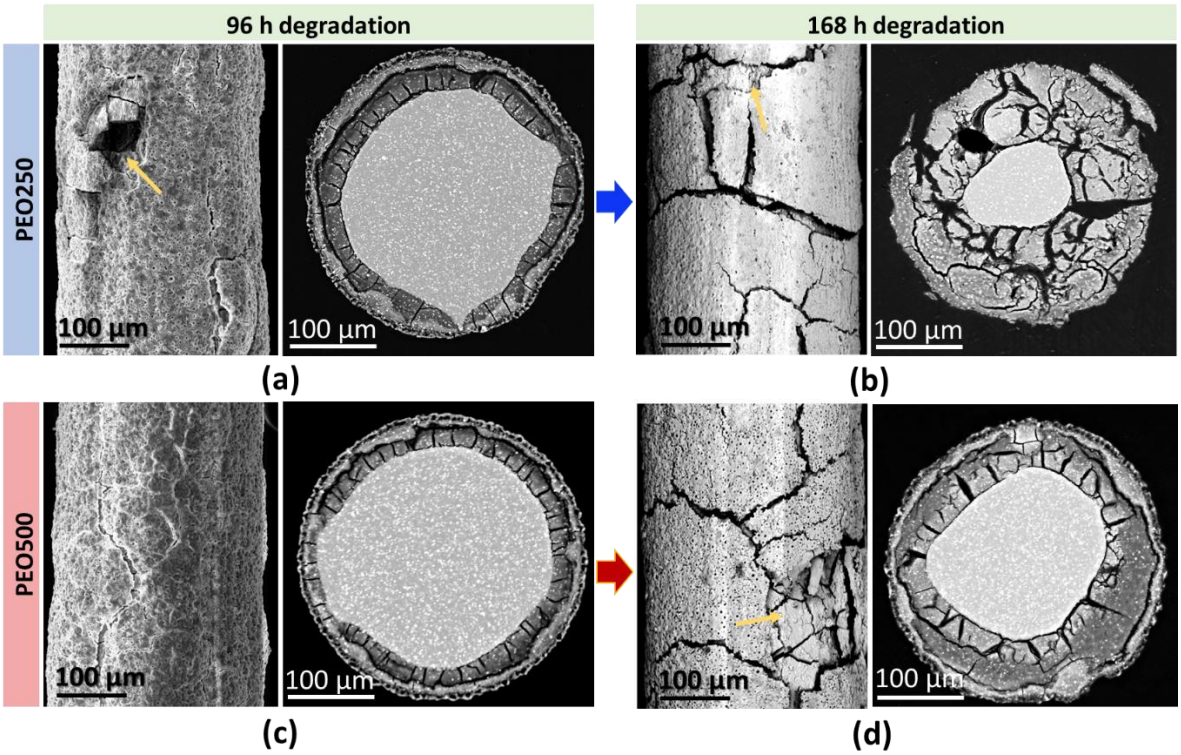

Fig. 3.2010. Back-scattered electron images of the cross-section and lateral surfaces of PEO250 (a-b) and PEO500 (c-d) after 96 h and 168 h of degradation in c-SBF, respectively. Yellow arrows point to the coating detachment

3.2.8. Limitations of oxide layer formed by continuous PEO

3.2.9. Biological performance of Mg wires and PEO surface-modified Mg wires

The mitochondrial activity of the MC3T3-E1 preosteoblasts after 24 h of incubation in extracts obtained from different Mg wires (HT450-5, PEO250, PEO500) immersed in the culture medium is depicted in Fig. 3.21a for extracts with different dilutions. Pure extracts stand for 100% while 50%, 25%, 12.5% and 6.25% indicate the concentration of the pure extract in the culture medium. HT450-5 Mg wire showed slight toxic behavior in 100% extract with cell viability of 68.4 ± 5.5 %, while both PEO-modified Mg wires did not show any cytotoxic potential. These results are supported by the optical microscopy images of 100% extracts in Fig. 3.21 which show alive (elongated) and dead (circular, marked with an arrow) cells in the 100% extracts of HT450-5,

PEO250 and PEO500 wires after 24 h of incubation. The differences in results in Fig. 3.21a are not significant which could be affected by the presence of corrosion products that can change the absorbance of the solutions. The fraction of dead cells in the 100% extracts followed the order HT450-5 > PEO250 > PEO500 and showed the higher cytotoxic activity of the HT450-5 wires. MC3T3-E1 cell viability is known to be drop when the concentration of Mg ions in the culture medium increases, in agreement with these observations [132]. In addition, no sample showed toxicity after one dilution.

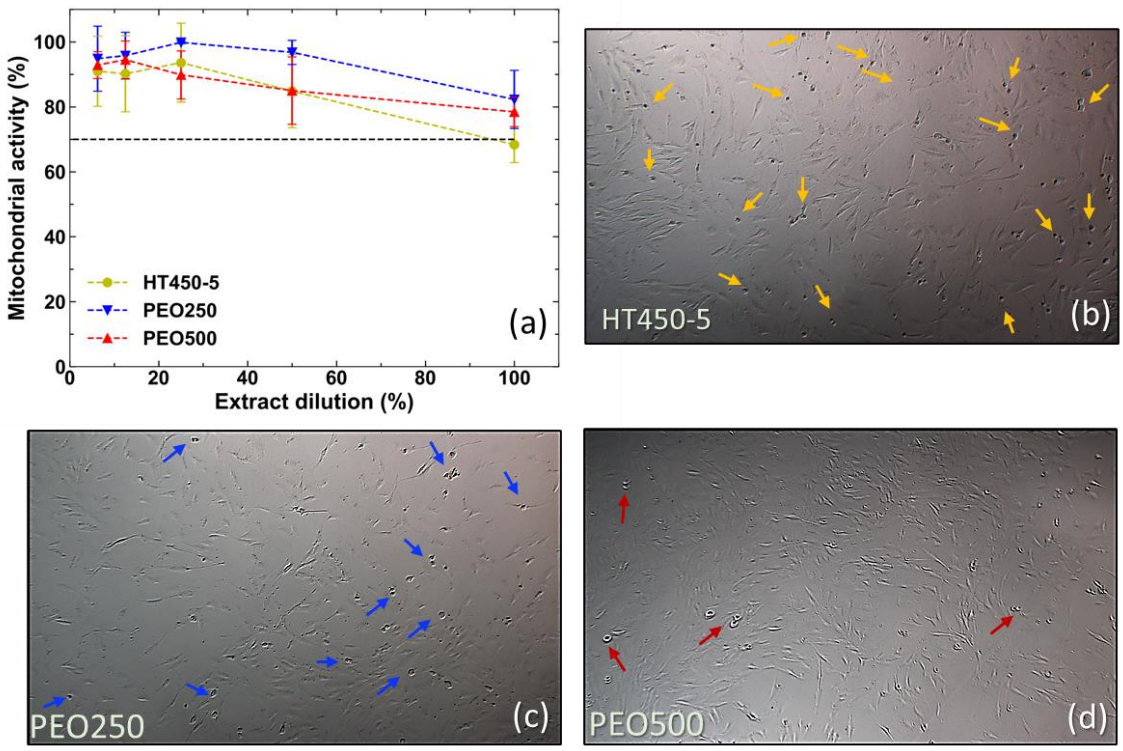

Fig. 3.21. (a) Mitochondrial activity of the MC3T3-E1 pre-osteoblasts after 24 h of incubation in extracts obtained from Mg wires immersed in the culture medium. (b), (c) and (d) Optical micrographs of alive (elongated) and dead (circular, marked with arrows) in the 100 % extracts of HT450-5, PEO250 and PEO500 Mg wires after 24 hours. Magnification was 10x. Arrows point to dead cells which show a dark round shape.

The direct interaction between the cells and the Mg wires was assessed by means of the observation in the confocal and SEM (3.22). After 24 h, the MC3T3-E1 cells covered the surface of the Ti control samples by cell-cell and cell-material interactions, as shown by both confocal and SEM images in Fig. 3.22a. On the contrary, cells could not attach on the surface of the HT450-5 Mg wire (Fig. 3.22b), and this behavior can be linked with the dynamic environment on the surface of the wire in which fast corrosion

leads to hydrogen gas release and/or to a local alkaline environment. The surface of the HT450-5 Mg wire appeared fully cracked in the SEM because of the dehydration and shrinkage of the corrosion layer by dehydration in the air or in the vacuum of the SEM. On the contrary, many live cells were able to attach on the surface of the PEO250 and PEO500 Mg wires. The connection between cells was promoted by bridging filopodia structure while the branched filopodia is the evidence of good cell adhesion to surface. Qualitatively both PEO250 and PEO500 Mg wires had the same favorable cell attachment behavior indicating that the presence of the oxide layer was necessary to favor the adhesion of cells to the wire surface by providing a porous surface with stable environment in terms of gas release and surface alkalinity.

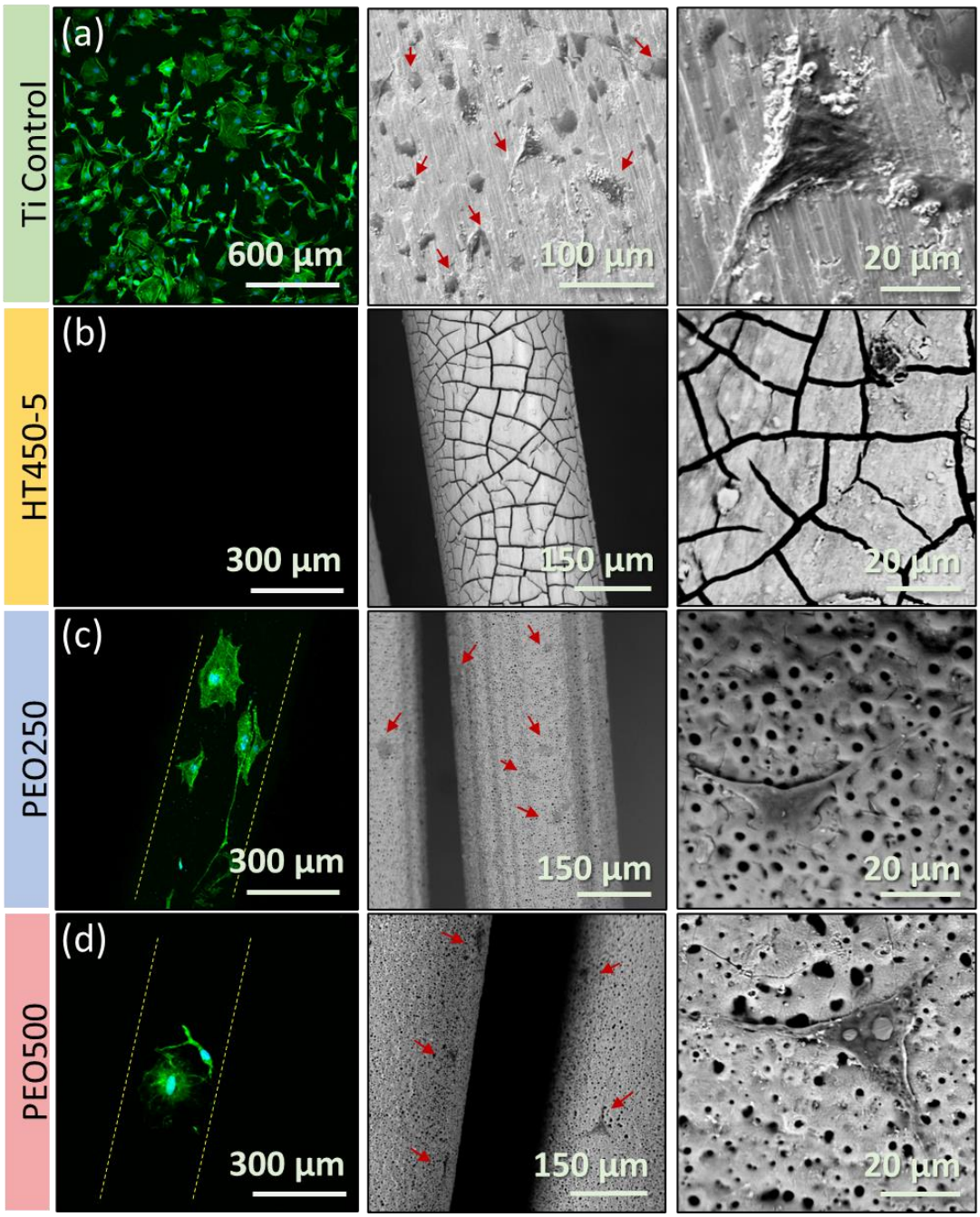

Fig. 3.22. Confocal and back-scattered SEM images of the interaction between MC3T3 pre-osteoblasts and the materials for 24 h. (a) Ti control sample. (b) HT450-5 Mg wire. (c) PEO250 Mg wire. (d) PEO500 Mg wire. Yellow dashed lines indicate the wire edges. Red arrows indicate the presence of cells on the wire surface.

3.2.10. Limitations of oxide layer formed by continuous PEO

It should be finally noted that the continuous oxide layer promoted by continuous PEO in our work presented good adhesion on the Mg wire but showed some typical brittleness which might lead to fine cracks in the presence of sufficient strains. For

instance, multiple parallel cracks appear on the surface when the wires are twisted or knotted, even though no detachment or delamination can be seen even at elevated strains (Fig. 3.23). To minimize this phenomenon of strain-induced cracking, we propose to reduce the oxide layer thickness (in order of 1~2 microns) which is possible by finely controlling the electrical parameters of the electrochemical PEO process. Another possibility might be to carry out PEO while subjecting the wires to tensile stress, so that the PEO oxide layer will be under compression once the wire is relaxed. These strategies are part of our future work.

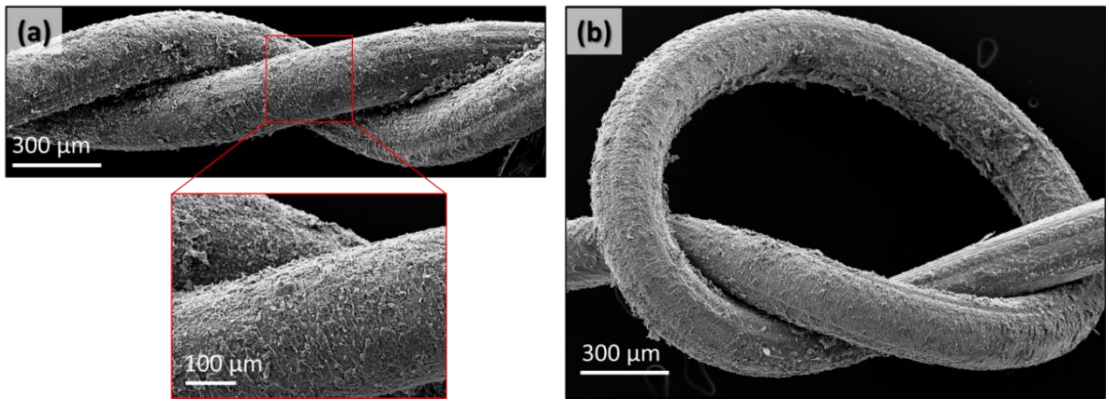

Fig. 3.23. SEM images of (a) twisted and (b) knotted PEO500 Mg wires, showing a fine network of cracks on the PEO oxide layer upon deformation.

3.3. Conclusions

The processing-microstructure-property (mechanical, corrosion, biocompatibility) relationships of Mg wires manufactured by cold drawing followed by a continuous surface treatment by PEO were successfully obtained. The scalable novel strategy can produce large quantities of surface-enhanced Mg wires for biomedical applications with significantly improved corrosion resistance and, thus, improved mechanical properties and cytocompatibility due to the presence of a continuous PEO oxide layer.

The cold draw process showed to be robust, and wires up to lengths of 20 m were successfully manufactured. The cold-drawn wires had a small grain size (around 1 µm) and strong basal texture, together with a large dislocation density and contained large, globular precipitates (in the range 0.5 to 1.5 µm) of $Mg_{12}YNd$ dispersed throughout the microstructure. Gentle annealing treatments at 400ºC/450ºC for 5/10 s were able to reduce the dislocation density (to improve the ductility) without inducing

recrystallization (that may potentially impair mechanical properties). The annealing treatments led to the nucleation of Nd- and Y-rich nm-sized precipitates at the grain boundaries.

It was found that the mechanical properties (in terms of strength and ductility) could be optimized by means of annealing treatments after cold drawing at 450ºC for 5s. Annealing led to a slight increase in the corrosion rate due to the nucleation of precipitates at grain boundaries and the corrosion rate of the Mg wires was very fast, and pitting corrosion was dominant in all processing conditions, while strength and ductility of the wires disappeared after 24 h of immersion in simulated body fluid at 37ºC. Direct tests did not show any MC3T3-E1 cells attachment on the surface of the Mg wires. Metallurgical processes cold work or annealing are unlikely to reduce the corrosion rates of thin Mg wires [111] below the thresholds needed for biomedical applications.

Surface modification of the annealed WE43 Mg wires by a continuous PEO process led to a homogeneous oxide layer of ≈ 8 μm in thickness made up of MgO and $Mg_3(PO_4)_2$. We were able to show that layers created at higher frequency presented lower porosity. Even though the PEO modification reduced the tensile properties of the wires slightly, sufficient strength of ≈ 300 MPa with a strain-to-failure ≈ 8% could ultimately be achieved for the first time using a continuous PEO process for biomedical Mg wires. PEO modification dramatically improved the corrosion resistance and biocompatibility. It was found that a dense layer Ca/P was deposited at the early stages of corrosion on top of the $Mg(OH)_2$ layer and hindered the diffusion of the Cl- ions which dissolve $Mg(OH)_2$ and accelerate the corrosion of Mg alloys. As a result, pitting corrosion was suppressed and the strength of the Mg wires was above 100 MPa after 96 h of immersion in simulated body fluid at 37ºC. Moreover, many live cells were able to attach on the surface of the PEO surface-modified wires. The results of the direct tests indicated that the PEO oxide layer was necessary to favor the adhesion of cells to the wire surface by providing a porous surface with stable environment in terms of gas release and surface alkalinity. These results demonstrated the potential in terms of mechanical/degradation/biological performance of thin Mg wires surface-modified by PEO for bioresorbable wire-based medical devices such wires reinforced polymer composites.

CHAPTER 4: MECHANICAL CHARACTERIZATION OF COMPOSITES

The modified strategy to manufacture Mg/PLA composite laminates was presented in chapter 2, which enabled the production of high-quality unidirectional and multi-directional composite laminates. Understanding of mechanical behavior of constituents of the composite and of unidirectional composite ply is necessary to design customized multi-directional composite laminate with optimum stacking sequence for orthopedic applications. Thus, the main objectives of this chapter were to determine the mechanical behavior of constituents of composite by means of tensile tests on Mg wire (with and without PEO modification) and PLA coupons, followed by the push-outs test to analyze wire/matrix interfacial behavior. In addition, the mechanical behavior of the unidirectional composite was characterized in longitudinal $[0^o]_n$ and transverse $[90^o]_n$ directions by tension and compression tests followed by $[\pm 45^o]_s$ tension tests to determine the in-plane shear properties. Finally, tension tests on quasi-isotropic (multi-directional) composite laminate $[0^o/90^o/\pm 45^o]_s$ were performed, and the elastic properties were compared with the predictions of the classical laminate theory from the elastic constants of the unidirectional lamina.

4.1.Experimental techniques

4.1.1. Materials

Mg wires of 0.3 mm in diameter manufactured by cold drawing with and without surface modification by PEO at 500 Hz were used for tensile tests. Similarly, unidirectional and multi-directional Mg/PLA composite laminates were used for different mechanical tests. Flat dog bones of pure PLA were manufactured by hot pressing of PLDL pellets (Corbion, Netherlands) in a mold cavity at 180 ºC with a cross-section of 5 mm x 2 mm and gage length of 35 mm for tensile tests of PLA.

4.1.2. Tensile tests of PLA coupons and Mg wires

The tensile tests on Mg wires with and without surface modification by PEO were carried out in a universal mechanical testing machine (ProLine Z010, ZwickRoell GmbH & Co. KG, Germany) at room temperature. The gauge length was 200 mm and tests were carried out at an average crosshead speed of 5 mm/min [55]. Flat dog bones of PLA were also tested in tension in a universal mechanical testing machine (Instron,

USA) with 10 kN load cell at a displacement rate of 2 mm/min. The strains in the PLA coupons were measured by Digital Image Correlation (VIC Correlated Solutions, USA). Specimen was first painted in white and black spray was sprayed to create random pattern of black dots over the white background. The displacements of black dots were recorded in a high-resolution camera to calculate strains in VIC-2D software.

4.1.3. Interface characterization by push-out tests

Wire push-out tests were performed on Mg/PLA and PEO-Mg/PLA composites to evaluate the mechanical properties of the interfaces, following previous investigations [133][134][89]. Unidirectional composite $[0^o]_3$ with dimensions of 12 mm x 12 mm x 2 mm were embedded (perpendicular to the wire direction) in an epoxy resin (SpeciFix resin system, Struers, Denmark). They were grinded with 1200 and 4000 SiC papers to prepare thin slices (perpendicular to the wire direction) with an approximate thickness of 0.6 mm. Finally, both sides of sample were polished with 1 µm diamond suspension, followed by water and ethanol cleaning and drying in air. The schematic of the experimental setup of the wire push-out test is shown in Fig. 4.1. Push-out tests of the wires were carried out in the thin slices that were placed on a stainless-steel support with a groove of 500 µm in width. The wire to be tested was positioned manually at the center of the groove with the help of an optical microscope and the slice was fixed with a tape. The support was attached to the XY stage to position the indenter punch over the desired wire. A stainless-steel flat punch with 180 µm in diameter was machined in-house and fixed to the upper cross-head of an Instron Universal Testing Machine (Minneapolis, MN, USA). The compressive load was applied on the wire under displacement control at 200 nm/s with the help of a 100 N load cell. A total of 4 wires were pushed out for each material and condition. Special care was taken to ensure that the distance between the centers of nearest neighbor wire and the pushed-out wire was at least 450 µm (1.5 times the wire diameter) to avoid constraint effects during the push-out test [135].

The average interfacial shear strength between the Mg wire and PLA matrix was calculated according to

$$\tau = \frac{P_{max}}{2\pi R l} \qquad (1)$$

where P_{max}, R and l represent the maximum load recorded during the push-out test (which indicates the onset of wire sliding at the interface), the wire radius and the thickness of the composite slice, respectively. The samples were also analyzed by SEM after testing.

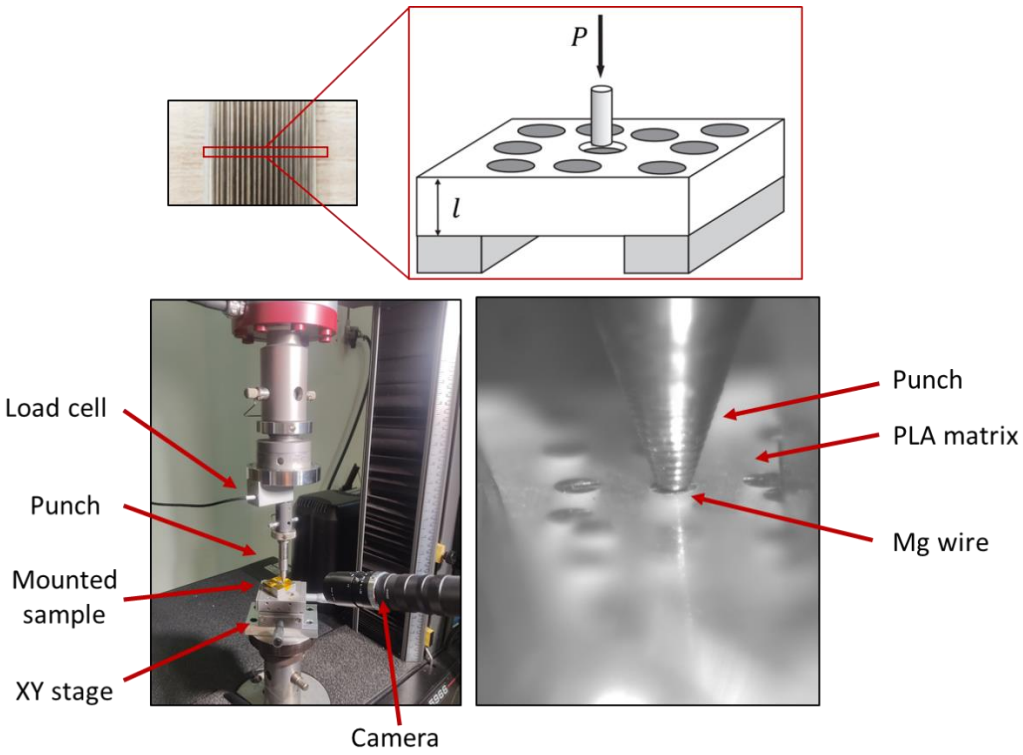

Fig. 4.1. (top) Schematic of the wire push-out test conducted on thin slices of the composites, (bottom left) experimental setup for push-out test, and (bottom right) detail of the punch/wire region.

4.1.4. Mechanical testing of composite laminates

Multiple mechanical tests were performed on the composite laminates in Universal Testing Machine (Instron, USA) with a 10 KN load cell (Fig. 4.2). ASTM guidelines for tensile (D 3039), compressive (D 3410) and in-plane shear (D 3518) tests were used for sample preparation and analysis of the results wherever possible. Nevertheless, samples were prepared with smaller dimensions as compared to ASTM recommendations to minimize cost. The dimensions of Mg/PLA and PEO-Mg/PLA composites for each type of test are schematically shown in Fig. 4.2. Volume fraction (V_f) of Mg wires was kept between 18~20% in all cases. Unidirectional laminates were prepared with dimensions of 120 mm x 12 mm x 2 mm and 50 mm x 50 mm x 2 mm

(Fig. 2.7). Multi-directional laminates were prepared with a quasi-isotropic stacking sequence $[0^o/90^o/\pm45^o]_s$ with dimensions of 50 mm x 50 mm x 4 mm (Fig. 2.8). Composites were later cut to achieve desired dimensions for each test (Fig. 4.2). In all composites, the thickness of lamina (or ply) was kept approximately 0.5 mm. All mechanical tests were carried out at 1 mm/min, while tensile tests in longitudinal and transverse directions were carried out at 2 mm/min and 0.5 mm/min, respectively. Stress was always calculated by dividing the load by the initial cross-sectional area while strains were measured by Digital Image Correlation (VIC Correlated Solutions, USA). Images for DIC were taken at the rate of 1 image/second in all tests except in the case of compression tests, where strains were calculated from the cross-head displacement of the mechanical testing machine.

The in-plane shear stress (τ_{12}) and strains (γ_{12}) were calculated from tensile tests in $[\pm45^o]_s$ laminates according to ASTM D 3518:

$$\tau_{12} = \frac{P}{2A} \qquad \text{Eq. (4.1)}$$

$$\gamma_{12} = \epsilon_x - \epsilon_y \qquad \text{Eq. (4.2)}$$

where P, A, ϵ_x, and ϵ_y stand for the applied load, the initial cross-sectional area of sample, and the longitudinal strain and transverse strains, respectively.

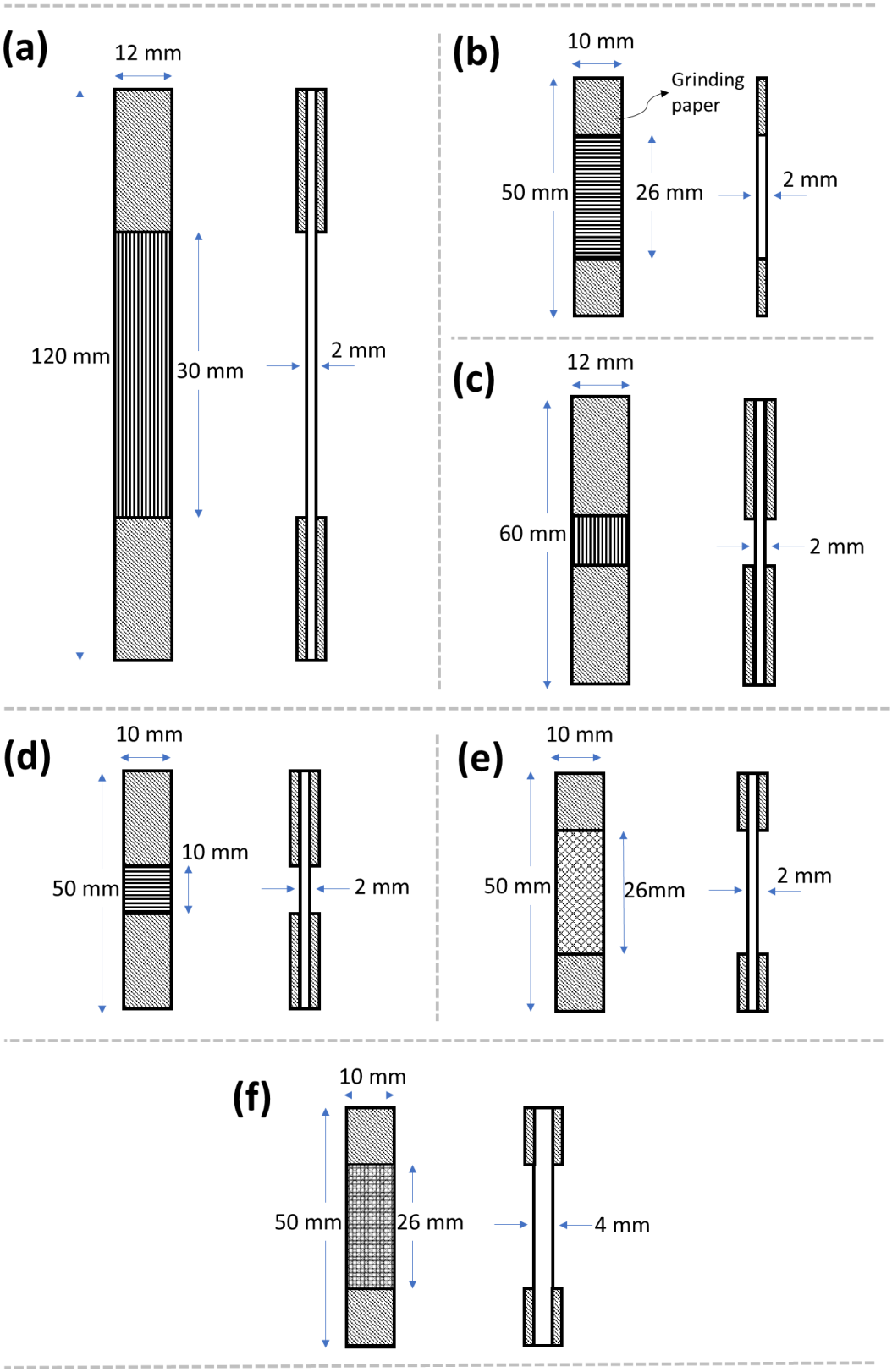

Fig. 4.2. Dimensions of unidirectional composite laminates for different mechanical tests. (a) Longitudinal tension $[0^o]_3$, (b) transverse tension $[90^o]_4$, (c) longitudinal compression $[0^o]_3$, (d) transverse compression $[90^o]_4$ and (e) in-plane shear $[\pm45^o]_s$. (f) Dimensions of quasi-isotropic composite laminate $[0^o/90^o/\pm45^o]_s$ for tensile tests. In all tests, glass/epoxy tabs of 2 mm in thickness were used.

4.2.Results and discussion

4.2.1. Tensile behavior of PLA coupons and Mg wires

Representative stress-strain curves of pure PLA coupons and Mg wires are shown in Fig. 4.3a and 4.3b, respectively, and the mechanical properties in tension are summarized in Table 4.1. The initial cross-section area was used to calculate the stress from the applied load while strains were recorded by DIC (engineering strains) and testing machine for PLA and wires, respectively. The elastic deformation of PLA was characterized by an elastic modulus of 3.6 GPa, followed by yielding at ~55 MPa and had 6 % strain-to-failure. The tensile properties of Mg and PEO-Mg wires were similar to those reported in section 3.2.2. Nevertheless, Mg wires for composite manufacturing were cold drawn at Fort Wayne Metals (US) and presented slightly superior strength (321 MPa) and ductility (14 %). Both decreased slightly after PEO surface modification (Fig. 4.3b). This reduction is due to the fact that the PEO process also grows inwards (consumes ~2 microns of wire) and introduces near-surface annealing. The range of elastic moduli, strengths and failure strains of PLA and Mg wires defines the design space to tailor the mechanical properties of Mg/PLA composites.

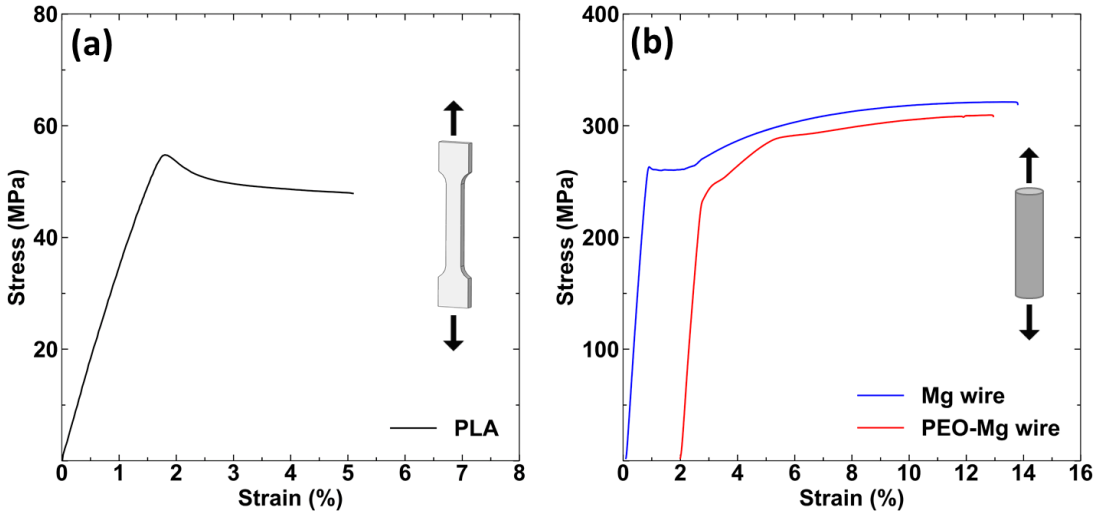

Fig. 4.3. Engineering stress-strain curves of (a) PLA and (b) Mg wires before and after continuous PEO modification.

Table 4.1. Tensile properties of PLA coupons and wires

Property	PLA	Mg wire	PEO-Mg wire
Elastic modulus (GPa)	3.6 ± 0.12	45	45
Tensile strength (MPa)	54.6 ± 0.88	321.2 ± 0.22	308.8 ± 4.5
Failure strain	0.06 ± 0.02	0.13 ± 0.12	0.10 ± 0.015

Here, the elastic modulus of Mg WE43MEO alloy was taken from [136].

4.2.2. Interface strength

Two representative load-displacement curves of the push-out tests on Mg/PLA and PEO-Mg/PLA composites are plotted in Fig. 4.4a. They have the typical shape reported in the literature [137][138]. The initial concave zone is followed by a linear region that stands for the elastic bending of the thin slice of composite in the groove of the stage. Further deformation led to the onset of non-linearity, which could be attributed to the progression of a crack at the wire/matrix interface, most likely from the bottom of the slice to the top (as the ratio of elastic moduli $E_{Mg}/E_{PLA} > 12$ [137]). The non-linear region ended with the complete fracture of the interface at the peak load. Afterwards, the load drops abruptly and the wire pushed out from the matrix against friction forces. The interfacial shear strengths, following eq. (1) were 10.9 ± 1.6 MPa and 26.3 ± 1.3 MPa for Mg/PLA and PEO-Mg/PLA composites, respectively. The oxide layer created by PEO improved the interface shear strength by 2.5. Two reasons induced this behavior. First, the penetration of PLA into the pores of the oxide layer provides a mechanical interlock effect as confirmed in Figs. 4b and 4c. Fractured PLA ligaments coming out from the pores of the oxide layer are clearly seen in Fig. 4c, where ductile tearing of PLA ligaments attached to the pores of the PEO oxide layer could be observed under SEM. The second could be the strong chemical interactions between the polymer chains and the MgO [15]. Finally, it should be noted that the load drop after the peak was smaller in PEO-Mg/PLA composite as compared with the Mg/PLA composite. Neither plastic deformation of the PLA matrix nor of the Mg wire (except a small footprint of punch generated on the top side of wire) was observed after the test on the top and bottom surfaces of the slice. Thus, the non-linear region in the push-out curves before the peak has to be associated with the progressive crack propagation at the interface, and area under load-displacement curves is a rough qualitative estimate of the interface toughness, which was much higher in the PEO-Mg/PLA composite.

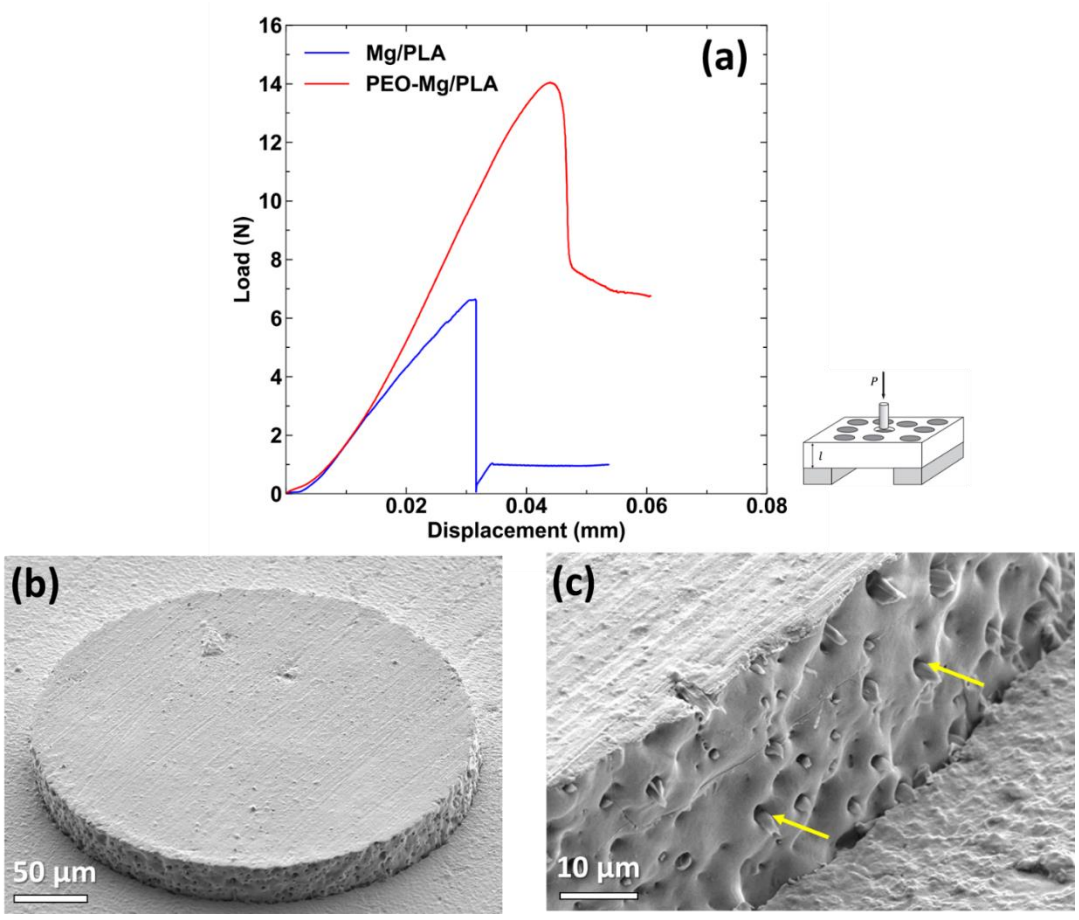

Fig. 4.4. (a) Representative load-displacement curves of the push-out tests in Mg/PLA and PEO-Mg/PLA composites. (b) Secondary electron image of the bottom surface of the slice after the push-out test. (c) Higher magnification view of (b) in which yellow arrows point to PLA ligaments stuck in the pores of oxide layer.

4.2.3. Mechanical behavior of unidirectional composite lamina

Representative stress-strain curves of various mechanical tests on unidirectional Mg/PLA and PEO-Mg/PLA composites are shown in Figs. 4.5a, 4.6a, 4.7a, 4.8a, 4.9a and 4.10d and average values of the mechanical properties with the standard deviation are summarized in Table 4.2. The initial cross-section area of samples was used to calculate the engineering stress from the applied load, while engineering strains were calculated by DIC except in the compression tests, in which the cross-head displacement of the mechanical testing machine was used.

Table 4.2. Mechanical properties of unidirectional composites

Mechanical property	Mg/PLA composite	PEO-Mg/PLA composite
Longitudinal elastic modulus - E_{11} (GPa)	10.7 ± 1.0	11.2 ± 0.3
Poisson's ratio - v_{12}	0.34	0.34
Strength (longitudinal tension) - X_t (MPa)	85.6 ± 4.1	91.5 ± 4.6
Strength (longitudinal compression) - X_c (MPa)	> 115.6 ± 9.3	> 115.7 ± 6.1
Transverse elastic modulus - E_{22} (GPa)	4.2 ± 0.3	4.29 ± 0.5
Strength (transverse tension) - Y_t (MPa)	24.3 ± 3.0	23.3 ± 4.0
Strength (transverse compression) - Y_c (MPa)	85.8 ± 3.5	84.0 ± 6.7
In-plane shear modulus - G_{12} (GPa)	1.4 ± 0.1	1.6 ± 0.2
In-plane shear strength - S_{12} (MPa)	24.9 ± 2.5	23.9 ± 1.7

The behavior of both Mg/PLA and PEO-Mg/PLA composites in tension in the longitudinal (parallel to wires) direction showed an initial elastic response with an approximate elastic modulus of 11 GPa and tensile strength of 90 MPa (Fig. 4.5a). Mg/PLA composites fractured below 2% strain, while PEO-Mg/PLA composite revealed a high strain-to-failure of 5 %, almost equal to the failure strain of PLA.

The fracture of the Mg/PLA composite was likely to be initiated by the shear failure of the wire/PLA interface and followed by the propagation of the interface shear crack across the cross section in PLA matrix. Most of the Mg wires remained intact (Fig. 4.5c and d) and were pulled out between fractured surfaces of PLA. The presence of PEO on the wire surface increased the interface shear strength and the formation of interface cracks by shear was impeded. Failure of the PEO-Mg/PLA composite occurred by the tensile failure of PLA matrix at the failure strain of PLA (~5 %). Several transversal cracks appeared in the gauge section of the composite (Fig 4.5f), revealing strong bonding between PLA and Mg wires due to the PEO oxide layer. As a result, multiple matrix cracks developed along the sample before the final fracture of the coupon. PEO-Mg wires could not be pulled out from the matrix because of the high interfacial

strength, resulting in the fracture of all Mg wires (Fig. 4.5c, 4.5g). The PEO oxide layer was also cracked near the failure surface of Mg wires due to its brittle nature (Fig. 4.5g).

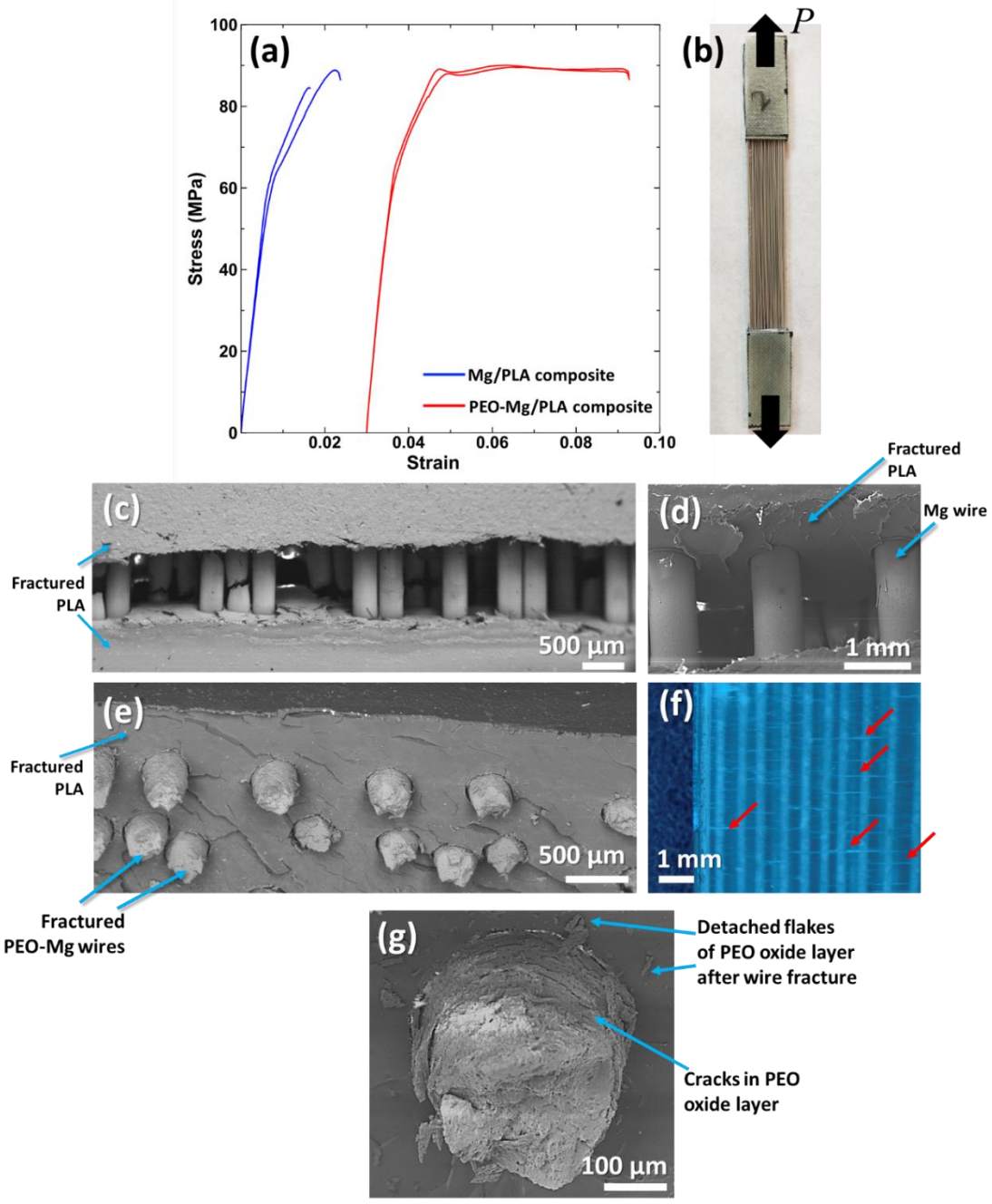

Fig. 4.5. (a) Representative stress-strain curves of unidirectional laminates $[0^o]_3$ of Mg/PLA and PEO-Mg/PLA composites in tension along the longitudinal direction. (b) Optical image of the PEO-Mg/PLA composite specimen for longitudinal tension test. (c) Back-scattered SEM image of the fracture surface of Mg/PLA composite, (d) *Idem* enlarged image of Mg/PLA composite, (e) *Idem* PEO-Mg/PLA composite. (f) Optical image of the gauge section of PEO-Mg/PLA composite specimen after tensile test in the longitudinal direction where red arrows show transverse cracks in the PLA matrix. (g) Back-scattered SEM image of the fracture of PEO-Mg wires.

The tensile stress-strain curves in the transverse (perpendicular to the wire) direction of the composite are plotted in Fig. 4.6a. Both composites (with and without PEO surface modification on the Mg fibers) showed similar brittle response with very low ductility. The elastic modulus was ~4.2 GPa and the transverse tensile strength ~24 MPa. Fracture of composite was facilitated by cracking of PLA matrix and interface debonding (Fig. 4.6c and 4.6d), which are two common fracture mechanisms in unidirectional composites deformed in transverse tension [139][140]. PEO modification did not provide any mechanical advantage in transverse tension in because the interface normal strength between Mg wire and PLA matrix was not significantly improved by PEO modification. However, PLA ligaments stuck in pores of PEO (see yellow arrows in Fig. 4.6e) which failed by ductile tearing during fracture but their contribution to enhance the toughness was negligible.

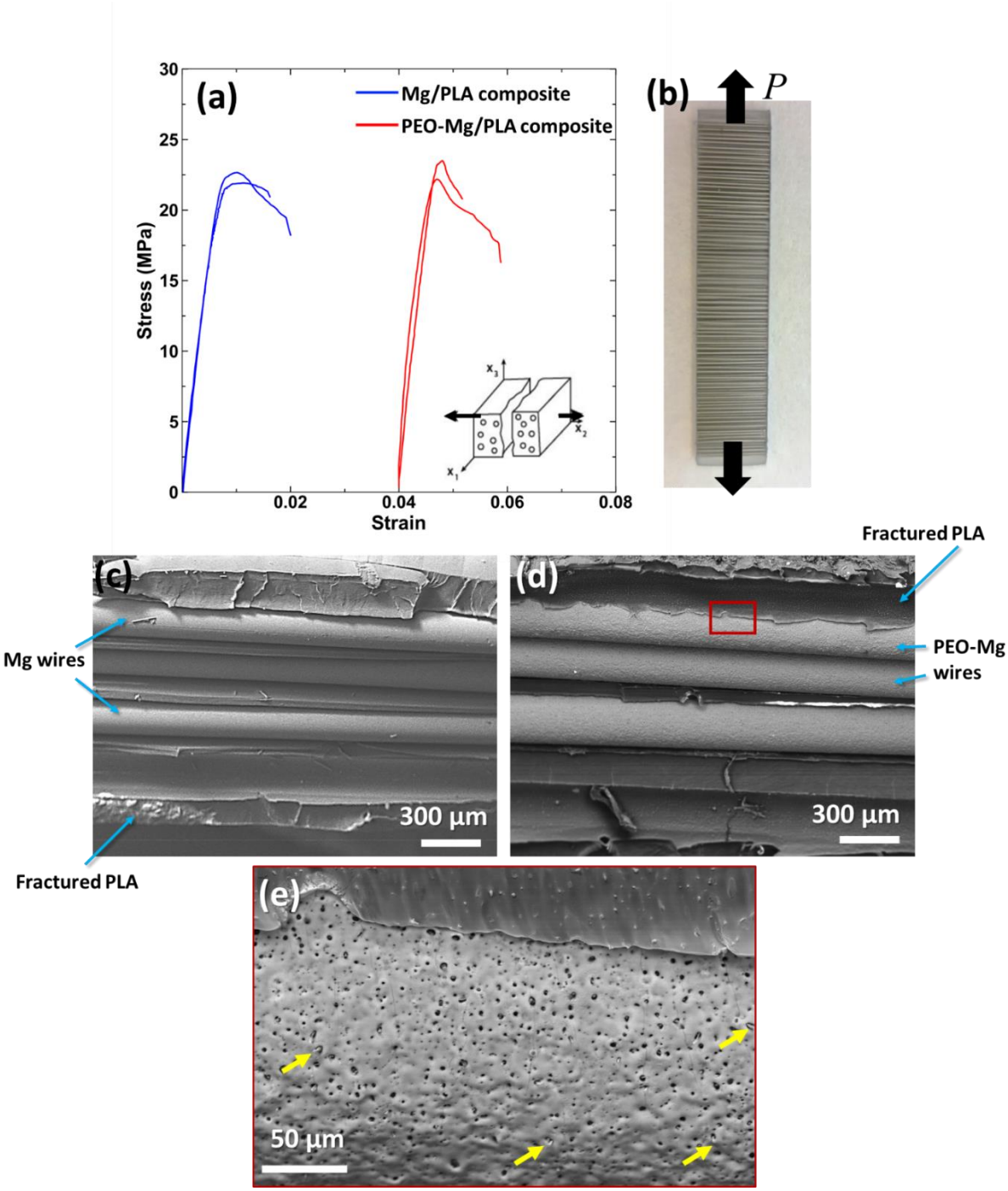

Fig. 4.6. (a) Representative stress-strain curves of unidirectional Mg/PLA and PEO-Mg/PLA composites $[90^o]_4$ deformed in tension along the transverse direction. (b) Optical image of the fracture of PEO-Mg/PLA composite. (c) Back-scattered SEM image of the fracture surface of Mg/PLA composite and (d) *Idem* of PEO-Mg/PLA composite. (e) Detail of the PEO oxide layer surface after fracture. Yellow arrows mark PLA ligaments stuck in the pores.

The stress-strain responses of both Mg/PLA and PEO-Mg/PLA composites during compression in longitudinal and transverse directions are shown in Figs. 4.7a and 4.8a, respectively. The specimens buckled macroscopically in the gauge length during all compression tests. However, they attained a failure strength of at least 115 MPa in the longitudinal direction which is higher than tensile strength in the same orientation. In the transverse direction, a compressive strength of at least 85 MPa was achieved which is close to the compressive strength of pure PLA and to the tensile strength of composites in the longitudinal direction.

Unidirectional composites during compression loading in longitudinal direction exhibit different damage mechanisms, including fiber kinking, fiber crushing, matrix damage, buckle delamination, etc. [141][142]. These mechanisms can occur separately or simultaneously depending on the loading scenario, and they affect the global response of the laminate [143]. Generally, buckling instability triggers the failure of composite far below the real compressive strength [144] and hinders the understanding of aforementioned damage mechanisms. In the case of Mg/PLA composites (with and without PEO), buckling instability was likely to be triggered by misalignments and non-uniform distribution of Mg wires within PLA matrix. Loading was continuously applied to study the endurance of the composite after buckling. It was found that the composite did not fail abruptly, and neither fracture in the PLA matrix nor in the Mg wires was observed (Fig. 4.7b).

Composite failure in transverse compression is mainly dictated by interface decohesion and shear yielding of polymer matrix [145]. Although the specimen buckled macroscopically before pure compression failure in the transverse direction, interface decohesion coupled with the yielding of the PLA matrix could be easily observed in PEO-Mg/PLA composites (Fig. 4.8c). Nevertheless, PEO modification in compression loading did not reveal any beneficial effects.

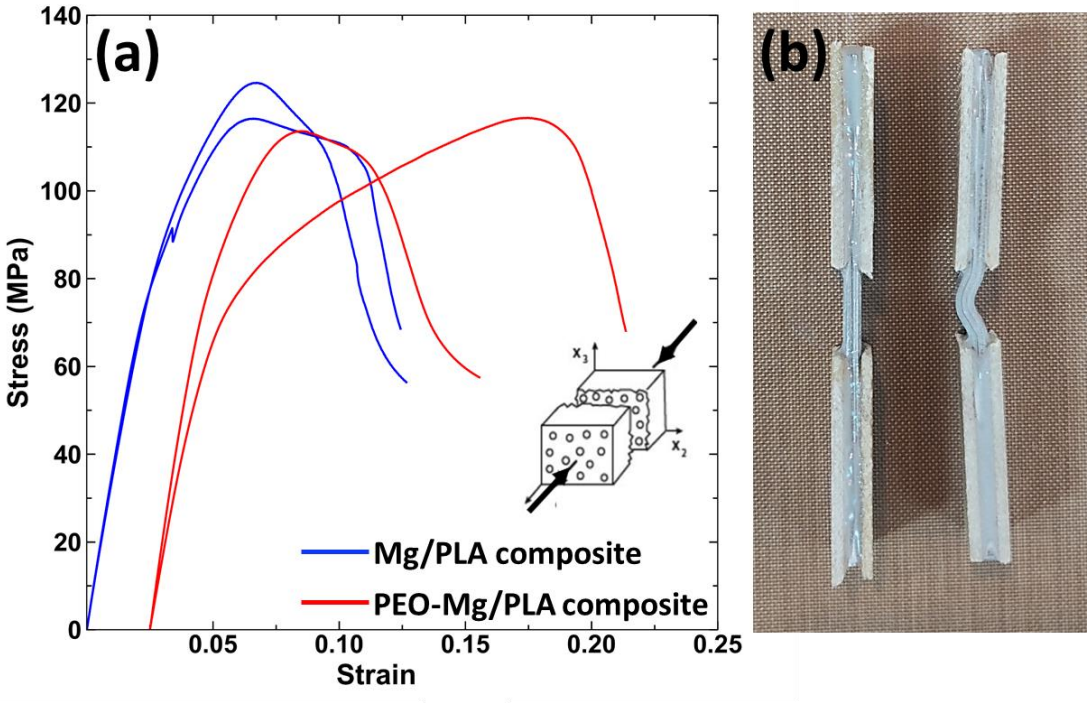

Fig. 4.7. (a) Representative stress-strain curves of unidirectional composites $[0^o]_3$ during compression along the longitudinal direction and (b) Optical image of PEO-Mg/PLA composite before and after buckling failure during compression.

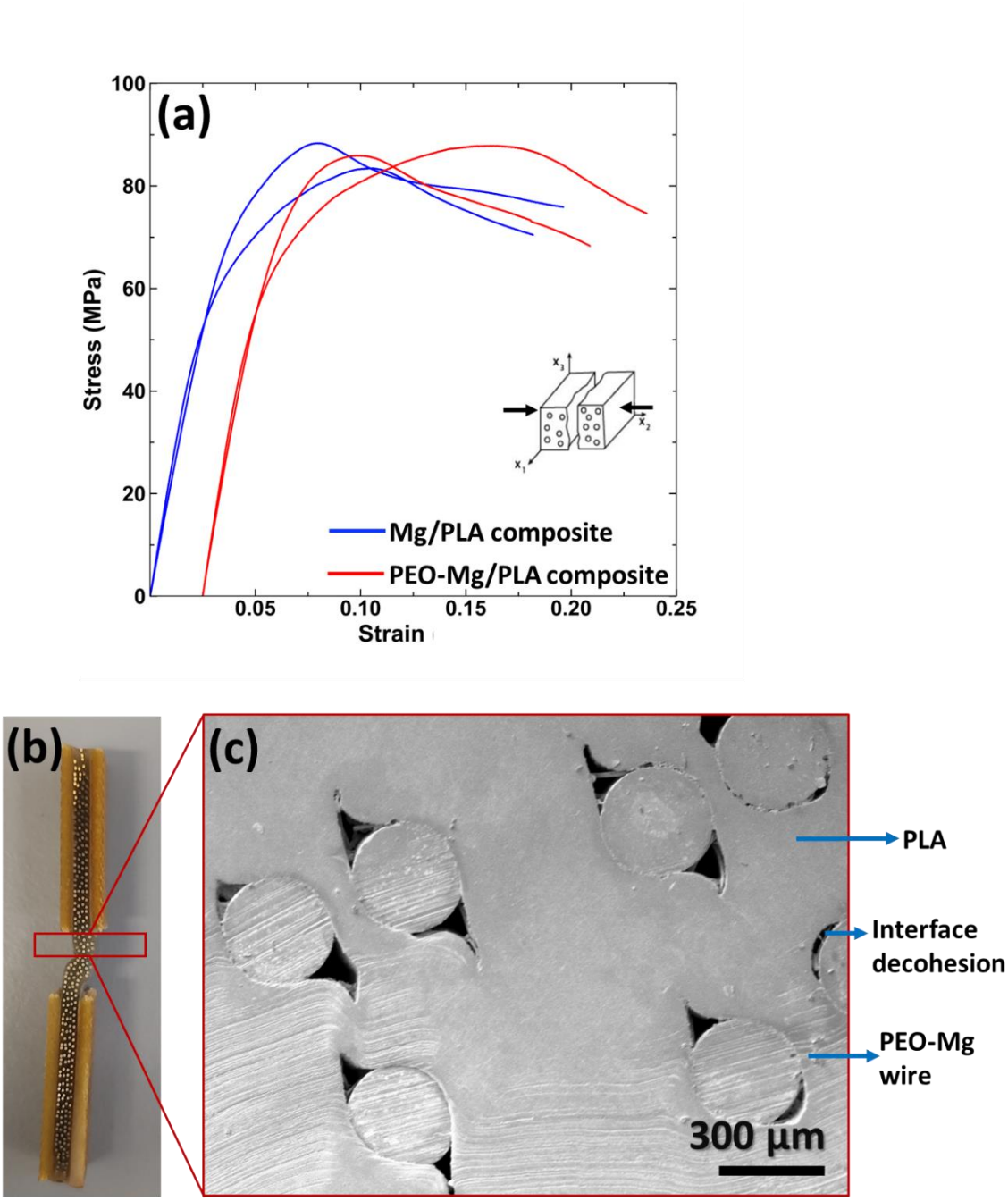

Fig. 4.8. (a) Representative stress-strain curves of unidirectional composites $[90^{o}]_4$ during compression along the transverse direction, (b) Optical image of buckled PEO-Mg/PLA composite during compression in the transverse orientation. (c) SEM image of PEO-Mg/PLA composite showing interface de-cohesion during compression along the transverse direction.

In-plane shear properties were determined by means of tensile tests on $[\pm 45^{o}]_{s}$ composite laminates (Fig. 4.9) and Eqs. (4.1) and (4.2). Both composites showed similar behavior with shear modulus and strength of ~1.5 GPa and 24 MPa, respectively. Generally, either matrix yielding or interface d-cohesion dictates failure during in-plane shear loading [146]. However, the microstructure of Mg/PLA and PEO-Mg/PLA composites is different from that of conventional fiber reinforced composites. Each lamina of Mg wires consists of an array of several Mg wires (one wire across lamina thickness) due to the large wire diameter and low volume fraction, and also includes rich regions of PLA matrix between laminas of Mg wire. Therefore, it could be reasonably assumed that the damage was predominantly controlled by yielding of PLA matrix between Mg wire laminas. PLA matrix cracked in Mg/PLA composites and Mg wires were being pulled out between fractured matrix ends (Fig 4.9c). PEO modification improved the interface strength and impeded the onset of fracture of the PLA matrix while matrix yielding was evident from the reduction of cross-sectional area and rotation of the wires (see Fig 4.9d).

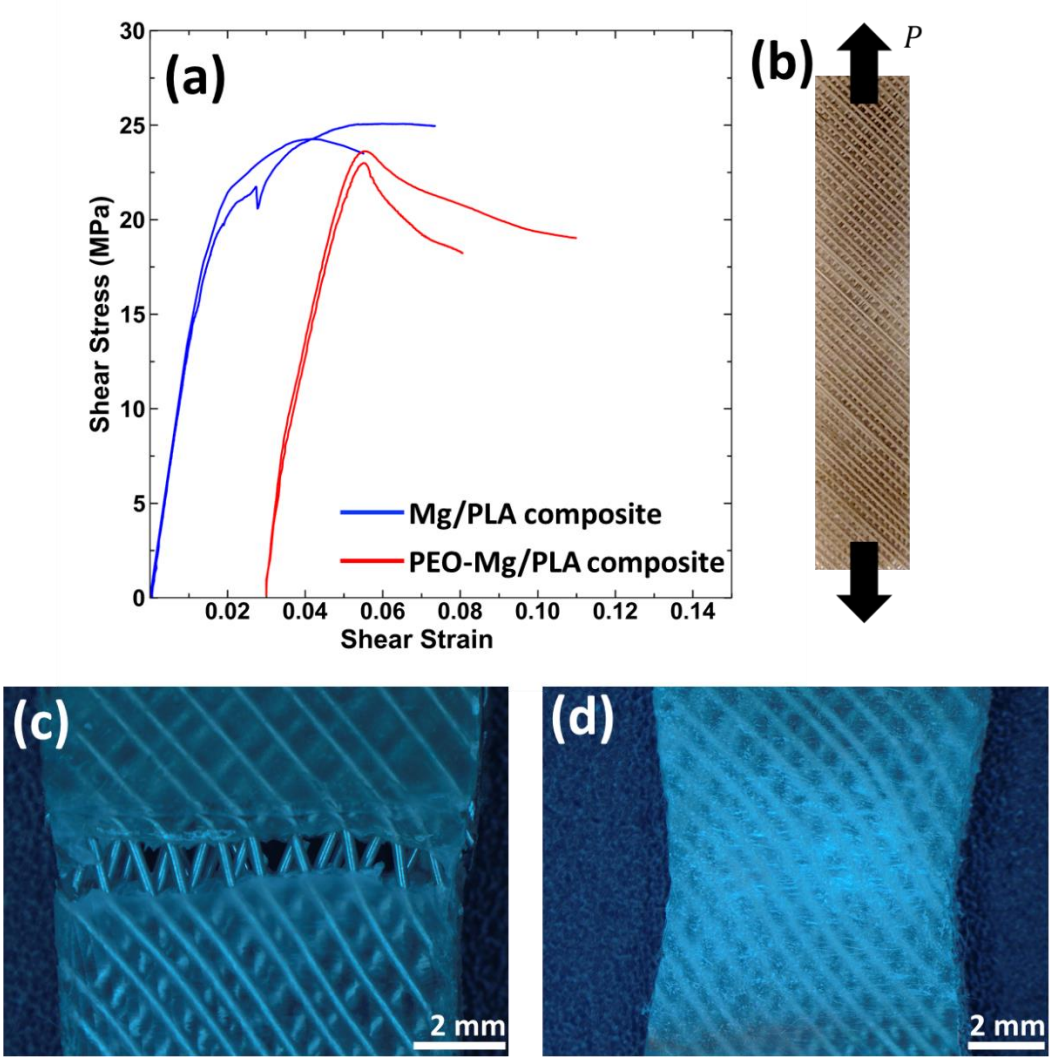

Fig. 4.9. (a) Representative stress-strain curves of tensile test on $[\pm 45^{o}]_{s}$ laminatse of Mg/PLA and PEO-Mg/PLA composite for in-plane shear response. (b) Optical image of $[\pm 45]_{s}$ laminate of PEO-Mg/PLA composite for the in-plane shear test. (c) Failure mechanisms of Mg/PLA composite showing fractured PLA matrix. (d) *Idem* PEO-Mg/PLA composite showing PLA matrix yielding without fracture.

4.2.4. Mechanical behavior of quasi-isotropic laminate

The stress-strain curves in tension of quasi-isotropic $[0^o/90^o/\pm45^o]_s$ laminates (Fig. 4.10) show that both Mg/PLA and PEO-Mg/PLA composites have approximately equal elastic modulus (5.4 GPa) and strength (52 MPa) but the PEO-Mg/PLA composite had high failure strain (~4.5 %). The higher ductility of the PEO-Mg/PLA quasi-isotropic composite is due higher failure strain of the unidirectional PEO-Mg/PLA composite (Fig. 4.5a). Therefore, Mg wire laminas oriented in the loading direction (at 0^o) played a key role in increasing the toughness of quasi-isotropic laminate of PEO-Mg/PLA composites.

The experimental value of elastic modulus of quasi-isotropic composites was compared with the prediction of classical laminate theory (CLT) [147] (see Table 4.3), where the elastic constants obtained from testing of unidirectional composites (Table 4.2) were used as input. The experimental elastic modulus closely matched with the CLT prediction (> 90%), demonstrating that the elastic constants obtained from unidirectional tests can be reliably used to design the stacking sequence to achieve desired elastic modulus of Mg/PLA composites.

Classical Laminate Theory (CLT) [147] can help to understand the onset of damage and sequential fracture behavior of quasi-isotropic laminates from the elastic constants and strengths measured in unidirectional composites (Table 4.2). Finite element numerical simulations using ABAQUS of quasi-isotropic composite $[0^o/90^o/\pm45^o]_s$ in tension were carried out to this end. The mechanical properties of unidirectional lamina were used as input, and it was found from the maximum stress failure criteria that damage of the quasi-isotropic laminate begins in the Mg wire laminas (or plies) oriented at 90^o followed by failure of 0^o and 45^o plies. Damage onset in the 90^o ply begins when the macroscopic stress reaches 39 MPa. This value is supported by the experimental observations in Fig. 4.10a where non-linear behavior appears above 39 MPa. The simulations also predict that Mg wire laminas (or plies) oriented at 0^o will fail first at 65 MPa under compressive loading. Experimental observations by DIC could not provide accurate engineering strains after fracture and therefore, load-displacement curves of tensile deformation of quasi-isotropic laminates are plotted in Fig. 4.10b. They provide better insights into the post-fracture mechanisms, which are further supported by SEM images of fractured surfaces of Mg/PLA and PEO-Mg/PLA

composites (Fig. 4.10(d-i)). PLA matrix fractured by transverse cracks in both composites, and damage was most likely to originate in lamina oriented at 90° as the unidirectional composite had ~0.9 % failure strain (Fig. 4.6a) in transverse tension. Damage was then transferred to laminas oriented at 0° and propagated to the 45° laminas (according to CLT), leading to sudden fracture of PLA matrix through the thickness of the composite. Mg wires in laminas oriented at 45° remained intact and were being pulled out from the PLA matrix. On the contrary, Mg wire in laminas oriented at 0° were pulled out (Fig. 4.10e) in Mg/PLA composites but fractured (Fig. 4.10g) in PEO-Mg/PLA composites due to high interface shear strength induced by PEO modification, in agreement with the observations during longitudinal tension tests on unidirectional composites.

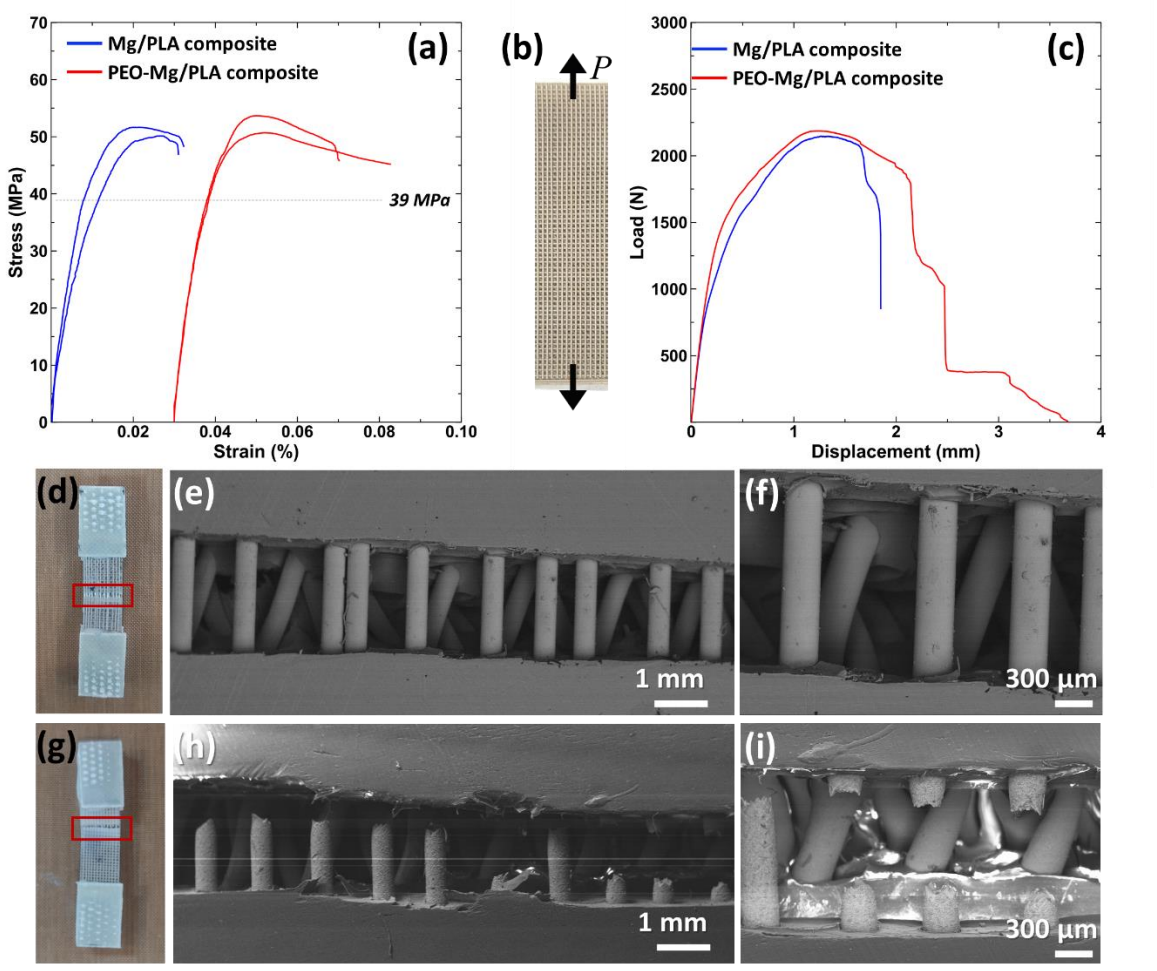

Fig. 4.10. Representative stress-strain curves of tensile test of quasi-isotropic laminates $[0^o/90^o/\pm45^o]_s$ of Mg/PLA and PEO-Mg/PLA composites. (b) Optical image of quasi-isotropic laminate of PEO-Mg/PLA composite for tensile test. (c) Representative load-displacement curve of tensile test of quasi-isotropic laminates of PEO-Mg/PLA composites, (d) Optical image of quasi-isotropic laminate of fractured Mg/PLA

composite after tensile test, (g) *Idem* of PEO-Mg/PLA composite, (e) Back-scattered SEM image of fracture surface of Mg/PLA composite, (f *Idem* enlarged image of Mg/PLA composite (h) *Idem* of PEO-Mg/PLA composite, (i) *Idem* enlarged image of PEO-Mg/PLA composite. Dashed line at 39 MPa in (a) shows onset of damage in 90º ply by max stress failure criteria of CLT.

Table 4.3. Tensile behavior of quasi-isotropic laminate $[0/90/\pm45]_s$

Mechanical property	**Mg/PLA composite**	**PEO-Mg/PLA composite**
Elastic modulus (GPa) - E_q	5.3 ± 0.05	5.4 ± 0.4
Theoretical Elastic Modulus (GPa) calculated by classical laminate theory	5.6 ~ 6.6	6.0 ~ 6.9
Tensile strength (MPa) - S_q	52.1 ± 2	52 ± 1.5

4.3. Conclusions

The mechanical behavior of matrix, Mg wires and interfaces as well as that of unidirectional and multi-directional composites, was measured through different mechanical tests. Tensile tests of the constituents of composite revealed that Mg wires are more ductile (9-14 % failure strain) and stronger (>300 MPa strength) than the PLA matrix which is relatively brittle (5 % failure strain) and weak (56 MPa strength). It was found that the presence of a PEO oxide layer significantly increased the toughness and shear strength of the interface between Mg wires and PLA matrix by a factor of ~2.5 due to the mechanical interlocking of PLA into the pores of the PEO oxide layer and the chemical interactions of the PLA with the oxide layer.

Mechanical tests (tension, compression and in-plane shear) of unidirectional composite laminates of Mg/PLA and PEO-Mg/PLA showed that modulus and strength depend on the orientation of Mg wire. The highest mechanical properties are attained in the longitudinal direction with tensile strength of 90 MPa and compressive one >115 MPa. PEO surface modification increased the ductility (due to the high interface strength) during tensile deformation in the longitudinal direction without improving the tensile strength, while other mechanical properties of unidirectional composites were not altered by PEO surface modification. The uniaxial elastic moduli in longitudinal and transverse directions are 11 GPa and 4.2 GPa, respectively, which defined the upper

and lower limit of modulus that can be achieved in Mg/PLA composite with 20 vol % of Mg wires. The elastic constants measured in tests on unidirectional laminas can be used in finite element simulations to design an optimizing stacking sequence of Mg wire laminas to achieve desirable mechanical properties of composite.

Finally, the quasi-isotropic laminate attained an elastic modulus of ~5.4 GPa, which matched closely with the theoretical predictions of classical laminate theory, using the elastic constants from unidirectional tests as inputs. The PEO surface modification improved the tensile ductility of quasi-isotropic composite laminates without compromising the modulus and strength. Moreover, the additional advantage of PEO surface modification will be reflected in the degradation of composite where PEO-modified Mg wires are expected to corrode more slowly and hence, will improve the retention of mechanical properties of composite.

CHAPTER 5. DEGRADATION MECHANISMS AND MECHANICAL DEGRADATION OF COMPOSITES

The mechanical properties of Mg/PLA composite are expected to degrade over time under *in vivo* and *in vitro* environments due to the degradation of the constituents of composite (wires, matrix and wire/matrix interfaces). Therefore, understanding of degradation mechanisms of Mg/PLA composite at constituent and bulk levels is essential to assess the application of these composites. In this chapter, the degradation mechanisms of Mg wires (with and without surface modification by PEO) embedded in the PLA matrix as well as of the PLA matrix in the presence of Mg wires are studied. And then they are related with the *in vitro* bulk degradation of the Mg/PLA composites during 180 days in SBF at 37ºC. In addition, the degradation of the interface shear strength along with degradation of the macroscopic mechanical properties of unidirectional and quasi-isotropic laminates after 42 days in SBF at 37ºC are presented.

5.1.Experimental techniques

5.1.1. Materials

Unidirectional and quasi-isotropic multi-directional Mg/PLA and PEO-Mg/PLA composite laminates were prepared as described in section 2.2. Specimens for mechanical testing after *in vitro* degradation were manufactured with the same dimensions, as detailed in Section 4.1.4. In addition, PLA coupons were manufactured by hot pressing of pellets at 180 ºC and used as reference in the degradation studies.

5.1.2. In vitro degradation tests

In vitro degradation tests of the PLA, Mg/PLA and PEO-Mg/PLA specimens were carried out at 37ºC in Simulated Body Fluid (c-SBF) with a composition (per liter) of 8.035 g NaCl, 0.355 g $NaHCO_3$, 0.225 g KCl, 0.231 g $K_2(HPO_4).3H_2O$, 0.311 g $MgCl_2.6H_2O$, 0.292 g $CaCl_2$, 0.072 g Na_2SO_4, 6.118 g Tris base and 40 mL 1M HCl to achieve pH of 7.4 [148]. The samples were cut to from the hot-pressed plates to 12 mm x 12 mm x 2 mm. Cross-sections perpendicular to the wires where Mg wires were directly exposed to SBF were sealed with a vinyl spray coating (Full Dip, Spain) to ensure that degradation occurs by diffusion of water through the thickness of the sample and not by pipeline diffusion along the wire/matrix interface from the exposed ends. In

addtion, some samples were intentionally not sealed (open edged samples) to study the effect of pipeline corrosion on the degradation of the composites.

Short-term (7, 14, 28 and 42 days) and long-term (180 days) degradation studies were carried out in different samples that were placed in a container with 200 mL of c-SBF which leads to a ratio between c-SBF volume to sample mass of approximately 450 mL/g (> 30 mL/g, as recommended by ISO 15814 [149]) and c-SBF volume to Mg wires surface area of 0.27 mL/mm^2 (> 0.2 mL/mm^2, as recommended by ASTM G31[123]). Currently, there is no standard to assess the degradation of bioabsorbable metal/polymer composites; therefore, a volume of buffer solution above the minimum limits defined by both ISO 15814 (for degradation of PLA) and ASTM G31 (for corrosion of metals) was selected. Moreover, corrosion of Mg wires inside the composite samples in the long-term study (180 days) was tracked by a hydrogen gas evolution setup involving glass containers, funnels, and burettes, as reported in [150]. pH variation was also recorded to ensure that the pH of solution remains between 7.4 to 8.2. Mass change (in wet and dry state) of samples was also measured. For wet mass, samples were taken out from the immersion medium at differnt times and weighted while dry mass was measured after desiccation of the samples in vacuum for 7 days. These dried samples were further used for the microscopic analysis and push-out tests to measure the interface properties. The degradation mechanisms were ascertained in scanning electron microscopy (SEM) (Apreo 2S LoVac ThermoScientific, Netherlands), using secondary and back-scattered electron modes at 10 kV after gold sputtering. Energy dispersive X-ray microanalysis (EDX) was also performed to ascertain the composition of degradation products.

Mass loss of Mg wires inside the PLA matrix was calculated by image analysis of wire cross-sections in the degraded samples. To this end, samples were extracted after *in vitro* study and embedded in an epoxy resin. They were grinded and polished to obtain clear images of the Mg wire in the cross-sections. Optical images (BX51 Olympus, Japan) of the wire cross sections were taken randomly. 5 and 15 images were taken from samples subjected to short-term (7, 14, 30, 42 days) and long-term degradation (180 days), respectively, and processed with ImageJ software. The area of the uncorroded regions in the Mg wire cross-sections was used to estimate the average mass loss. Similarly, at least 5 images were taken randomly in the optical microscope to measure lengths of pipeline corrosion in samples where edges were not sealed.

5.1.3. Mechanical tests on degraded samples

Push-out tests were performed on degraded samples to study the effect of degradation on interface shear strength. Samples for push-out tests were prepared according to section 4.1.3 and immersed in SBF at 37ºC. Samples were taken out from SBF after different times (7, 14, 28 and 42 days), dried in vacuum for 7 dies and prepared for the wire push-out tests.

Degradation of macroscopic mechanical properties of unidirectional (longitudinal tension, transverse tension and in-plane shear) and quasi-isotropic composites were determined after 42 days of immersion in c-SBF. Prior to the immersion in SBF, tabs were glued to the specimen and the tabs along with the regions where Mg wires directly exposed (after cutting during sample preparation) were sealed with vinyl spray coating (Full Dip, Spain) to block pipeline corrosion from these regions. Specimens were taken out from immersion medium after 42 days and quickly sprayed with paint to measure strains by DIC imaging. After drying of paint for 2 hours, the specimen (still in wet state) were taken to the universal testing machine for mechanical tests that were performed as detailed in Section 4.1.4.

5.1.4. Thermal characterization

The thermal characteristics of as-manufactured and degraded samples of the PLA coupons and composites were analyzed by differential scanning calorimetry (Q200, TA Instruments, USA) by two heating cycles performed at 10 ºC/min. The glass transition temperature (T_g) from the 2nd heating cycle of DSC was used as an indicator of PLA matrix degradation because T_g values of the 1st heating cycle are artificially increased (in case of sample degradation) by physical aging of the polymer. The molecular weight of samples was also measured by means of gel permeation chromatography (GPC) (GPC 2414, Waters).

5.2.Results and discussion

5.2.1. Degradation of Mg and PEO-Mg wires inside PLA matrix

The oxide layer created by PEO on the Mg wires had a strong effect on the *in vitro* degradation of the wires inside the PLA matrix. The hydrogen gas generated due to corrosion of the Mg wires in the Mg/PLA and PEO-Mg/PLA composites is plotted in

Fig. 5.1a as a function of the immersion time in c-SBF at 37ºC. The presence of the PEO oxide layer dramatically reduced the hydrogen gas release rate. The hydrogen release volume of Mg/PLA composites increased linearly with time during the first 100 days, followed by a plateau. After 180 days, the hydrogen volume released by Mg/PLA (60.8 ± 3.6 ml) or (7.6 ml/cm^2) was approximately 8 times lower than that released by PEO-Mg/PLA (7.4 ± 3.5 ml) or (0.9 ml/cm^2). The equivalent hydrogen gas volume normalized with respect to the original surface area of Mg wires clearly highlights the protection effect of PLA matrix and can be used to compare their corrosion rate with naked Mg wires [50]. Mass loss of Mg wire cores (Fig. 5.1b) was also estimated by image processing to prove the superior performance of PEO-Mg wires inside the PLA matrix. The results are plotted in Fig. 5.1a assuming that one atom of Mg leads to the release of one molecule of hydrogen. Representative cross-sections (Fig. 5.1c) confirmed that Mg wires in Mg/PLA composites corroded faster. Pit formation was evident after 42 days and Mg wires practically disappeared after 180 days. On the contrary, Mg wires in PEO-Mg/PLA suffered much less mass loss (although some pits could be observed after 180 days) due to synergetic protection provided by the oxide layer and the PLA matrix.

The estimations of hydrogen release from the image analysis of the cross-section of the Mg wires are in good agreement with hydrogen gas evolution for the whole period in the case of PEO-Mg/PLA and for the first 42 days in Mg/PLA. The total hydrogen gas volume released after 180 days in Mg/PLA was only 62% of the theoretical volume after the complete corrosion of the Mg wires. This difference, however, is in agreement with previous reports [151][112] and could be attributed to leakages or oxygen reduction reactions likely to occur during the slow corrosion of Mg [152][153].

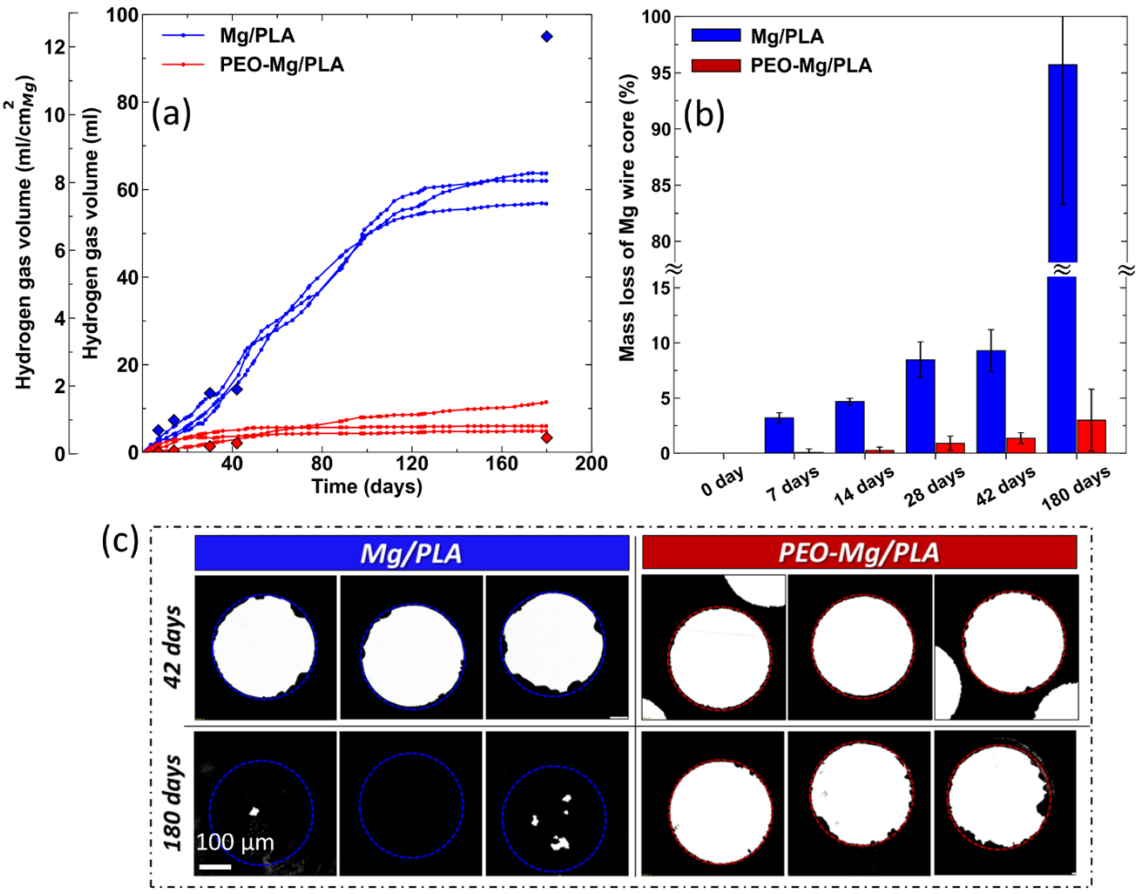

Fig. 5.1. (a) Hydrogen gas evolution and (b) mass loss of Mg wire core estimated by image processing as a function of immersion time in c-SBF at 37ºC for Mg/PLA and PEO-Mg/PLA composites. Here, (♦) represents the hydrogen gas volume estimated by mass loss in (b) in (a) using the equation of an ideal gas. (c) Representative cross-sections of Mg wires after 42 and 180 days of degradation with and without PEO oxide layer.

5.2.2. Degradation of PLA matrix in presence of Mg wires

DSC and GPC were used to assess the degradation of pure PLA and PLA matrix in presence of Mg wires (with and without PEO) from the average molecular weight (M_w), and glass transition temperature (T_g), as shown in Fig. 5.2a and 5.2b, respectively for the as-manufactured and degraded conditions after immersion in c-SBF at 37ºC.

T_g and M_w of the as-manufactured samples decreased in the presence of Mg and PEO-Mg wires, in agreement with the previous studies that showed that the presence of Mg (and MgO) catalyzes the hydrolysis of PLA during high temperature processing [4]. After 42 days of *in vitro* immersion, there were not significant changes in M_w of PLA in the pure coupons and in the composites. After *in vitro* degradation during 180 days,

T_g did not change in pure PLA coupons, but M_w decreased most likely due to the random chain scission of PLA oligomers triggered by hydrolytic degradation. The presence of Mg wires accelerated the degradation of PLA matrix after 180 days of *in vitro* degradation and led to sharp drops in T_g and M_w to 42.1 ºC and 84000 g/mol, respectively. The presence of the oxide layer on PEO-Mg wires reduced this drop and limited the degradation of the PLA matrix. It should be noted that the PLA matrix underwent localized degradation at the wire/matrix interface in the short-term degradation study (discussed in Section 5.2.8 and 5.2.9) but the volume of polymer involved in the local degradation was insufficient to influence the GPC and DSC tests in bulk samples after 42 days.

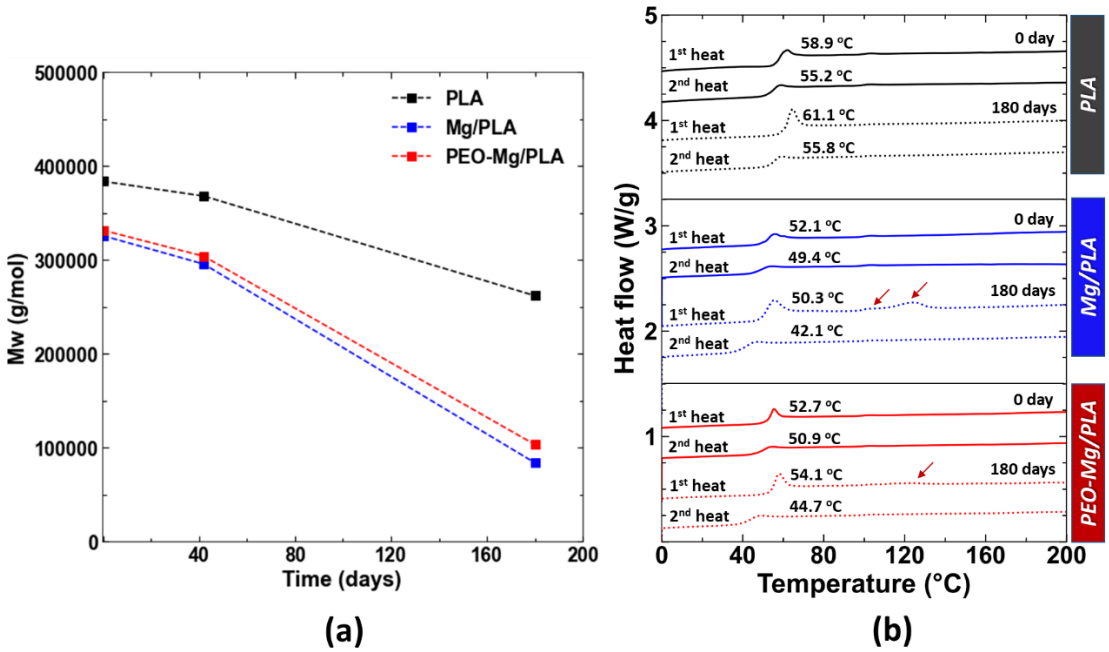

Fig. 5.2. Average molecular weight (M_w) and glass transition temperature (T_g) of PLA in the as-processed condition and after *in vitro* degradation of 180 days in c-SBF at 37 ºC. Red arrow shows minor peaks of crystal melting appeared in 1st heating cycle of composites after 180 days immersion.

5.2.3. Degradation of Mg/PLA and PEO-Mg/PLA composites

Visual inspection and wet/dry mass changes were used to assess overall degradation of pure PLA, Mg/PLA and PEO-Mg/PLA composites, as shown in Fig. 5.3 and 5.4. The ends of composites (where Mg wires were directly exposed after cutting process) were sealed by vinyl coating to avoid pipeline corrosion.

Pure PLA coupons did not reveal any changes in visual appearance or physical deterioration during 180 days of *in vitro* degradation in c-SBF immersion (Fig. 5.3a). Its wet mass increased by ~0.7 % after 7 days and then remained constant, suggesting that PLA coupons were saturated after absorbing ~0.7 % water (Fig. 5.5a). However, its dry mass remained unchanged and close to zero for, indicating a negligible mass loss during 180 days. This is also in agreement with the trends of T_g and M_w (Fig. 5.2a and 5.2b).

The appearance of Mg/PLA composites continuously changed during *in vitro* degradation due to the corrosion of Mg wires (turning blackish), which were clearly visible through transparent PLA matrix (Fig. 5.3b). Mg wires were completely corroded and transformed into powder within the PLA matrix in the Mg/PLA composites after 180 days immersed in c-SBF at 37ºC. The corrosion products of Mg wires also accelerated the degradation of the PLA matrix, as evident by its whitish color and swelling (red arrows) which indicates severe hydrolysis of PLA [154]. The wet mass of the composite increased linearly during the first 42 days due to water uptake and corrosion of Mg wires (Fig. 5.4a) while the dry mass increased slightly and remained closed to 1 % during the first 42 days and reached 8.5 % after 180 days (Fig. 5.4b). These results support the argument that the rate of formation of corrosion products of Mg is faster than the rate of dissolution (by diffusion) of the PLA matrix resulting in the accumulation of corrosion products within composite.

In PEO-Mg/PLA composites, the corrosion of Mg wires was significantly slowed down by protection of PEO oxide layer. The appearance of the PEO-Mg wires inside PLA matrix changed slightly (random grey marks) after 42 days (Fig. 5.3c). Afterwards, their corrosion was suppressed and PEO-Mg wires were still present after 180 days. This result was also confirmed by cross-sectional images of wires (Fig. 5.1c). The PLA matrix turned to whitish color after 180 days due to hydrolysis and the degradation of PLA matrix was also confirmed by the reduction in M_w (Fig. 5.2a). The wet mass of PEO-Mg/PLA composite increased up to ~1.3 % for the first 42 days due water uptake and minor corrosion of Mg wires. The wet and dry mass dropped up to 0.4 % and -5 %, respectively, after 180 days of immersion in c-SBF at 37ºC, most likely due to mass loss of PLA matrix as corrosion of PEO-Mg wires was suppressed.

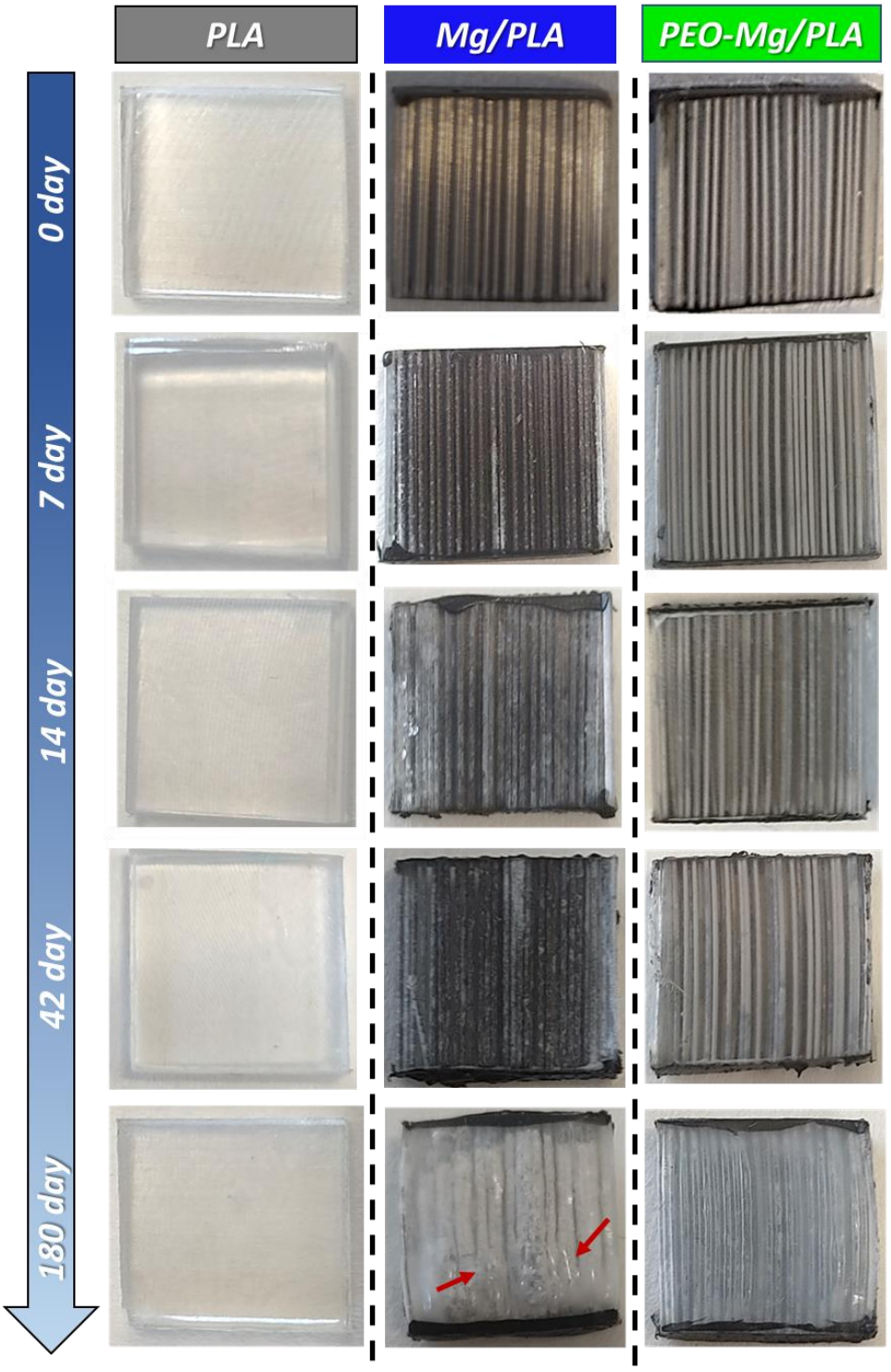

Fig. 5.3. Optical images of (a) pure PLA, (b) Mg/PLA and (c) PEO-Mg/PLA composite specimens before (0 day) and after 7, 14, 28, 42 and 180 days of *in vitro* immersion in c-SBF at 37 ^{o}C. Red arrows show swelling in Mg/PLA composite.

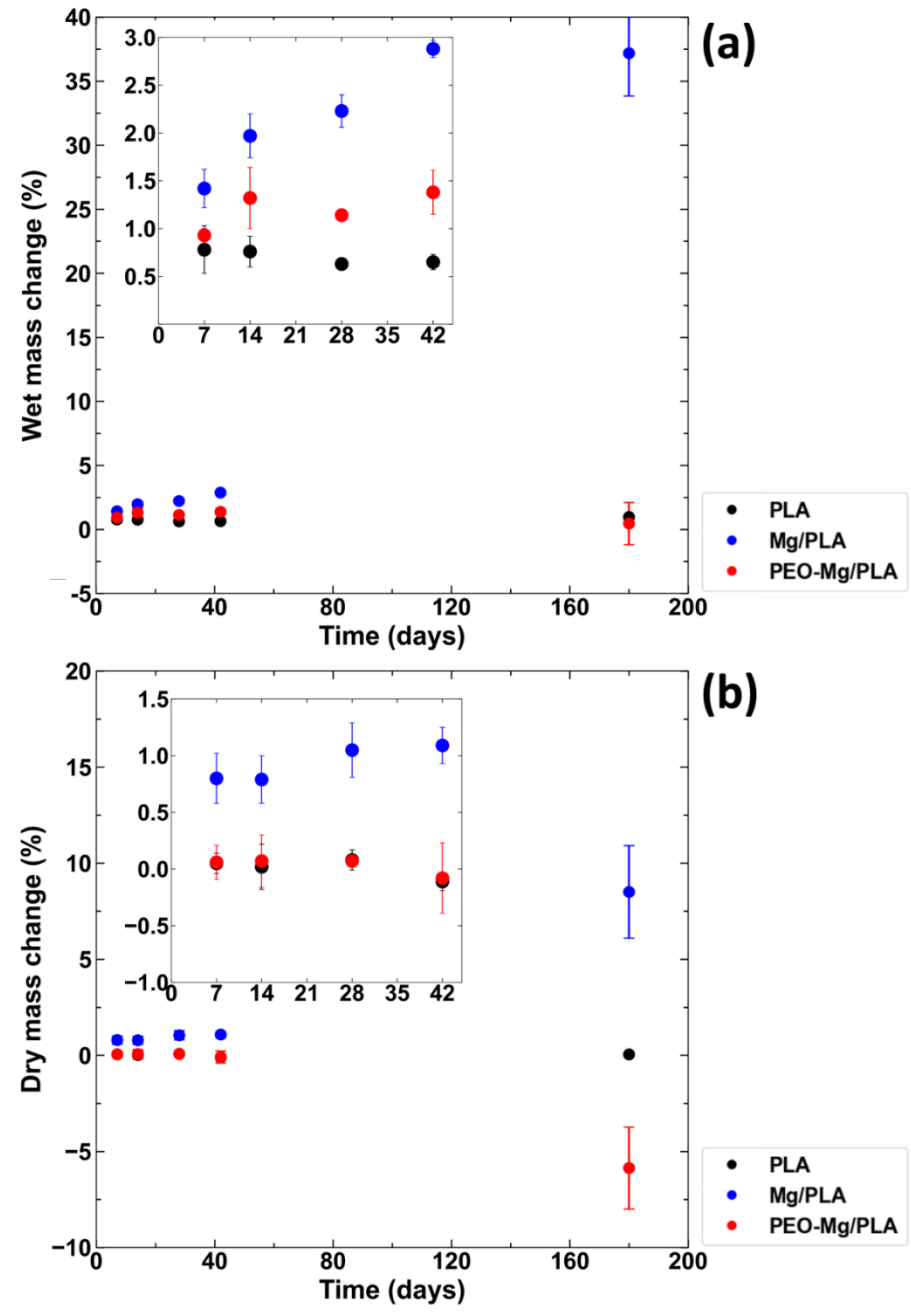

Fig. 5.4. Changes in (a) wet and (b) dry mass of PLA, Mg/PLA and PEO-Mg/PLA composites during 180 days of *in vitro* immersion in c-SBF at 37 ºC.

5.2.4. Degradation of open edge Mg/PLA and PEO-Mg/PLA composites

In vitro degradation studies were also performed in Mg/PLA and PEO-Mg/PLA composites where the Mg wires were directly exposed to c-SBF from edges (Fig. 5.5a). Mg wires are expected to undergo accelerated corrosion by pipeline diffusion of water along the interface from these regions. Understanding this process is important for two reasons, Firstly, to demonstrate the feasibility of preparing composite implants by machining, which will expose Mg wires to body fluids. Secondly, to accelerate the degradation of the composite from edges by intentionally exposing Mg wires from some regions.

The pipeline corrosion for PEO-Mg wires from exposed edges of PEO-Mg/PLA composites after 28 days of immersion in c-SBF is depicted in Fig. 5.5b. Lengths of completely corroded wires in both Mg/PLA and PEO-Mg/PLA composites were measured from exposed edges and they are plotted in Fig. 5.5c as a function of the immersion time. Surface modification of the Mg wires by PEO slowed down the rate of pipeline corrosion by providing corrosion protection from the lateral surface of wire. Even after 95 days of immersion in c-SBF, only 1.4 mm of PEO-Mg wires were completely corroded from the surface. On the contrary, Mg wires without any PEO modification suffered accelerated pipeline corrosion due to the additional effect of lateral corrosion.

The dry mass of composites with sealed edges (Fig. 5.4b) was compared with that of the specimens that underwent pipeline corrosion, and they are plotted together in Fig. 5.6a. It can be clearly seen that pipeline corrosion of wires significantly accelerated the degradation of Mg/PLA and PEO-Mg/PLA composites. This could be due to two mechanisms. Firstly, corrosion products of Mg wires near edges can directly interact with c-SBF and dissolve into medium, resulting in less accumulation of corrosion products. The second mechanism is schematically depicted in Fig. 5.6b, which shows the accelerated degradation of PLA matrix near edges in the presence of corrosion products of Mg. Therefore, it could be interesting from design point-of-view to intentionally expose Mg wires from selected regions of composite to achieve customized degradation rates.

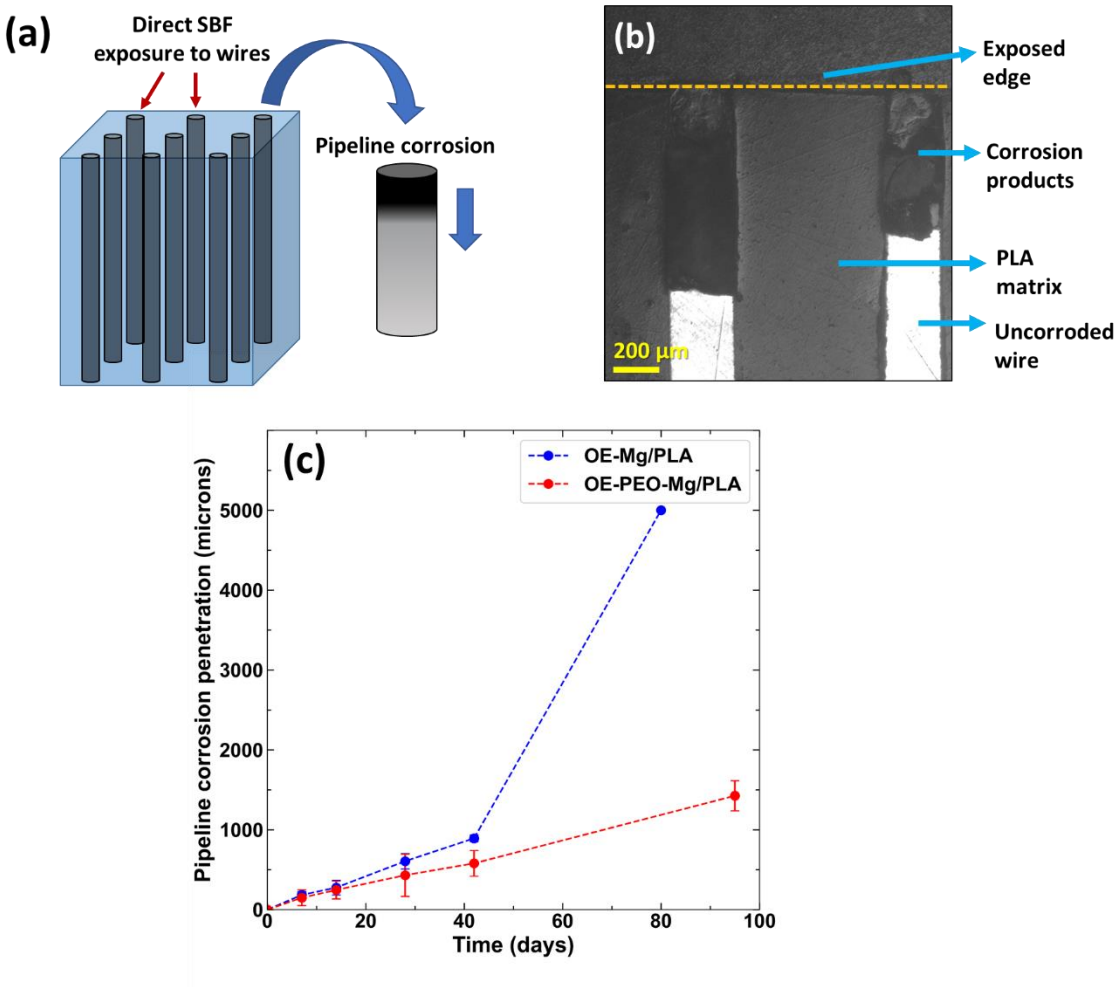

Fig. 5.5. (a) Schematic depiction of pipeline corrosion of Mg wires by direct exposure to c-SBF during *in vitro* tests, (b) optical image of pipeline corrosion of PEO-Mg wires in PEO-Mg/PLA composite after *in vitro* degradation during 28 days. Uncorroded Mg wires appear white. (c) Length of corroded of Mg wires from edges in open edged (OE) Mg/PLA and PEO-Mg/PLA composites.

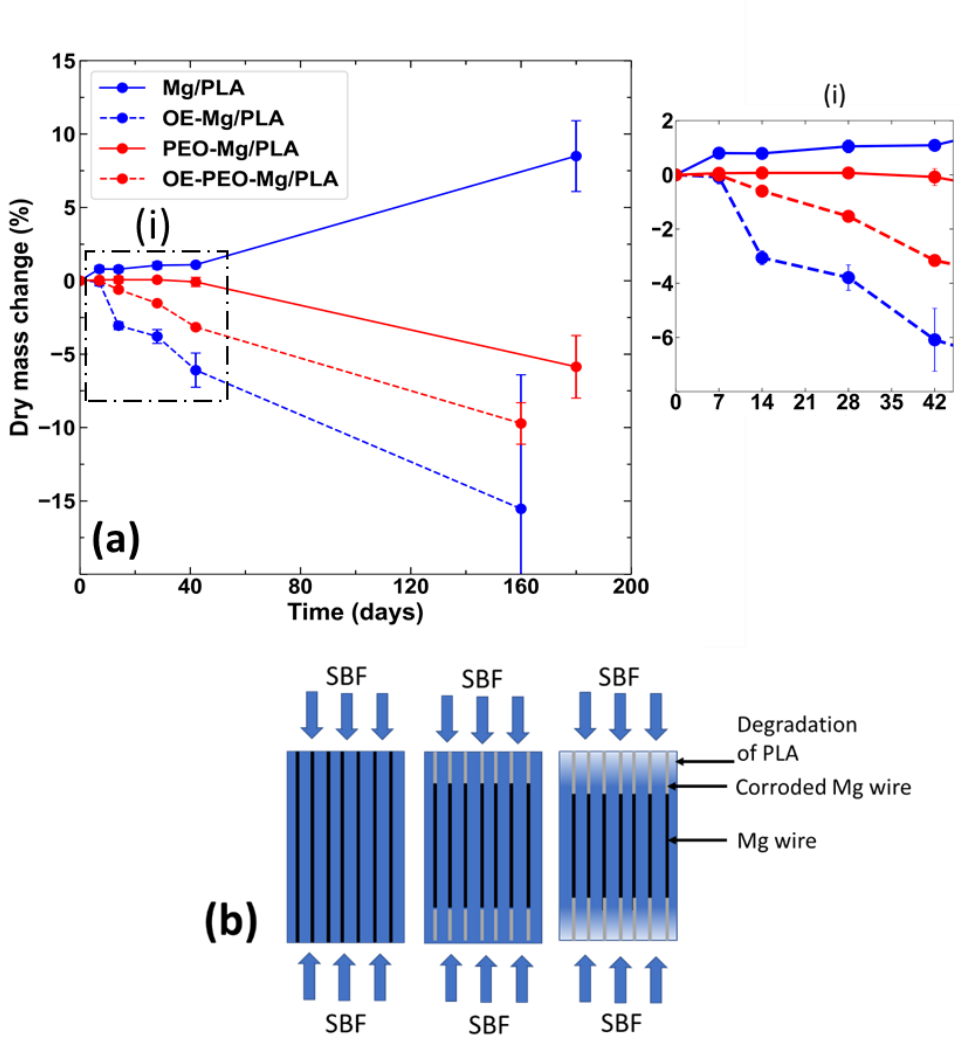

Fig. 5.6. (a) Evolution of dry mass of sealed and open edged (OE) Mg/PLA and PEO-Mg/PLA composites as a function of immersion time in c-SBF at 37 ^{o}C. (b) Schematic of accelerated degradation of PLA matrix from edges due to pipeline corrosion of Mg wires.

5.2.5. Degradation of interface strength

The load-displacement curves of the push-out tests on composites immersed in c-SBF during 7, 14, 28 and 42 days are plotted in Figs. 5.7a and 5.7b for Mg/PLA and PEO-Mg/PLA composites, respectively. The interface shear strength (calculated from peak load before first abrupt load drop) is plotted in Fig 5.7c as a function of degradation time. The interface shear strength of the Mg/PLA composite increased slightly after 7 days of immersion and then decreased up to 8.1 ± 2.1 MPa after 42 days. More interestingly, the stress necessary to push-out the wires (indicated by the plateau region after the drop from the peak load) increased with degradation time. The interface

strength of the PEO-Mg/PLA composite decreased with degradation time up to 13.6 ± 3.2 MPa after 42 days. The variation of the shear stress necessary to push-out the wires from the PLA matrix did not change with degradation time. The differences in stress necessary to push-out the wires after interface fracture between Mg/PLA and PEO-Mg/PLA can be associated with the interlock effect of the corrosion products around the wire in the former (Fig. 5.8a), which do not appear the in the latter (Fig. 5.8b). Overall, the PEO oxide layer on the Mg wires improved the shear strength retention and toughness of the interface during immersion in c-SBF.

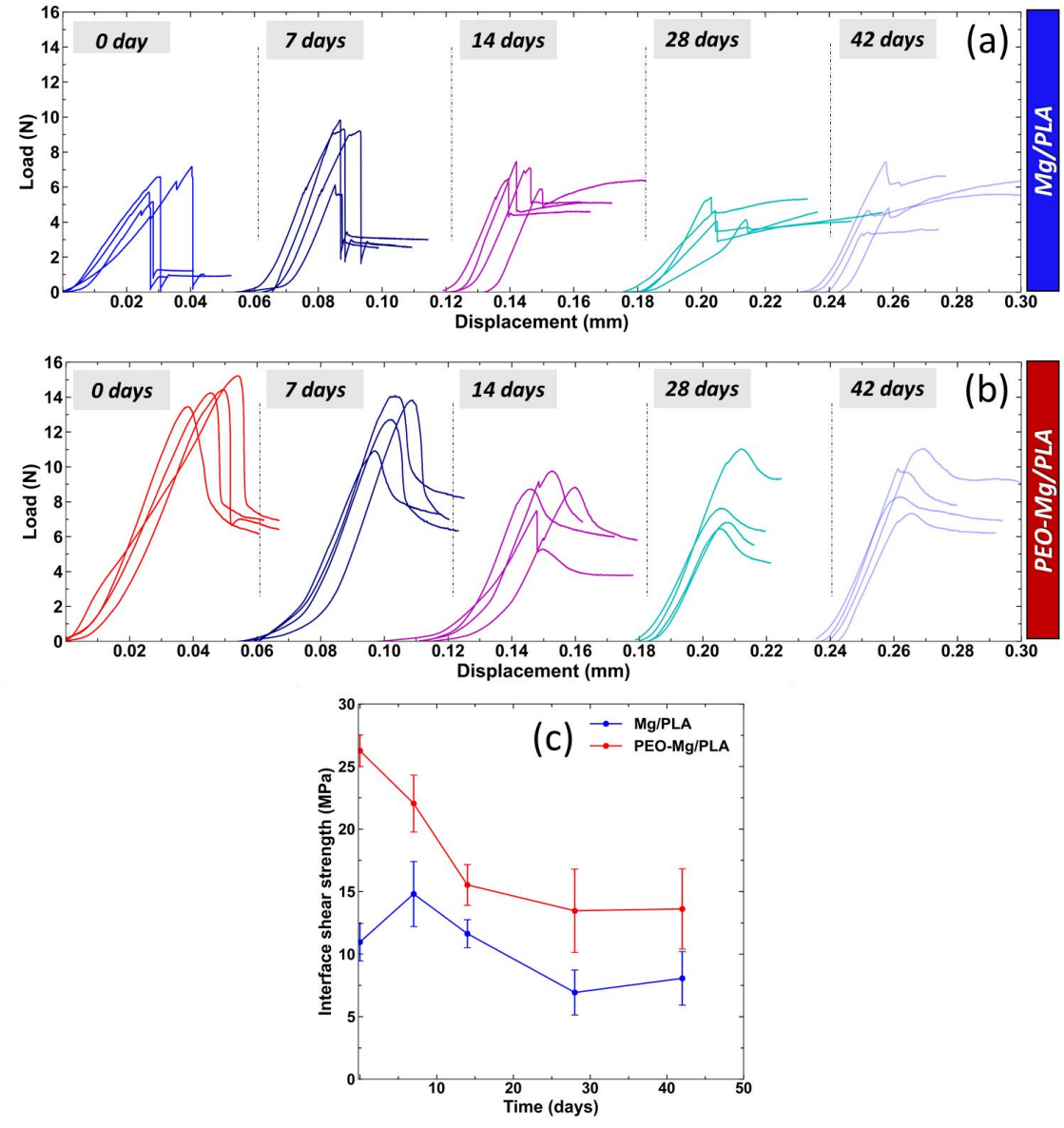

Fig. 5.7. (a) Load-displacement curves of the push-out tests after 0, 7, 14, 28, 42 days of immersion in c-SBF at 37 ºC for Mg/PLA composites. (b) *Idem* for PEO-Mg/PLA composites. (c) Influence of immersion time in c-SBF on the interface shear strength.

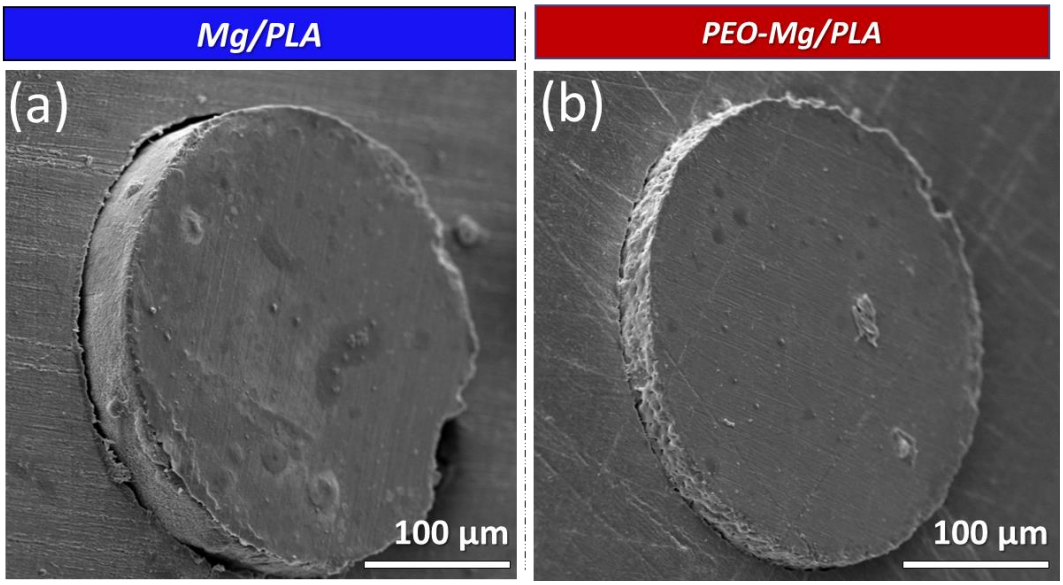

Fig. 5.8. (a-b) Secondary electron image of the bottom surface of the Mg/PLA and PEO-Mg/PLA interfaces after the push-out test after 42 days immersion in c-SBF at 37 ºC.

5.2.6. Degradation of mechanical properties of unidirectional composite lamina

Representative stress-strain curves of longitudinal tension, transverse tension and in-plane shear response of unidirectional Mg/PLA and PEO-Mg/PLA composites before and after 42 days of *in vitro* degradation in c-SBF are presented in Fig. 5.9a, 5.9b and 5.9c. The mechanical properties are summarized in Table 5.1. Macroscopic mechanical properties of unidirectional composite lamina degraded after 42 days of immersion due to the degradation of constituents of composite. Particularly, the strength of the wires and the interface shear strength decreased due to corrosion while the PLA matrix degraded at interfacial regions (see section 5.2.8 and 5.2.9).

Mg/PLA and PEO-Mg/PLA composites showed similar stress-strain response in longitudinal tension direction after 42 days of immersion in c-SBF and their elastic modulus decreased slightly from 10.7 GPa to 10 GPa and 11.2 to 10.65 GPa while strengths dropped to 81 and 75 MPa, respectively. Both composites exhibited brittle fracture at ~1.4 % strain. Fracture of the degraded composites was likely to be initiated by the shear failure of wire/PLA interface and followed by the propagation of the interface shear crack across the cross section in PLA matrix (Figs. 5.10). This explanation is supported by the reduction in the interface shear strength (Fig. 5.7c). Immediately after the fracture of PLA, most of the wires were also fractured between

PLA surfaces by different mechanisms. In Mg/PLA composite, wires were fractured at their smallest cross section (due to pitting corrosion), while most of PEO-Mg wires failed in the same plane in PEO-Mg/PLA composites (Fig. 5.10d and 5.10e) due to the strong bonding of PEO oxide layer with PLA which impeded the pullout.

Tensile properties of composites in transverse tension drastically decreased after 42 days (Fig. 5.9b). PEO-Mg/PLA composites presented slightly higher modulus and strength (2.2 GPa and 18 Mpa) as compared to Mg/PLA composites (1.8 Gpa and 16 Mpa). A corrosion layer was developed at the interface in Mg/PLA composites during c-SBF immersion (see section 5.2.8) which weakened the load transfer between wire and matrix and caused a significant drop in elastic modulus while only the degradation of the PLA matrix around PEO-Mg wires caused the drop in modulus in the PEO-Mg/PLA composites. Fracture of the composites in transverse tension was most likely to be initiated by interface debonding and cracking of PLA matrix [139]. Fracture of composite occurred at lower stresses because the wire/matrix interface was more prone to debond due to low interface strength in tension between the corrosion layer and PLA matrix, and also because the PLA matrix was weakened at the interface due to alkaline degradation.

In-plane shear properties of Mg/PLA and PEO-Mg/PLA composite decreased by 30 % after 42 days of degradation in c-SBF at 37ºC and the shear modulus and shear strength decreased to 1 GPa and 18 MPa, respectively (Fig. 5.9c). Probably, the degradation of PLA matrix near interfacial regions of Mg wires favored the yielding the PLA matrix between Mg wires laminas at lower loads as compared to the as-processed condition.

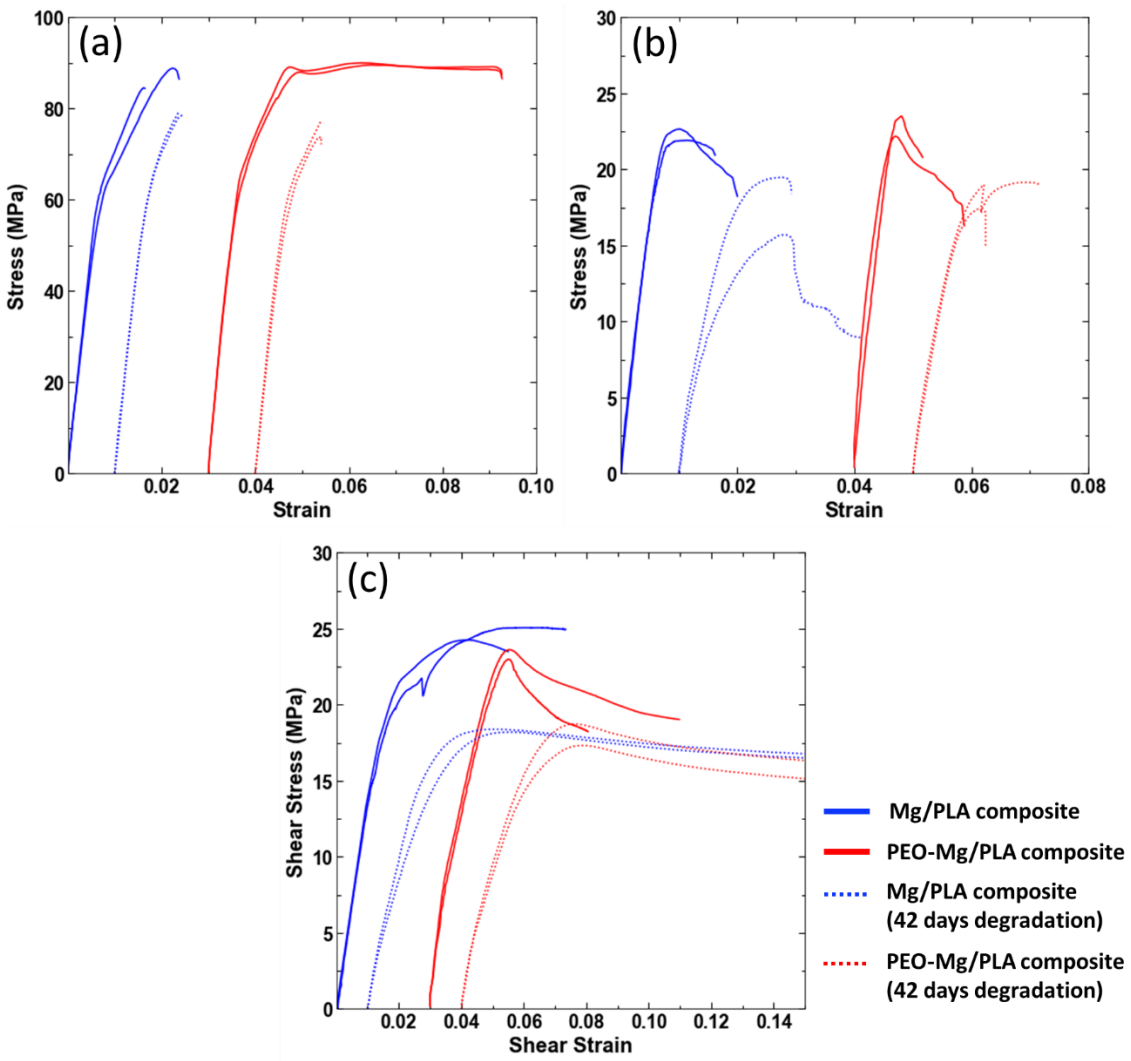

Fig. 5.9. (a) Representative stress-strain curves of unidirectional Mg/PLA and PEO-Mg/PLA composites before and after 42 days of degradation in c-SBF at 37ºC in longitudinal tension, (b) *Idem* in transverse tension and (c) *Idem* in-plane shear.

Table 5.1. Mechanical properties of unidirectional Mg/PLA and PEO-Mg/PLA composites before and after 42 days of degradation in c-SBF.

Mechanical property	Mg/PLA composite		PEO-Mg/PLA composite	
	0 day	42 days	0 day	42 days
Longitudinal elastic modulus - E_{11} (GPa)	10.7 ± 1.0	10.0 ± 0.3	11.2 ± 0.3	10.7 ± 0.6
Poisson's ratio - v_{12}	0.34	0.30	0.34	0.34
Longitudinal tension - X_t (MPa)	85.6 ± 4.1	81.7 ± 2.2	91.5 ± 4.6	75.7 ± 4.0
Transverse elastic modulus - E_{22} (GPa)	4.2 ± 0.3	1.8 ± 0.2	4.3 ± 0.5	2.2 ± 0.1
Transverse tension - Y_t (MPa)	24.3 ± 3.0	16.3 ± 2.9	23.3 ± 4.0	18.2 ± 1.3
In-plane shear modulus - G_{12} (GPa)	1.4 ± 0.1	1 ± 0.1	1.6 ± 0.2	1 ± 0.1
In-plane shear strength - S_{12} (MPa)	24.9 ± 2.5	18.5 ± 0.3	23.9 ± 1.7	18 ± 0.7

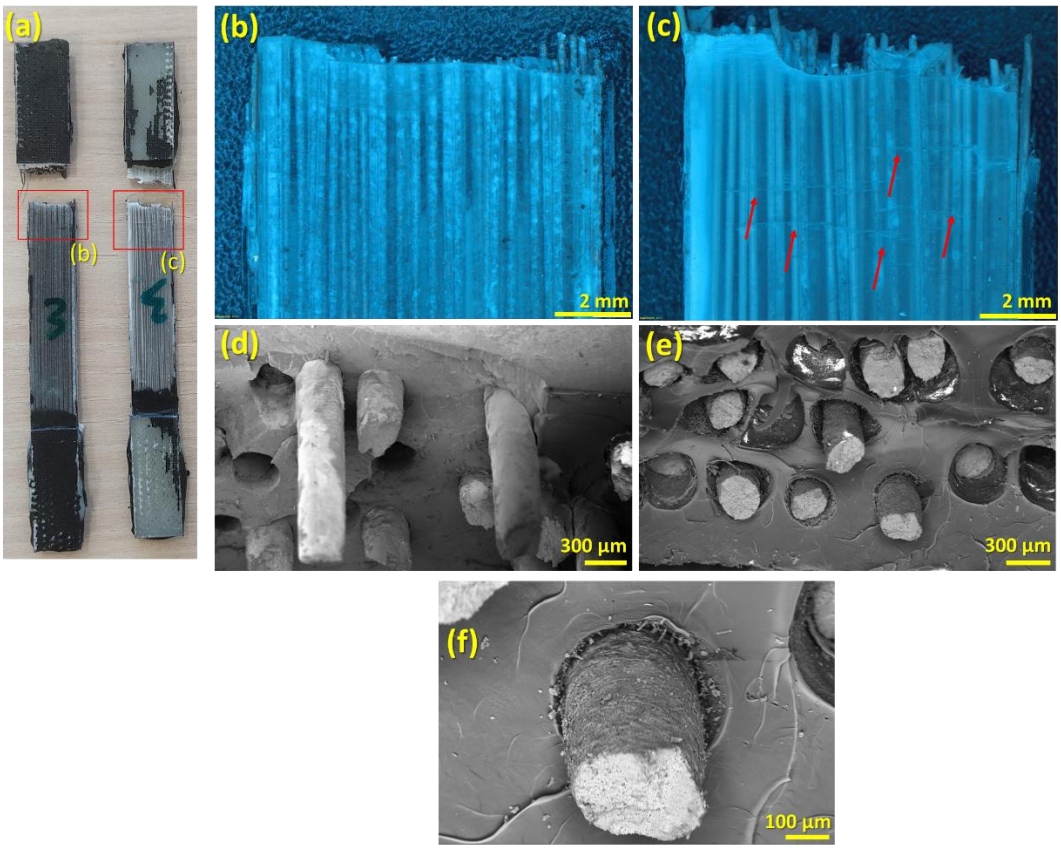

Fig. 5.10. (a) fractured samples of degraded Mg/PLA and PEO-Mg/PLA composites in longitudinal tension. Optical image of fractured surface in longitudinal tension of (b) Mg/PLA and (b) PEO-Mg/PLA composite where red arrows show transverse cracks in the PLA matrix. Back-scattered SEM image of the fracture surface of Mg/PLA composite deformed in tension along the wires after 42 days in c-SBF at 37ºC., (b) *Idem* of PEO-Mg/PLA composites and (c) *Idem* enlarged view of fractured PEO-Mg wire

5.2.7. Degradation of mechanical properties of quasi-isotropic composite lamina

Representative stress-strain curves of quasi-isotropic composite lamina after 42 days of immersion in c-SBF at 37ºC are shown in Fig. 5.11 along with curves of as-processed composites. Both Mg/PLA and PEO-Mg/PLA composite showed similar tensile properties after degradation, with elastic modulus and strength of approximately 4.5 GPa and 37 MPa, respectively. Quasi-isotropic laminate of PEO-Mg/PLA composites showed higher ductility as compared to Mg/PLA in the as-processed condition due to high toughness in the longitudinal direction of unidirectional laminates. However, this beneficial effect was lost after 42 days of *in vitro* degradation because the ductility in longitudinal tension of Mg/PLA and PEO-Mg/PLA composites was similar after degradation.

Failure mode quasi-isotropic composites switched from abrupt fracture of PLA matrix by a single crack (as-processed condition) to multiple cracking along the gage length (after degradation) of composites as shown in Figs. 5.12a and 5.12c. The condition of the PEO-Mg wires in different laminas was analyzed in more detailed in the fractured regions in the SEM (Fig. 5.12c to 51.2g). The PEO-Mg wires oriented at 0^o were fractured and the PEO oxide layer was cracked (Fig. 5.12e). PEO-Mg wires oriented at 90^o and 45^o remained intact after fracture. The PEO oxide layer remained intact in wires oriented at 90^o (Fig. 5.12f) while several cracks can be observed in oxide layer of wires oriented at 45^o due to pull-out of wires by shear (Fig. 5.12g).

Elastic constants obtained from testing of unidirectional composites after 42 days of degradation (Table 5.1) were used as input in classical laminate theory (CLT) [147] to predict the modulus of quasi-isotropic laminate after 42 days. It provided reasonable predictions, as shown in Table 5.2. Therefore, elastic constants obtained from unidirectional tests can be reliably used to design the stacking sequence to achieve desired elastic modulus of Mg/PLA composites not only in intact conditions but also after degradation in c-SBF at 37ºC.

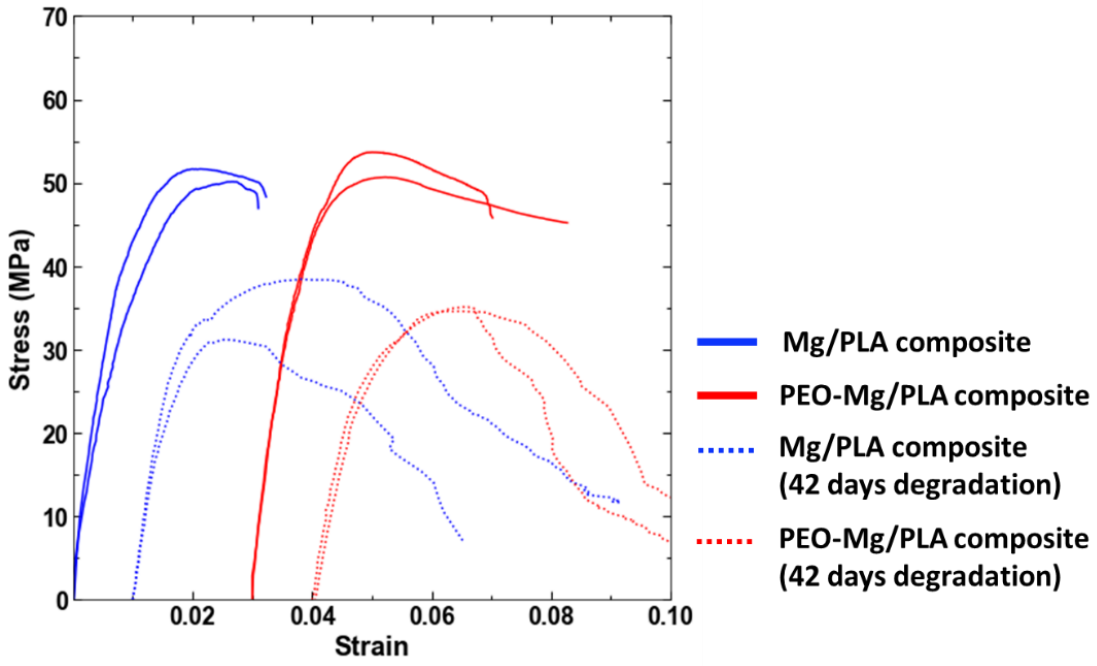

Fig. 5.11. Representative stress-strain curves of quasi-isotropic laminate $[0^o/90^o/\pm45^o]_s$ of Mg/PLA and PEO-Mg/PLA composites during the tensile test before and after 42 days of degradation in c-SBF at 37ºC.

Table 5.2. Tensile properties of quasi-isotropic laminate $[0/90/\pm45]_s$ of Mg/PLA and PEO-Mg/PLA composites before and after 42 days of degradation in c-SBF at 37ºC.

Mechanical property	Mg/PLA composite		PEO-Mg/PLA composite	
	0 day	42 days	0 day	42 days
Elastic modulus (GPa) - E_q	5.3 ± 0.05	4.6 ± 0.1	5.4 ± 0.4	4.4 ± 0.0
Theoretical Elastic Modulus (GPa) calculated by Classical Laminate Theory	5.6 – 6.6	4.5 – 4.9	6.0 – 6.9	4.9 – 5.4
Tensile strength (MPa) - S_q	52.1 ± 2	34.6 ± 3.1	52 ± 1.5	32.7 ± 7

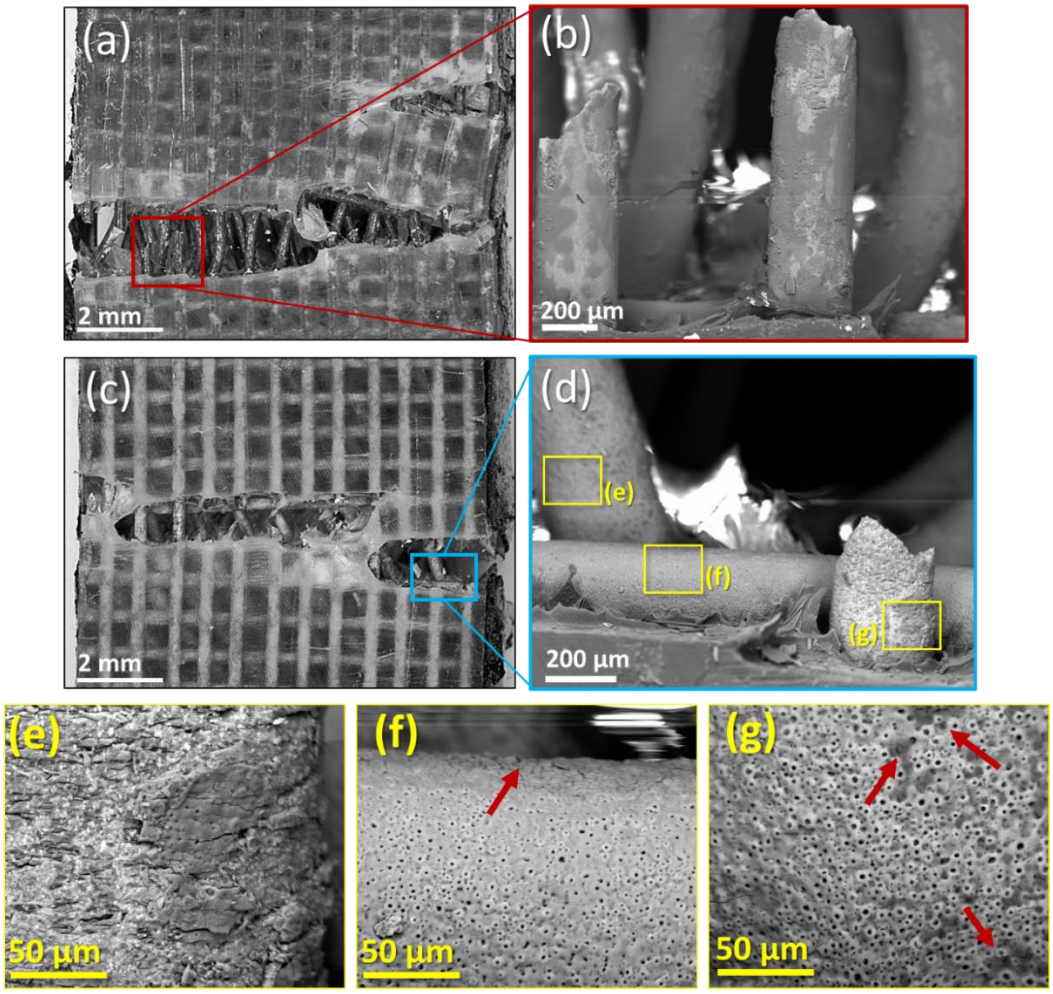

Fig. 5.12. Optical images of quasi-isotropic laminates deformed in tension of (a) Mg/PLA and (c) PEO-Mg/PLA composites. Enlarged back-scattered SEM image of fractured surfaces of (b) Mg/PLA and (d) PEO-Mg/PLA composites. Enlarged back-scattered SEM images of PEO-Mg wires laminas oriented at (e) 0º, (f) 90º and (g) 45º showing the condition of PEO oxide layer after fracture of PEO-Mg/PLA composite. Red arrows point towards corrosion of the outer surface of PEO oxide layer after 42 days of immersion in c-SBF at 37ºC.

5.2.8. Corrosion mechanisms at Mg/PLA interface

The corrosion of Mg wires (with and without PEO surface modification) directly exposed to c-SBF was analyzed in detail in section 3. It was concluded that –in the absence of a PEO oxide layer– pitting corrosion was accelerated by the presence of chlorine ions and led to the fast corrosion of the wires which significantly deteriorated their mechanical integrity within only 24 hours. On the contrary, pitting corrosion was suppressed by the PEO oxide layer due to the formation of a dense corrosion layer containing O, Ca and P beneath the PEO oxide layer, while still on top of the typical porous oxide layer resulting from the progressive oxidation of Mg to form $Mg(OH)_2$. The dense corrosion layer slowed down the diffusion of chlorine ions, limiting pitting corrosion and enhancing the mechanical integrity of the wires, whose strength was still above 100 MPa after 96 hours in c-SBF.

In the case of the Mg/PLA composites, corrosion of Mg wires began when water molecules and chlorine ions quickly diffused (< 1 day) into the PLA matrix and reached the wire surfaces. It is generally accepted that the primary corrosion reaction for magnesium involves the hydrogen evolution reaction (HER) [33]

$$Mg + 2H_2O \rightarrow 2Mg(OH)_2 + H_2 \uparrow \quad (2)$$

but the role of the oxygen reduction reaction (ORR)

$$Mg + 2H_2O + O_2 \rightarrow 2Mg(OH)_2 \quad (3)$$

cannot be ruled out, and it was pointed out recently in several studies that reported less hydrogen collection (~ 40%) than expected during bio-corrosion of magnesium [151] [153]. In particular, Wang et al. [34] reported that the contribution of ORR to the total cathodic process was up to 16.5% during the slow corrosion of high-purity Mg [155]. The limited amount of hydrogen released (as compared with the theoretical one) during the degradation of our composite samples seems to indicate that the ORR played an important role.

The $Mg(OH)_2$ layer formed during corrosion can react with chlorine ions, leading to soluble $MgCl_2$ and OH^- ions according to

$$Mg(OH)_2 + 2Cl^- \rightarrow MgCl_2 + 2OH^- \quad (4)$$

and allowing the ingress of corroding fluids to the Mg wire surface. $MgCl_2$ (where Mg^{2+} can be dissociated) and OH^- ions can react with the PLA by-products or diffuse outside the PLA matrix into the c-SBF solution according to several studies [65][45][99]. As a result, the formation rate of $Mg(OH)_2$ on the Mg wires was higher than the dissolution rate and a thick $Mg(OH)_2$ layer was formed on the wire surface (Fig. 5.13a). This layer was neither dense nor continuous due to the localized chlorine attack, still allowing the progress of the wire corrosion. Moreover, the corrosion layer expanded inwards and outwards due to the increase in volume associated with the oxide formation and subjected the PLA around the wire to tensile hoop stresses. These tensile stresses were large enough to promote the cracking of PLA around wires in our previous study on the corrosion of Mg/PLA interfaces with wires of 100 μm in diameter, following a theoretical model [21]. The same model predicts that the corrosion layer around the Mg wires of 300 μm in diameter (Fig. 5.13b) was not thick enough to promote PLA cracking. Instead, the interaction of OH^- ions with the polymeric chains in an alkaline environment facilitated the progressive hydrolysis and retreat of PLA.

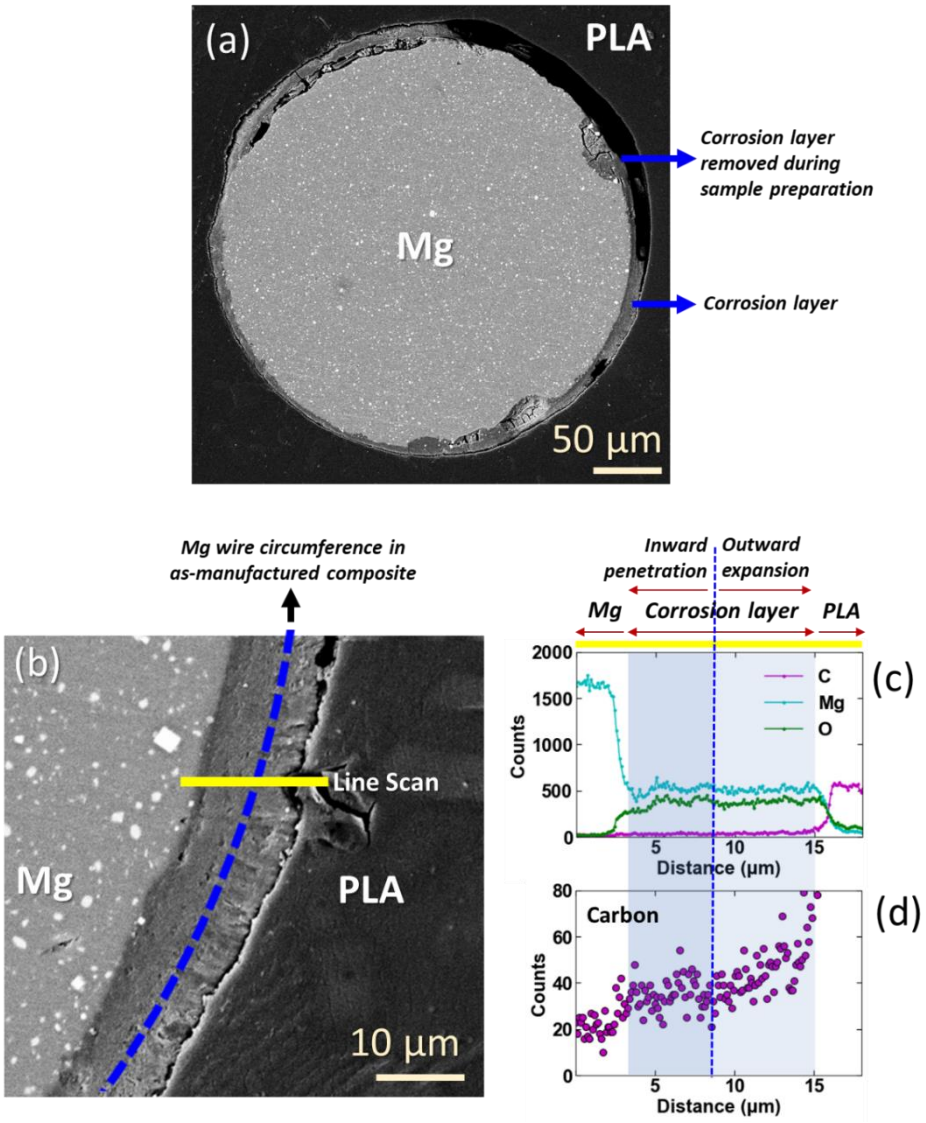

Fig. 5.13. Back-scattered electron images of the (a) cross-section of corroded Mg wire inside PLA matrix of composite after 42 days of *in vitro* degradation, (b) Detail of the corrosion layer at higher magnification. (c) and (d) EDX analysis along the yellow line in (b) shows the elemental composition in Mg, O and C. The blue shaded region shows the width of corrosion layer.

The possible degradation mechanisms of PLA are presented in Fig. 5.14 [156][157]. Hydrolysis of PLA chains in neutral or acidic environments takes place by cleavage of ester bonds into two chains having carboxylic and alcohol end groups (Fig. 5.14a). However, PLA degrades much faster in alkaline environment [156] which is most likely to be the cause of degradation of PLA at the interface of Mg wires because the pH can increase up to 10 near the corrosion layer of Mg [152]. Vaid et al. [33] reported rapid degradation of PLA fibers at a pH value of 10 compared to neutral (pH value 7.4) and acidic (pH values 2 and 3) environments. Therefore, high pH at the interface of the

corrosion layer can accelerate alkali-assisted hydrolytic degradation of PLA by possible mechanisms of intra-chain (Fig. 5.14b) [156] and end-chain scissions (Fig. 5.14c) [157]. During intra-chain scission, OH^- ions hydrolyze PLA chains by randomly attacking the carbonyl group of esters, resulting in two smaller chains with an alcohol end group. While in end-chain scission, OH^- ions attack the carbonyl group nearest to the alcohol end group of PLA chain and form a six-membered lactide ring which converts into 2 molecules of lactic acid after further hydrolysis. Lactic acid is highly soluble in water and, therefore, can diffuse out of the PLA matrix and/or remain with water at the interface or in bulk PLA.

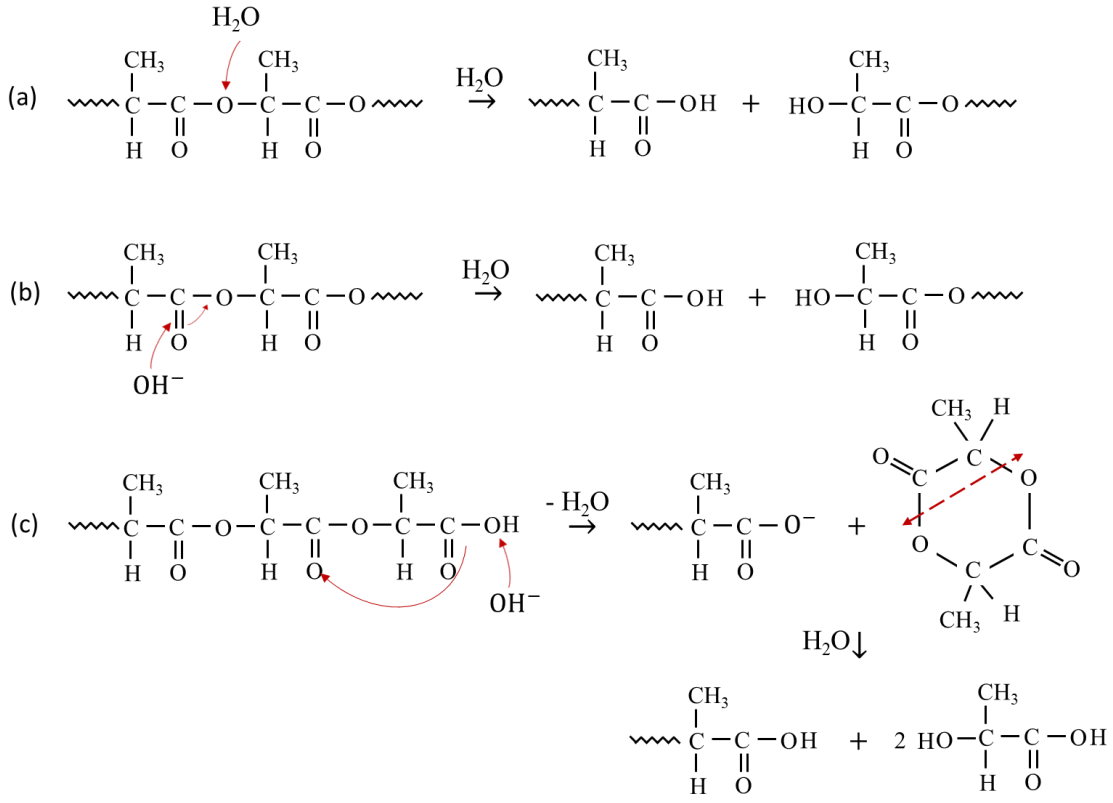

Fig. 5.14. (a) Hydrolysis degradation of PLA in neutral and acidic environments. (b) Hydrolysis of PLA in alkaline environments through intra-chain. (c) *Idem* through end-chain attack by hydroxyl ions [156][157].

The elemental analysis by EDX along the corrosion line in Fig. 5.13b is plotted in Fig. 5.13c. It shows the presence of Mg and O, confirming the formation of $Mg(OH)_2$ as a main corrosion product. Low amounts of carbon were also detected (Fig. 9d) and the concentration increased with the distance to the surface of the Mg wire, revealing the interaction of PLA degradation products with corrosion products of the Mg wires. The

C source could be lactic acid, a by-product of the alkaline hydrolysis of PLA (Fig. 5.14b and 5.14c), or magnesium acetate formed after the reaction of Mg with -COOH released by hydrolysis of PLA according to [158][159].

$$Mg^{2+} + 2R - COOH \rightarrow (R - COOH)_2 Mg + 2H^+ \quad (5)$$

The completely corroded Mg wire inside the PLA matrix is shown in Fig. 5.15. The initial cross-section of the Mg wire is depicted with a dashed blue line. It shows that Mg wire expanded by the accumulation of corrosion products and the physical retreat of the PLA matrix. EDX maps confirm that corrosion products are made of $Mg(OH)_2$ while there are some carbon-rich (dark) regions indicating the presence of some PLA matrix not being fully degraded. It should be noted that traces of Ca and P (that are present in c-SBF) were not found in the corrosion products of the Mg wire even after complete degradation. They are typically found in the corrosion layer when Mg wires are directly exposed to c-SBF [50], but the PLA matrix stopped the penetration of Ca^{2+} and PO_4^{3-} ions towards the wire surface [159].

Interface shear strength between Mg wire and PLA matrix is dictated by the corrosion mechanisms at the interface. The strength increased from 10.9 MPa to 14.8 MPa after 7 days of *in vitro* degradation due to the accumulation of corrosion products at interface (expansion of corrosion layer) which increased the compressive normal stresses at interface. Soon, PLA also started to retreat by physical degradation due to the combination of alkali-assisted hydrolytic degradation and tensile hoop stresses. The retreat of PLA relaxed the compressive normal stresses at interface which caused the gradual reduction of interface shear strength with immersion time. This corrosion layer also deteriorated the macroscopic mechanical properties due the formation of a weak interface between the corrosion layer and PLA matrix and the degradation of the PLA matrix at the interface.

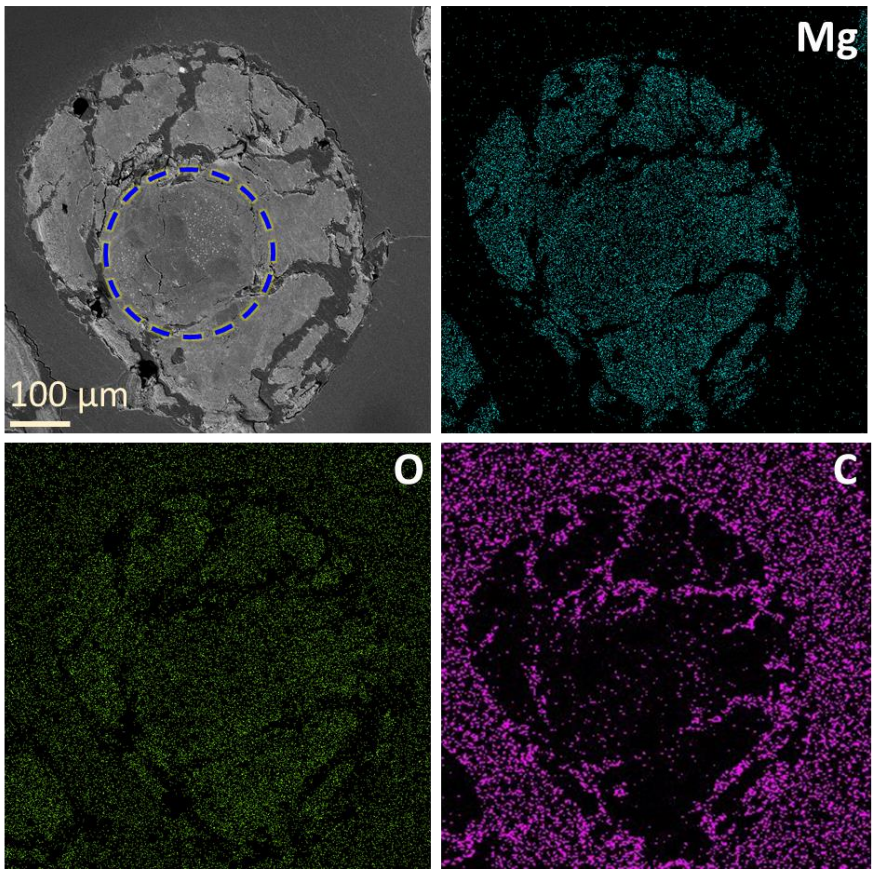

Fig. 5.15. Back-scattered electron image of the cross-section of a completely corroded Mg wire in Mg/PLA composite after 180 days of *in vitro* degradation. The spatial distribution of Mg, O and C obtained by EDX is plotted in the adjacent figures. The dashed blue lines indicates the initial Mg wire cross-section.

5.2.9. Corrosion mechanisms at PEO-Mg/PLA interface

The corrosion mechanisms at PEO-Mg/PLA interfaces after 42 and 180 days of immersion in c-SBF are depicted in the back-scattered electron images in Figs. 5.16 and 5.17, respectively. Corrosion of the Mg wire core was very limited, even after 180 days of immersion, because corrosion products filled the cracks and pores in the PEO oxide layer and blocked the diffusion of water. The PEO oxide layer did not show corrosion after 42 days and only slight corrosion after 180 days. Since there is no corrosion layer growth outside the PEO oxide layer, the PLA matrix was not subjected to tensile stresses associated with the volumetric expansion induced by corrosion. Thus, the degradation of the PLA after 42 days of immersion was very limited (Fig. 5.16b) and likely to occur by alkali-assisted hydrolytic degradation (Fig. 5.14b and 15.14c) caused by slight corrosion of Mg wires beneath the PEO oxide layer. However, the

degradation-affected zone of the PLA matrix around the interface was noticeable after 180 days (Fig. 5.17a). PLA in this region became softer due to degradation and leached out during the sample preparation. Overall, the physical degradation of PLA at the PEO-Mg/PLA interfaces was very mild in comparison with the Mg/PLA interfaces (Fig. 5.15).

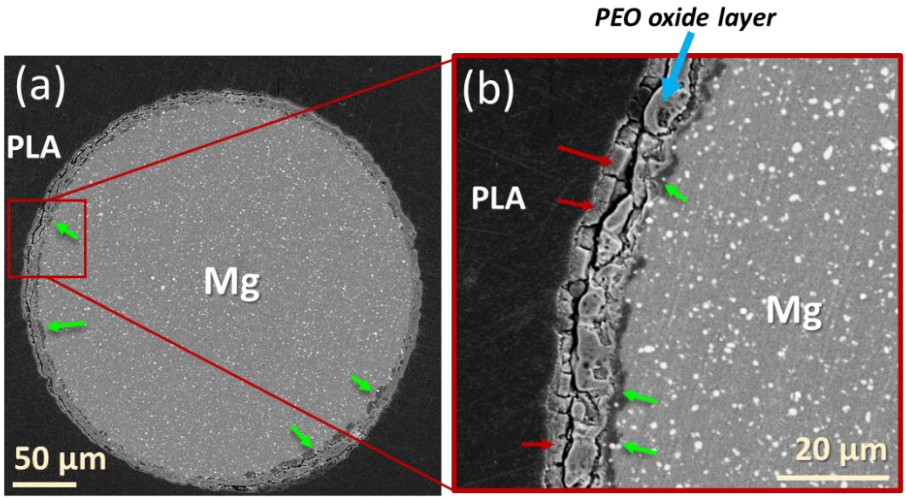

Fig. 5.16. (a) Back-scattered electron image of the cross-section of corroded PEO-Mg wire in PEO-Mg/PLA composite after 42 days of *in vitro* degradation. (b) Higher magnification image of the interface region. Red arrows show degradation of PLA matrix, while green arrows show the corrosion of Mg wires below the PEO oxide layer.

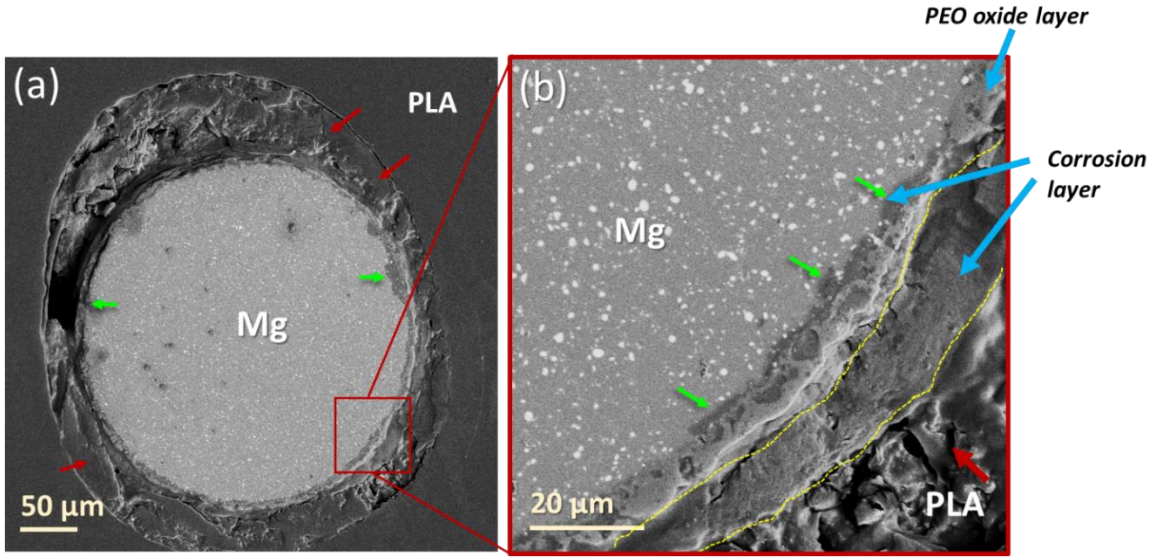

Fig. 5.17. Back-scattered electron image of the cross-section of corroded PEO-Mg wire in PEO-Mg/PLA composite after 180 days of *in vitro* degradation. (b) Higher magnification image of the interface region. Red arrows show degradation of PLA matrix which was very soft and leached out during grinding process while green arrows show corrosion of Mg wires below PEO oxide layer.

The PEO oxide layer was porous and contained micro-cracks [55]; therefore, water and chlorine ions could reach the Mg wire by diffusion through the PLA matrix and pores/cracks of the oxide layer, leading to initial corrosion according to eq. (2), (3) and (4). However, further corrosion of the Mg wire cores was suppressed because corrosion products filled the cracks and pores, blocking water diffusion. The PEO oxide layer did not show corrosion after 42 days and only slightly after 180 days since it is mainly composed of MgO and $Mg_3(PO_4)_2$ which are sparingly soluble in water and slow diffusion of water through the PLA matrix provided additional protection. However, MgO is less stable than $Mg_3(PO4)_2$ in an aqueous solution of Cl^- ions [160]. Therefore, the corrosion of PEO oxide layer proceeded to form $Mg(OH)_2$ through the reaction of MgO with water, according to [131]

$$MgO + H_2O \rightarrow Mg(OH)_2 \quad (6).$$

This reaction disturbed the structure of the PEO oxide layer and might cause minor degradation of $Mg_3(PO4)_2$ as shown by small traces of P in the corrosion layer (Fig. 5.18), but most of the PEO oxide layer remained intact (Fig. 5.17) since PO_4^{3-} can neither diffuse out nor penetrate in PLA matrix [159]. The EDX maps of the interface region in Fig. 5.18 also confirmed the presence of P in the PEO oxide layer. At the same time, a corrosion layer was developed below the PEO oxide layer and also outwards. It was mainly formed by $Mg(OH)_2$ with small traces of C and P.

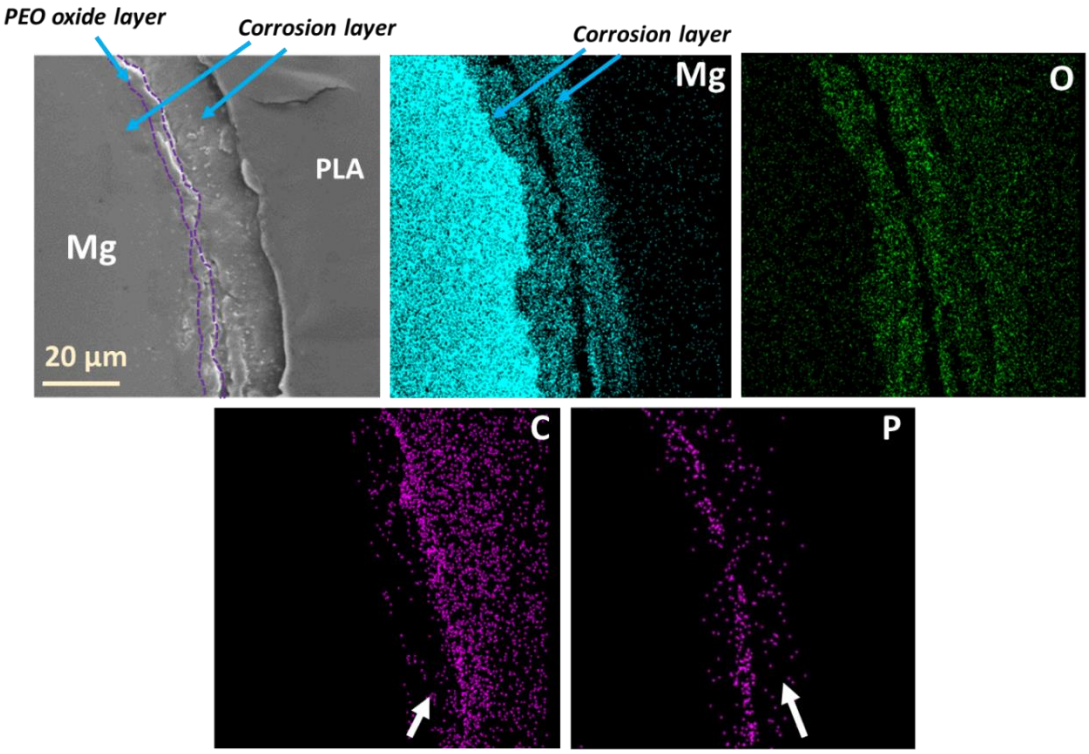

Fig. 5.18. SEM and EDS maps of enlarged view of corroded PEO-Mg wire in PEO-Mg/PLA composite after 180 days of *in vitro* degradation, (b) *Idem* enlarged view. White arrows points to traces of C and P in the corrosion layer developed outside PEO oxide layer.

Hence, the proposed corrosion mechanism also explains and confirms the trend observed in the reduction of interface shear strength of PEO-Mg/PLA composite. The strength never increased with immersion time (as opposed to the initial behavior in Mg/PLA) because the PEO oxide layer suppressed the corrosion of Mg wires and did not allow accumulation of corrosion products after 42 days (Fig. 5.16b). These mechanisms also indicated that the sharp drop of interface shear strength till 14 days was most likely due to the degradation of PLA present in pores of the PEO oxide layer as PLA ligaments were not observed in the pores of pushed-out wires (Fig. 5.8b). Afterwards, the gradual decrease of strength could be attributed to the slight physical degradation of PLA at the interface (Fig. 5.16). Overall, PEO surface modification improved the interfacial performance between Mg wires and PLA matrix in as-manufactured as well as in degraded conditions by protecting the Mg wires from corrosion. However, the macroscopic mechanical properties of PEO-Mg/PLA composite deteriorated after 42 days of immersion in c-SBF at 37ºC, mainly due to the degradation of PLA matrix at the interfacial regions.

5.3. Conclusions

The mechanical behavior and degradation mechanisms of Mg wire/PLA and PEO-Mg wire/PLA composites were studied after immersion in simulated body fluid at 37ºC up to 180 days. Immersion in simulated body fluid reduced the shear strength of the interface even though the shear strength of the interfaces comprising of PEO oxide layer was always higher. The proposed degradation mechanisms for Mg/PLA and PEO-Mg/PLA composites explain and confirm the effect of PEO on the corrosion protection of the Mg wires during immersion in fluids. They reduce to degradation of the Mg wires (less hydrogen) but also of the surrounding PLA matrix. In the absence of a PEO oxide layer, corrosion was triggered by the degradation of the Mg wires, which led to the formation of a corrosion layer that grew inwards and outwards. At the same time, PLA retreated by physical degradation accelerated by the tensile hoop stresses induced by the expansive corrosion layer. Mg wires were completely corroded after 180 days of immersion in simulated body fluid. On the contrary, the PEO oxide layer efficiently suppressed the corrosion of Mg wires (only 3 % mass loss after 180 days) and limited the degradation of the PLA matrix at the interfaces.

The degradation behavior of composites with exposed (open edge OE) and sealed edges was also compared. It was found that direct exposure of Mg wires accelerated the degradation of composite but PEO modification slowed down this effect by protecting wires from lateral corrosion.

The corrosion mechanism at the interface were found be in agreement with the degradation of interfacial shear strength and mechanical properties of unidirectional and quasi-isotropic composites. Although interface shear strength in PEO-Mg/PLA composites was higher after 42 days of immersion, this effect was not reflected in macroscopic mechanical response (during 42 days) as both Mg/PLA and PEO-Mg/PLA composites showed similar properties. Tensile properties decreased slightly in the longitudinal direction and the elastic modulus was 10 GPa after 42 days of *in vitro* exposure. However, the properties in transverse tension and in-plane shear deteriorated faster. Quasi-isotropic laminates $[0^o/90^o/\pm45^o]_s$ were able to provide modulus of 4.5 GPa (higher than PLA) and strength of 37 MPa after 42 days of *in vitro* tests and the modulus prediction using classical laminate theory agreed with experimental observations even in degraded conditions. Therefore, mechanical properties of

unidirectional composites in as-manufactured and degraded conditions can be reliably used to design the suitable stacking sequence to achieve optimized mechanical properties. Moreover, PEO surface modification provides an opportunity to tailor the degradation rate of Mg/PLA composites.

CHAPTER 6: BIOLOGICAL RESPONSE OF COMPOSITES

The modified strategy to manufacture Mg/PLA composite laminates enabled the production of high-quality unidirectional and multi-directional composite laminates with and without PEO-modified Mg wires. Composites had higher mechanical properties than pure PLA, sufficient for many orthopedic fixation device applications and can be tailored by stacking the sequence of Mg wire laminas. During *in vitro* degradation, the mechanical properties of the composite decreased but still suitable retention of mechanical properties was achieved even after 42 days of immersion in simulated body fluid (SBF). PEO modification of wires slowed down the corrosion of Mg wires inside PLA matrix and suppressed hydrogen gas release. In summary, processing, and mechanical and degradation characterization of composite has been discussed in previous chapters, showing the potential of Mg/PLA composites in orthopedic implant applications. However, concerns about the biological safety of composite need to be resolved. Therefore, this chapter aims to study the cytotoxicity, proliferation and differentiation of Mg/PLA and PEO-Mg/PLA composites compared to medical-grade PLA by different indirect and direct assays to check the biological performance.

6.1.Experimental techniques

6.1.1. Materials

In vitro biological assays were performed on pure PLA coupons, Mg/PLA and PEO-Mg/PLA composites. PLA coupons were manufactured by hot pressing of pellets at 180 ºC while unidirectional Mg/PLA and PEO-Mg/PLA composite were manufactured by the process described in section 2.2 with dimensions of 120 mm x 12 mm x 2 mm and wire volume fraction of 20%. Samples were cut perpendicular to wire direction to achieve the desired dimensions for each test to fulfill the sample surface area to medium volume ratio requirements. The surfaces generated by machining were grinded successively up to 1200 sandpaper. Nevertheless, machining exposed wires from the edges of the lamina and the samples were used without sealing the edges to study biocompatibility. Before the biological assay, samples were cleaned in ethanol in an ultrasonic bath for 2 minutes and dried in air.

6.1.2. Indirect cytotoxicity assessment by MTT assay

The biocompatibility of the PLA, Mg/PLA and PEO-Mg/PLA composite samples was tested following ISO 10993-5 [161] and 10993-12 [162]. Indirect tests were carried out using pre-osteoblasts from the cell line MC3T3-E1 Subclone 4 (ATCC-CRL-2593) that were grown in a complete culture medium consisting of alpha MEM medium (Invitrogen, USA), supplemented with 10% of fetal bovine serum (FBS) (Invitrogen, USA), and 1% penicillin/streptomycin (Invitrogen, USA). Samples were first immersed in 70 % ethanol for 20 min and air-dried. Then, extracts for the indirect tests were obtained by immersion of the samples (3 cm^2/ml) in the complete culture medium, followed by incubation for 72 h at 37°C. Afterward, samples were removed and extracts were collected in centrifuge tubes for further studies.

Viability and proliferation of cells was assessed by MTT assay. For this purpose, MC3T3-E1 cells were seeded with 5,000 cells/cm^2 density in three 96-well plates and incubated for 24 h at 37°C in an atmosphere with 5% CO_2 concentration and 95% relative humidity. Then, culture medium was replaced with original and diluted extracts (50%, 25%, 12.5% and 6.25%) in all three well-plates and incubated for 24 h, 48 h and 72 h. Plates were taken out after 24 h, 48 h, and 72 h and mitochondrial activity of the cells was measured by conversion of MTT (3-(4, 5-dimethyl thiazolyl-2)-2, 5-diphenyltetrazolium bromide) (Sigma-Aldrich, Germany) into formazan. MTT was prepared in a concentration of 5 mg/ml in PBS and added to the cells in a proportion of 10 µl of MTT stock solution by 100 µl of culture medium. Then culture plates were incubated for 3 h protected from light. After that, formazan crystals were dissolved by adding dimethyl sulfoxide (DMSO) (Sigma-Aldrich, Germany), and the absorbance of the solutions was measured at 570 nm in a spectrophotometer (Tecan Infinite Mplex). Mitochondrial activity (%) was calculated according to Eq. 6.1. Cells were grown in culture medium in wells dedicated for positive control. The experiments were performed in triplicates for each sample and data was analyzed by average values along with standard deviation.

$$Mitochondirial\ activity\ \% = \frac{absorbance\ value\ of\ extract}{absorbance\ value\ of\ control} \times 100 \qquad (6.1)$$

6.1.3. Preparation of cell culture plates for direct tests

The direct interaction of pre-osteoblast (MC3T3-E1) with the surfaces of PLA and the composites was studied by SEM and immunofluorescent assays (actin staining and Live/Dead test). Cell interaction was studied on longitudinal (only PLA) and cross-sectional surfaces (PLA and Mg wires) in the case of composite samples, as shown schematically in Fig. 6.1. PLA and composite samples were cut with dimensions of 5 mm x 12 mm x 2 mm and placed in a 24 well-plate lying flat while composites for the interaction of cells with cross-sectional surfaces were placed perpendicular to wire direction. Samples were immersed in 70 % ethanol for 20 minutes and air-dried. Then cells were added in each well with a density of 20,000 cells/cm^2 for SEM observation and phalloidin/DAPI staining while 10,000 cells/cm^2 for Live/Dead assays and incubated at 37°C in a humidified 5% CO_2 atmosphere for 1 h and 24 h.

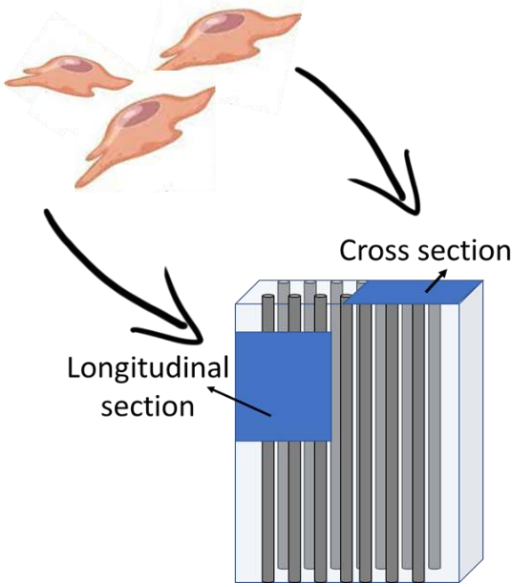

Fig. 6.1. Schematic of cell seeding on longitudinal and cross-sectional surface of unidirectional composites. On longitudinal surface, cells will interact with only outer surface of PLA matrix while cells with both Mg and PLA on cross-sectional surface.

6.1.4. Direct cytotoxicity assessment by Live/Dead assay

Live/Dead assay (Invitrogen, USA) identifies cell viability immunofluorescence staining in which the live cells are stained in green (by Calcein-AM) and dead cells are stained in red (by Ethidium) are dead cells. Fresh cells (non-fixed) after 24 h of seeding were washed with DPBS solution (with Ca and P) (Gibco). Then, a mixture of 4 μM Calcein-AM and 2 μM Ethidium homodimer-1 diluted in DPBS (with Ca and P) was

added to each well and incubated for 20 min at 37 °C. Afterwards, samples were properly mounted and imaged in a confocal microscope (Olympus FV3000, Japan) at 10x magnification. Cells cultured directly in well plates were used as positive controls (live cells), while for the negative control (dead cells), cells were lysed by 9 % Triton X-100 and then stained.

6.1.5. Cell morphology and cell-material interaction

The interaction between the cells and longitudinal and cross-sectional surfaces of the composites was observed by SEM. Well plates were taken out after 1 h and 24 h, cells washed in PBS and fixed in 4% PFA solution for 15 min. Fixed cells were dehydrated by serial immersion in ethanol/H_2O solutions with increasing concentrations (30%, 50%, 70, 80%, 90%, and 100%) of ethanol for 10 minutes each. Samples having fixed and dehydrated cells on its surface were carefully attached to pin mounts of SEM with carbon tape. Afterwards, samples were coated by gold sputtering and analyzed in a SEM at an accelerated voltage of 5~10 kV to study the morphology and interaction of cells with the surface of the materials.

Cell morphology was also analyzed using immunofluorescent staining in which cells were first fixed by 4 % PFA and then washed with PBS. Then cytoskeleton of the cells was labelled with phalloidin Alexa 488 (1:300) (Invitrogen, USA) and nucleus with DAPI (1:3000) (Sigma-Aldrich, Germany). For this purpose, cell were treated with 0.1% Triton X-100 for 10 min to permeabilize the cell membranes. Then, cells were washed with PBS and stained with Alexa 488 and DAPI in solution of PBS and incubated for 1 h in solution of PBS at room temperature. Finally, samples were observed under the confocal microscope (Olympus FV3000, Japan).

6.1.6. Preparation of extracts and cell culture plate for differentiation assays

The effect of PLA, Mg/PLA and PEO-Mg/PLA composites on the bone differentiation of pre-osteoblasts MC3T3-E1 was analyzed by RT-qPCR, ALP activity, and alizarin red staining. Extracts of samples were prepared in differentiation medium having the following composition: α-MEM medium (Invitrogen), 10% FBS (Invitrogen), 1% penicillin/streptomycin (Invitrogen), 50 µg/mL ascorbic acid (Sigma Aldrich), 0.1 µM dexamethasone (Sigma Aldrich), 10 mM beta- glycerophosphate (Sigma Aldrich). For extract preparation, PLA and composite samples were first sterilized in 70 % ethanol

for 15 minutes and dried. Then samples were immersed in a differentiation medium keeping a surface area ratio of 3 cm^2/ml, and then incubated for 72 h at 37°C in a humidified 5% CO_2 atmosphere. Afterward, samples were removed, extracts were passed through 0.22 µm sterile syringe filter to remove any debris and stored in centrifuge tubes at 4 ºC until its use.

MC3T3-E1 pre-osteoblasts cells were seeded in 12 wells (for RT-qPCR), 24 wells (for ALP activity) and 48 wells (for alizarin red staining) cutlure-plates dedicated for 7 and 14 day of differentiation of cells. For this purpose, cells were initially cultured at a density of 3,000 cells/cm^2 in complete culture medium (α-MEM + 10% FBS + 1% penicillin/streptomycin). After one day, the culture medium was replaced with fresh differentiation medium (for control wells) and extracts prepared in differentiation medium. The respective culture mediums were then replaced after every 3-4 days.

6.1.7. RT-PCR testing

Cell expression of the MC3T3-E1 pre-osteoblasts after 7 and 14 days in the differentiation culture medium was quantified to evaluate the effect of the degradation products of PLA and composites on the differentiation in bone linage. The osteogenesis-related genes [65][163], were alkaline phosphatase ALP, runt-related transcription factor 2 (Runx2), osteocalcin (OCN), type I collagen (Col1A1). These genes were studied by using real-time polymerase chain reaction (RT-PCR). Cells cultured for 7 and 14 days in control and extracts (duplicates) were collected in lysis buffer containing β-mercaptoethanol (Fisher Scientific) and homogenized by passing the lysate through a 20-gauge needle at least 10 times following RNeasy® Mini Kit (Qiagen) instructions for RNA isolation, and stored at -80 °C until analysis. After RNA isolation, purity and quantity was evaluated using the NanoQuant Plate in a microplate reader (TECAN Infinite 200 Pro). The same amount of RNA was used for reverse transcription following QuantiTect Reverse Transcription kit (Qiagen) instructions. The real-time PCR was performed using the RealQ Plus 2x Master Mix Green (Isogen) in a StepOnePlus™ Real-Time PCR system (Applied Biosystems). Primers (IDT) used are listed in Table 6.1. After activation of the polymerase at 95 °C for 15 min, 40 cycles of denaturation-extension were performed at 95 °C for 20 s and 60 °C for 1 min, followed by melting curve analysis. The results were analyzed by the $\Delta\Delta C_T$ method using GAPDH as housekeeping gene.

Table 6.1. Sequences of primer pairs used for PCR analysis.

Gene	Forward 5' → 3'	Reverse 5' → 3'
ALP	GCCTTCTCATCCAGTTCGTAT	CAAGGACATCGCATATCAGCTA
Col1A1	CATTGTGTATGCAGCTGACTTC	CGCAAAGAGTCTACATGTCTAGG
OCN	CTTTCTGCTCACTCTGCTG	TATTGCCCTCCTGCTTGG
Runx2	CCGTCCACTGTCACTTTAATAGC	GTAGCCAGGTTCAACGATCTG
GAPDH	AATGGTGAAGGTCGGTGTG	GTGGAGTCATACTGGAACATGTAG

6.1.8. Alkaline phosphatase (ALP) activity assay

ALP is a representative enzymatic protein of bone differentiation and is an early stage marker of differentiation MC3T3-E1 pre-osteoblasts [164][165]. To determine ALP activity, first well-plates were taken out after 7 and 14 days of culture in differentiation media of control and extracts. Medium was removed and washed twice with PBS followed by adding 0.1% Triton X-100 to lyse cells and then plates were stored at -80 °C. Plates were taken out from freezer and thawed to room temperature. The medium of each well (in triplicates) was mixed by pipetting in and out several times and then transferred in a 1.5 ml tubes for centrifuging at 13.000 rpm, at 4°C for 5 min. Supernatant of each tube which was carefully transferred to new tube for further analysis of samples. BCA Pierce^{TM} protein assay kit (ThermoFisher Scientific) was used to determine intracellular total protein content in samples where Albumin protein content in PBS was used to get the standard curve for relationship between absorbance (at 562 nm wavelength) and total protein content from 0 µg/ml to 2000 µg/ml. To determine ALP activity of each sample, 100 µl of each sample was added in 96 well-plate followed by addition of 100 µl of ALP reagent containing p-nitrophenyl phosphate (p-NPP) (Sigma Aldrich) which turned the solution to yellow color by reacting with ALP. The yellow color intensity depends on the amount of ALP protein quantified in the plate reader (Tecan Infinite Mplex) by absorbance at 405 nm of wavelength. Finally, ALP activity of each samples was normalized with respect to the corresponding total protein content. Each sample was analyzed by triplicate.

6.1.9. Mineralization testing by Alizarin Red staining

Alizarin Red staining was used to visualize calcium deposition by MC3T3-E1 pre-osteoblasts after 7 and 14 days in culture in presence of the extracts of the materials. After 7 and 14 days, cells were washed with DPBS and then fixed in 4% PFA solution for 15 min. Then cells were washed twice with DPBS and about 500 ul of Alizarin Red/H_2O solution (2 % w/v) was added to each well for 30 min and incubated at room temperature. Afterwards, the staining solution was removed and cells were washed several times with DI water. Finally, calcium deposits were observed as permanent red stains which were visualized in an optical microscope (AE31E, MOTIC) at 4x, 10x and 20x magnifications in three wells (triplicates) for each sample.

6.2.Results and discussion

6.2.1. Nature of material extracts prepared for indirect tests

The visual appearance of 100 % extracts after 72 h of immersion of samples in culture medium at 37 °C in humidified 5 % CO_2 environment is shown in Fig. 6.2. The nature of the extract is crucial to interpret the results of cytotoxicity and differentiation assays. The differences in appearance of the extracts are due to the change in pH which resulted from the release of degradation products of materials into medium. Normally, pH of α-MEM culture medium remains between 7.0 to 7.6 in 5 % CO_2 atmosphere [166] and manifests pink orangish color which is similar to the one of 100 % extracts of control and PLA. Although degradation products of PLA are acidic, their release rate was very small during 72 h and, therefore, pH and color of the extracts did not change and was similar to the control. In Mg/PLA composites, culture medium diffused into PLA matrix and started to corrode Mg wires, releasing Mg^{2+} and OH^- ions into the medium. OH^- ions increased the pH and turned the medium to purple. On the contrary, corrosion of wires was minimized in PEO-Mg/PLA composites due to the protection offered by PEO surface modification. However, Mg wires at the edges were directly exposed to the medium and were corroded. Corrosion rates of the Mg wires inside PLA matrix in SBF during the first 72 h were estimated by hydrogen gas evolution (Fig. 5.1), which revealed six times less hydrogen in case of PEO modification. Even though corrosion rates of Mg can be different in c-SBF and culture medium [167], it can be reliably assumed that PEO-Mg/PLA composites released much less Mg^{2+} and OH^- ions as

compared to Mg/PLA, leading to a slight purple color. Moreover, PEO-Mg/PLA composites might have also released small amount PO_4^{2-} ions into the medium due to direct corrosion of the PEO oxide layer present at the circumference of wires at the edges of the composite (Fig. 6.5b).

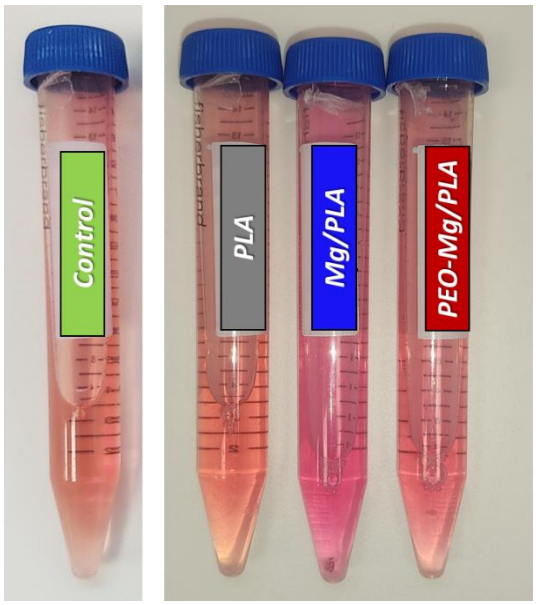

Fig. 6.2. Visual appearance of 100 % extracts prepared by immersing PLA, Mg/PLA and PEO-Mg/PLA composites for 72 h in normal culture medium. Control was prepared without any sample. Extracts prepared in differentiation medium also exhibited the same appearance.

6.2.2. Viability and proliferation of cells in material extracts

The mitochondrial activity (an indicator of cell viability) of the MC3T3-E1 pre-osteoblasts after 24 h of incubation in extracts was determined by MTT assay after immersion of PLA, Mg/PLA and PEO-Mg/PLA composites in the culture medium (Fig. 6.3a). None of the materials showed toxic behavior with 100 % and diluted extracts and this results confirmed that 20 % volume fraction of Mg wires (with and without PEO modification) in the composite did not compromise the biocompatibility of medical grade PLA. Mitochondrial activity in pure extracts was 100 %, 93 % and 99 % for PLA, Mg/PLA and PEO-Mg/PLA composites, respectively.

Proliferation of MC3T3-E1 cells was assessed by comparing the absorbance of purplish color (produced by formazan product during MTT assay) in wells of different samples (Fig. 6.3b). Cell proliferated at faster rate for the first 48 h and then remained stable or slightly increased between 48 h and 72 h, most likely due to the formation of a

monolayer in which cells had no more space to expand. PLA and composites showed comparable proliferation rates and their viability was always similar to the control, showing excellent proliferation of the cells in presence of the material extracts. Viability of MC3T3-E1 cells is known to drop below toxic level after 72 h when Mg ions concentration in the extract reach 15 mM [132] but this reduction was not observed in this study. More recently, Cai et al. [99] reported excellent viability and proliferation of MC3T3-E1 cells in extracts (having ~30 mM concentration of Mg ions) of Mg/PLA composites after 72 h., The volume fraction of PEO modified Mg wires in their study [99] was 10 vol. % and extracts were prepared with a composite surface area to medium volume ratio of 1.25 cm^2/ml. Our composites contained 20 vol. % of Mg wires (with and without PEO modification) and extracts were prepared with a composite surface area to medium volume ratio of 3 cm^2/ml which should have resulted in a higher concentration of Mg ions. Nevertheless, our Mg/PLA and PEO-Mg/PLA composites presented excellent cell cytocompatibility and proliferation.

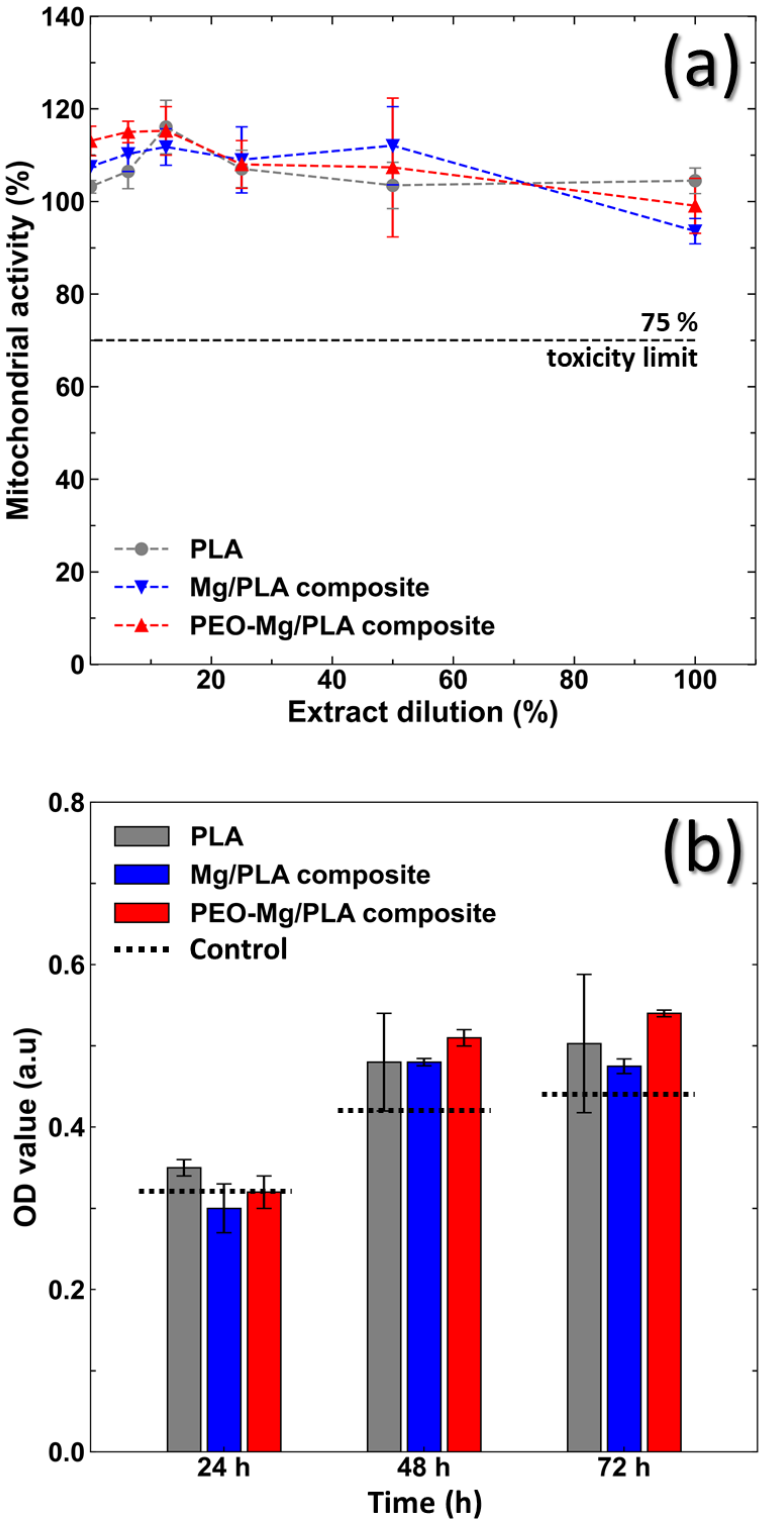

Fig. 6.3. (a) Mitochondrial activity assessed by MTT assay of the MC3T3-E1 pre-osteoblasts after 24 h of incubation in extracts obtained from PLA, Mg/PLA and PEO-Mg/PLA composites immersed in culture medium, (b) Proliferation of MC3T3-E1 pre-osteoblasts in 100 % extracts of materials assessed by MTT assay after 24h, 48h and 72h.

6.2.3. Adhesion and proliferation of cells on material surface

Adhesion and proliferation behavior of MC3T3-E1 cells on the surface of PLA, Mg/PLA and PEO-Mg/PLA composites were analyzed by SEM (Figs. 6.4 and 6.5) and fluorescent microscopy using Phalloidin/DAPI staining (Fig. 6.6) and Live/Dead assay (Fig. 6.7). After 1 h of seeding, cells started to adhere on the surface of PLA (Fig. 6.4a) and on the longitudinal surface of the composites (Figs. 6.4c, 6.4d and 6.6a). A cell can be seen extending its lamellipodia and filopodia structure in Figs. 6.5c and 6.6b. After 24 h of seeding, cells proliferated and covered most of the surface of PLA and of the longitudinal surface of the composites, as confirmed by SEM images in Figs. 6.4c, d and f. Cells were able to form a monolayer in most of the regions of PLA (Fig. 6.6c). Expanded (> 200 μm) and merged cytoskeleton of cells along with bridging filopodia structures among cells and surface can be observed on the surface of Mg/PLA (Fig. 6.6d) and PEO-Mg/PLA (Fig. 6.6e) composites which is evidence of good adhesion of cells. Live/Dead assay shows more cells on PLA than on Mg/PLA and PEO-Mg/PLA but the number of dead cells is negligible in all cases showing the excellent direct cytocompatibility of materials. Moreover, the Mg ions released by the composites into the medium during 24 h of immersion did not compromise the direct cytocompatibility, and all tests confirmed that the early adhesion (1 h) and initial proliferation (24 h) behavior of cells on the longitudinal surface of composite is similar to that on PLA and no toxicity was observed in any case.

MC3T3-E1 pre-osteoblasts were seeded on the cross-section of the composites for understating cell-material interaction when cells have a choice between Mg and PLA. This information is relevant because the fabrication of customized orthopedic plates of Mg/PLA composites by machining can expose Mg wires directly to body fluids, affecting the behavior of cells near the implant. After 1 hour of seeding, cells were moving away from the locations occupied by the Mg wires towards the PLA, irrespective of the presence of the PEO oxide layer (Figs 6.5a and 6.5b). Corrosion of Mg began as soon as it came in contact with the culture medium, leading to a near-surface increase in alkalinity and the release of hydrogen gas, and both phenomena triggered the migration of the cells to PLA regions. Cells on PLA regions could attach and proliferate rapidly, forming a monolayer to fully cover the surface after 24 h while avoiding the regions of Mg wires as shown by blue arrows in Fig. 6.5(e-f). However,

some cells migrated on regions of Mg wires after 24 h due to continuous proliferation and/or formation of passivation layer over Mg wire regions (Fig. 6.5e and 6.5f).

Live/Dead assay after 24 h of interaction of cells with cross-sectional surface of composites also showed that cells try to avoid regions of Mg wires and preferred attachment on regions of PLA matrix (Figs. 6.7f and g) but some cells successfully migrated back to the Mg wires due to the formation of a passivation layer which is a relatively stable environment as compared to the early degrading surface of Mg wire. Overall, the fraction of dead cells on the transversal cross-section is negligible, still proving the cytocompatibilty of the composites in general. Many cells were also found residing on the edge of Mg wires (yellow circles) to avoid direct contact with Mg. The behavior of cells on the cross-sections of the composites was similar irrespective of the PEO oxide layer.

Overall, the direct experiments showed that cells are not likely to proliferate on the surface of Mg wires. This results is relevant for the design of Mg/PLA composite implants as the final implant shape can be achieved by either machining from a parent plate (which exposes Mg wire cross-sections to the surface) or compression in molds with the final shape. This latter strategy (in which Mg wires) are encapsulated within the PLA matrix thus seems preferable from the biocompatibility viewpoint.

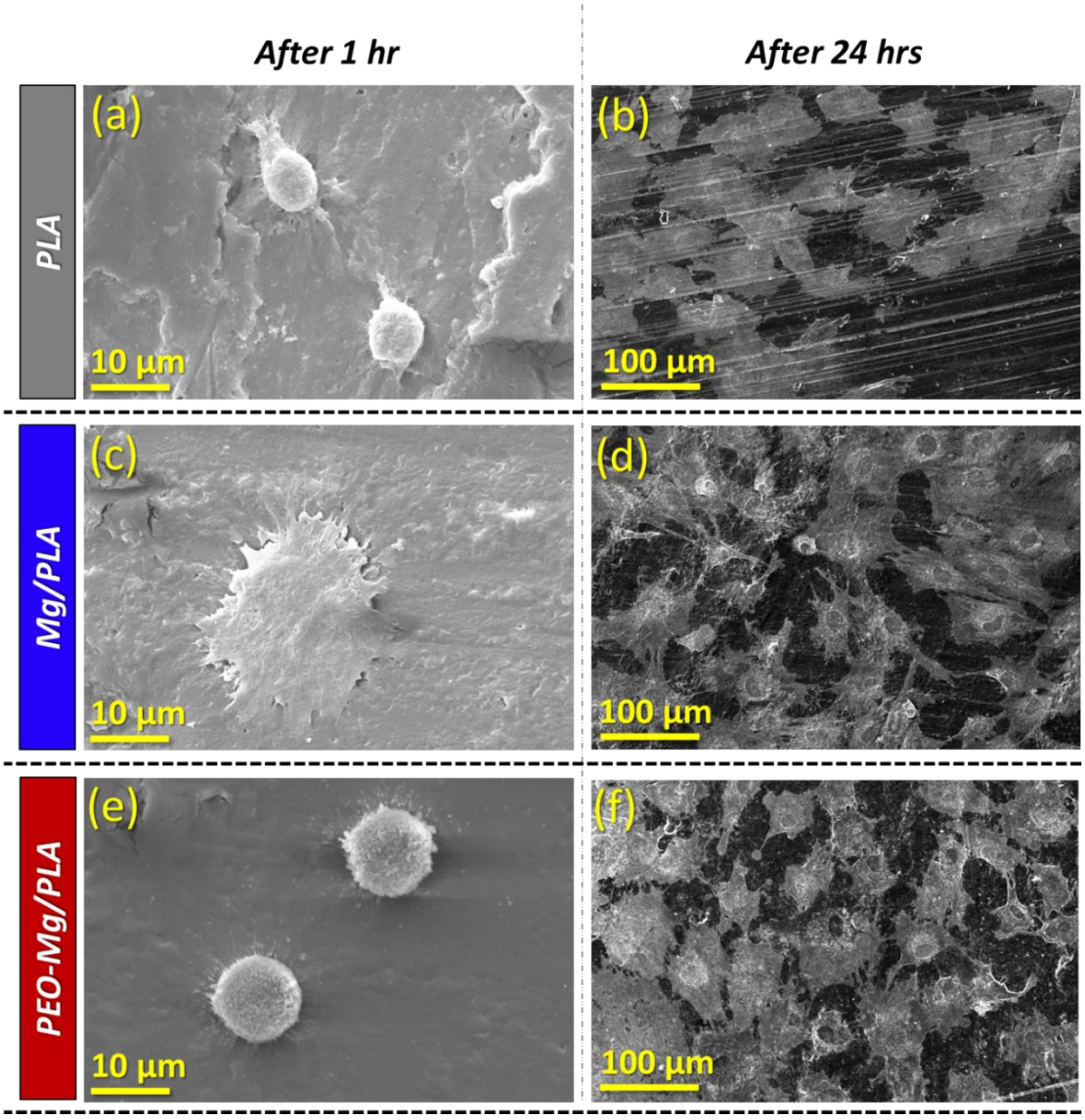

Fig. 6.4. (a, b) SEM images of interaction between MC3T3-E1 pre-osteoblasts and PLA surface after 1 h and 24 h of seeding the cells, (c, d) *Idem* longitudinal surface of Mg/PLA composite, and (e, f) *Idem* longitudinal surface of PEO-Mg/PLA composite.

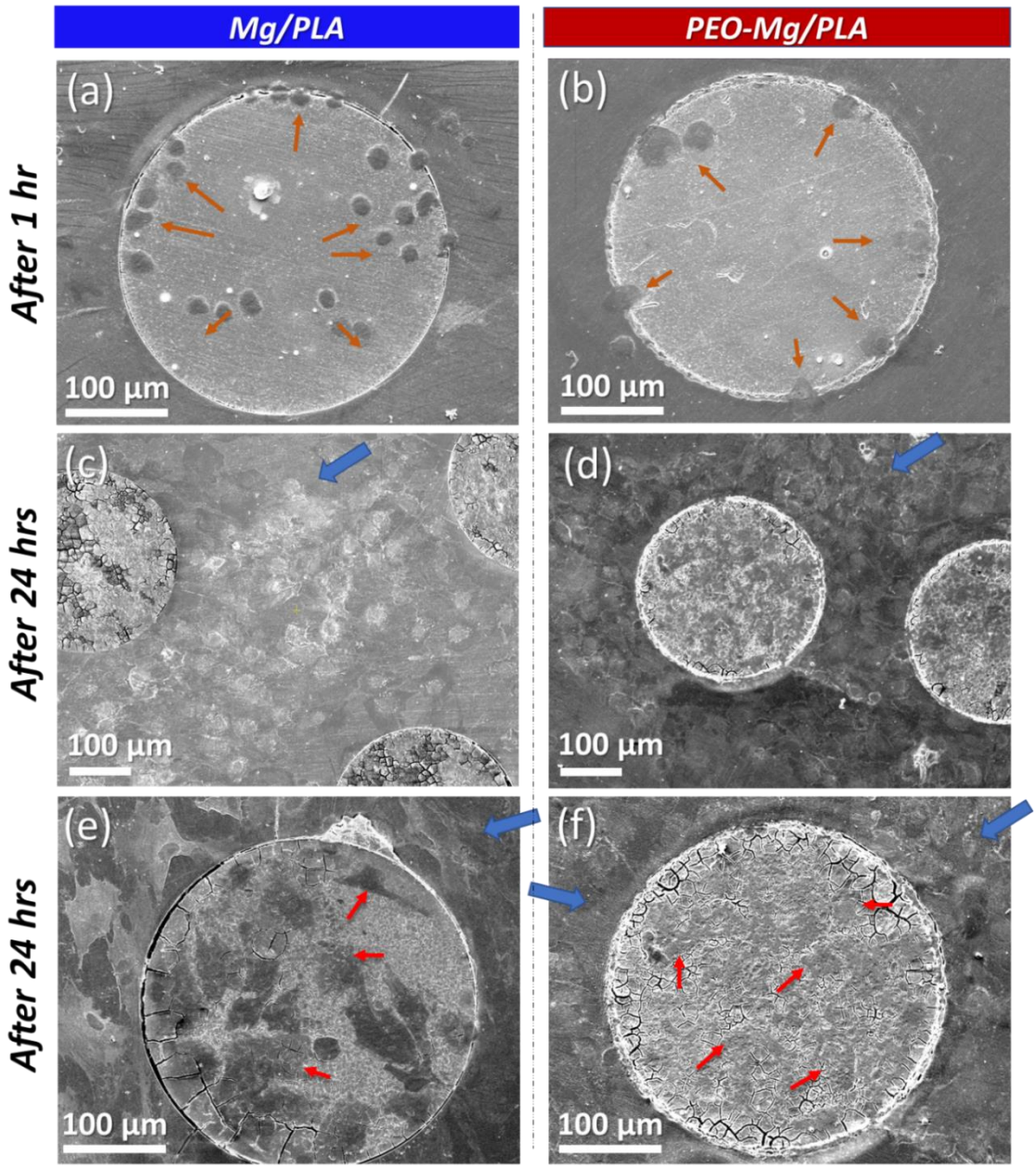

Fig. 6.5. (a, b) SEM images of MC3T3-E1 pre-osteoblasts on the cross-sectional surface of the Mg/PLA and PEO-Mg/PLA composites, respectively, after 1 h of seeding the cells. (c-d) *Idem* after 24 h of seeding the cells. Cells indicated with orange arrows tend to move away from Mg wires to PLA matrix. Thick blue arrows show the formation of a monolayer of cells between Mg wires. Red arrows show cells that are either dead or moved back to Mg wires after the formation of a passivation layer on top of the Mg wire cross-section.

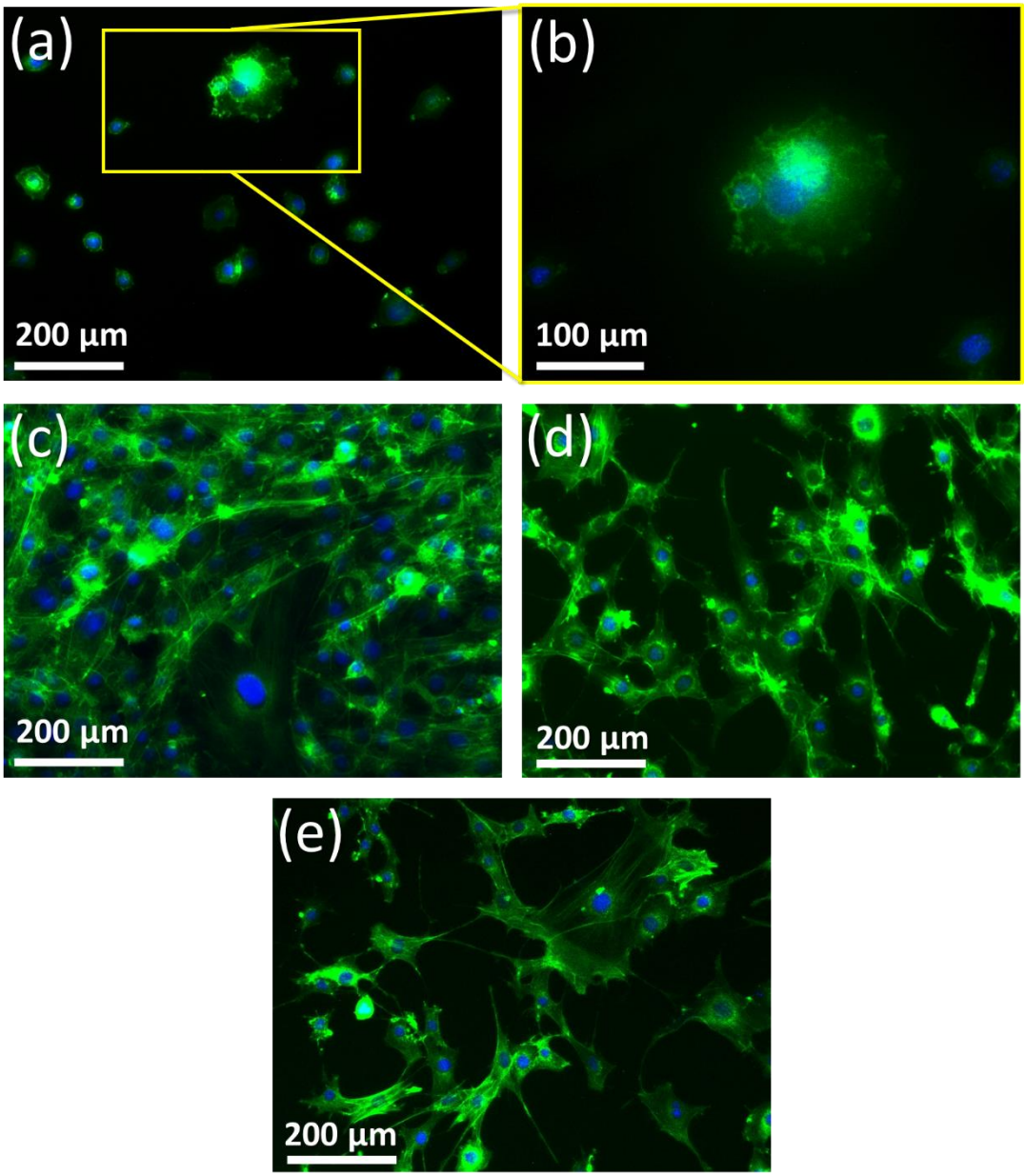

Fig. 6.6. (a) Confocal microscopy images of the surface interaction between MC3T3-E1 cells and longitudinal surface of Mg/PLA composite after 1 h, (b) Enlarged image of (a), (c) Confocal microscopy images of 24 h surface interaction between MC3T3-E1 cells and PLA, (d) *Idem* longitudinal surface of Mg/PLA composite and (e) *Idem* longitudinal surface of PEO-Mg/PLA composite. Green and blue colored regions represent the cytoskeleton and nucleus of cells stained with phalloidin and DAPI, respectively.

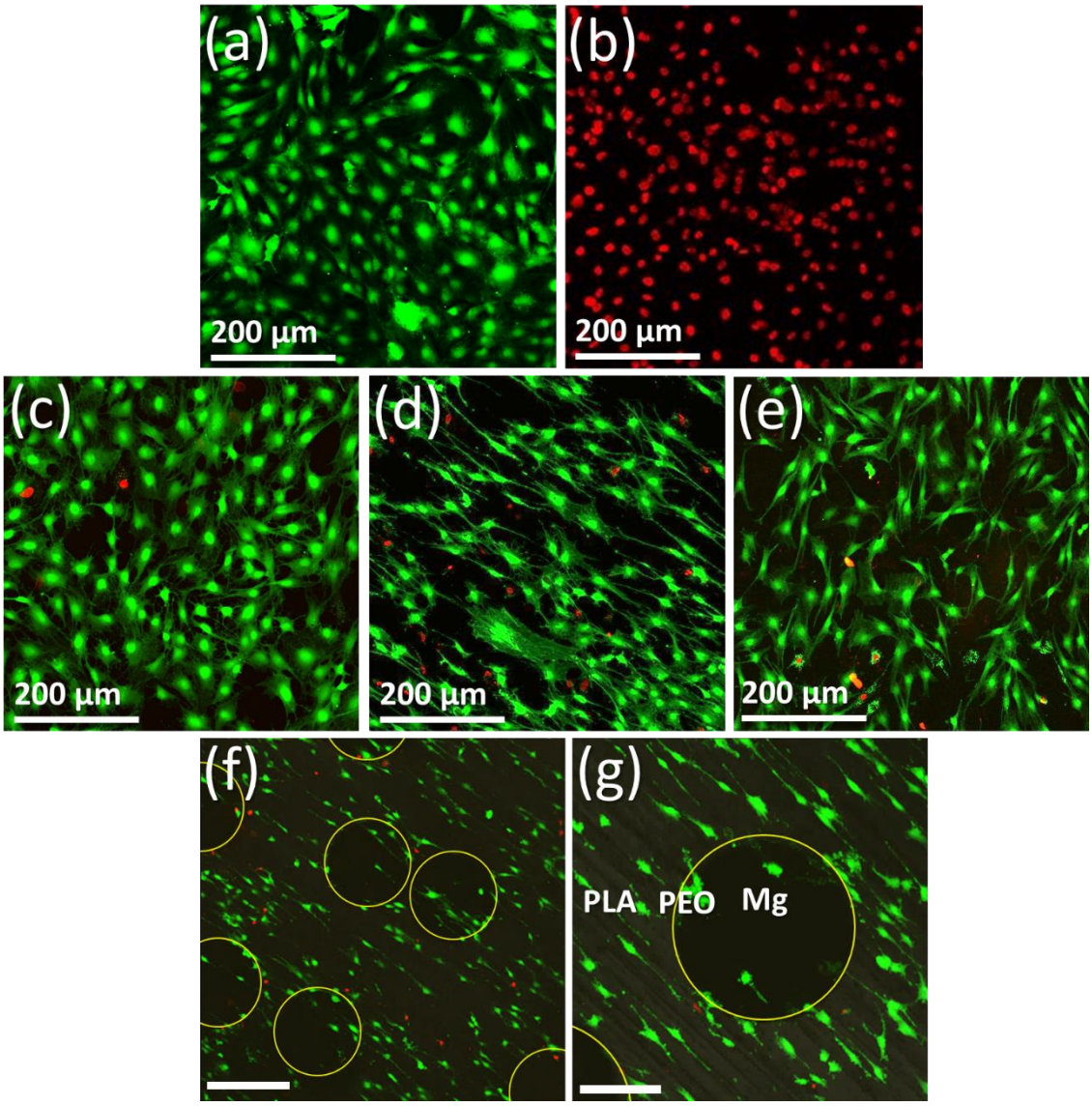

Fig. 6.7. Confocal microscopy images of MC3T3-E1 cells after 24 h in (a) positive control, (b) negative control, (c) surface of PLA, longitudinal surfaces of (d) Mg/PLA and (e) PEO-Mg/PLA composites. (f, g) Confocal microscopy images of MC3T3-E1 cells after 24 h of interaction with the transversal surface of PEO-Mg/PLA composite. Yellow circles show the position of Mg wires. Cells stained in green and red are live and dead, respectively.

6.2.4. Differentiation of cells in material extracts

The effect of PLA, Mg/PLA and PEO-Mg/PLA composites on the bone differentiation of MC3T3-E1 cells was measured by gene expressions using RT-PCR (Fig. 6.9), quantification of Alkaline Phosphatase (ALP) protein activity (Fig. 6.9) and mineral detection through Alizarin Red staining (Fig. 6.10), after exposure to the different material extracts during 7 and 14 days.

The relative mRNA expressions of genes (Runx2, OCN, Col1A1 and ALP) in MC3T3-E1 cells, which are indicators of bone differentiation, are shown in Fig. 6.8 after 7 and 14 days in extracts of PLA, Mg/PLA and PEO-Mg/PA composites. mRNA expression of Runx2, Col1A1 and ALP increased after 7 and 14 days in all extracts (Figs. 6.8a, c and d) while OCN remained at same level (Fig. 6.8b). These results confirms that MC3T3-E1 cells have not yet differentiated into mature osteoblasts after 14 days and are still pre-osteoblasts but in the differentiation phase as Runx2, Col1A1, ALP are expressed in the pre-osteoblast stage while OCN is expressed in mature osteoblast stage [168][169]. mRNA expressions of Runx2, ALP and OCN in PLA are similar to PEO-Mg/PLA composites suggesting that influence of Mg^{2+} ions and/or relatively high pH that were present in the extracts of Mg/PLA composite. Particularly, ALP expression of Mg/PLA composites was 4 times higher than in PLA and PEO-Mg/PLA composites (Fig. 6.8d) which is in agreement with several reports where Mg^{2+} ions promoted high ALP expression and ALP activity [170][171]. However, this trend disagrees with ALP activity –the most recognizable biochemical markers of osteoblasts activity[165]– found in this study which revealed the highest ALP activity in PEO-Mg/PLA composites followed by PLA and Mg/PLA composites after 7 and 14 days, as shown in Fig. 6.9. This discrepancy of opposing trends in ALP expression and activity could be justified by the fact that mRNA expression of a certain protein does not always result into formation of protein due to several spatial-temporal factors [172]. The main difference between extracts of Mg/PLA and (PLA and PEO-Mg/PLA) is that the former has high Mg^{2+} ions with basic pH, and both factors increase ALP activity [65]. However, the effects of alloying elements of WE43 Mg wire (Y and Nd), degradation products of PLA, and PEO coating on ALP activity are not discussed in the literature, which could be crucial for this discrepancy. For instance, the ALP activity of Mg particles/PLGA composites was doubled after 14 days when Mg particles of ZK61 (Mg-6Zn-1Zr) alloy were used instead of pure Mg [65]. In another study, IM nails of

Mg alloy with 2 % silver (Mg-2Ag) reduced the differentiation of osteoclasts without impairing functions of osteoblasts and resulted in excessing bone formation in rat tibia [57], showing that even small amounts of alloying elements can alter the differentiation pathways of cells. Therefore, the high ALP activity of PEO-Mg/PLA could be due to the above reasons and it shows that pre-osteoblasts in extracts of PEO-Mg/PLA composites are more differentiated as compared to PLA and Mg/PLA composite.

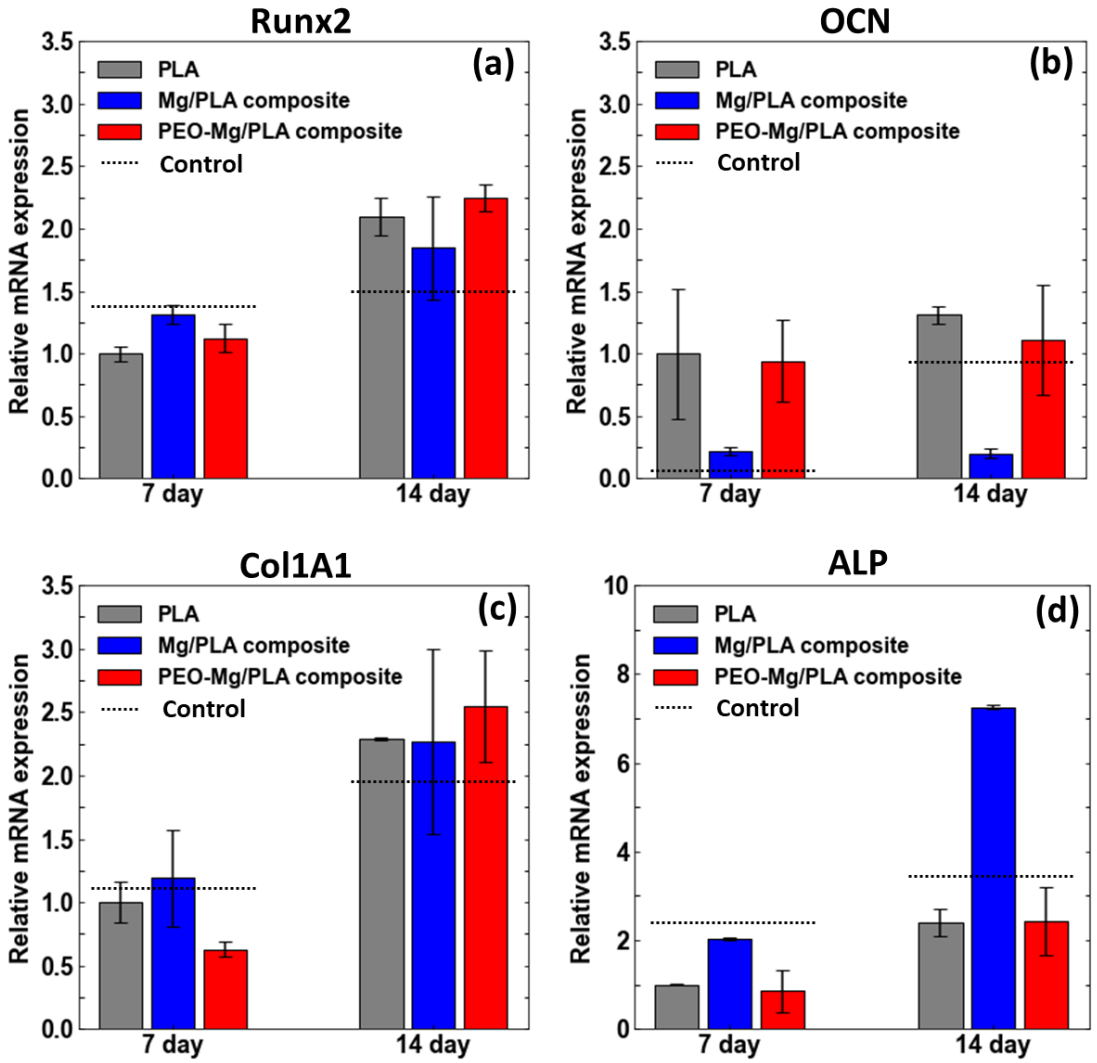

Fig. 6.8. Relative mRNA expression of differentiation related genes (a) Runx2, (b) OCN, (c) Col1A1 and (d) ALP in MC3T3-E1 pre-osteoblast cells cultured in extracts of control, PLA, Mg/PLA and PEO-Mg/PLA composites after 7 and 14 days. First expression levels of each gene were normalized with respect to housekeeping gene GAPDH followed by another normalization with respect to mRNA level obtained in PLA extracts after 7 days.

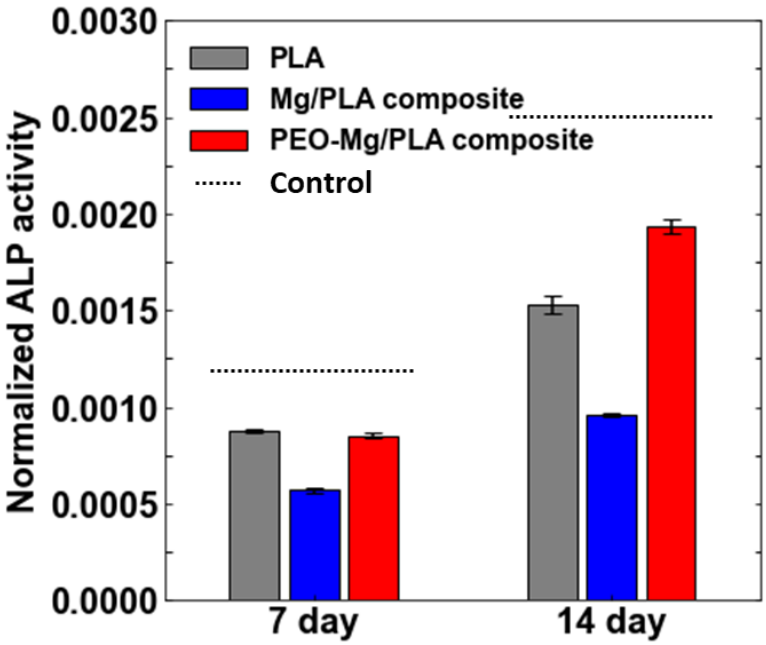

Fig. 6.9. Normalized ALP activity (absorbance units/(µg.ml^{-1} of total protein)) in MC3T3-E1 pre-osteoblast cells cultured in extracts of control, PLA, Mg/PLA and PEO-Mg/PLA composites for 7 and 14 days. The ALP activity of each sample was normalized with respect to its total protein content.

Calcium deposition is also an important marker of bone mineralization process [165]. Representative images after Alizarin Red staining are shown in Fig. 6.10. This shows the confluent monolayer of MC3T3-E1 cells after 7 and 14 days of culture and calcium depositions detection by red stains. After 7 days, the amount of calcium deposits were in the order: PLA > Mg/PLA > PEO-Mg/PLA > control (Fig. 6.10a), revealing that PLA and composites triggered mineralization faster as compared to the control (only differentiation medium). After 14 days (Fig. 6.10b), all samples showed enhanced mineralization except negative control (medium without differentiation supplements). Interestingly, the calcium depositions in PEO-Mg/PLA composites were denser (intense red stains) and organized. Degradation products of PLA are mainly lactic acid or small oligomers [156][157]. It was found that small quantities of lactic acid increased calcium deposition in MC3T3-E1 cells in 14 days of culture and even minute amounts (5 µg.ml^{-1}) doubled the calcium deposition rate [164]. Therefore, early mineralization of calcium in PLA extracts was likely triggered by its degradation products. Calcium deposition in MC3T3-E1 cells also increased in the presence of Mg ions (up to a threshold level) [65] and in a medium with slightly alkaline pH [173]. More recent

studies showed that adding Mg particles into PLA resulted in enhanced biomineralization [65][78]. This could explain why calcium deposition in the composite was higher than in the control. However, the differences in mineralization rate of Mg/PLA and PEO-Mg/PLA composites could also be due to the differences in the amount of Mg^{2+} ions in the extract and the pH that also play crucial role. Qualitative trends of mineralization (PLA, Mg/PLA > PEO-Mg/PLA) after 7 days (Fig. 6.10a), which enhanced after 14 days for all materials (Fig. 6.10b), are also in agreement with mRNA expression of Col1A1 (Fig. 6.8c) after 7 and 14 days because Col1A1 expression promotes secretion of extracellular collagen which provides the organic matrix upon which calcium minerals are deposited. Overall, it was confirmed by mineralization test that cells started to differentiate in extracts of material.

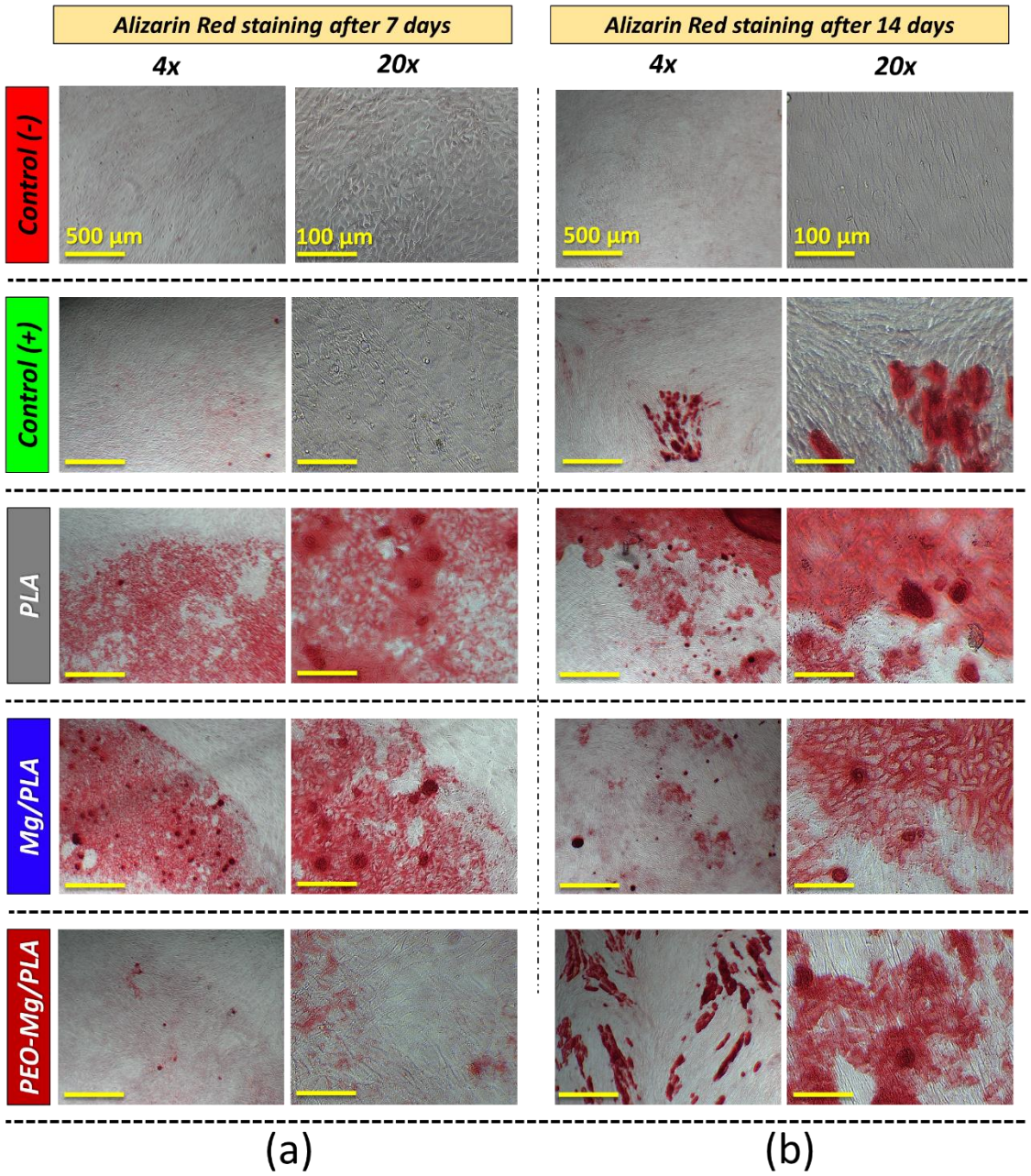

Fig. 6.10. 4x and 20x magnified optical microscopy images of MC3T3-E1 cells in extracts of negative control, positive control, PLA, Mg/PLA and PEO-Mg/PLA composites after (a) 7 and (b) 14 days of culture. Calcium depositions were stained with red color by Alizarin Red.

6.3.Conclusion

Cytotoxicity, proliferation and differentiation of MC3T3-E1 pre-osteoblast cells were studied for PLA, Mg/PLA and PEO-Mg/PLA composites by indirect and direct assays. It was found in the MTT assay that composites were fully cytocompatible, favored proliferation of cells in its extracts and revealed excellent cell viability after 24 h, 48 h and 72 h of culture in pure extracts of materials. Direct cytocompatibility of composites was also excellent as the negligible number of cells were found in live/dead assay. Cell-material interactions were observed SEM and immunofluorescent (actin staining), which revealed that cells could attach on the surface of PLA and composites in 1 h and covered most of the sample surface in 24 h by rapid proliferation. On the cross-sectional surface of the composite, cells avoided Mg wire regions due to unstable environment caused by its rapid corrosion, and migrated towards PLA regions and formed a monolayer which suggests that Mg/PLA composites should be manufactured in such a way that Mg reinforcement is preferentially fully encapsulated within the PLA matrix.

During the differentiation assay of 14 days, mRNA expression of Runx2, Col1A1 and ALP in extracts of all material increased after 7 and 14 days except OCN, suggesting that MC3T3-E1 cells are differentiating but not yet fully differentiated into mature osteoblasts in 14 days. ALP activity, an important indicator of bone differentiation, revealed high activity in PEO-Mg/PLA composite followed by PLA and Mg/PLA composite after 7 and 14 days. Alizarin red staining also confirmed the differentiation process of cells in extracts of PLA and composites as mineral depositions were clearly observed after 7 days which were enhanced after 14 day. Differences in qualitative analysis of the mineralization of materials also agreed with mRNA expression of Col1A1, which produces collagen that favors calcium deposition. In summary, Mg/PLA composites (with and without PEO) are cytocompatible and favor proliferation (direct and indirect), and do not impair the differentiation performance of cells compared to medical-grade PLA.

CHAPTER 7: CONCLUSIONS AND FUTURE WORK

6.4. Conclusions

7.1.1.Mg wires

A novel and scalable strategy was developed to manufacture Mg wires of 0.30 mm in diameter by cold drawing. Cold-drawn Mg wires manufactured with 13 % cold work had small grain size (~1 μm), strong basal texture and a large dislocation density. The microstructure of cold-drawn wire could be tailored by imparting more cold work or gentle annealing treatments at 400 ºC/450 ºC to optimize the mechanical properties. Corrosion rates of cold-drawn Mg wires (with 13 % cold work) in simulated body fluids always increased with cold work and/or annealing treatments, and pitting corrosion was always dominant, leading to a drastic drop in strength.

A novel process of Continuous Plasma Electrolytic Oxidation (C-PEO) was developed to generate a homogenous and porous oxide layer made up of MgO and $Mg_3(PO_4)2$ of ~8 μm in thickness on the surface of the Mg wires. The morphology of the oxide layer was tunable by optimizing electrical parameters. PEO modification did not significantly modify the mechanical properties of the wires but dramatically improved the corrosion rate and hindered pitting corrosion, which resulted in high strength retention after immersion in simulated body fluids. Moreover, PEO modification also improved the cytocompatibility of Mg wires and favored cell adhesion on their surface. These results demonstrated the potential of thin Mg wires surface-modified by PEO for bioabsorbable wire-based medical devices.

7.1.2.Mg/PLA composites

Bioabsorbable unidirectional and multi-directional composites laminates of PLA reinforced with Mg wires (with and without PEO surface modification) were successfully manufactured by hot compression with controlled positioning and orientation of the wires. The flat plates of composites can be further processed by thermoforming and machining to achieve a curved surface and customized shapes.

The PEO oxide layer significantly increased the shear strength (~2.5 times) and toughness of the interface between Mg wires and PLA matrix by mechanical interlocking of PLA into the pores of the PEO oxide layer. PEO oxide layer also dramatically improved the corrosion resistance of the composite interface, suppressed

hydrogen gas release, and wires suffered only 3 % mass loss in 180 days of *in vitro* degradation. On the contrary, corrosion of Mg wires in the absence of a PEO was very fast, and wires were completely corroded after 180 days. Degradation of the PLA matrix was accelerated at the interface in the presence of wires, irrespective of the PEO modification,

Mechanical properties of unidirectional composite laminates of Mg/PLA and PEO-Mg/PLA composites were found to be dependent on the loading direction and orientation of wires. As expected, the highest strengths were achieved in the longitudinal direction (tensile: 90 MPa and compressive >115 MPa). The uniaxial elastic moduli in longitudinal and transverse directions were 11 GPa and 4.2 GPa, respectively, with a 20 vol. % fraction of Mg wires. PEO modification improved the ductility of the composite in longitudinal tension but did not change the strength or modulus. The mechanical properties of composites in longitudinal tension decreased slightly after 42 days of degradation and drastically in transverse tension and in-plane shear, irrespective of PEO modification of Mg wires. The quasi-isotropic laminate attained an elastic modulus and strength of ~5.4 GPa and 52 MPa, respectively, that dropped to ~4.5 GPa (higher than PLA) and 37 MPa after 42 days. Moreover, the experimental modulus of quasi-isotropic laminates (in the as-manufactured and degraded conditions) closely matched the theoretical predictions of classical laminate theory.

Finally, composites were found to be fully cytocompatible, favored proliferation, and did not impair the bone differentiation performance of cells compared to medical-grade PLA. Therefore, Mg wires reinforced PLA composite can be a suitable candidate for the next generation of bioabsorbable orthopedic implants, such as fixation plates.

6.5. Future work

7.2.1.Mg wires

1. **Investigation on mechanisms of surface modification during Continuous Plasma Electrolytic Oxidation:** In *vitro* corrosion mechanisms of Mg wires modified by C-PEO revealed an additional Ca-P layer below the PEO oxide that provided additional protection and minimized detachment of the oxide layer. The formation mechanism and composition of this Ca-P are, however, unknown and should be explored to design better PEO coatings.

2. **Application of PEO-modified Mg wires as a conductor in bioabsorbable sensors:** Recently, some studies used polymer-coated Mg wires in bioabsorbable cardiovascular and brain sensors. Application of PEO-modified Mg wires for these applications could be interesting as the PEO oxide layer is an insulator and could replace the polymer coating. Similarly, the effect of Mg wire corrosion on electrical resistance/conductivity is also interesting for functional bioabsorbable sensors.
3. **Discovering size-specific applications of Mg wires:** Mg wires have been produced with wide range of diameters, from a few millimeters to as small as 25 µm. New size-specific applications of bioabsorbable PEO-modified Mg wires should be explored, e.g. smaller wires (< 100 µm) for nerve regeneration, neural sensors etc., and larger wires (> 300 µm) in wound closure, cerclage wires, etc.
4. **Wire drawing of suitable alloys of Mg:** Alloying elements significantly impact cold drawing process to achieve Mg wires of small diameter. For instance, the author experienced that drawing of Mg1Y to achieve 0.3 mm in diameter was easier than drawing WE43 alloy. Therefore, a Mg alloy that does not compromise the biocompatibility for a particular application but is easier to cold draw will reduce the costs of cold drawing.
5. **Development of bio-safe lubricants for the cold drawing of Mg wires:** Using lubricants is inevitable during the cold drawing process of Mg wires. Currently, companies are using lubricants which are commonly used for non-medical wires, such as Al, for the production of Mg wires. This could be a bottleneck when Mg wire or any other bioabsorbable wire go into regulatory approval. Therefore, developing bio-safe lubricants is a necessary research direction for developing trust in bioabsorbable wires produced by cold drawing.

7.2.2.Mg/PLA composites

1. **Optimization of the manufacturing process:** This thesis demonstrated that is possible to manufacture Mg/PLA composites by hot compression with up to 20 vol. % fraction of Mg wires. This limit can be increased up to 30-35 % to achieve a modulus of quasi-isotropic laminates > 9 GPa.
2. ***In vivo* testing:** Mechanical, degradation, and biological tests in the thesis proved that bioabsorbable Mg/PLA composites (with and without PEO) could be suitable

for orthopedic fixation applications. A successful *in vivo* animal trial is necessary for translation into clinical trials.

3. **Manufacturing of Mg/PLA composites by advanced technologies:** Although the Mg/PLA flat plates developed in the thesis were void-free, surface adaptable, and machinable, advanced manufacturing technologies like 3D printing can provide more independence in wire placement inside the PLA matrix. The application of PEO-modified Mg wires for this purpose is also interesting. However, 3D printing usually results in high porosity of the composites that can reduce the strength and accelerate degradation. Therefore, these processes should be optimized to produce defect-free samples.
4. **Fatigue behavior of composites:** The static mechanical properties of as-manufactured and degraded composites are suitable for many fixation applications. However, fatigue tests are also important to understand the effect of cyclic loads on corrosion.
5. **Numerical framework for developing optimized layup of bioabsorbable wire reinforced composites:** There are no guidelines and publications to design bioabsorbable composite laminates for orthopedic applications. Questions on whether to use as-manufactured properties with some safety factor or degraded properties could be answered by developing a numerical approach for a particular loading scenario that should propose the optimized stacking sequence by considering both initial and degradation mechanical properties.
6. **Determination of reactions of alloying elements of magnesium with PLA:** This thesis and also previous studies have neglected the effect of alloying elements on the corrosion behavior of PLA matrix. Understanding corrosion products that result from the reaction of alloying with PLA matrix is essential for further development and will most likely be a requirement for regulatory approvals.

REFERENCES

[1] D. Wu, P. Isaksson, S.J. Ferguson, C. Persson, Young's modulus of trabecular bone at the tissue level: A review, Acta Biomater. 78 (2018) 1–12. https://doi.org/10.1016/j.actbio.2018.08.001.

[2] R.B. Martin, D.B. Burr, N.A. Sharkey, Skeletal Tissue Mechanics, Springer, 2019.

[3] D. Lopes, C. Martins-Cruz, M.B. Oliveira, J.F. Mano, Bone physiology as inspiration for tissue regenerative therapies, Biomaterials. 185 (2018) 240–275. https://doi.org/10.1016/j.biomaterials.2018.09.028.

[4] A. Goharian, Trauma Plating Systems, Elsevier, 2016.

[5] S. Wei, J.X. Ma, L. Xu, X.S. Gu, X.L. Ma, Biodegradable materials for bone defect repair, Mil. Med. Res. 7 (2020) 1–25.

[6] C.Y. Lin, J.H. Kang, Mechanical properties of compact bone defined by the stress-strain curve measured using uniaxial tensile test: A concise review and practical guide, Materials (Basel). 14 (2021). https://doi.org/10.3390/ma14154224.

[7] T.P. Ng, S.S. R. Koloor, J.R.P. Djuansjah, M.R. Abdul Kadir, Assessment of compressive failure process of cortical bone materials using damage-based model, J. Mech. Behav. Biomed. Mater. 66 (2017) 1–11. https://doi.org/10.1016/j.jmbbm.2016.10.014.

[8] R. Havaldar, S. Pilli, B. Putti, Insights into the effects of tensile and compressive loadings on human femur bone, Adv. Biomed. Res. 3 (2014) 101. https://doi.org/10.4103/2277-9175.129375.

[9] H. Mehboob, S. Chang, Application of composites to orthopedic prostheses for effective bone healing : A review, Compos. Struct. 118 (2014) 328–341. https://doi.org/10.1016/j.compstruct.2014.07.052.

[10] C. Bergh, D. Wennergren, M. Möller, H. Brisby, Fracture incidence in adults in relation to age and gender: A study of 27,169 fractures in the Swedish Fracture Register in a well-defined catchment area, PLoS One. 15 (2021) 1–18. https://doi.org/10.1371/journal.pone.0244291.

[11] Y. Sun, H. Helmholz, R. Willumeit-Römer, Preclinical in vivo research of magnesium-based implants for fracture treatment: A systematic review of animal model selection and study design, J. Magnes. Alloy. 9 (2021) 351–361. https://doi.org/10.1016/j.jma.2020.09.011.

[12] Fracture and Dislocation Classification, Classif. AO/OTA Fract. Dislocation. (2018).

[13] F. Loi, L.A. Córdova, J. Pajarinen, T.-H. Lin, Z. Yao, S.B. Goodman, Inflammation, Fracture and Bone Repair HHS Public Access, Bone. 86 (2016) 119–130. https://doi.org/10.1016/j.bone.2016.02.020.Inflammation.

[14] T. Kim, C.W. See, X. Li, D. Zhu, Orthopedic implants and devices for bone fractures and defects: Past, present and perspective, Eng. Regen. 1 (2020) 6–18. https://doi.org/10.1016/j.engreg.2020.05.003.

[15] L. Claes, C.A.C.A. Heigele, C. Neidlinger-Wilke, D. Kaspar, W. Seidl, K.J.K.J. Margevicius, P. Augat, Effects of Mechanical Factors on the Fracture Healing Process, Clin. Orthop. Relat. Res. 355S (1998) S132–S147. https://doi.org/10.1097/00003086-199810001-00015.

[16] P.R.T. Kuzyk, E.H. Schemitsch, The basic science of peri-implant bone healing, Indian J. Orthop. 45 (2011) 108–115. https://doi.org/10.4103/0019-5413.77129.

[17] B. Heimbach, M. Wei, Composite orthopedic fixation devices, in: Orthop. Biomater., 2017. https://doi.org/10.1007/978-3-319-73664-8_15.

[18] G. Harasen, Orthopedic hardware and equipment for the beginner: Part 1. Pins and wires, Can. Vet. J. 52 (2011) 1025–1026.

[19] G. Harasen, Orthopedic hardware and equipment for the beginner. Part 2: Plates and screws, Can. Vet. J. 52 (2011) 1359–1360.

[20] T. Kim, C.W. See, X. Li, D. Zhu, Orthopedic implants and devices for bone fractures and defects: Past, present and perspective, Eng. Regen. 1 (2020) 6–18. https://doi.org/10.1016/j.engreg.2020.05.003.

[21] surgeryreference.aofoundation.org, (n.d.). https://surgeryreference.aofoundation.org/.

[22] P. Pankaj, Devices for traumatology: Biomechanics and design, INC, 2022. https://doi.org/10.1016/B978-0-12-824481-4.00033-0.

[23] M. Niinomi, Metals for biomedical devices, 2019. https://doi.org/10.1016/C2017-0-03429-8.

[24] V. Sansone, P. Davide, M. Marco, The effects on bone cells of metal ions released from orthopaedic implants . A review, Clin. Cases Miner. Bone Metab. 10 (2013) 34–40.

[25] D. Xia, F. Yang, Y. Zheng, Y. Liu, Y. Zhou, Research status of biodegradable metals designed for oral and maxillofacial applications: A review, Bioact. Mater. 6 (2021) 4186–4208. https://doi.org/10.1016/j.bioactmat.2021.01.011.

[26] C. Rendenbach, H. Fischer, A. Kopp, K. Schmidt-Bleek, H. Kreiker, S. Stumpp, M. Thiele, G. Duda, H. Hanken, B. Beck-Broichsitter, O. Jung, N. Kröger, R. Smeets, M. Heiland, Improved in vivo osseointegration and degradation behavior of PEO surface-modified WE43 magnesium plates and screws after 6

and 12 months, Mater. Sci. Eng. C. (2021) 112380. https://doi.org/10.1016/j.msec.2021.112380.

[27] C. Li, C. Guo, V. Fitzpatrick, A. Ibrahim, M.J. Zwierstra, P. Hanna, A. Lechtig, A. Nazarian, S.J. Lin, D.L. Kaplan, Design of biodegradable, implantable devices towards clinical translation, Nat. Rev. Mater. (2019). https://doi.org/10.1038/s41578-019-0150-z.

[28] W. Ali, A. Mehboob, M.-G. Han, S.-H. Chang, Experimental study on degradation of mechanical properties of biodegradable magnesium alloy (AZ31) wires/poly(lactic acid) composite for bone fracture healing applications, Compos. Struct. 210 (2019) 914–921. https://doi.org/10.1016/j.compstruct.2018.12.011.

[29] R. Mittal, J. Morley, H. Dinopoulos, E.G. Drakoulakis, E. Vermani, P. V. Giannoudis, Use of bio-resorbable implants for stabilisation of distal radius fractures: The United Kingdom patients' perspective, Injury. 36 (2005) 333–338. https://doi.org/10.1016/j.injury.2004.09.015.

[30] F. Buchanan, Degradation rate of bioresorbable materials, prediction and evaluation, Woodhead Publishing Limited, 2008.

[31] N. Johari, A. Khodaei, A. Samadikuchaksaraei, R.L. Reis, S.C. Kundu, L. Moroni, Ancient fibrous biomaterials from silkworm protein fibroin and spider silk blends: Biomechanical patterns, Acta Biomater. 153 (2022) 38–67. https://doi.org/10.1016/j.actbio.2022.09.030.

[32] O.M. Böstman, H.K. Pihlajamäki, Adverse tissue reactions to bioabsorbable fixation devices, Clin. Orthop. Relat. Res. 371 (2000) 216–227. https://doi.org/10.1097/00003086-200002000-00026.

[33] N.A. Weir, F.J. Buchanan, J.F. Orr, G.R. Dickson, Degradation of poly-L-lactide. Part 1: In vitro and in vivo physiological temperature degradation, Proc. Inst. Mech. Eng. Part H J. Eng. Med. 218 (2004) 307–319. https://doi.org/10.1243/0954411041932782.

[34] N. Ostrowski, A. Roy, P.N. Kumta, Magnesium Phosphate Cement Systems for Hard Tissue Applications: A Review, ACS Biomater. Sci. Eng. 2 (2016) 1067–1083. https://doi.org/10.1021/acsbiomaterials.6b00056.

[35] implantable-peek @ invibio.com, (n.d.). https://invibio.com/en/materials-solutions/implantable-peek.

[36] Y. Shikinami, M. Okuno, Bioresorbable devices made of forged composites of hydroxyapatite (HA) particles and poly L-lactide (PLLA). Part II: Practical properties of miniscrews and miniplates, Biomaterials. 22 (2001) 3197–3211. https://doi.org/10.1016/S0142-9612(01)00072-2.

[37] www.nanomag.us, (n.d.). https://www.nanomag.us/.

[38] www.syntellix.de, (n.d.). https://www.syntellix.de/home.html.

[39] teijin-medical.co.jp, (n.d.). https://teijin-medical.co.jp/en/.

[40] R. Willumeit-Römer, The Interface Between Degradable Mg and Tissue, J. Miner. Met. Mater. Soc. 71 (2019) 1447–1455. https://doi.org/10.1007/s11837-019-03368-0.

[41] Z. Sheikh, M.N. Abdallah, A.A. Hanafi, S. Misbahuddin, H. Rashid, M. Glogauer, Mechanisms of in vivo degradation and resorption of calcium phosphate based biomaterials, Materials (Basel). 8 (2015) 7913–7925. https://doi.org/10.3390/ma8115430.

[42] J.W. Lee, H.S. Han, K.J. Han, J. Park, H. Jeon, M.R. Ok, H.K. Seok, J.P. Ahn, K.E. Lee, D.H. Lee, S.J. Yang, S.Y. Cho, P.R. Cha, H. Kwon, T.H. Nam, J.H. Lo Han, H.J. Rho, K.S. Lee, Y.C. Kim, D. Mantovani, Long-term clinical study and multiscale analysis of in vivo biodegradation mechanism of Mg alloy, Proc. Natl. Acad. Sci. U. S. A. 113 (2016) 716–721. https://doi.org/10.1073/pnas.1518238113.

[43] S. Farah, D.G. Anderson, R. Langer, Physical and mechanical properties of PLA, and their functions in widespread applications — A comprehensive review, Adv. Drug Deliv. Rev. 107 (2016) 367–392. https://doi.org/10.1016/j.addr.2016.06.012.

[44] H. Tsuji, Autocatalytic hydrolysis of amorphous-made polylactides: Effects of L-lactide content, tacticity, and enantiomeric polymer blending, Polymer (Guildf). 43 (2002) 1789–1796. https://doi.org/10.1016/S0032-3861(01)00752-2.

[45] W. Ali, A. Mehboob, M.G. Han, S.H. Chang, Effect of fluoride coating on degradation behaviour of unidirectional Mg/PLA biodegradable composite for load-bearing bone implant application, Compos. Part A Appl. Sci. Manuf. 124 (2019) 105464. https://doi.org/10.1016/j.compositesa.2019.05.032.

[46] J. Pan, X. Chen, Modelling degradation of amorphous biodegradable polyesters: Advanced model, Woodhead Publishing Limited, 2015. https://doi.org/10.1533/9781782420255.1.33.

[47] I. Grizzi, H. Garreau, S. Li, M. Vert, Hydrolytic degradation of devices based on poly(dl-lactic acid) size-dependence, Biomaterials. 16 (1995) 305–311. https://doi.org/10.1016/0142-9612(95)93258-F.

[48] T. Kanno, S. Sukegawa, Y. Furuki, Y. Nariai, J. Sekine, Overview of innovative advances in bioresorbable plate systems for oral and maxillofacial surgery, Jpn. Dent. Sci. Rev. 54 (2018) 127–138. https://doi.org/10.1016/j.jdsr.2018.03.003.

[49] S. Pina, J. Ferreira, Bioresorbable Plates and Screws for Clinical Applications: A Review, J. Healthc. Eng. 3 (2012) 243–260. https://doi.org/10.1260/2040-2295.3.2.243.

[50] W. Ali, M. Echeverry-Rendón, G. Dominguez, K. van Gaalen, A. Kopp, C. González, J. LLorca, Bioabsorbable WE43 Mg alloy wires modified by continuous plasma-electrolytic oxidation for implant applications. Part II: degradation and biological performance, Biomater. Adv. 147 (2023). https://doi.org/10.1016/j.bioadv.2023.213325.

[51] P. Tian, X. Liu, Surface modification of biodegradable magnesium and its alloys for biomedical applications, Regen. Biomater. 2 (2015) 135–151. https://doi.org/10.1093/rb/rbu013.

[52] J. Xue, A.J. Griebel, Y. Zhang, C. Romany, B. Chen, J. Schaffer, T.P. Weihs, Influence of Thermal Processing on Resoloy Wire Microstructure and Properties, Adv. Eng. Mater. 23 (2021) 1–12. https://doi.org/10.1002/adem.202001278.

[53] F. Witte, N. Hort, C. Vogt, S. Cohen, K.U. Kainer, R. Willumeit, F. Feyerabend, Degradable biomaterials based on magnesium corrosion, Curr. Opin. Solid State Mater. Sci. 12 (2008) 63–72. https://doi.org/10.1016/j.cossms.2009.04.001.

[54] S. Agarwal, J. Curtin, B. Duffy, S. Jaiswal, Biodegradable magnesium alloys for orthopaedic applications: A review on corrosion, biocompatibility and surface modifications, Mater. Sci. Eng. C. 68 (2016) 948–963. https://doi.org/10.1016/j.msec.2016.06.020.

[55] W. Ali, M. Li, L. Tillmann, T. Mayer, C. González, J. LLorca, A. Kopp, Bioabsorbable WE43 Mg alloy wires modified by continuous plasma-electrolytic oxidation for implant applications. Part I: Processing, microstructure and mechanical properties, Biomater. Adv. 146 (2023) 213314. https://doi.org/10.1016/j.bioadv.2023.213314.

[56] A. Chaya, S. Yoshizawa, K. Verdelis, S. Noorani, B.J. Costello, C. Sfeir, Fracture healing using degradable magnesium fixation plates and screws, J. Oral Maxillofac. Surg. 73 (2015) 295–305. https://doi.org/10.1016/j.joms.2014.09.007.

[57] K. Jähn, H. Saito, H. Taipaleenmäki, A. Gasser, N. Hort, F. Feyerabend, H. Schlüter, J.M. Rueger, W. Lehmann, R. Willumeit-römer, E. Hesse, Intramedullary Mg2Ag nails augment callus formation during fracture healing in mice, Acta Biomater. 36 (2016) 350–360. https://doi.org/10.1016/j.actbio.2016.03.041.

[58] J. Gonzalez, R.Q. Hou, E.P.S. Nidadavolu, R. Willumeit-r, F. Feyerabend, Bioactive Materials Magnesium degradation under physiological conditions - Best practice, 3 (2018) 174–185. https://doi.org/10.1016/j.bioactmat.2018.01.003.

[59] Y. Luo, C. Zhang, J. Wang, F. Liu, K.W. Chau, L. Qin, J. Wang, Clinical translation and challenges of biodegradable magnesium-based interference screws in ACL reconstruction, Bioact. Mater. 6 (2021) 3231–3243. https://doi.org/10.1016/j.bioactmat.2021.02.032.

[60] R.C. Zeng, X.T. Li, S.Q. Li, F. Zhang, E.H. Han, In vitro degradation of pure Mg in response to glucose, Sci. Rep. 5 (2015) 1–14. https://doi.org/10.1038/srep13026.

[61] W. Yan, Y.J. Lian, Z.Y. Zhang, M.Q. Zeng, Z.Q. Zhang, Z.Z. Yin, L.Y. Cui, R.C. Zeng, In vitro degradation of pure magnesium—the synergetic influences of glucose and albumin, Bioact. Mater. 5 (2020) 318–333. https://doi.org/10.1016/j.bioactmat.2020.02.015.

[62] N.R. Mercier, H.R. Costantino, M.A. Tracy, L.J. Bonassar, Poly(lactide-co-glycolide) microspheres as a moldable scaffold for cartilage tissue engineering, Biomaterials. 26 (2005) 1945–1952. https://doi.org/10.1016/j.biomaterials.2004.06.030.

[63] G. Zhu, S.R. Mallery, S.P. Schwendeman, Stabilization of proteins encapsulated in injectable poly (lactide-co- glycolide), Nat. Biotechnol. 18 (2000) 52–57. https://doi.org/10.1038/71916.

[64] S.C. Cifuentes, Processing and characterization ofnovel biodegradable and bioresorbable PLA/Mg composites for osteosynthesis, Universidad Carlos III de Madrid, 2015. https://doi.org/10.1016/j.

[65] X. Yu, W. Huang, D. Zhao, K. Yang, L. Tan, X. Zhang, J. Li, M. Zhang, S. Zhang, T. Liu, B. Wu, M. Qu, R. Duan, Y. Yuan, Study of engineered low-modulus Mg/PLLA composites as potential orthopaedic implants: An in vitro and in vivo study, Colloids Surfaces B Biointerfaces. 174 (2019) 280–290. https://doi.org/10.1016/j.colsurfb.2018.10.054.

[66] H. Mobedi, M. Nekoomanesh, H. Orafaei, H. Mivehchi, Studying the Degradation of Poly(L-lactide) in Presence of Magnesium Hydroxide, Polym. J. 15 (2006) 31–39.

[67] P. Wan, C. Yuan, L.L. Tan, Q. Li, K. Yang, Fabrication and evaluation of bioresorbable PLLA/magnesium and PLLA/magnesium fluoride hybrid composites for orthopedic implants, Compos. Sci. Technol. 98 (2014) 36–43. https://doi.org/10.1016/j.compscitech.2014.04.011.

[68] Y.H. Wu, N. Li, Y. Cheng, Y.F. Zheng, Y. Han, Invitro Study on Biodegradable AZ31 Magnesium Alloy Fibers Reinforced PLGA Composite, J. Mater. Sci. Technol. 29 (2013) 545–550. https://doi.org/10.1016/j.jmst.2013.03.004.

[69] X. Li, C.L. Chu, L. Liu, X.K. Liu, J. Bai, C. Guo, F. Xue, P.H. Lin, P.K. Chu, Biodegradable poly-lactic acid based-composite reinforced unidirectionally with high-strength magnesium alloy wires, Biomaterials. 49 (2015) 135–144. https://doi.org/10.1016/j.biomaterials.2015.01.060.

[70] C. Chu, X. Li, W. Yu, L. Han, J. Bai, F. Xue, Degradation behaviors of PLA-matrix composite with 20 vol% magnesium alloy wires under static loading conditions, J. Mater. Sci. 54 (2018) 4701–4709. https://doi.org/10.1007/s10853-018-03199-5.

[71] W. Ali, M. Echeverry-Rendón, A. Kopp, C. González, J. LLorca, Strength, corrosion resistance and cellular response of interfaces in bioresorbable poly-lactic acid/Mg fiber composites for orthopedic applications, J. Mech. Behav. Biomed. Mater. 123 (2021) 104781. https://doi.org/10.1016/j.jmbbm.2021.104781.

[72] X. Li, C. Chu, L. Zhou, J. Bai, C. Guo, F. Xue, P. Lin, P.K. Chu, Fully degradable PLA-based composite reinforced with 2D-braided Mg wires for orthopedic implants, Compos. Sci. Technol. 142 (2017) 180–188. https://doi.org/10.1016/j.compscitech.2017.02.013.

[73] C. Guo, X. Liu, L. Liu, J. Bai, F. Xue, P. Lin, C. Chu, Impact behaviors of poly-lactic acid based biocomposite reinforced with unidirectional high-strength magnesium alloy wires, Prog. Nat. Sci. Mater. Int. 24 (2014) 472–478. https://doi.org/10.1016/j.pnsc.2014.08.003.

[74] M.S. Butt, J. Bai, X. Wan, C. Chu, F. Xue, H. Ding, G. Zhou, Mechanical and degradation properties of biodegradable Mg strengthened poly-lactic acid composite through plastic injection molding, Mater. Sci. Eng. C. 70 (2017) 141–147. https://doi.org/10.1016/j.msec.2016.08.051.

[75] H. Cai, X. Li, C. Chu, F. Xue, C. Guo, Q. Dong, J. Bai, Insight into the effect of interface on the mechanical properties of Mg/PLA composite plates, Compos. Sci. Technol. 183 (2019) 107801. https://doi.org/10.1016/j.compscitech.2019.107801.

[76] W. Ali, A. Mehboob, M.-G. Han, S.-H. Chang, Effect of fluoride coating on degradation behaviour of unidirectional Mg/PLA biodegradable composite for load-bearing bone implant application, Compos. Part A Appl. Sci. Manuf. 124 (2019) 105464. https://doi.org/10.1016/j.compositesa.2019.05.032.

[77] X. Li, C. Chu, Y. Wei, C. Qi, J. Bai, C. Guo, F. Xue, P. Lin, P.K. Chu, In vitro degradation kinetics of pure PLA and Mg/PLA composite: Effects of immersion temperature and compression stress, Acta Biomater. 48 (2017) 468–478. https://doi.org/10.1016/j.actbio.2016.11.001.

[78] J. Long, W. Zhang, Y. Chen, B. Teng, B. Liu, H. Li, Z. Yao, D. Wang, L. Li, X.F. Yu, L. Qin, Y. Lai, Multifunctional magnesium incorporated scaffolds by 3D-Printing for comprehensive postsurgical management of osteosarcoma, Biomaterials. 275 (2021) 120950. https://doi.org/10.1016/j.biomaterials.2021.120950.

[79] R. Bakhshi, M. Mohammadi-zerankeshi, M. Mehrabi-dehdezi, Additive manufacturing of PLA-Mg composite scaffolds for hard tissue engineering applications, J. Mech. Behav. Biomed. Mater. 138 (2023) 105655. https://doi.org/10.1016/j.jmbbm.2023.105655.

[80] A. Ferrández-Montero, M. Lieblich, R. Benavente, J.L. González-Carrasco, B. Ferrari, Study of the matrix-filler interface in PLA/Mg composites manufactured by Material Extrusion using a colloidal feedstock, Addit. Manuf. 33 (2020)

101142. https://doi.org/10.1016/j.addma.2020.101142.

[81] A. Ferrández-Montero, M. Lieblich, J.L. González-Carrasco, R. Benavente, V. Lorenzo, R. Detsch, A.R. Boccaccini, B. Ferrari, Development of biocompatible and fully bioabsorbable PLA/Mg films for tissue regeneration applications, Acta Biomater. (2019). https://doi.org/10.1016/J.ACTBIO.2019.05.026.

[82] A. Srivastava, R. Ahuja, P. Bhati, S. Singh, P. Chauhan, P. Vashisth, A. Kumar, N. Bhatnagar, Fabrication and characterization of PLLA/Mg composite tube as the potential bioresorbable/biodegradable stent(BRS), Materialia. 10 (2020) 100661. https://doi.org/10.1016/j.mtla.2020.100661.

[83] A. Brown, S. Zaky, H. Ray, C. Sfeir, Porous magnesium/PLGA composite scaffolds for enhanced bone regeneration following tooth extraction, Acta Biomater. 11 (2015) 543–553. https://doi.org/10.1016/j.actbio.2014.09.008.

[84] C. Zhao, H. Wu, J. Ni, S. Zhang, X. Zhang, Development of PLA/Mg composite for orthopedic implant: Tunable degradation and enhanced mineralization, Compos. Sci. Technol. 147 (2017) 8–15. https://doi.org/10.1016/j.compscitech.2017.04.037.

[85] I. Antoniac, D. Popescu, A. Zapciu, A. Antoniac, F. Miculescu, H. Moldovan, Magnesium Filled Polylactic Acid (PLA) Material for Filament Based 3D Printing, Materials (Basel). 12 (2019) 719.

[86] M. Shoaib, J. Bai, X. Wan, C. Chu, F. Xue, H. Ding, G. Zhou, Mg alloy rod reinforced biodegradable poly-lactic acid composite for load bearing bone replacement, SCT. 309 (2017) 471–479. https://doi.org/10.1016/j.surfcoat.2016.12.005.

[87] M.S. Butt, A. Maqbool, M. Saleem, M.A. Umer, F. Javaid, R.A. Malik, M.A. Hussain, Z. Rehman, Revealing the Effects of Microarc Oxidation on the Mechanical and Degradation Properties of Mg-Based Biodegradable Composites, ACS Omega. 5 (2020) 13694–13702. https://doi.org/10.1021/acsomega.0c00836.

[88] X. Du, Y. Song, X. Xuan, S. Chen, X. Wu, H.B. Jiang, E.S. Lee, X. Wang, Characterization of a Bioresorbable Magnesium-Reinforced PLA-Integrated GTR/GBR Membrane as Dental Applications, Scanning. 2020 (2020). https://doi.org/10.1155/2020/6743195.

[89] W. Ali, M. Echeverry-Rendón, A. Kopp, C. González, J. LLorca, Strength, corrosion resistance and cellular response of interfaces in bioresorbable poly-lactic acid/Mg fiber composites for orthopedic applications, J. Mech. Behav. Biomed. Mater. 123 (2021) 104781. https://doi.org/10.1016/j.jmbbm.2021.104781.

[90] A. Ferrandez-Montero, M. Lieblich, R. Benavente, J.L. González-Carrasco, B. Ferrari, New approach to improve polymer-Mg interface in biodegradable PLA/Mg composites through particle surface modification, Surf. Coatings

Technol. 383 (2020) 125285. https://doi.org/10.1016/j.surfcoat.2019.125285.

[91] H. Cai, Y. Zhang, J. Meng, X. Li, F. Xue, C. Chu, L. Tao, J. Bai, Enhanced fully-biodegradable Mg/PLA composite rod: Effect of surface modification of Mg-2Zn wire on the interfacial bonding, Surf. Coatings Technol. 350 (2018) 722–731. https://doi.org/10.1016/j.surfcoat.2018.07.045.

[92] A. Kopp, H. Fischer, A.P. Soares, K. Schmidt-Bleek, C. Leber, H. Kreiker, G. Duda, N. Kröger, K. van Gaalen, H. Hanken, O. Jung, R. Smeets, M. Heiland, C. Rendenbach, Long-term in vivo observations show biocompatibility and performance of ZX00 magnesium screws surface-modified by plasma-electrolytic oxidation in Göttingen miniature pigs, Acta Biomater. 157 (2023) 720–733. https://doi.org/10.1016/j.actbio.2022.11.052.

[93] E. Hasanpur, A. Ghazavizadeh, A. Sadeghi, M. Haboussi, In vitro corrosion study of PLA/Mg composites for cardiovascular stent applications, J. Mech. Behav. Biomed. Mater. 124 (2021) 104768. https://doi.org/10.1016/j.jmbbm.2021.104768.

[94] A. Mehboob, H. Mehboob, S.-H. Chang, Evaluation of unidirectional BGF/PLA and Mg/PLA biodegradable composites bone plates-scaffolds assembly for critical segmental fractures healing, Compos. Part A Appl. Sci. Manuf. 135 (2020) 105929. https://doi.org/https://doi.org/10.1016/j.compositesa.2020.105929.

[95] unity-b @ www.amggastro.com, (n.d.). https://www.amggastro.com/unity-b.html.

[96] D. Zhao, F. Witte, F. Lu, J. Wang, J. Li, L. Qin, Current status on clinical applications of magnesium-based orthopaedic implants: A review from clinical translational perspective, Biomaterials. 112 (2017) 287–302. https://doi.org/10.1016/j.biomaterials.2016.10.017.

[97] C. Pascual-González, C. Thompson, J. de la Vega, N. Biurrun Churruca, J.P. Fernández-Blázquez, I. Lizarralde, D. Herráez-Molinero, C. González, J. LLorca, Processing and properties of PLA/Mg filaments for 3D printing of scaffolds for biomedical applications, Rapid Prototyp. J. 28 (2022) 884–894. https://doi.org/10.1108/RPJ-06-2021-0152.

[98] X. Li, W. Yu, L. Han, C. Chu, J. Bai, F. Xue, Degradation behaviors of Mg alloy wires/PLA composite in the consistent and staged dynamic environments, Mater. Sci. Eng. C. 103 (2019) 109765. https://doi.org/10.1016/J.MSEC.2019.109765.

[99] H. Cai, X. Li, F. Xue, C. Chu, C. Guo, J. Bai, X. Zhang, In Vitro Study on Cytocompatibility of Mg Wire/Poly(Lactic Acid) Composite Rods, J. Mater. Eng. Perform. (2021). https://doi.org/10.1007/s11665-021-05883-1.

[100] Medical Magnesium GmbH, (n.d.). https://www.medical-magnesium.com/.

[101] J.M. Seitz, E. Wulf, P. Freytag, D. Bormann, F.W. Bach, The manufacture of

resorbable suture material from magnesium, Adv. Eng. Mater. 12 (2010) 1099–1105. https://doi.org/10.1002/adem.201000191.

[102] M. Asgari, R. Hang, C. Wang, Z. Yu, Z. Li, Y. Xiao, Biodegradable metallicwires in dental and orthopedic applications: A review, 2018. https://doi.org/10.3390/met8040212.

[103] S.K. Kang, R.K.J. Murphy, S.W. Hwang, S.M. Lee, D. V. Harburg, N.A. Krueger, J. Shin, P. Gamble, H. Cheng, S. Yu, Z. Liu, J.G. McCall, M. Stephen, H. Ying, J. Kim, G. Park, R.C. Webb, C.H. Lee, S. Chung, D.S. Wie, A.D. Gujar, B. Vemulapalli, A.H. Kim, K.M. Lee, J. Cheng, Y. Huang, S.H. Lee, P. V. Braun, W.Z. Ray, J.A. Rogers, Bioresorbable silicon electronic sensors for the brain, Nature. 530 (2016) 71–76. https://doi.org/10.1038/nature16492.

[104] R. Zan, W. Ji, S. Qiao, H. Wu, W. Wang, T. Ji, B. Yang, S. Zhang, C. Luo, Y. Song, J. Ni, X. Zhang, Biodegradable magnesium implants: a potential scaffold for bone tumor patients, Sci. China Mater. 64 (2021) 1007–1020. https://doi.org/10.1007/s40843-020-1509-2.

[105] C. Redlich, A. Schauer, J. Scheibler, G. Poehle, P. Barthel, A. Maennel, V. Adams, T. Weissgaerber, A. Linke, P. Quadbeck, In vitro degradation behavior and biocompatibility of bioresorbable molybdenum, Metals (Basel). 11 (2021) 1–16. https://doi.org/10.3390/met11050761.

[106] K. TESAŘ, K. BALÍK, Z. SUCHARDA, A. JÄGER, Direct extrusion of thin Mg wires for biomedical applications, Trans. Nonferrous Met. Soc. China (English Ed. 30 (2020) 373–381. https://doi.org/10.1016/S1003-6326(20)65219-0.

[107] W. Roger N, Wire Technology: Process Engineering and Metallurgy, 2010. https://www.elsevier.com/books/wire-technology/wright/978-0-12-382092-1.

[108] A.L. Oppedal, H. El Kadiri, C.N. Tomé, S.C. Vogel, M.F. Horstemeyer, Anisotropy in hexagonal close-packed structures: Improvements to crystal plasticity approaches applied to magnesium alloy, Philos. Mag. 93 (2013) 4311–4330. https://doi.org/10.1080/14786435.2013.827802.

[109] J.Y. Wang, N. Li, R. Alizadeh, M.A. Monclús, Y.W. Cui, J.M. Molina-Aldareguía, J. LLorca, Effect of solute content and temperature on the deformation mechanisms and critical resolved shear stress in Mg-Al and Mg-Zn alloys, Acta Mater. 170 (2019) 155–165. https://doi.org/10.1016/j.actamat.2019.03.027.

[110] N. Stanford, M.R. Barnett, The origin of “rare earth” texture development in extruded Mg-based alloys and its effect on tensile ductility, Mater. Sci. Eng. A. 496 (2008) 399–408. https://doi.org/10.1016/j.msea.2008.05.045.

[111] A.J. Griebel, J.E. Schaffer, T.M. Hopkins, A. Alghalayini, T. Mkorombindo, K.O. Ojo, Z. Xu, K.J. Little, S.K. Pixley, An in vitro and in vivo characterization of fine WE43B magnesium wire with varied thermomechanical processing

conditions, J. Biomed. Mater. Res. - Part B Appl. Biomater. 106 (2018) 1987–1997. https://doi.org/10.1002/jbm.b.34008.

[112] M. Li, F. Benn, T. Derra, N. Kröger, M. Zinser, R. Smeets, J.M. Molina-Aldareguia, A. Kopp, J. LLorca, Microstructure, mechanical properties, corrosion resistance and cytocompatibility of WE43 Mg alloy scaffolds fabricated by laser powder bed fusion for biomedical applications, Mater. Sci. Eng. C. 119 (2021) 111623. https://doi.org/10.1016/j.msec.2020.111623.

[113] Y. TIAN, H. wei MIAO, J. lin NIU, H. HUANG, B. KANG, H. ZENG, W. jiang DING, G. yin YUAN, Effects of annealing on mechanical properties and degradation behavior of biodegradable JDBM magnesium alloy wires, Trans. Nonferrous Met. Soc. China (English Ed. 31 (2021) 2615–2625. https://doi.org/10.1016/S1003-6326(21)65680-7.

[114] H.F. Sun, H.Y. Chao, E. De Wang, Microstructure stability of cold drawn AZ31 magnesium alloy during annealing process, Trans. Nonferrous Met. Soc. China (English Ed. 21 (2011) s215–s221. https://doi.org/10.1016/S1003-6326(11)61581-1.

[115] G. Barati Darband, M. Aliofkhazraei, P. Hamghalam, N. Valizade, Plasma electrolytic oxidation of magnesium and its alloys: Mechanism, properties and applications, J. Magnes. Alloy. 5 (2017) 74–132. https://doi.org/10.1016/j.jma.2017.02.004.

[116] O. Jung, R. Smeets, P. Hartjen, R. Schnettler, F. Feyerabend, M. Klein, N. Wegner, F. Walther, D. Stangier, A. Henningsen, C. Rendenbach, M. Heiland, M. Barbeck, A. Kopp, Improved in vitro test procedure for full assessment of the cytocompatibility of degradable magnesium based on ISO 10993-5/-12, Int. J. Mol. Sci. 20 (2019). https://doi.org/10.3390/ijms20020255.

[117] A. Kopp, T. Derra, M. Müther, L. Jauer, J.H. Schleifenbaum, M. Voshage, O. Jung, R. Smeets, N. Kröger, Influence of design and postprocessing parameters on the degradation behavior and mechanical properties of additively manufactured magnesium scaffolds, Acta Biomater. 98 (2019) 23–35. https://doi.org/10.1016/j.actbio.2019.04.012.

[118] C.L. Chu, X. Han, J. Bai, F. Xue, P.K. Chu, Fabrication and degradation behavior of micro-arc oxidized biomedical magnesium alloy wires, Surf. Coatings Technol. 213 (2012) 307–312. https://doi.org/10.1016/j.surfcoat.2012.10.078.

[119] N. Dodyim, K. Yoshida, T. Murata, Y. Kobayashi, Drawing of of magnesium magnesium fine wire and and medical medical application application of of drawn drawn wire wire, Procedia Manuf. 50 (2020) 271–275. https://doi.org/10.1016/j.promfg.2020.08.050.

[120] X. Li, C. Shi, J. Bai, C. Guo, F. Xue, P.H. Lin, C.L. Chu, Degradation behaviors of surface modified magnesium alloy wires in different simulated physiological environments, Front. Mater. Sci. 8 (2014) 281–294. https://doi.org/10.1007/s11706-014-0257-5.

[121] M. Echeverry-Rendon, V. Duque, D. Quintero, S.M. Robledo, M.C. Harmsen, F. Echeverria, Improved corrosion resistance of commercially pure magnesium after its modification by plasma electrolytic oxidation with organic additives, J. Biomater. Appl. 33 (2018) 725–740. https://doi.org/10.1177/0885328218809911.

[122] K. van Gaalen, F. Gremse, F. Benn, P.E. McHugh, A. Kopp, T.J. Vaughan, Automated ex-situ detection of pitting corrosion and its effect on the mechanical integrity of rare earth magnesium alloy - WE43, Bioact. Mater. 8 (2022) 545–558. https://doi.org/10.1016/j.bioactmat.2021.06.024.

[123] ASTM G31-72: Standard Practice for Laboratory Immersion Corrosion Testing of Metals, 2004.

[124] W. Ali, M. Li, L. Tillman, T. Mayer, C. González, J. LLorca, and A. Kopp, Bioabsorbable WE43 Mg alloy wires modified by continuous plasma-electrolytic oxidation for implant applications. Part I: Processing, microstructure and mechanical properties, (2022).

[125] A.L. Yerokhin, X. Nie, A. Leyland, A. Matthews, S.J. Dowey, Plasma electrolysis for surface engineering, Surf. Coatings Technol. 122 (1999) 73–93. https://doi.org/10.1016/S0257-8972(99)00441-7.

[126] F. Simchen, M. Sieber, A. Kopp, T. Lampke, Introduction to plasma electrolytic oxidation-an overview of the process and applications, Coatings. 10 (2020). https://doi.org/10.3390/coatings10070628.

[127] M. Zheng, G. Xu, D. Liu, Y. Zhao, B. Ning, M. Chen, Study on the Microstructure, Mechanical Properties and Corrosion Behavior of Mg-Zn-Ca Alloy Wire for Biomaterial Application, J. Mater. Eng. Perform. 27 (2018) 1837–1846. https://doi.org/10.1007/s11665-018-3278-x.

[128] R.O. Hussein, X. Nie, D.O. Northwood, An investigation of ceramic coating growth mechanisms in plasma electrolytic oxidation (PEO) processing, Electrochim. Acta. 112 (2013) 111–119. https://doi.org/10.1016/j.electacta.2013.08.137.

[129] B. Zeller-Plumhoff, M. Gile, M. Priebe, H. Slominska, B. Boll, B. Wiese, T. Würger, R. Willumeit-Römer, R.H. Meißner, Exploring key ionic interactions for magnesium degradation in simulated body fluid – A data-driven approach, Corros. Sci. 182 (2021). https://doi.org/10.1016/j.corsci.2021.109272.

[130] Y. Jang, B. Collins, J. Sankar, Y. Yun, Effect of biologically relevant ions on the corrosion products formed on alloy AZ31B: An improved understanding of magnesium corrosion, Acta Biomater. 9 (2013) 8761–8770. https://doi.org/10.1016/j.actbio.2013.03.026.

[131] R.C. Zeng, L.Y. Cui, K. Jiang, R. Liu, B.D. Zhao, Y.F. Zheng, In Vitro Corrosion and Cytocompatibility of a Microarc Oxidation Coating and Poly(l -lactic acid) Composite Coating on Mg-1Li-1Ca Alloy for Orthopedic Implants, ACS Appl.

Mater. Interfaces. 8 (2016) 10014–10028. https://doi.org/10.1021/acsami.6b00527.

[132] J. Wang, F. Witte, T. Xi, Y. Zheng, K. Yang, Y. Yang, D. Zhao, J. Meng, Y. Li, W. Li, K. Chan, L. Qin, Recommendation for modifying current cytotoxicity testing standards for biodegradable magnesium-based materials, Acta Biomater. 21 (2015) 237–249. https://doi.org/10.1016/j.actbio.2015.04.011.

[133] C. González, J. Llorca, Micromechanical modelling of deformation and failure in Ti-6Al-4V/SiC composites, Acta Mater. 49 (2001) 3505–3519. https://doi.org/10.1016/S1359-6454(01)00246-4.

[134] B. Collard, F. Giuliani, G. Ingenbleek, G. Verbist, D. Dini, A fracture mechanics analysis of the micromechanical events in finite thickness fibre push-out tests, Theor. Appl. Fract. Mech. 121 (2022) 103441. https://doi.org/10.1016/j.tafmec.2022.103441.

[135] W. Ali, A. Kopp, C. González, J. Llorca, Strength of interface in bioresorbable poly-lactic acid / Mg fiber composites for orthopedic applications, in: Nanobrücken 2021 Nanomechanical Test. Conf., 2020.

[136] K. Van Gaalen, C. Quinn, M. Weiler, F. Gremse, F. Benn, P.E. Mchugh, T.J. Vaughan, A. Kopp, Predicting localised corrosion and mechanical performance of a PEO surface modified rare earth magnesium alloy for implant use through in-silico modelling, Bioact. Mater. 26 (2023) 437–451. https://doi.org/10.1016/j.bioactmat.2023.03.009.

[137] V.T. Bechel, N.R. Sottos, Application of debond length measurements to examine the mechanics of fiber pushout, J. Mech. Phys. Solids. 46 (1998) 1675–1697. https://doi.org/10.1016/S0022-5096(97)00040-9.

[138] S. Schönen, B. Jasper, J.W. Coenen, J. Du, T. Höschen, J. Riesch, G. Natour, R. Neu, C. Linsmeier, Insight into single-fiber push-out test of tungsten fiber-reinforced tungsten, Compos. Interfaces. 26 (2019) 107–126. https://doi.org/10.1080/09276440.2018.1475696.

[139] Z. Tang, C. Wang, Y. Yu, Failure response of fiber-epoxy unidirectional laminate under transverse tensile/compressive loading using finite-volume micromechanics, Compos. Part B Eng. 79 (2015) 331–341. https://doi.org/10.1016/j.compositesb.2015.04.054.

[140] M. Herráez, D. Mora, F. Naya, C.S. Lopes, C. González, J. Llorca, Transverse cracking of cross-ply laminates: A computational micromechanics perspective, Compos. Sci. Technol. 110 (2015) 196–204. https://doi.org/10.1016/j.compscitech.2015.02.008.

[141] O.T. Thomsen, Experimental Characterisation of Parameters Controlling the Compressive Failure of Pultruded Unidirectional Carbon Fibre Composites Experimental Characterisation of Parameters Controlling the Compressive Failure of Pultruded Unidirectional Carbon Fibre Co, Appl. Mech. Mater. 24–25

(2010). https://doi.org/10.4028/www.scientific.net/AMM.24-25.15.

[142] C.C. Chamis, Simplified Composite Micromechanics Equations for Strength, Fracture Toughness, Impact Resistance and Environmental Effects, in: 39th Annu. Conf. Soc. Plast. Ind., 1984.

[143] P. Prabhakar, A.M. Waas, Micromechanical modeling to determine the compressive strength and failure mode interaction of multidirectional laminates, Compos. Part A Appl. Sci. Manuf. 50 (2013) 11–21. https://doi.org/10.1016/j.compositesa.2013.03.006.

[144] L.A. Carlsson, D.F. Adams, R.B. Pipes, Basic experimental characterization of polymer matrix composite materials, Polym. Rev. 53 (2013) 277–302. https://doi.org/10.1080/15583724.2013.776588.

[145] C. González, J. LLorca, Mechanical behavior of unidirectional fiber-reinforced polymers under transverse compression: Microscopic mechanisms and modeling, Compos. Sci. Technol. 67 (2007) 2795–2806. https://doi.org/10.1016/j.compscitech.2007.02.001.

[146] E. Totry, J.M. Molina-Aldareguía, C. González, J. LLorca, Effect of fiber, matrix and interface properties on the in-plane shear deformation of carbon-fiber reinforced composites, Compos. Sci. Technol. 70 (2010) 970–980. https://doi.org/10.1016/j.compscitech.2010.02.014.

[147] D.G. Lee, N. Suh, Axiomatic design and fabrication of composite structures, 2006.

[148] A. Oyane, H. Kim, T. Furuya, T. Kokubo, T. Miyazaki, T. Nakamura, Preparation and assessment of revised simulated body, J. Biomed. Mater. Res. - Part A. 65A (2003) 188–195.

[149] ISO 15814:1999 Implants for surgery — Copolymers and blends based on polylactide — In Vitro degradation testing, (1999).

[150] G.L. Song, 1 - Corrosion electrochemistry of magnesium (Mg) and its alloys, Woodhead Publishing Limited, 2011. https://doi.org/10.1533/9780857091413.1.3.

[151] N.T. Kirkland, N. Birbilis, M.P. Staiger, Assessing the corrosion of biodegradable magnesium implants: A critical review of current methodologies and their limitations, Acta Biomater. 8 (2012) 925–936. https://doi.org/10.1016/j.actbio.2011.11.014.

[152] C. Wang, W. Xu, D. Höche, M.L. Zheludkevich, S. V. Lamaka, Exploring the contribution of oxygen reduction reaction to Mg corrosion by modeling assisted local analysis, J. Magnes. Alloy. (2022). https://doi.org/10.1016/j.jma.2022.09.031.

[153] D. Mei, S. V. Lamaka, X. Lu, M.L. Zheludkevich, Selecting medium for

corrosion testing of bioabsorbable magnesium and other metals – A critical review, Corros. Sci. 171 (2020) 108722. https://doi.org/10.1016/j.corsci.2020.108722.

[154] N.A. Weir, F.J. Buchanan, J.F. Orr, G.R. Dickson, Degradation of poly-L-lactide. Part 2: increased temperature accelerated degradation, Proc IME H J Eng Med. 218 (2004) 321–30.

[155] C. Wang, D. Mei, G. Wiese, L. Wang, M. Deng, S. V. Lamaka, M.L. Zheludkevich, High rate oxygen reduction reaction during corrosion of ultra-high-purity magnesium, Npj Mater. Degrad. 4 (2020) 1–5. https://doi.org/10.1038/s41529-020-00146-1.

[156] R. Vaid, E. Yildirim, M.A. Pasquinelli, M.W. King, Hydrolytic degradation of polylactic acid fibers as a function of ph and exposure time, Molecules. 26 (2021). https://doi.org/10.3390/molecules26247554.

[157] A. Koterwa, I. Kaczmarzyk, S. Mania, M. Cieslik, R. Tylingo, T. Ossowski, R. Bogdanowicz, P. Niedziałkowski, J. Ryl, The role of electrolysis and enzymatic hydrolysis treatment in the enhancement of the electrochemical properties of 3D-printed carbon black/poly(lactic acid) structures, Appl. Surf. Sci. 574 (2022). https://doi.org/10.1016/j.apsusc.2021.151587.

[158] H. Cai, J. Meng, X. Li, F. Xue, C. Chu, C. Guo, J. Bai, In vitro degradation behavior of Mg wire/poly(lactic acid) composite rods prepared by hot pressing and hot drawing, Acta Biomater. (2019). https://doi.org/10.1016/J.ACTBIO.2019.05.059.

[159] J. Dai, C. Wu, J. Yang, L. Zhang, Q. Dong, L. Han, X. Li, J. Bai, F. Xue, P.K. Chu, C. Chu, Poly-lactic acid coatings on the biomedical WE43 Mg alloy: Protection mechanism and ion permeation effects, Prog. Org. Coatings. 177 (2023) 107427. https://doi.org/10.1016/j.porgcoat.2023.107427.

[160] X. Lu, S.P. Sah, N. Scharnagl, M. Störmer, M. Starykevich, M. Mohedano, C. Blawert, M.L. Zheludkevich, K.U. Kainer, Degradation behavior of PEO coating on AM50 magnesium alloy produced from electrolytes with clay particle addition, Surf. Coatings Technol. 269 (2015) 155–169. https://doi.org/10.1016/j.surfcoat.2014.11.027.

[161] I.O. for Standardization, ISO 10993-5 Tests for in vitro cytotoxicity, Biokhimiya. 40 (2009) 984–989.

[162] ISO 10993 Part 12: Sample preparation and reference materials, Semicond. Semimetals. 13 (1978) 1–52. https://doi.org/10.1016/S0080-8784(08)60069-1.

[163] S.K. Lee, C.-M. Han, W. Park, I.H. Kim, Y.K. Joung, D.K. Han, Synergistically enhanced osteoconductivity and anti-inflammation of PLGA/β-TCP/Mg(OH)2 composite for orthopedic applications, Mater. Sci. Eng. C. 94 (2019) 65–75. https://doi.org/10.1016/J.MSEC.2018.09.011.

[164] K. Isama, T. Tsuchiya, Enhancing effect of poly (l -lactide) on the differentiation of mouse, 24 (2003) 3303–3309. https://doi.org/10.1016/S0142-9612(03)00216-3.

[165] M. Li, P. He, Y. Wu, Y. Zhang, H. Xia, Y. Zheng, Y. Han, Stimulatory effects of the degradation products from Mg-Ca-Sr alloy on the osteogenesis through regulating ERK signaling pathway, Nat. Publ. Gr. (2016) 1–13. https://doi.org/10.1038/srep32323.

[166] S. Aldrich, Technisches Datenblatt - Minimum Essential Medium, (n.d.). https://www.sigmaaldrich.com/DE/de/specification-sheet/SIGMA/M4655.

[167] Y. Xin, T. Hu, P.K. Chu, Influence of test solutions on in vitro studies of biomedical magnesium alloys, J. Electrochem. Soc. 157 (2010) 238–243. https://doi.org/10.1149/1.3421651.

[168] R.J. Miron, Y. Zhang, Osteoinduction: A Review of Old Concepts with New Standards, J. Dent. Res. (2012). https://doi.org/10.1177/0022034511435260.

[169] G.R. Beck, B. Zerler, E. Moran, Phosphate is a specific signal for induction of osteopontin gene expression, (2000). https://doi.org/10.1073/pnas.140021997.

[170] H. Man, S. Wu, P.K. Chu, S. Han, K.D.K. Luk, K.M.C. Cheung, K.W.K. Yeung, Biomaterials Low-modulus Mg / PCL hybrid bone substitute for osteoporotic fracture fi xation, Biomaterials. 34 (2013) 7016–7032. https://doi.org/10.1016/j.biomaterials.2013.05.062.

[171] P. Gao, B. Fan, X. Yu, W. Liu, J. Wu, L. Shi, D. Yang, L. Tan, P. Wan, Y. Hao, S. Li, W. Hou, K. Yang, X. Li, Z. Guo, Bioactive Materials Biofunctional magnesium coated Ti6Al4V sca ff old enhances osteogenesis and angiogenesis in vitro and in vivo for orthopedic application, Bioact. Mater. 5 (2020) 680–693. https://doi.org/10.1016/j.bioactmat.2020.04.019.

[172] Y. Liu, A. Beyer, R. Aebersold, On the Dependency of Cellular Protein Levels on mRNA Abundance, Cell. 165 (2016) 535–550. https://doi.org/10.1016/j.cell.2016.03.014.

[173] A. Galow, A. Rebl, D. Koczan, S.M. Bonk, W. Baumann, J. Gimsa, Increased osteoblast viability at alkaline pH in vitro provides a new perspective on bone regeneration, Biochem. Biophys. Reports. 10 (2017) 17–25. https://doi.org/10.1016/j.bbrep.2017.02.001.